ASSESSING THE IMPACTS OF CLIMATE CHANGE ON CLIMATIC EXTREMES AND HYDROLOGICAL REGIMES IN THE CONGO RIVER BASIN USING STATISTICAL ANALYSIS AND HYDROLOGICAL MODELLING

SARA KARAM

Thesis submitted to the University of Ottawa
in partial Fulfillment of the requirements for the
Doctorate in Philosophy degree in Environmental Engineering

Department of Environmental Engineering
Faculty of Engineering
University of Ottawa

DIRECTEUR DE LA THÈSE / THESIS SUPERVISOR

Dr. Ousmane Seidou (University of Ottawa)

EXAMINATEURS (EXAMINATRICES) DE LA THÈSE /
THESIS EXAMINERS

Dr. Musandji Fuamba (Polytechnique Montréal)

Dr. Colin Rennie (University of Ottawa)

Dr. Majid Mohammadian (University of Ottawa)

Dr. Duminda Perera (University of Ottawa)

March 11th, 2024

DATE DE LA SOUTENANCE / DATE OF ORAL DEFENCE

Abstract

The Congo River Basin (CRB) in central Africa holds tremendous environmental importance due to its rich biodiversity, serving as a haven for countless unique plant and animal species. It stands as one of the world's most biodiverse regions, and safeguarding this diversity is critical for global conservation efforts. The basin provides a crucial source of freshwater for millions of people in Central Africa, supporting their livelihoods, agriculture, and industrial needs. The CRB encompasses a vast drainage area that crosses nine political boundaries, including countries like Angola, Burundi, Central African Republic, Democratic Republic of Congo, Cameroon, Republic of Congo, Rwanda, Tanzania, and Zambia. Within this basin lies the world's second-largest rainforest, which plays a pivotal role in the global carbon cycle. Similar to other rainforests, its structure and distribution are likely to be affected by shifts in regional rainfall patterns linked to global warming. This basin, along with the western Pacific Ocean and the Amazon basin, serves as a significant source of major storms, while also experiencing periods of drought. Therefore, a comprehensive study of climatic changes in the region is imperative to provide valuable insights for mitigation and adaptation planning. Despite its significance, the basin has received limited attention in hydrological and climate research, leaving it largely understudied. Extreme events in the Congo basin, which are tied to rainfall variability, may intensify due to climate change, posing challenges to the well-being of local communities. Hence, it is of utmost importance to examine the present and future trends of extreme events like precipitation and drought frequency and intensity for the preservation of local infrastructure and sustainable livelihoods. This thesis contributes to better water resources management in the CRB by a) assessing the impacts of climate change on climatic extremes in the Congo basin from the present day to the year 2100 and b) developing, calibrating, and validating a Soil and Water Assessment Tool (SWAT) model to

assess the impacts of climate change on hydrological regimes in the CRB and c) developing an efficient method to generate flood maps in a data-scarce environment.

The first part of the thesis deals with the challenge of evaluating the anticipated shifts in selected hydroclimatic extremes, some of which are proxies for rainfall-triggered flash floods and drought. These indicators encompass total annual precipitation (PCPTOT), the count of days with rainfall exceeding 20 mm (PCP20), the standardized precipitation index (SPI), and the standardized precipitation-evapotranspiration index (SPEI). To perform this analysis, the selected indices were computed using the statistically downscaled data from eleven Regional Climate Models (RCMs) participating in the Coordinated Downscaling Experiment (CORDEX-AFRICA). This was done under two distinct Representative Concentration Pathways: RCP 8.5, a high emissions scenario, and RCP 4.5, a moderate emissions scenario.

The second part of the thesis utilizes the results from the climate study to examine future modifications of the hydrological regime of the CRB and discuss the potential impacts of these projected changes. To achieve this, a SWAT model for the CRB was calibrated and validated. Subsequently, the calibrated model was utilized to assess variations in discharge throughout all segments of the basin.

The third part of the thesis deals with the development of an innovative and computationally efficient approach to mapping floods in the Oubangui River section of the Congo Basin, as an alternative to the resource-intensive 2D hydrodynamic modeling. The methodology involves extracting surface water data from Sentinel-1 Synthetic Aperture Radar (SAR) imagery and establishing a relationship between pixels and water discharge values. This information enables the creation of a spatial pixel probability distribution, facilitating accurate mapping of flooded and dry areas. By harnessing the capabilities of Sentinel-1 SAR imagery, this novel approach aims to provide a more accurate and timely flood assessment for the Oubangui River region within the Congo Basin. The fusion of remote sensing data and advanced analytical methods will contribute to more effective flood monitoring and mitigation strategies.

Acknowledgements

I would like to express my gratitude to my supervisor, Dr. Ousmane Seidou for all of his support, encouragement, and guidance during my studies. Dr. Seidou's ability to provide constructive guidance and constructive feedback, all while nurturing my independence as a researcher, has been an invaluable gift. I have not only gained an exceptional academic mentor but also a role model who embodies the qualities of a dedicated researcher.

I would like to thank my thesis evaluation committee members Dr. Musandji Fuamba, Dr. Colin Rennie, Dr. Majid Mohammadian, and Dr. Duminda Perera for providing important and essential suggestions and comments on my thesis.

I would also like to convey my appreciation to the University of Ottawa for awarding me with academic scholarships, which have contributed towards the success of achieving my PhD.

I would like to thank my mother, Naima, and my father, Abdellah, who gave me continuous love and support while I pursued this degree, and throughout my entire life. Without their constant encouragement, I would not be able to produce this piece of scientific work.

Thank you to my brother Yassin and to my sister Leila for all kinds of help and support. My heartfelt appreciation goes out to all those who have played a role in my PhD studies. While words may not fully capture my gratitude, I want to convey my sincere thanks for everything.

To my mother and father

Content

List of Figures

List of Tables

List of Acronyms

ARS	Agricultural Research Service
ASF	Alaska Satellite Facility
BSVG	Barren or sparsely vegetated
CCM3	Community Climate Model version 3.6
CDF	Cumulative Distribution Function
CMIP3	Climate Model Intercomparison Project phase 3
CMIP5	Climate Model Intercomparison Project phase 5
CMS	Cubic Meters Per Second
CN	Curve Number
CORDEX	Coordinated Downscaling Experiment
CRB	Congo River Basin
CRDY	Dryland cropland and pasture
CRGR	Mosaic cropland/grassland
CRREBaC	Congo basin Water Resources Research Center
CRWO	Mosaic cropland/woodland
DJF	December-February Season
DRC	Democratic Republic of Congo
ERI	Extreme Rainfall Indices
ESA	European Space Agency
ETCCDI	The Expert Team on Climate Change Detection and Indices
FCRF	Fully Connected Conditional Random Field
FODB	Deciduous broad-leaf forest
FOEB	Evergreen broad-leaf forest
FOMI	Mixed forest
GCM	Global Climate Model
GFM	Global Flood Mapper

GGMM	Generalized Gaussian Mixture Model
GRAS	Grassland
GRD	Ground Range Detected
GW	Groundwater
HMD	Humidity
HRU	Hydrological Response Unit
ID	Identification
IDW	Inverse Distance Weighting
KNN	K-Nearest Neighbor
LOCA	Localized Constructed Analogs
MD	Mean Flood Date
N-S	Nash–Sutcliffe Efficiency Coefficient
PBIAS	Percentage Bias
PCP	Precipitation
PCP20	Number of days with precipitation exceeding 20 mm
PCPTOT	Total annual precipitation
PDF	Probability Distribution Function
POT	Peaks-Over-Threshold
Q-Q	Quantile–Quantile
RCM	Regional Climate Model
RCP	Representative Concentration Pathway
RMSE	Root-Mean-Square-Error
RSDS	Solar Radiation
SAR	Synthetic Aperture Radar
SAVA	Savanna
SHRB	Shrubland
SNAP	Sentinel Application Platform
SPEI	Standard Precipitation-Evapotranspiration Index

SPI	Standard Precipitation Index
SRI	Standardized Runoff Index
SUFI2	Sequential Uncertainty Fitting program
SWAT	Soil and Water Assessment Tool
SWATCUP	Soil and Water Assessment Tool Calibration and Uncertainty Programs
SWE	Surface Water Extent
SWH	Surface Water Height
TIFF	Tagged Image File Format
TMP	Temperature
TRMM	Tropical Rain Measuring Mission
UCB	Upper Congo Basin
URMD	Residential area (urban)
USDA	United States Department of Agriculture
VH	Vertical-Horizontal
WATR	Water
WFDEI	Watch Forced Era Interim
WMO	World Meteorological Organization
WND	Wind Speed

List of Symbols

$Y_{seasonal,obs}$	Year of observed rainfall for a specific timeseries
$Y_{seasonal,WFDEI}$	Year of WFDEI rainfall for a specific timeseries
Y_{sim}	Year of simulated rainfall
STA_i	Station number indicator
F_{OBS}	Observed calibrated period
F_{RCM}	RCM output
X_{CORR}	Corrected variable
X_{RCM}	Extracted value from the raw RCM simulations
RR_{ij}	Daily precipitation on wet days
S_i	Standard deviation of precipitation
ET_0	The reference evapotranspiration
PCPTOT,I	Sum of precipitation for a given year i
PCPTOT,m	Mean value of precipitation over a reference period
$CDF^{-1}_{norm(0,1)}$	Inverse cumulative distribution function of the normal distribution
$CDF_{log-logistic}$	Cumulative distribution function of the log-logistic distribution
SW_t	Soil water content at a time step, t.
SW_0	Soil water content at time 0
R_{day}	Precipitation amount on a specific day
Q_{surf}	Surface runoff
E_a	Evapotranspiration
w_{seep}	Water entering the vadose zone from the soil profile
Q_{gw}	Return flow on a specific day
S	Soil moisture content
P	Total precipitation
Q	Discharge
g	Objective function used to determine model calibration effectiveness

α	Regression constant
β	Technical coefficient attached to the variable *b*
m	Number of parameters
$P(x,y)$	Percent chance that a pixel at coordinate (x,y) will be labeled as water
$B(x,y)$	Number of pixel values labeled as water
T	Total number of images in the Sentinel-1 radar image set
ΔX	Delta change between model-simulated and observed values
X_{model}	Model-simulated variable
a	Scaling factor
λE	Latent heat flux density (MJ $m^{-2}d^{-1}$)
E	Depth rate evaporation
Δ	Slope of saturation vapor pressure-temperature curve (kPa $^{\circ}C^{-1}$)
H_{net}	Net radiation (MJ $m^{-2}d^{-1}$)
G	Heat flux density to the ground (M.J. $m^{-2}d^{-1}$)
ρ_{air}	Air density (kg/m^{-3})
c_p	Specific heat at constant pressure (MJ kg^{-1} $^{\circ}C^{-1}$)
e_z^0	Saturation vapor pressure of air at height z (kPa)
e_z	Water vapor pressure of air at height z (kPa)
Υ	Psychrometric constant (kPa $^{\circ}C^{-1}$)
r_c	Plant canopy resistance (s/m
r_a	Aerodynamic resistance/diffusion resistance of the air layer (s/m)
CO_2	Concentration of carbon dioxide in part per millions (400)

Chapter 1

Introduction

1.1 Background

The Congo River Basin (CRB), situated in central Africa (see Figure 1.1), has a vast drainage area of around 3.7 million square kilometers. It ranks as the world's second-largest river basin, second only to the Amazon (Tshimanga et al. 2021). This basin encompasses nine political boundaries, including Angola, Burundi, Central African Republic, Democratic Republic of Congo, Cameroon, Republic of Congo, Rwanda, Tanzania, and Zambia. The Congo Basin also houses the world's second-largest rainforest, which plays a crucial role in the global carbon cycle (Paris et al., 2022). Climate change, driven by anthropogenic factors, has begun to exert its influence on the CRB. Alterations in precipitation patterns, temperature, and increased variability in weather conditions have disrupted the hydrological and climatic regimes of the basin (Tshimanga et al., 2014). This has resulted in pronounced shifts in the patterns of rainfall, floods, and droughts, further impacting the local communities and the fragile ecosystem. It is increasingly clear that the changes in climate and their associated effects on the basin, pose a serious threat to both human and ecological systems in the region (Malhi and Wright, 2004).

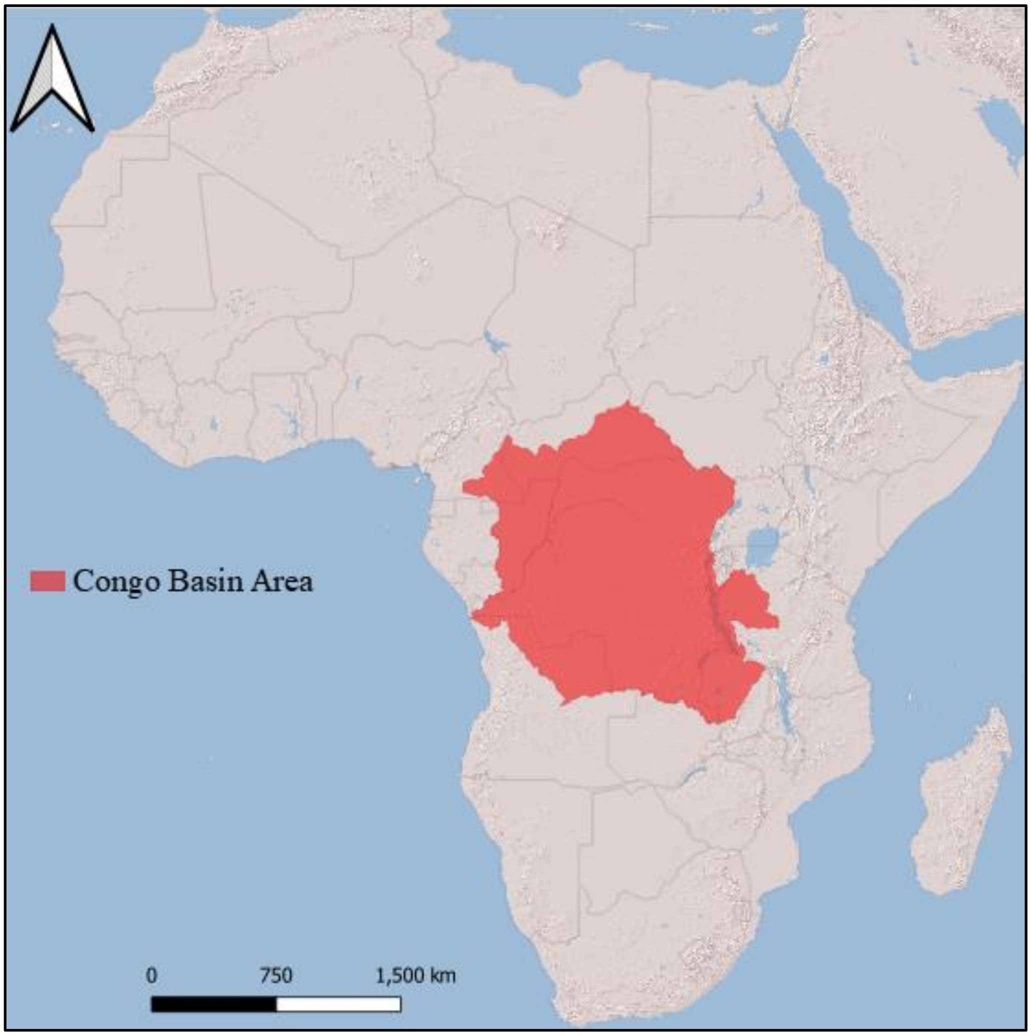

Figure 1.1: The delineated Congo River Basin area located in central Africa

Figure 1.2 shows a closeup of the delineated Congo basin along with its associated river network, and the location of the discharge outlet, bordering the Atlantic Ocean.

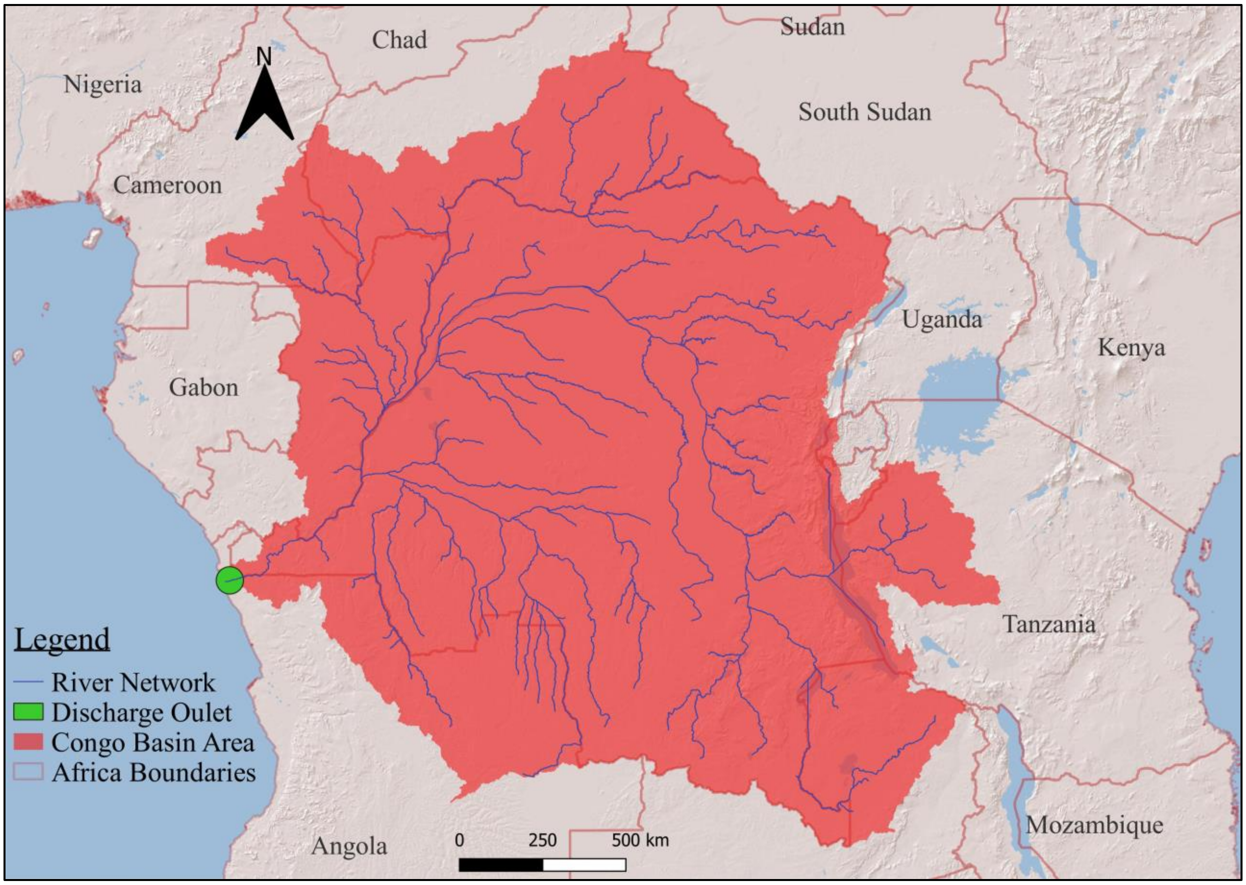

Figure 1.2: Congo basin area with river network and discharge outlet location

Over the past 3,000 years, historical records indicate that the CRB's rainforest has shown a tendency to contract and experience shifts in its composition during dry periods (Lewis et al., 2009 & Malhi et al., 2013). Between 1960 and 2019, the countries in the Congo Basin witnessed over 11,566,029 people affected by flooding, resulting in 3,062 casualties and an estimated total economic loss of 96 billion USD (EM-DAT, 2020).

Despite its ecological and socio-economic significance, the CRB has remained relatively understudied in the context of hydrological and climate change research. Previous research of the basin has primarily focused on either extreme events in the recent past (Ndehedehe et al., 2019 & Mao et al., 2019) or average annual and seasonal precipitation and evapotranspiration in the future (Creese et al., 2019). The only study dealing with extreme events in the future (Onyutha, 2020) focused on east Africa and only considered rainfall-related indices. Furthermore, previous studies have attempted to enhance flood mapping accuracy and efficiency through simplified approaches, yet often lacked comprehensive validation against ground truth data, undermining result reliability. Some studies introduced complex flood mapping methods, achieving high accuracy but making them less user-friendly and less accessible to non-technical users, limiting their practical use.

This study aims to conduct an in-depth analysis of the current and future trends in extreme events and hydrological regimes, including precipitation patterns and the frequency and intensity of droughts, as well as the potential increase and decrease of future flood extent. This analysis spans from a historical reference period of 1976-2005 to three future periods; Period 1 (P1): 2011-2040, Period 2 (P2): 2041-2070, and Period 3 (P3): 2071-2100.

Climate change modeling uses mathematical and computational tools to simulate and project how the earth's climate system will respond to changes in factors like greenhouse gas concentrations, solar radiation, and other environmental influences. These models use complex equations, statistical analysis, and data to forecast future climate patterns, providing valuable insights into the potential impacts of climate change. The assessment of extreme weather events can be utilized to better understand and predict the consequences of these events. In this context, several key climate indices are employed to quantify and analyze various aspects of climate extremes. Total annual precipitation (PCPTOT), which quantifies the amount of rainfall over an entire year, offers valuable insights into changes in precipitation patterns and water resource availability. The number of days with precipitation exceeding 20 mm (PCP20) provides critical information about the frequency of heavy rainfall events, which can lead to flash-flooding and other water-related hazards. Additionally, the Standard Precipitation Index (SPI) measures precipitation anomalies, helping to identify periods of drought or excessive rainfall. The Standard Precipitation-Evapotranspiration Index (SPEI) incorporates evapotranspiration, making it a robust tool for assessing water availability, as it considers not only precipitation but also the influence of temperature on water demand and supply. These indices are fundamental in monitoring and understanding the changing dynamics of extreme weather events under the influence of climate change, aiding in the development of strategies for adaptation and mitigation.

High-quality input data is essential for a hydrological model to yield accurate outputs. Nevertheless, modeling large area watersheds can become particularly challenging in regions characterized by data scarcity, where insufficient or entirely absent data pose a significant obstacle to model development. This scarcity of data is a prevalent issue in many developing countries, often due to financial limitations and security concerns that hinder the collection of reliable and comprehensive datasets (Haque et al., 2019). Consequently, model developers often resort to leveraging secondary data sources for the construction of their models. In this context, the utilization of the Watch Forced Era Interim (WFDEI) reanalysis data set and temporal disaggregation techniques can provide valuable alternatives to address data limitations and enhance the quality of model inputs.

Statistical downscaling is a vital technique in climate science, aiming to bridge the gap between the coarse-scale predictions provided by Global Climate Models (GCMs) and the finer-scale information needed for regional and local decision-making. One commonly used approach for reducing biases in GCM-RCM (Regional Climate Model) precipitation predictions is quantile mapping (Hakala et al., 2018). This method involves statistical adjustments that align the probability distribution of simulated precipitation data with historical observations, helping to correct systematic errors and biases in the model's outputs (Onyutha, 2020). By doing so, quantile mapping improves the reliability of downscaled precipitation projections, making them more valuable for assessing potential impacts on water resources, agriculture, and other critical sectors.

Hydrological modeling is a fundamental component of water resource management and environmental planning, and relies on tools such as the Soil and Water Assessment Tool (SWAT) developed by the Agricultural Research Service (ARS) of the United States Department of Agriculture (USDA) by Arnold et al. (1998). SWAT is a comprehensive computer model that can simulate discharge inside of a watershed, helping to understand and predict their behaviors. It takes into account factors such as rainfall, evapotranspiration, soil properties, land use, and land cover to generate insights into water flow, sediment transport, and nutrient dynamics within a given area. Calibration and validation of such models are key, such that the model's parameters are adjusted to fit observed data, ensuring that the model's predictions closely match real-world conditions (Sridhar et al., 2021). This process enhances the model's accuracy and reliability, making it an instrumental tool for water resource planning, flood risk assessment, and environmental impact studies.

Hydrological modeling using Sentinel-1 Synthetic Aperture Radar (SAR) imagery has emerged as a powerful tool for understanding and managing water resources and environmental systems. SAR technology offers a unique advantage by providing all-weather imaging capabilities, making it particularly valuable for monitoring surface water dynamics, such as river discharge and flood mapping (Li et al., 2018 & Vekaria et al., 2023). By capturing radar reflections from the Earth's surface, SAR imagery can detect changes in water levels, flow patterns, and flood extents (Kitambo et al., 2022). This data can be used for calibrating and validating hydrological models, and enhancing our ability to predict and respond to hydrological events like floods, droughts, and other environmental phenomena derived from climate variability. The integration of SAR technology into hydrological modeling has greatly improved our capacity to address water-related challenges and support sustainable water resource management in various regions worldwide.

1.2 Objectives

The objective of this study is to develop tools that can improve water resources management in the CRB.

The specific objectives are:

- Develop a methodology that allows to assess future changes from the present day to the year 2100 in four selected extreme climatic indices used as proxies to rainfall-induced floods and drought. The methodology has to be applicable in a data-scarce environment such as the CRB;

- Develop, calibrate, and validate a SWAT model in order to assess future modifications of the hydrological regime of the CRB and qualitatively discuss the potential socio–economic impacts of these projected changes for three future periods: 2011–2041, 2041–2070, and 2071–2100;
- Develop a computationally efficient approach to mapping floods in the Oubangui River section of the Congo Basin by combining Sentinel-1 SAR imagery with a meticulously calibrated and validated SWAT model.

1.3 Scope of the Study

Integrated water management is a complex challenge, especially in the CRB, a region characterized by a variety of pressing issues. In this thesis, we will create tools designed to enhance decision-makers' comprehension and forecasting capabilities related to climate variability, hydrological changes, and flood extent within the CRB. These tools will be used to illustrate their capacity to deliver improved information within the CRB. However, it is important to note that our objective is not to assess or propose a specific water management strategy for the CRB. Flood risk in the study is assessed using precipitation indices or an empirical relationship between flooded area and river discharge – there is no modeling of water propagation on the land surface using a hydraulic model.

1.4 General Methodology

The general methodology of the first paper can be outlined as follows:

1. Data Screening and Temporal Disaggregation:

In the initial phase, monthly observed precipitation and temperature time series are subject to screening. The selected time series then undergo temporal disaggregation using the fragment method to transform them from a monthly time series into daily time series. The observed precipitations were complemented using global precipitation sources.

2. Statistical Downscaling of precipitation and temperature time series

The second phase involves the statistical downscaling of daily precipitation and temperature time series. This is achieved through quantile mapping, utilizing the outputs of eleven RCM/GCM combinations under both RCP 4.5 and RCP 8.5 scenarios. The outcome provides downscaled and bias-corrected precipitation and temperature time series, representing historical, present, and future conditions from 1976 to 2100.

3. Downscaling of Additional Variables:

Daily humidity, wind speed, and solar radiation time series are downscaled using the nearest-neighbor approach.

4. Selection of indices of extreme events:

The third and final phase focuses on the selection of four indices for assessing low and high precipitation extremes. These indices are analyzed across a reference period (1976-2005) and three future study periods:

- Future Period 1: 2011-2040
- Future Period 2: 2041-2070
- Future Period 3: 2071-2100

5. Estimation of evapotranspiration:

Present and future daily maximum temperature, daily minimum Temperature (TMP), Humidity (HMD), Wind speed (WND), and Solar radiation (RSDS) are employed to assess both present and future evapotranspiration.

6. SPEI Index Development:

Finally, the combination of HMD, WND, RSDS, and daily PCP is utilized to develop the Standardized Precipitation Evapotranspiration Index (SPEI). This comprehensive index contributes to the overall understanding of hydrological conditions by integrating multiple meteorological variables.

This multi-phase methodology enables a thorough evaluation of precipitation and temperature changes over specific time periods, facilitating a comprehensive assessment of future hydrological conditions in the watershed.

The general methodology of the second paper can be outlined as follows:

1. Model Setup with SWAT and ArcSWAT:

A SWAT model was developed using a total of 223 delineated sub-watersheds and 223 Hydrological Response Units (HRUs), based on specified locations of outlets and the HRU definition method and land use characteristics of the CRB. The remainder of the model development consists of setting up and calibrating the model, validating the model's predictions, and analyzing and interpreting the results to inform land use and management decisions.

2. Model Calibration and Validation:

Calibration and validation constitute crucial phases in the model development process. Calibration involves adjusting model parameters and input data to enhance prediction accuracy. Validation, on the other hand, assesses the model's performance using additional data not utilized in the calibration. These steps ensure that the model accurately represents the simulated processes and provide insights into potential biases or errors under different conditions.

3. Sensitivity Analysis Using SUFI2 Algorithm:

The study employs the SUFI2 (Sequential Uncertainty Fitting) algorithm within the SWATCUP program for both calibration and sensitivity analysis. Sensitivity analysis evaluates the model's responsiveness to changes in various input parameters. This involves altering one parameter while keeping others constant. The impact of the altered parameter is then assessed using statistical measures such as t-stat and p-value, determined through multiple regression analysis.

These steps collectively contribute to a robust understanding of the model's performance and its applicability in informing land use and management decisions.

The general methodology of the third paper can be outlined as follows:

1. Sentinel-1 Image Acquisition and Processing:

A Sentinel-1 image is a synthetic aperture radar (SAR) observation captured by the European Space Agency's Sentinel-1 satellite, providing all-weather, day-and-night Earth surface monitoring for various applications such as agriculture, forestry, and disaster management. The initial step involves acquiring Sentinel-1 satellite images specific to the study area. These images are processed using techniques tailored for surface water extraction. Pre-processing steps include radiometric calibration, speckle filtering, and geometric correction to ensure the images are suitable for subsequent analysis.

2. Histogram Analysis and Threshold Determination:

Following image processing, a histogram analysis is conducted to understand the pixel intensity distribution. Subsequently, an appropriate threshold is determined to create a binary pixel image of the study area. In this binary image, each pixel is assigned either a "water" or "land" classification based on its intensity level.

3. SWAT Simulation and Pixel-Discharge Relationship:

The SWAT simulation discharge output from the second paper is utilized to establish a relationship between discharge values and the corresponding number of water pixels. This pixel-discharge relationship allows for the translation of discharge data into a spatial representation, where each discharge value corresponds to a specific number of water pixels within the study area.

4. Spatial Pixel Probability Distribution:

The pixel-discharge relationship is integrated into a spatial pixel probability distribution. This distribution reflects the likelihood of encountering water pixels at different locations within the study area based on SWAT simulation discharge values. This probabilistic mapping forms the foundation for subsequent analyses.

5. Remapping of Flooded or Dry Areas:

Leveraging the spatial pixel probability distribution, the study area is remapped to distinguish between flooded and dry areas. This involves assigning a likelihood of water presence to each pixel, allowing for the creation of a spatial representation highlighting areas prone to flooding and those that remain dry.

6. Accuracy Assessment and discussion:

The accuracy of the developed method is assessed through comparing the model's predictions with reference data. A detailed analysis and discussion of the results is conducted to explore the insights gained from the spatial representation of surface water, and considerations for the method's applicability and limitations.

1.5 Novelty

This research demonstrates its novelty in the following aspects:

1. Originality in Terms of the Nature of Work:
    - The area modeled in this study is a large floodplain of about 3.7M km2. Model setup, simulation, and calibration of such a large area are rare especially in a region where data scarcity is a major challenge. The authors had to resort to alternative methodologies to derive climatic data.
    - By using four specific extreme climatic indices, the study provides a unique perspective on understanding the effects of climate change on extreme climatological events in the CRB.
    - First ever substantial time frame assessment of the CRB (from the present day to the year 2100), assessing future changes in extreme climatic events. The inclusion of such a long-term perspective is unique and valuable for understanding the long-reaching impacts of climate change on the CRB.

- First in-depth long-term examination of the hydrological regime of the CRB in correlation with socio-economic implications for three distinct future periods.
- First geospatially specific assessment of the CRB, visually indicating long-term vulnerabilities to climate change-induced changes in river discharge under RCP 4.5 and RCP 8.5. This level of detail and geographic specificity is unique and highly valuable for targeted adaptation and mitigation strategies in the region.
- First-ever satellite derived flood map of the CRB.

2. Originality in Terms of Methods/Approaches Taken:

- The study utilizes a combination of eleven RCMs from the Coordinated Downscaling Experiment (CORDEX-AFRICA) and two Representative Concentration Pathways (RCP 8.5 and RCP 4.5) to project future climate scenarios in the CRB.
- The combination of the applications used, including temporal disaggregation, quantile mapping for statistically downscaling precipitation and temperature, as well as the use of K-nearest neighbor downscaling for wind speed, solar radiation, and relative humidity.
- Combination of SWAT model and Sentinel-1 SAR imagery to project future flood extent in order to efficiently generate flood maps.
- Despite the observed rise in precipitation, the novelty of this study lies in its counterintuitive finding that the CRB is projected to experience an increase in

drought conditions, as indicated by the Standardized Precipitation Evapotranspiration Index (SPEI).

1.6 Outcome

The main outcomes of the present thesis are two published and one submitted journal papers. The papers form Chapters 4-6 of this thesis. The papers are as follows:

- Karam, S., Seidou, O., Nagabhatla, N., Perera, D., & Tshimanga, R. M. (2022). Assessing the impacts of climate change on climatic extremes in the Congo River Basin. Climatic Change, 170(3-4), 40.
- Karam, S., Zango, B. S., Seidou, O., Perera, D., Nagabhatla, N., & Tshimanga, R. M. (2023). Impacts of Climate Change on Hydrological Regimes in the Congo River Basin. Sustainability, 15(7), 6066.
- Karam, S., Seidou, O., Zango, B., Perera, D., & Nagabhatla, N. (2023). An efficient method to generate flood maps using Sentinal-1 SAR imagery and SWAT modelling: a case study of the upper Congo River sub-basin. Journal of Hydrology: Regional Studies (Revised).

1.7 Thesis Outline

The thesis is organized in seven chapters, as follows:

Chapter 1 provides the background and objectives of this research work. This chapter contains the problem statement, the objectives, scope of the research, major outcomes, and the overall organization of the thesis.

Chapter 2 is a comprehensive literature review. The chapter starts with a brief overview of climate modelling in large flood plains worldwide, followed by an overview of the previous studies conducted in the CRB. The theory behind the methods, including quantile-quantile downscaling, extreme climate index assessment, SWAT model development of large-scale regions, and use of sentinel-1 SAR images for surface water extraction is presented. A description of model evaluation performance measures is provided.

Chapter 3 presents the characteristics of the study area that are relevant to this work, such as the location of the precipitation and temperature stations, the domain, the present temperature and rainfall variability, etc. The various data sets used in the study are presented. These data sets include observed climate data and discharge, and simulated discharges at ungauged locations.

Chapter 4 assesses the future impact of climate change on the Congo River Basin by examining changes in rainfall-induced flash floods and drought regimes from the present day to the year 2100. The utilization of four extreme climatic indices allowed for a comprehensive analysis, shedding light on the nuanced shifts in precipitation and climate patterns.

Chapter 5 focuses on the development of a Soil and Water Assessment Tool (SWAT) model of the CRB, which was meticulously calibrated, and validated. Daily rainfall observations, combined with comprehensive time series data allowed for the assessment and projections of changes in streamflow across all reaches of the Congo River from the present day to the year 2100.

Chapter 6 introduces an innovative approach to flood mapping using a combination of Sentinel-1 Synthetic Aperture Radar imagery and a calibrated Soil and Water Assessment Tool model to accurately map floods in the Oubangui River section of the CRB. This chapter demonstrates how to extract surface water data from SAR images and establish a relationship between pixels and water discharge values. This information enables the creation of a spatial pixel probability distribution, facilitating accurate mapping of flooded and dry areas.

Chapter 7 summarizes the major findings and gives conclusions of this research work. This chapter also provides recommendations for future studies.

1.8 References

Arnold, Jeffrey G., et al. "Large area hydrologic modeling and assessment part I: model development 1." JAWRA Journal of the American Water Resources Association 34.1 (1998): 73-89.

Creese, Amy, R. Washington, and R. Jones. "Climate change in the Congo Basin: processes related to wetting in the December–February dry season." Climate Dynamics 53 (2019): 3583-3602.

EM-DAT, CRED, EM-DAT, The Emergency Events Database, Univ. Cathol. Louvain - CRED, Brussels, Belgium, 2020. www. emdat. be. Accessed 04 08, 2021

Hakala, Kirsti, Nans Addor, and Jan Seibert. "Hydrological modeling to evaluate climate model simulations and their bias correction." Journal of Hydrometeorology 19.8 (2018): 1321-1337.

Haque, Md Mominul, et al. "Improving the accuracy of hydrodynamic simulations in data scarce environments using Bayesian model averaging: A case study of the inner Niger Delta, Mali, West Africa." Water 11.9 (2019): 1766.

Karam, S., Seidou, O., Nagabhatla, N., Perera, D., & Tshimanga, R. M. (2022). Assessing the impacts of climate change on climatic extremes in the Congo River Basin. Climatic Change, 170(3-4), 40.

Karam, S., Zango, B. S., Seidou, O., Perera, D., Nagabhatla, N., & Tshimanga, R. M. (2023). Impacts of Climate Change on Hydrological Regimes in the Congo River Basin. Sustainability, 15(7), 6066.

Kitambo, Benjamin, et al. "Large-scale spatio-temporal variability of the Congo Basin surface hydrologic components from space." EGU General Assembly Conference Abstracts. 2022.

Lewis, Simon L., et al. "Changing ecology of tropical forests: evidence and drivers." Annual Review of Ecology, Evolution, and Systematics 40 (2009): 529-549.

Li, Yu, et al. "An automatic change detection approach for rapid flood mapping in Sentinel-1 SAR data." International journal of applied earth observation and geoinformation 73 (2018): 123-135.

Malhi, Yadvinder, and James Wright. "Spatial patterns and recent trends in the climate of tropical rainforest regions." Philosophical Transactions of the Royal Society of London. Series B: Biological Sciences 359.1443 (2004): 311-329.

Malhi, Yadvinder, et al. "African rainforests: past, present and future." Philosophical Transactions of the Royal Society B: Biological Sciences 368.1625 (2013): 20120312.

Mao, Yuna, et al. "Flood inundation generation mechanisms and their changes in 1953–2004 in global major river basins." Journal of Geophysical Research: Atmospheres 124.22 (2019): 11672-11692.

Ndehedehe, Christopher E., et al. "Modelling the impacts of global multi-scale climatic drivers on hydro-climatic extremes (1901–2014) over the Congo basin." Science of The Total Environment 651 (2019): 1569-1587.

Onyutha, Charles. "Analyses of rainfall extremes in East Africa based on observations from rain gauges and climate change simulations by CORDEX RCMs." Climate Dynamics 54.11-12 (2020): 4841-4864.

Paris, Adrien, et al. "Monitoring Hydrological Variables from Remote Sensing and Modeling in the Congo River Basin." Congo Basin Hydrology, Climate, and Biogeochemistry: A Foundation for the Future (2022): 339-366.

Sridhar, Venkataramana, et al. "Water Budgets and Droughts under Current and Future Conditions in the Congo River Basin." Congo Basin Hydrology, Climate, and Biogeochemistry: A Foundation for the Future (2021).

Tshimanga, Raphael M., et al. "An integrated information system of climate-water-migrations-conflicts nexus in the Congo Basin." Sustainability 13.16 (2021): 9323.

Tshimanga, Raphael M., and Denis A. Hughes. "Basin-scale performance of a semidistributed rainfall-runoff model for hydrological predictions and water resources assessment of large rivers: The Congo River." Water Resources Research 50.2 (2014): 1174-1188.

Vekaria, Darshil, et al. "A change detection approach to flood inundation mapping using multi-temporal Sentinel-1 SAR images, the Brahmaputra River, Assam (India): 2015–2020." Journal of Earth System Science 132.1 (2022): 3.

Chapter 2

Literature review

2.1 Hydrological and climate modeling in data sparse regions

Insufficient climate and land-use data can create significant challenges for hydrological modeling in data-sparce regions.

1. Limited Data Availability: Insufficient meteorological data, including precipitation and temperature, poses a significant challenge for accurately estimating hydrological processes. Similarly, sparse or unreliable streamflow data makes it difficult to effectively calibrate and validate hydrological models (Holmes, 2023).

2. Uncertain Land Use and Land Cover Information: The lack of accurate land use and land cover information in data-scarce regions impacts the representation of surface characteristics and their influence on hydrological processes (Mengistu et al., 2022).

3. Poorly Characterized Soil Properties: Inaccurate or limited soil information leads to uncertainties in modeling processes such as infiltration, runoff, and water storage capacities in the soil (Fatichi et al., 2020).

4. Sparse Gauge Network: The absence of an adequate river gauge network and monitoring infrastructure results in challenges in obtaining reliable streamflow data for the calibration and validation of hydrological models (Sirisena et al., 2020).

5. Limited Remote Sensing Data: While remote sensing can provide valuable information, data-scarce regions may lack sufficient satellite or aerial imagery for essential parameters related to land surface and vegetation dynamics (Mashala et al., 2023).

6. Data Quality and Reliability: Quality issues, such as errors, gaps, and inconsistencies in available data, compromise the reliability of hydrological models (Ocio and Smart, 2019).

7. Limited Institutional Capacity: Data-scarce regions often lack the necessary institutional capacity and resources for effective data collection, monitoring, and maintenance of hydrological databases (Wheeler et al., 2017).

Addressing these challenges in data-scarce regions involves adopting innovative approaches such as incorporating alternative data sources and utilizing remote sensing technology. Developing robust hydrological models in such regions requires a combination of data-driven and physically based modeling approaches, along with careful consideration of uncertainties.

Amorim et al., (2022) quantified the climate change-driven impacts on the hydrology of a 51 237 km^2 data-scarce watershed located in the Brazilian Tropical Savanna. Haque et al., (2019) studied the accuracy of hydrodynamic simulations in the Inner Niger Delta, which has a maximum inundated area that can exceed 30,000 km^2. Komi et al., (2017) developed a flood modeling approach for predicting flood extent in data-scarce regions using a calibrated, distributed hydrological model and a hydraulic model along a 140 km stretch of the Oti River. Yan et al., (2014) studied flood extents maps derived for a 280 km river reach of the Blue Nile, in Sudan. Knoche et al., (2014) studied the uncertainty of hydrological model complexity and satellite-based forcing data in two data-scarce catchments in Ethiopia that have sizes of 4531 km^2 (upper Awash) and 2950 km^2 (Kessem).

2.2 Hydroclimatic and hydrological modelling of the CRB

Various authors have conducted studies on how climate change affects hydroclimatic conditions in the CRB. Bola et al., (2022) studied the impacts of climate change on the Congo basin's flood seasonality and flood regime shift, specifically focusing on seasonal changes in the past and present, of four sub-basins comprising the CRB. They discovered a consistent unimodal flood distribution in the northern and southern regions of the basin, contrasting with the bimodal flood pattern observed across the broad equatorial band from west to east in the basin (see figure 2.1, Bola et al., (2022)). The time lag in flood indices indicated that the flood regime was not constant.

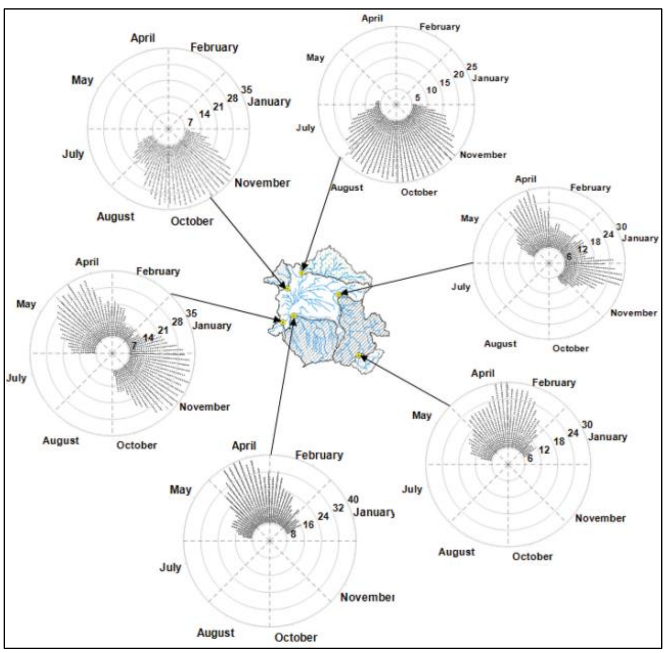

Figure 2.1 Flood seasonality patterns in specified sub-basins of CRB; values are expressed in terms of relative frequency (%) (Bola et al., 2022)

Ndehedehe et al., (2019) modeled the impacts of global climatic drivers on hydroclimatic extremes in the Congo basin between 1901 and 2014. They developed a predictive framework using a non-linear autoregressive standard neural network to analyze the connectivity between climatic patterns and ocean–atmosphere regimes. As depicted in figure 2.2 (Ndehedehe et al., 2019) the study highlighted severe multi-year droughts affecting 40–50% of the Congo basin's land area between 1901 and 2014, with changes in hydrological regimes since 1994 due to drought intensification.

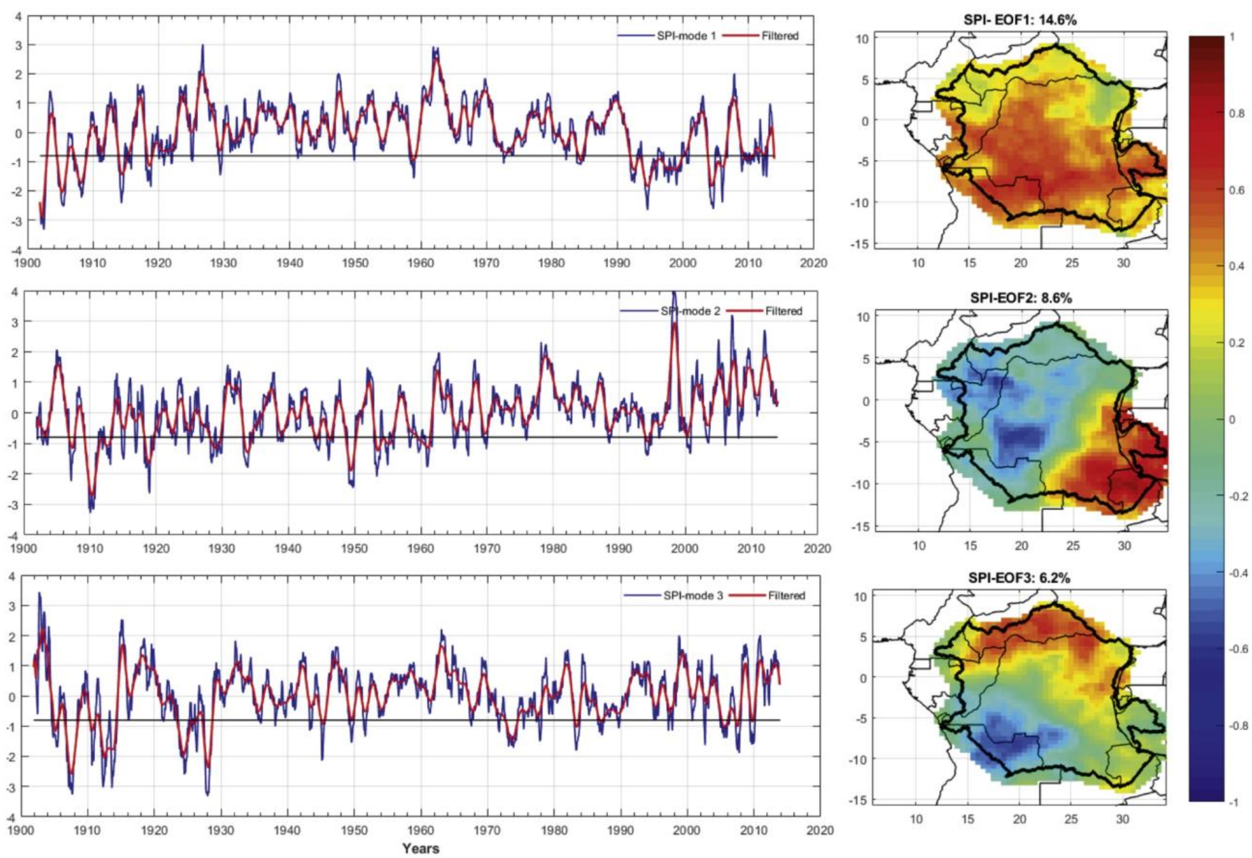

Figure 2.2 Spatial and temporal SPI patterns over the CRB between 1901 and 2013

Kitambo et al., (2022) used a comprehensive analysis of in situ and satellite-derived data to characterize surface hydrology and its variability in the CRB. The research combines long-term records of surface water height (SWH) from radar altimetry and surface water extent (SWE) from multi-satellite observations. The study demonstrates the agreement between SWH and in situ water stage across various locations, offering insights into the spatial and temporal variability of hydrological patterns in the basin. The study highlights significant annual amplitude variations in SWH in northern subbasins and demonstrates the spatial distribution and timing of the CRB's annual flood dynamic, including contributions from various subbasins and tributaries to the hydrological regime at the basin outlet. The results from this study enhance the characterization of the seasonal hydrological variability in the CRB.

Dos Santos et al. (2022) made a comprehensive comparison of different satellite-based precipitation products' inputs for a hydrological model in the Congo River Basin. The hydrographs presented in figure 2.3 demonstrate that the SWAT model which was developed, calibrated, and validated by the authors, aligns well with the essential characteristics of the satellite precipitation products. This alignment is evident in both the dry and wet seasons observed at five separate gauge sites.

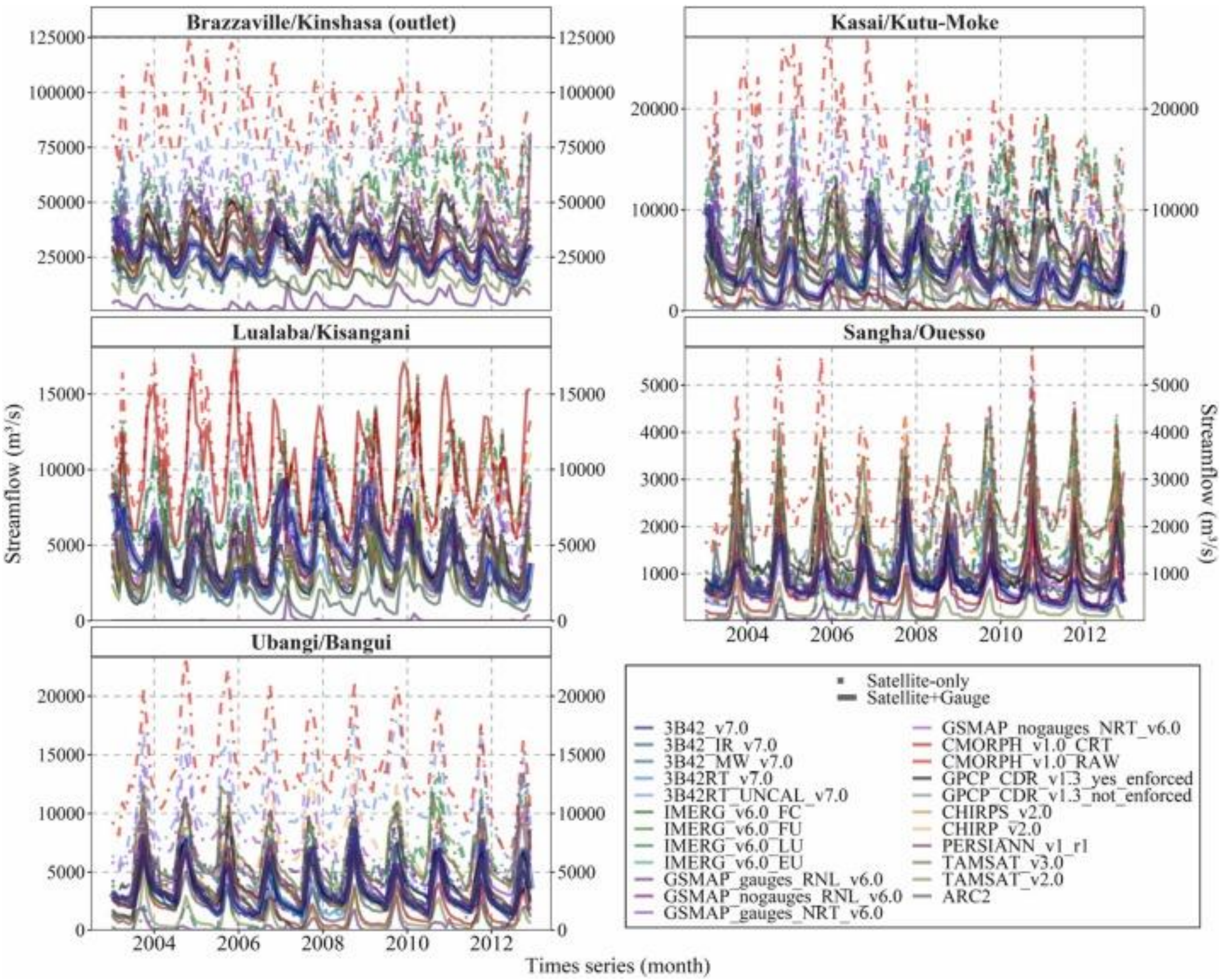

Figure 2.3 Simulated streamflow (in m^3/s) hydrographs during the period from 2003–2012 in various locations within the Congo River Basin (Dos Santos et al., 2022)

Aloysius and Saiers (2017) simulated hydrologic response to projected changes in PCP and TMP in the CRB. The authors used a spatially explicit hydrological model driven by PCP and TMP projections from 25 global climate models under two RCP scenarios (table 2.1, Aloysius and Saiers (2017)).

Table 2.1 Global climate models used by Aloysius and Saiers (2017)

Model number	Model name
M1	ACCESS1-3
M2	bcc-csm1-1
M3	BNU-ESM
M4	CanESM2
M5	CCSM4
M6	CESM1-CAM5
M7	CNRM-CM5
M8	CSIRO-Mk3-6-0
M9	EC-EARTH
M10	FIO-ESM
M(11–13) ∗	GISS-E2-H∗
M(14–16) ∗	GISS-E2-R∗
M17	HadGEM2-CC
M18	HadGEM2-ES
M19	INM-CM4
M20	IPSL-CM5A-LR
M21	MIROC5
M22	MIROC-ESM
M23	MPI-ESM-LR
M24	MRI-CGCM3
M25	NorESM1-M

This study examines the anticipated variability in modeled runoff in the near future (2016–2035) and mid-century (2046–2065). The study projects a 5% increase in runoff over the next two decades and a 7% increase by mid-century. Changes vary across sub-watersheds, with increased precipitation and runoff in the equatorial, northern, and southwestern regions of the CRB. Simulated reduced precipitation led to decreased runoff in northeastern and southeastern regions.

The study underscores the importance of considering uncertainties in climate model and emission scenario selection in decision-making for climate change mitigation and adaptation.

Tshimanga and Hughes (2012) studied climate change and its impacts on the hydrology of the CRB, notably in the norther Oubangui catchment. The authors utilize downscaled and bias-corrected data from eight GCMs to drive a semi-distributed rainfall-runoff model. The list of GCMs used for the study are summarized in table 2.2.

Table 2.2 list of GCMs used by Tshimanga and Hughes (2012)

Model	**Modelling group**
CCCMA-CGCM3.1	Centre for Climate Modelling and Analysis, Canadian
CNRM-CM3	Centre National de Recherches Meteorologiques, France
GFDL-CM2.1	Geophysical Fluid Dynamics Lab., USA NOOA
GISS-ER	Goddard Institute for Space Studies, USA
IPSL-CM4	Institut Pierre Simon Laplace, France
MIUB-ECHO	Meteorological Institute of the University of Bonn, Germany
MPI-ECHAM5	Max-Planck Institute for Meteorology, Germany
MRI-CGCM	Meteorological Research Institute, Japan

The analysis focuses on various hydrological process variables, including rainfall, interception, potential evapotranspiration, soil moisture store, surface runoff, soil moisture runoff, and recharge. The findings indicate a decrease in runoff for near-future (2046–2065) projections. Despite minimal changes in rainfall from historical conditions for the GCMs, there is a notable increase in evapotranspiration due to rising air temperatures. This study highlights a clear translation of the climate signal into flows, resulting in more than a 10% decrease in total runoff. This decline is attributed to a relatively modest increase in rainfall and a consistent rise in potential evapotranspiration.

2.3 Climatic modelling and projections

The evolution of climatic modeling focuses on the critical aspects of climate model validation, data assimilation, and the inherent uncertainties in climate projections (Smith et al., 2014). Understanding the strengths and limitations of current modeling approaches is crucial for informed decision-making.

2.3.1 Climate Modelling

Climate modeling utilizes mathematical representations to simulate and predict the Earth's climate system by integrating various components such as the atmosphere, oceans, land surface, and ice (Moges et al., 2019). Important aspects of climate modelling include the use of climate models, general and regional circulation models, and emission scenarios.

2.3.1.1 Climate Models

Climate models aim to understand the complex interactions that drive weather patterns and long-term climate trends. These models provide valuable insights into the impacts of natural processes and human activities on the climate (Flato et al., 2014). The following table 2.3 shows an example of just a few prominent climate models developed by various institutions worldwide. Each model has its strengths, focuses, and areas of expertise (Feser et al., 2011). The field of climate modeling is dynamic, and new models or updates to existing models may be introduced over time.

Table 2.3 Example of prominent climate models developed by various institutions worldwide

Climate Model	Source/Institution
Community Earth System Model	National Center for Atmospheric Research (NCAR)
Hadley Centre Climate Model	Met Office Hadley Centre for Climate Science and Services

Model for Interdisciplinary Research on Climate (MIROC)	Atmosphere and Ocean Research Institute (AORI), Japan
Geophysical Fluid Dynamics Laboratory Model (GFDL)	NOAA's Geophysical Fluid Dynamics Laboratory
European Centre for Medium-Range Weather Forecasts (ECMWF)	ECMWF
Goddard Institute for Space Studies Model (GISS)	NASA Goddard Institute for Space Studies
Max Planck Institute for Meteorology Earth System Model (MPI-ESM)	Max Planck Institute for Meteorology
Canadian Centre for Climate Modelling and Analysis (CCCma) Models	CCCma, Environment and Climate Change Canada

2.3.1.2 General and Regional Circulation Models

General Circulation Models (GCMs) and Regional Circulation Models (RCMs) are specialized types of climate models designed to study global and local climate patterns, respectively (Kendon et al., 2010). GCMs provide a broad overview of the Earth's climate by simulating large-scale atmospheric and oceanic processes, while RCMs focus on smaller geographic regions with higher spatial resolution (Giorgi et al., 2019). RCMs rely on the driving GCMs for boundary conditions, using their output to define the initial and boundary states of the climate system for regional simulations. This dependence means that the choice of GCM can significantly influence the results produced by the RCM. Different GCMs incorporate varying representations of physical processes and parameterizations, leading to differences in climate projections for the same region. While RCMs provide higher-resolution climate information at the regional scale, their output may vary depending on the driving GCM. To address this uncertainty, ensemble approaches, involving multiple RCM simulations driven by different GCMs are often employed to assess the range of possible future climate scenarios for a given region. Figure 2.4 shows a schematic depiction of global and regional climate modeling.

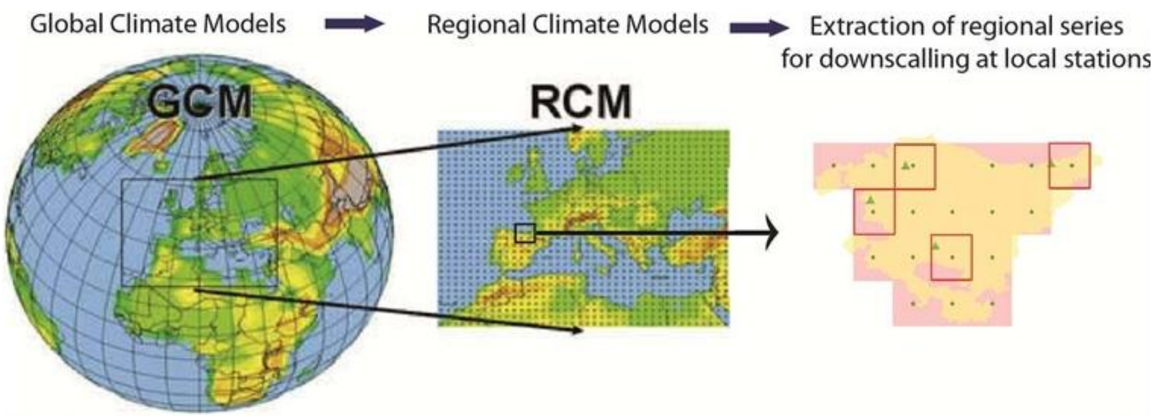

Figure 2.4 Schematic depiction of global and regional climate modeling (Gonzalez and Zucker., 2015)

GCM/RCM models are subject to various sources of data uncertainty such as:

- Input Data Uncertainty: GCMs and RCMs rely on input data such as historical climate observations, greenhouse gas emissions scenarios, land cover data, and aerosol concentrations. Uncertainties in these input datasets can stem from various sources, including measurement errors, spatial and temporal resolution limitations, data gaps, and biases. For example, historical climate observations may not cover all regions or may have inconsistencies due to changes in measurement techniques over time.

- Parameterization Uncertainty: GCMs and RCMs use complex mathematical representations (parameterizations) to simulate physical processes such as cloud formation, precipitation, and atmospheric circulation. These parameterizations involve simplifications and assumptions due to computational constraints and incomplete understanding of underlying processes. As a result, uncertainties arise in how well these parameterizations capture real-world phenomena, leading to uncertainties in model projections.

- Model Structure Uncertainty: The structural design of GCMs and RCMs also introduces uncertainty. Different models may use different equations, numerical schemes, and spatial resolutions to represent the Earth's climate system. Model developers make choices about which processes to include, how to represent interactions between different components (e.g., atmosphere, ocean, land surface), and how to parameterize sub-grid-scale processes. These structural uncertainties can impact model projections and contribute to overall uncertainty in climate change predictions.

- Scenario Uncertainty: Future climate projections are based on different greenhouse gas emissions scenarios, such as those developed by the Intergovernmental Panel on Climate Change (IPCC). These scenarios represent different possible pathways of future emissions and socio-economic developments. Uncertainty arises because future emissions depend on factors such as population growth, technological advancements, and policy decisions, which are inherently uncertain.

- Downscaling Uncertainty: RCMs are often used to provide higher-resolution climate information for specific regions compared to GCMs, which typically operate at coarser spatial scales. However, downscaling methods introduce additional uncertainty, particularly in capturing local-scale climate variability and extreme events. Uncertainties in downscaling arise from the choice of downscaling technique, biases in driving GCM outputs, and limitations in representing local-scale processes.

Addressing data uncertainty in GCM/RCM projections involves techniques such as statistical downscaling, ensemble modeling, sensitivity analysis, and quantifying uncertainty in model outputs. Ensemble approaches involve running multiple simulations with variations in input parameters, model structures, and emissions scenarios to characterize the range of possible future climate outcomes and associated uncertainties. Sensitivity analysis helps identify which factors contribute most to uncertainty in model predictions, guiding efforts to improve model performance and reduce uncertainties.

2.3.1.3 Emission scenarios

Emission scenarios are hypothetical pathways, otherwise known as representative concentration pathways (RCP), that describe the future release of greenhouse gases and other pollutants into the atmosphere (Riahi et al., 2011). These scenarios are used as inputs for climate models, which help to explore different possible futures based on varying levels of human activities and policy decisions. These scenarios consider factors such as population growth, technological advancements, and socio-economic trends to project how human activities may contribute to changes in the Earth's climate (Mokhov and Eliseev, 2012). There are four RCP scenarios used in climate modelling: RCP2.6, RCP4.5, RCP6.0, and RCP8.5, the details for each scenario are provided in table 2.4. However, it is important to note that RCP2.6 is no longer considered an active scenario, as the scientific community has concluded that achieving such low emission levels seems increasingly unlikely given current global trends and challenges (Van Vuuren et al., 2011).

Global emissions have generally followed a trajectory closer to the higher RCP scenarios, particularly RCP8.5, which represents a high-emission future. The decision to discontinue RCP2.6 emphasizes the urgency of addressing climate change and the need for more realistic scenarios to guide mitigation and adaptation strategies.

Table 2.4 Description of four RCP scenarios used in climate modelling (Van Vuuren et al., 2011)

RCP Scenario	Radiative Forcing (W/m^2) by 2100	Description
RCP2.6	2.6	Aggressive mitigation, limiting global warming to well below 2°C.
RCP4.5	4.5	Moderate mitigation, aiming to stabilize radiative forcing.
RCP6.0	6.0	Balanced emissions with slower growth, assumes some mitigation.
RCP8.5	8.5	High-emission scenario with continued growth in greenhouse gases.

2.3.2 Temporal Disaggregation

Temporal disaggregation is a statistical method used to transform or disaggregate time series data from one frequency to another (Guan et al., 2023). This process involves breaking down data from a higher frequency (e.g., yearly) into a lower frequency (e.g., monthly or daily) or vice versa. The goal is to provide more detailed and granular information for analysis or modeling. The fragment method is a temporal disaggregation method originally introduced by Harms and Campbell (1967), and has undergone continuous development since then. Sittichok et al., (2016) used the fragment method to extend the time scale of a seasonal rainfall time series to a daily time series by utilizing standardized historical data to create a fragment series for each year. The following procedure was used:

For every year of simulated seasonal rainfall (Yseasonal,sim) in the simulated rainfall series:

(i) The year of historical seasonal rainfall (Yseasonal,hist) with the closest average historical seasonal rainfall to the simulated seasonal rainfall was chosen.

(ii) The daily rainfall of Ysim at station STi was estimated using equation 2.1. This approach successfully generated rainfall time series for 11 stations while preserving the overall rainfall distribution across the entire basin.

$$Y_{daily,sim,STi} = Y_{daily,hist,STi}\left(Y_{seasonal,sim} / Y_{seasonal,hist}\right) \qquad (2.1)$$

2.3.3 Statistical Downscaling

Statistical downscaling methods play an important role in bridging the gap between the coarse resolution of GCMs and the finer scales relevant for decision-making. GCMs are a complex numerical representation of the Earth's climate system (Laprise et al., 2013). These models are designed to simulate and understand the interactions between the atmosphere, oceans, land surface, and ice components on a global scale (Lorenz et al., 2022). GCMs use mathematical equations to represent the physical processes that govern climate, such as atmospheric circulation, ocean currents, temperature, humidity, and more (Eghdamirad et al., 2017). Key components of a GCM include:

- Atmosphere Model: Represents the behavior of the Earth's atmosphere, including processes like air movement, temperature, and moisture.
- Ocean Model: Simulates ocean currents, sea surface temperatures, and interactions between the ocean and the atmosphere.

- Land Surface Model: Accounts for processes occurring on land, such as vegetation, soil moisture, and heat transfer between the land surface and the atmosphere.
- Sea Ice Model: Represents the presence and behavior of sea ice in polar regions.

Users must input data, including historical climate observations and estimates of future greenhouse gas emissions, into these models. The models then simulate how the climate system would respond under different scenarios (Hernadez-Diaz et al., 2013). By establishing these statistical relationships, downscaling models can then be applied to project future regional or local climate scenarios based on the outputs of GCMs.

Dynamical downscaling, however, utilizes RCMs to simulate climate conditions at a finer spatial scale by integrating coarse-resolution output from GCMs as boundary conditions. This approach captures detailed local-scale climate features.

2.3.3.1 Quantile mapping technique

Quantile-Quantile (Q-Q) mapping is a statistical technique used to bias-correct climate model outputs based on observed data. The method aims to improve the reliability and accuracy of climate model simulations by aligning their probability distributions with those of observed data (Sarr et al., 2015). Q-Q mapping is used to align the cumulative distribution function (CDF) of model-simulated variables with the observed CDF. The basic form of the Q-Q mapping equation is demonstrated in equation 2.2 (Cannon et al., 2015).

$$X_{CORR} = F_{-OBS1}(F_{RCM}(X_{RCM})) \qquad (2.2)$$

X_{CORR} is the corrected variable and X_{RCM} is the extracted value from the raw RCM simulations. (F_{OBS}) is the empirical cumulative distribution functions of the observed calibrated period and (F_{RCM}) is the RCM outputs. According to Hakala et al. (2018), the quantile mapping technique outperforms other methods such as the delta-change approach, local intensity scaling, and power transformation.

2.3.3.2 The delta-change approach

The delta-change approach addresses biases in the simulated climate variables by applying adjustments based on the differences, or "delta changes," between model-simulated and observed data (Das et al., 2022). The fundamental equation for the delta change approach can be expressed as:

$$X_{corrected} = X_{model} + \Delta X \quad (2.3)$$

Where $X_{corrected}$ is the bias-corrected variable, X_{model} is the model-simulated variable, and ΔX represents the calculated difference (delta change) between the model-simulated and observed values. The delta change approach is valuable for its simplicity and transparency, making it an accessible method for bias correction (Hundecha et al., 2016). However, its effectiveness can be influenced by the assumption that the relationship between the model bias and observed data remains constant over time and under changing climate conditions (Sarr et al., 2015).

2.3.3.3 Local intensity scaling

Localized Constructed Analogs (LOCA) is a statistical downscaling method that addresses biases in the simulated intensity (magnitude) of climate variables at a local scale (Pierce et al., 2014). The approach is particularly useful when there are systematic errors in the representation of extreme values or the variability of climate model projections. The local intensity scaling equation can be represented as:

$$X_{corrected} = a \times X_{model} \qquad (2.4)$$

Where $X_{corrected}$ is the bias-corrected variable, X_{model} is the model-simulated variable, and a is a scaling factor, determined based on the ratio of the observed local intensity to the model-simulated intensity (Fang et al., 2015). The scaling factor a can be computed by comparing the observed intensity to the corresponding model-simulated intensity over a reference period. This ratio is then applied to the model-simulated intensities in future projections to adjust for biases in the simulated data. Local intensity scaling is particularly relevant in situations where climate models may struggle to accurately capture the local characteristics of extreme events, however, it's important to note some disadvantages of this method (Schmidli et al., 2006; Risser et al., 2021). One limitation is that local intensity scaling assumes a linear relationship between the observed and model-simulated intensities, which may not hold under all conditions. Additionally, the effectiveness of the scaling factor a may vary across different time periods or climate scenarios, making it challenging to ensure consistent and accurate bias correction.

2.3.3.4 Power transformation

Power transformation is applied to climate variables to stabilize variance or to make the data more symmetric (Fang et al., 2015). This can be particularly useful when working with data that exhibit non-constant variance or non-normal distributions. The general form of the power transformation equation is given by:

$$Y = (X + c)^p \qquad (2.5)$$

Where Y is the transformed variable, X is the original variable, c is a constant that is often chosen to handle data with zero or negative values, and p is the power to which the variable is raised. Power transformations, while effective in addressing data distribution issues, have downsides (Paz & Willems, 2023). Interpretability may suffer as transformed values lack direct physical meaning, and parameter choice sensitivity can influence results, i.e. handling zero or negative values, and introducing nonlinearity.

2.3.4 Extreme Climatic Indices

Extreme climatic indices serve as crucial metrics for assessing and quantifying the occurrence of extreme weather events, aiding in our understanding of climate change impacts. Temperature-related indices, such as those measuring heatwaves and cold spells, provide insights into the frequency, duration, and intensity of prolonged temperature extremes. Precipitation-related indices focus on heavy precipitation events, offering data on the frequency and intensity of extreme rainfall or snowfall, while drought indices assess the severity and duration of dry periods through metrics like the Standardized Precipitation Index (SPI) (Mckee et al., 1993) and the Standardized Precipitation-Evaporation Index (SPEI) (Lebel and Ali, 2009). The Expert Team on Climate Change Detection and Indices (ETCCDI) is a part of the World Meteorological Organization (WMO) and has worked in standardizing definitions and methodologies for various climate indices. These indices are designed to capture different aspects of climate extremes and help researchers and meteorologists analyze and communicate changes in climate patterns. The 27 core climate indices developed by ETCCDI cover a wide range of climate variables, including temperature, precipitation, and other relevant parameters. (https://etccdi.pacificclimate.org/list_27_indices.shtml).

The Climdex project is also focused on creating and analyzing indices related to climate extremes. It involves developing metrics for measuring extreme weather events, using historical climate data to identify trends, and collaborating with scientists globally. The project's goal is to monitor and communicate changes in climate extremes, providing valuable information for policymakers and researchers in addressing the impacts of climate change (https://www.climdex.org/learn/indices/#index).

2.4 Hydrological Modelling using SWAT

2.4.1 SWAT Model Setup

Hydrological modeling refers to the use of mathematical and computational models to simulate the movement and distribution of water within a river basin or watershed, with a specific focus on predicting the discharge of water at various points in a river system (Cerkasova et al., 2018; Park et al., 2014; Anjum et al., 2019).

There are various types of hydrological models, ranging from simple conceptual models to more complex physically based models (Pan et al., 2022). Conceptual models simplify the representation of the hydrological cycle by dividing a watershed into conceptual components, such as rainfall, runoff, and storage. The parameters of these components are calibrated based on observed data to simulate the system's behavior (Dos Santos et al., 2022). Whereas a physically based model attempts to represent the actual physical processes occurring in the watershed using mathematical equations. They take into account factors such as topography, soil properties, land use, and meteorological data to simulate the movement of water more realistically (Sridhar et al., 2021).

The Soil and Water Assessment Tool (SWAT) developed by the Agricultural Research Service (ARS) of the United States Department of Agriculture (USDA) (Arnold et al., 1998) is considered a physically based hydrological model. It is used to simulate the complex processes of movement of water, sediment, and nutrients in large, complex watersheds (Zango et al., 2022). SWAT accounts for the physical characteristics of the landscape, such as topography, soil properties, land use, and climate, to simulate processes like precipitation, evaporation, runoff, infiltration, and the transport of sediments and nutrients. The model is organized into sub-basins, each further divided into hydrological response units (HRUs) that represent homogeneous land cover, soil, and slope characteristics (Yasir et al., 2020). The schemtic representation of the SWAT model developped by Yasir et al. (2020) is given in figure 2.5.

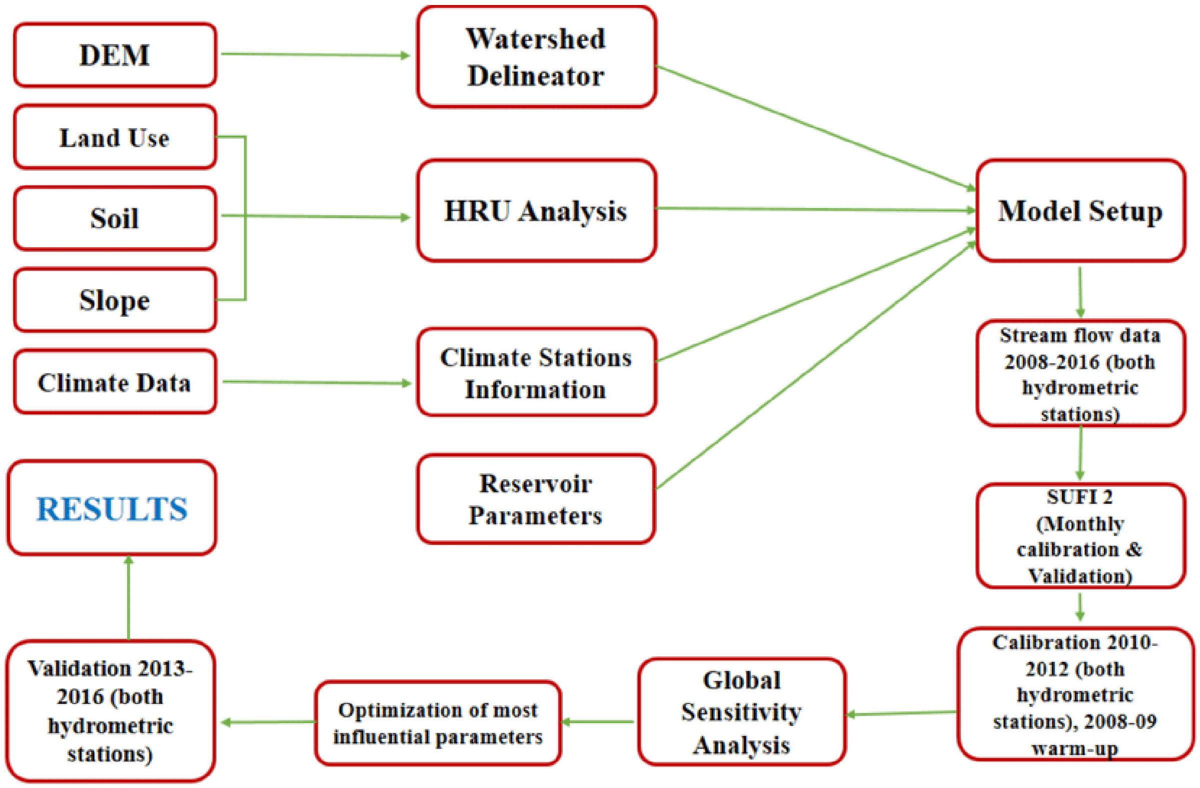

Figure 2.5 Schematic representation of SWAT model setup (Yasir et al., 2020)

In a SWAT model, the daily hydrological cycle of a watershed is simulated based on the water balance equation, given in equation 2.6 (Arnold et al. 1998):

$$SW_t = SW_0 + \sum_{i=1}^{n}(R_{day} - Q_{surf} - E_a - W_{seep} - Q_{gw}) \quad (2.6)$$

where SW is the soil water content at time 0 and at a time step, t. Rday is the precipitation amount, Qsurf is the surface runoff, Ea is the evapotranspiration, wseep is the water entering the vadose zone from the soil profile, and Qgw is the return flow on a specific day, I, in units of mm. Rainfall is then subdivided into infiltration and surface runoff using the curve number (CN) method (Neitsch et al., 2011):

$$Q_{surf} = \frac{(P-0.2)^2}{(P-0.8S)} \qquad (2.7)$$

where the surface runoff (Qsurf) is derived as a function of the total precipitation (P) in mm and the soil moisture content (S), a no-dimension parameter expressed in terms of a CN ranging from 0 to 100. The coefficients 0.2 and 0.8 serve as important factors in adjusting the relationship between surface runoff and other variables. An increase in total precipitation corresponds to a rise in surface runoff, as more precipitation contributes to heightened runoff (Neitsch et al., 2011). Also, higher soil moisture content leads to a reduction in surface runoff. This is because increased soil moisture enables the soil to absorb more precipitation, decreasing the amount that runs off the surface (Arnold et al., 2012).

2.4.1.1 Topographic Data

Topographic data comes from Digital Elevation Models (DEM). It is a digital representation of the topography or relief of a terrain. A DEM provides a set of elevation values for regularly spaced ground positions (or pixels), creating a three-dimensional representation of the Earth's surface. The elevation data is typically derived from various sources, such as topographic maps, satellite imagery, LiDAR (Light Detection and Ranging) data, or other remote sensing technologies (Haque et al., 2020). The topography is the key factor in estimating the extent of the flood.

2.4.1.2 Hydrological Response Units (HRUs)

A Hydrological Response Unit is a subdivision of a watershed or catchment area that shares similar land use, soil, and slope characteristics. It is assumed that within each HRU, hydrological processes can be reasonably represented as uniform (Arnold et al., 1998). HRUs are defined based on the variability of key factors that influence hydrological responses, including land cover, soil type, and slope. The idea is to group together areas with similar hydrological behaviors (Shrestha et al., 2020).

2.4.2 SWAT Calibration and Validation Performance

Calibration and validation are fundamental stages in the SWAT model development process, their objectives are to ensure that the model is accurately representing the processes that are being simulated (Mengistu et al., 2019). During calibration, model parameters and input data are adjusted to enhance prediction accuracy. Validation, on the other hand, assesses the calibrated model's performance using independent data not employed in the calibration, assessing the model's overall accuracy and reliability (Jajarmizadeh et al., 2017; Bui et al., 2019). This systematic approach helps identify potential biases or errors in the model and ensures its robustness in capturing real-world dynamics. Figure 2.6 shows the conceptualization of model calibration (Abbaspour et al., 2017).

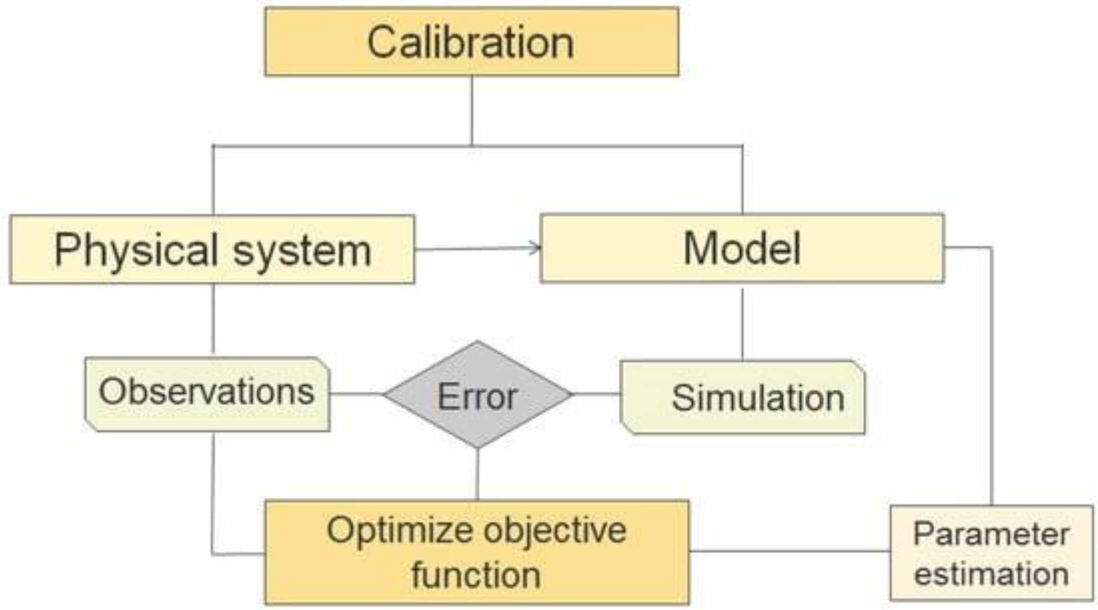

Figure 2.6 The conceptualization of a SWAT model calibration (Abbaspour et al., 2017).

The performance of the calibration and validation is evaluated using statistical and graphical methods. The Nash–Sutcliffe efficiency coefficient (NS) (Nash & Sutcliffe, 1970), and the percentage bias (PBIAS) (Gupta & Patrice, 1999) can be used as statistical measures of the accuracy and performance of the model. The NS coefficient is a dimensionless measure that ranges from $-\infty$ to 1, with values closer to 1 indicating a better fit between the observed and simulated values. It is given by the following equation:

$$NS = 1 - \frac{\sum_{i=1}^{n}(Q_m - Q_s)_i^2}{\sum_{i=1}^{n}(Q_{m,i} - \bar{Q}_m)^2} \qquad (2.8)$$

where Q is the discharge, m is the measured data, s is the simulated data, i is the time step, and n is the total number of periods.

The PBIAS is calculated by comparing the mean of observed values to the mean of simulated values, expressing the difference as a percentage of the observed mean. A PBIAS value of 0 indicates an unbiased model, while positive and negative values suggest a tendency to either underestimate or overestimate the observed values, respectively (Gupta & Patrice, 1999).

$$\mathrm{PBIAS} = 100 \times \frac{\sum_{i=1}^{n}(Q_m - Q_s)_i}{\sum_{i=1}^{n} Q_{m,i}} \tag{2.9}$$

The statistical measures commonly found in hydrological modelling publications are related to the model performance criteria illustrated in table 2.5 (Moriasi et al., 2007):

Table 2.5 Model performance criteria (Moriasi et al., 2007)

	Satisfactory	Good	Very Good
NS	0.5–0.7	0.7–0.8	0.8–1.0
PBIAS (%)	15–25	10–15	Less than 10%

2.4.2.1 Parameter Selection

When discussing parameter selection in the context of the calibration of the SWAT model, the focus is on adjusting model parameters to achieve a good match between simulated and observed data. Here are key considerations for parameter selection during the calibration of the SWAT model (Arnold et al., 2012; Zango et al., 2022; Abbaspour et al., 2015; El-Khoury et al., 2015; Khoi & Thom, 2015):

- Hydrological Parameters: Parameters related to hydrological processes, such as the Curve Number (CN), Manning's roughness coefficient (n-value), baseflow alpha factor, and groundwater delay, are commonly adjusted during calibration. These parameters influence the runoff response and the overall water balance.

- Sediment Parameters: Parameters governing sediment transport, such as the sediment routing factor and sediment detachment and transport coefficients, are adjusted to improve the model's ability to simulate sediment yield accurately.
- Nutrient Parameters: SWAT includes parameters related to nutrient cycling, such as the nutrient decay rate and nutrient transformation coefficients. Calibration is necessary to ensure the model adequately represents nutrient dynamics in the watershed.
- Land Use and Soil Parameters: SWAT divides the watershed into different land use and soil types, each with specific parameters. Land use parameters, such as crop coefficients and management practices, as well as soil parameters like available water content and erodibility, are adjusted during calibration.
- Weather Input Parameters: Parameters related to weather input, such as temperature lapse rates and precipitation adjustment factors, may be adjusted to improve the match between simulated and observed meteorological data.
- Reach and Reservoir Parameters: Parameters related to river reaches and reservoirs, such as channel Manning's roughness, bankfull depth, and reservoir routing coefficients, may be adjusted to improve the representation of flow in rivers and reservoirs.
- Initial Conditions: Initial conditions, such as initial soil moisture and groundwater levels, may be adjusted during calibration to account for the specific conditions at the start of the simulation period.

Selecting appropriate initial values for these parameters is essential to initiate the calibration process effectively. Typically, initial values for SWAT input parameters are chosen based on available literature, local knowledge, or data from relevant sources such as soil surveys, land cover maps, and meteorological stations. These initial values should reflect the best estimates of the parameter values for the specific watershed or area of interest. However, they are subject to refinement during the calibration process as model predictions are compared with observed data. Iterative adjustments are made to parameter values until a satisfactory match between simulated and observed data is achieved, thereby improving the accuracy of the SWAT model for the particular watershed or study area (Zango et al., 2022).

2.4.3 Sensitivity Analysis

The Sequential Uncertainty Fitting (SUFI2) algorithm within the Soil and Water Assessment Tool Calibration and Uncertainty Programs (SWATCUP) is used to carry out calibration and sensitivity analysis of a developed SWAT model (Abbaspour, 2007). The purpose of the sensitivity analysis is to assess how variations in specific input parameters affect the model's output. This involves modifying one parameter at a time while keeping all other parameters constant. The impact of the altered parameter is assessed using t-stat and p-value, determined through a multiple regression analysis based on the following equation (Abbaspour, 2007):

$$g = \alpha + \sum_{i=1}^{m} \beta_i b_i \qquad (2.10)$$

where g is the objective function used to determine the model calibration effectiveness, b is the parameter in question, α is equal to the regression constant, β is the technical coefficient attached to the variable b, and m corresponds to the number of parameters.

The p-value serves as a statistical indicator reflecting the likelihood of observing a test statistic as extreme as the one observed, under the assumption that the null hypothesis is valid. Meanwhile, the t-statistic is employed to assess whether the mean of a population significantly differs from a hypothesized value. When the absolute value of the t-statistic is notably high and the p-value is correspondingly small, the parameter is deemed highly sensitive (Abbaspour, 2007). Generally, a p-value below 0.05 suggests significant sensitivity for the parameter (Verhagen, 2004).

2.5 Hydrological Modelling using Remote-Sensing

Sentinel-1 and Sentinel-2 are two distinct satellites within the European Space Agency's Copernicus program, each designed for specific Earth observation purposes. Sentinel-1 is equipped with synthetic aperture radar (SAR) technology (Vekaria et al., 2023). SAR is particularly advantageous for all-weather and day-and-night imaging. It operates in the microwave portion of the electromagnetic spectrum, providing valuable information about the Earth's surface, including terrain, land cover, and surface deformation. Sentinel-1 is widely used for applications such as monitoring changes in land use, detecting subsidence, and assessing natural disasters like floods. Sentinel-2 however, is an optical imaging satellite (Uddin et al., 2019; Hu et al., 2020). It captures imagery in multiple spectral bands, including visible and infrared, with a focus on providing high-resolution and multispectral data. Sentinel-2 is valuable for monitoring crop health, assessing deforestation, and mapping changes in land cover over time.

2.5.1 Remote Sensing for surface Water Extraction

Utilizing Sentinel-1, for surface water extraction involves leveraging the sentinel-1's ability to operate in all weather conditions and during both day and night (Vekaria et al., 2023). These images can be downloaded from the Alaska Satellite Facility (ASF) Data Search Vertex (https://www.earthdata.nasa.gov/). SAR imagery from Sentinel-1 can be employed to detect surface water by exploiting its sensitivity to changes in backscatter intensity. Water bodies typically exhibit low backscatter values, allowing for their differentiation from surrounding land cover types (Kitambo et al., 2022). By acquiring Sentinel-1 SAR data over time, it is possible to track changes in water extent, making it useful for monitoring surface water dynamics, including floods and seasonal variations. Additionally, the dual-polarization capability of Sentinel-1 enables the extraction of additional information about surface water properties (Tripathy & Malladi, 2022). Advanced techniques, such as polarimetric decomposition and change detection, can be applied to enhance the accuracy of surface water mapping (Uddin et al., 2019). Figure 2.7 shows an example of extracted water surface using a tile-based KI thresholding method on a sentinel-1 image taken of the Dongting Lake, China (Hu et al., 2020).

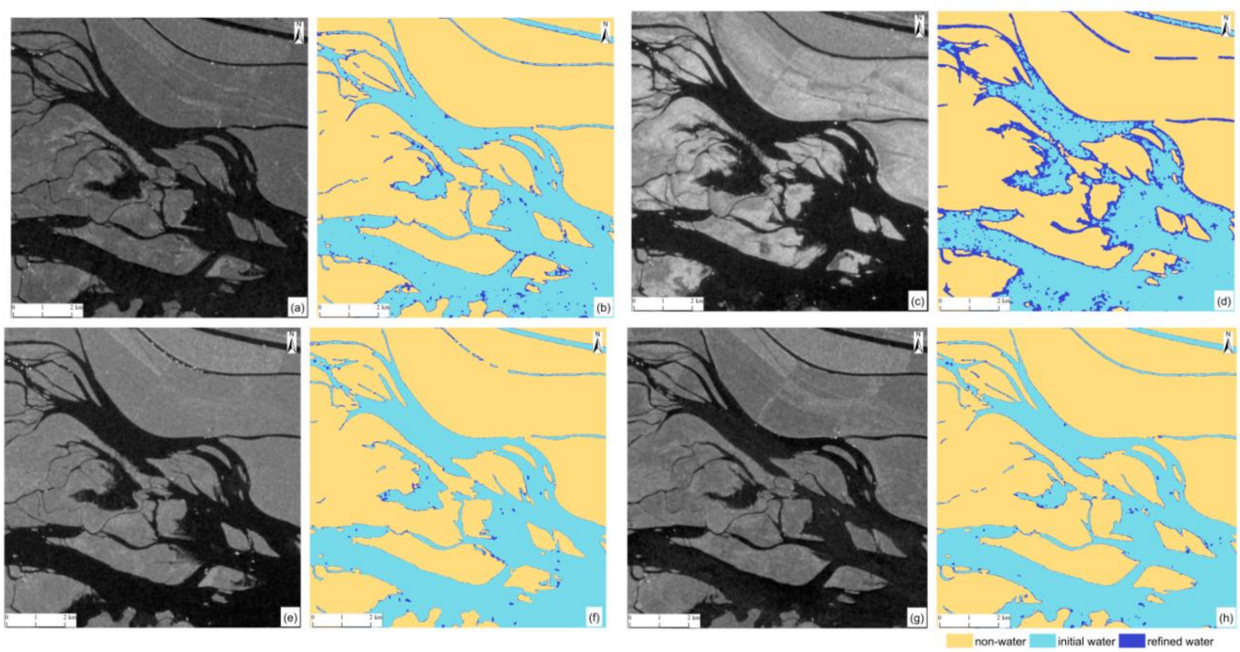

Figure 2.7 extracted water surface using a tile-based KI thresholding method on a sentinel-1 image taken of the Dongting Lake, China (Hu et al., 2020).

2.5.2 Sentinel-1 Image Processing

The following figure 2.8 demonstrates a graphical depiction of the Sentinel Application Platform (SNAP) software process used on sentinel-1 images. This graph was based on processing suggestions and comparisons made by several authors (Mancini et al., 2021; Amitrano et al., 2018; Li et al., 2018; Vekaria et al., 2022). To facilitate the extraction of surface water and mapping of floods using downloaded Sentinel-1 images, the Sentinel Application Platform (SNAP) software, a comprehensive tool developed by the European Space Agency (ESA), can be used. SNAP offers a suite of tools and functionalities for the analysis, visualization, and manipulation of satellite remote-sensing data.

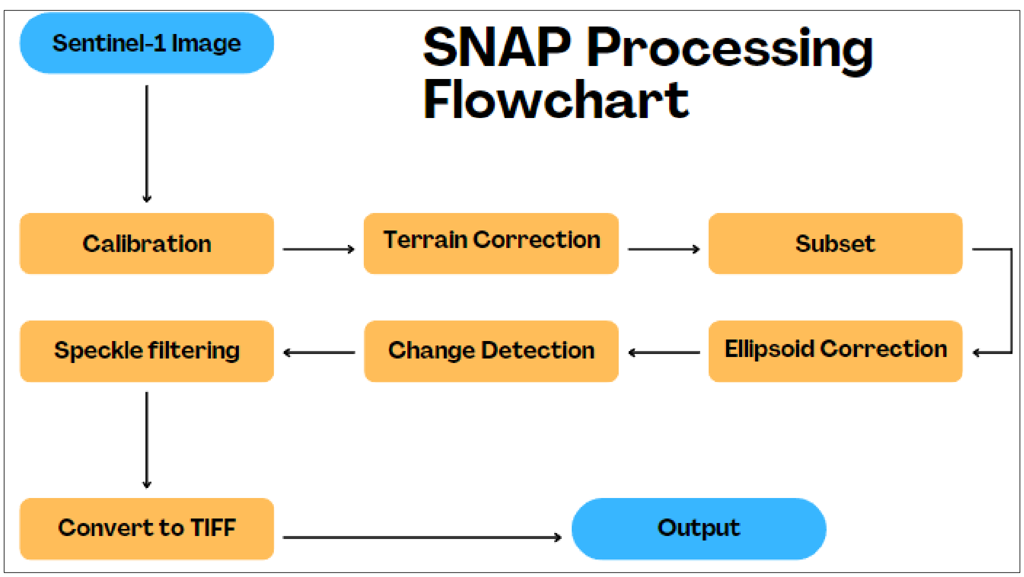

Figure 2.8 Graphical depiction of the Sentinel Application Platform (SNAP) software process used on sentinel-1 images

- Calibration: this can be implemented to refine the satellite sensor data by addressing inherent sensor biases, radiometric distortions, and atmospheric interferences. This step significantly improved the accuracy of subsequent analysis and interpretation of the target image. The Terrain Correction module played a crucial role in correcting terrain effects, particularly in regions with notable topography, ensuring precision in flood mapping.
- Image Subset: this ca be applied to focus the analysis on the specific area of interest, while speckle filtering, using techniques such as Lee, Gamma-MAP, or Enhanced Lee filters, was employed to reduce noise inherent in radar images. The "Change Detection" module identified areas experiencing significant changes between two or more radar acquisitions, with flooded regions often displaying alterations in backscatter intensity.
- Ellipsoid correction: To compensate for the Earth's surface curvature, ellipsoid correction can be applied, adjusting the satellite image to conform to a theoretical ellipsoid model. This ensures accurate geometric representation and measurements in the remote sensing data.
- Convert to TIFF: Finally, the processed image should be converted to a Tagged Image File Format (TIFF), a widely used format that preserves georeferencing and metadata. This conversion facilitates compatibility with various software, enabling further analysis and visualization of the remote sensing data.

2.5.3 Histogram and Threshold Analysis

Threshold determination in Sentinel-1 images is a crucial step in the process of extracting meaningful information from the radar data. Thresholding is often used for tasks such as segmentation, change detection, and feature extraction. The following table 2.6 describes key considerations and methods for threshold determination in Sentinel-1 images:

Table 2.6 Threshold determination for binary image processing

Method	Description
Otsu's Method	Finds the threshold that maximizes the variance between two classes of pixel intensities, effectively separating foreground, and background (Liu & Jian, 2009)
Kapur's Method	Entropy-based method seeking a threshold that maximizes the entropy of the resulting binary image (Yang et al., 2022)
Sauvola's Method	Designed for documents with varying background intensities; adapts the threshold based on local mean and standard deviation (Mustafa et al., 2018)
Minimum Cross Entropy	Minimizes the cross entropy between the original image and the binary image, effective for bimodal histograms (Yin et al., 2007)
Moment-Preserving Thresholding	Aims to preserve certain moments of the pixel intensity distribution, maintaining

	characteristics like mean, variance, and skewness (Chen et al., 2008)

2.6 Concluding Remarks of the literature review

Previous climatic research on the CRB are primarily centered around either recent extreme events (Ndehedehe et al., 2019; Mao et al. 2019) or projections of average annual and seasonal precipitation as well as evapotranspiration for the future (Creese et al., 2019). Notably, the sole study addressing future extreme events (Onyutha, 2020) concentrated on east Africa and exclusively examined rainfall-related indices.

In terms of previous hydrological studies conducted on the CRB, authors have primarily examined seasonal variations in hydrological regimes surrounding the basin (Santos et al., 2022; Tshimanga et al., 2022; Kitambo et al., 2022). Given the study area's significance and its susceptibility to hydrological changes, it is essential to gain a contemporary understanding of both flood and drought patterns in both current and future contexts. Investigating near and distant future hydrological regimes provides a more comprehensive insight into the physical variations occurring within the basin, thereby offering a clearer understanding of its potential vulnerabilities. This understanding of hydrological conditions is instrumental in enhancing water resource management, mitigating the risks of water-related disasters, and formulating effective adaptation policies.

Researchers have also been working on improving flood maps, aiming for both accuracy and efficiency without relying on overly technical or complex methods (Amitrano et al., 2018; Li et al., 2018; Shahabi et al., 2020). While some studies highlight the accuracy of their flood mapping methods, there's a notable lack of validation against ground truth data, which is crucial for confirming the reliability of the results. Some studies introduce complex methodologies that achieve high accuracy but may not be user-friendly for non-technical users, limiting their practical application. Many studies examining flood trends over multiple years assume the stationarity of flood patterns (Tripathy et al., 2022; Vekaria et al., 2022; Uddin et al., 2019). However, with changing climate conditions, this assumption may not hold true, leading to potentially significant differences in future flood patterns. To address these issues, this study proposes a new method that combines discharge data from a well-calibrated and validated SWAT model with Sentinel-1 SAR data. This approach aims to streamline and enhance flood mapping, providing a more efficient alternative to conventional software methods. By using this approach, the study aims to speed up the mapping process while maintaining precision, offering a practical solution for various users involved in flood management.

2.7 References

Abbaspour, Karim C., Saeid Ashraf Vaghefi, and Raghvan Srinivasan. "A guideline for successful calibration and uncertainty analysis for soil and water assessment: a review of papers from the 2016 international SWAT conference." Water 10.1 (2017): 6.

Abbaspour, Karim C., et al. "A continental-scale hydrology and water quality model for Europe: Calibration and uncertainty of a high-resolution large-scale SWAT model." Journal of hydrology 524 (2015): 733-752.

Abbaspour, Karim C. "User manual for SWAT-CUP, SWAT calibration and uncertainty analysis programs." Swiss Federal Institute of Aquatic Science and Technology, Eawag, Duebendorf, Switzerland 93 (2007).

Al-Kassab, Mowafaq Muhammed, and Aveen Hameed Majeed. "The Use Of Two-Sample T-Test In The Real Data." Advances and Applications in Statistics 81 (2022): 13-22.

Aloysius, Noel, and James Saiers. "Simulated hydrologic response to projected changes in precipitation and temperature in the Congo River basin." Hydrology and Earth System Sciences 21.8 (2017): 4115-4130.

Amitrano, Donato, et al. "Unsupervised rapid flood mapping using Sentinel-1 GRD SAR images." IEEE Transactions on Geoscience and Remote Sensing 56.6 (2018): 3290-3299.

Amorim, Jhones da Silva, et al. "Quantifying the climate change-driven impacts on the hydrology of a data-scarce watershed located in the Brazilian Tropical Savanna." Hydrological Processes 36.7 (2022): e14638.

Anjum, Muhammad Naveed, Yongjian Ding, and Donghui Shangguan. "Simulation of the projected climate change impacts on the river flow regimes under CMIP5 RCP scenarios in the westerlies dominated belt, northern Pakistan." Atmospheric Research 227 (2019): 233-248.

Arnold, Jeffrey G., et al. "Large area hydrologic modeling and assessment part I: model development 1." JAWRA Journal of the American Water Resources Association 34.1 (1998): 73-89.

Arnold, Jeffrey G., et al. "SWAT: Model use, calibration, and validation." Transactions of the ASABE 55.4 (2012): 1491-1508.

Bola, Gode B., et al. "Understanding flood seasonality and flood regime shift in the Congo River Basin." Hydrological Sciences Journal 67.10 (2022): 1496-1515.

Bui, Huy Hoang, et al. "Integration of SWAT and QUAL2K for water quality modeling in a data scarce basin of Cau River basin in Vietnam." Ecohydrology & Hydrobiology 19.2 (2019): 210-223.

Cannon, Alex J., Stephen R. Sobie, and Trevor Q. Murdock. "Bias correction of GCM precipitation by quantile mapping: how well do methods preserve changes in quantiles and extremes?." Journal of Climate 28.17 (2015): 6938-6959.

Čerkasova, Natalja, Georg Umgiesser, and Ali Ertürk. "Development of a hydrology and water quality model for a large transboundary river watershed to investigate the impacts of climate change–A SWAT application." Ecological Engineering 124 (2018): 99-115.

Chen, I-Ping, Ming-Yi Lai, and Ling-Ling Wang. "An improvement in the moment-preserving thresholding method." International Journal of Imaging Systems and Technology 18.5-6 (2008): 365-370.

Creese, Amy, R. Washington, and R. Jones. "Climate change in the Congo Basin: processes related to wetting in the December–February dry season." Climate Dynamics 53 (2019): 3583-3602.

Das, Apurba, Prabin Rokaya, and Karl-Erich Lindenschmidt. "The impact of a bias-correction approach (delta change) applied directly to hydrological model output when modelling the severity of ice jam flooding under future climate scenarios." Climatic Change 172.1-2 (2022): 19.

Dos Santos, V., et al. "Evaluating the performance of multiple satellite-based precipitation products in the Congo River Basin using the SWAT model." Journal of Hydrology: Regional Studies 42 (2022): 101168.

Eghdamirad, Sajjad, Fiona Johnson, and Ashish Sharma. "How reliable are GCM simulations for different atmospheric variables?" Climatic Change 145 (2017): 237-248.

El-Khoury, Antoun, et al. "Combined impacts of future climate and land use changes on discharge, nitrogen and phosphorus loads for a Canadian river basin." Journal of environmental management 151 (2015): 76-86.

Fang, G. H., et al. "Comparing bias correction methods in downscaling meteorological variables for a hydrologic impact study in an arid area in China." Hydrology and Earth System Sciences 19.6 (2015): 2547-2559.

Fatichi, Simone, et al. "Soil structure is an important omission in Earth System Models." Nature communications 11.1 (2020): 522.

Feser, Frauke, et al. "Regional climate models add value to global model data: a review and selected examples." Bulletin of the American Meteorological Society 92.9 (2011): 1181-1192.

Flato, Gregory, et al. "Evaluation of climate models." Climate change 2013: the physical science basis. Contribution of Working Group I to the Fifth Assessment Report of the Intergovernmental Panel on Climate Change. Cambridge University Press, 2014. 741-866.

Holmes, Tegan L., et al. "Guidance on large scale hydrologic model calibration with isotope tracers." Journal of Hydrology 621 (2023): 129604.

Giorgi, Filippo. "Thirty years of regional climate modeling: where are we and where are we going next?." Journal of Geophysical Research: Atmospheres 124.11 (2019): 5696-5723.

Gonzalez-Aparicio, I., and A. Zucker. "Meteorological data for RES-E integration studies-State of the art Review." European Commission (2015).

Guan, Xiaoxiang, et al. "Multisite temporal rainfall disaggregation using methods of fragments conditioned on circulation patterns." Journal of Hydrology 621 (2023): 129640.

Gupta, Hoshin Vijai, Soroosh Sorooshian, and Patrice Ogou Yapo. "Status of automatic calibration for hydrologic models: Comparison with multilevel expert calibration." Journal of hydrologic engineering 4.2 (1999): 135-143.

Haque, Md Mominul, et al. "Improving the accuracy of hydrodynamic simulations in data scarce environments using Bayesian model averaging: A case study of the inner Niger Delta, Mali, West Africa." Water 11.9 (2019): 1766.

Haque, Md Mominul. Modeling Flood Extent of a Large Wetland in a Data-Scarce Region Using Hydrodynamic and Empirical Models. Diss. Université d'Ottawa/University of Ottawa, 2020.

Harms, Archie A., and Thomas H. Campbell. "An extension to the Thomas-Fiering Model for the sequential generation of streamflow." Water Resources Research 3.3 (1967): 653-661.

Hernández-Díaz, Leticia, et al. "Climate simulation over CORDEX Africa domain using the fifth-generation Canadian Regional Climate Model (CRCM5)." Climate Dynamics 40 (2013): 1415-1433.

Hu, Shunshi, et al. "Automatic extraction of water inundation areas using Sentinel-1 data for large plain areas." Remote Sensing 12.2 (2020): 243.

Hundecha, Yeshewatesfa, et al. "Inter-comparison of statistical downscaling methods for projection of extreme flow indices across Europe." Journal of hydrology 541 (2016): 1273-1286.

Jajarmizadeh, Milad, et al. "Optimal calibration and uncertainty analysis of SWAT for an arid climate." Air, Soil and Water Research 10 (2017): 1178622117731792.

Kendon, Elizabeth J., et al. "Using and designing GCM–RCM ensemble regional climate projections." Journal of Climate 23.24 (2010): 6485-6503.

Khoi, Dao Nguyen, and Vu Thi Thom. "Parameter uncertainty analysis for simulating streamflow in a river catchment of Vietnam." Global ecology and conservation 4 (2015): 538-548.

Kitambo, Benjamin, et al. "A combined use of in situ and satellite-derived observations to characterize surface hydrology and its variability in the Congo River Basin." Hydrology and Earth System Sciences 26.7 (2022): 1857-1882.

Kitambo, Benjamin, et al. "Large-scale spatio-temporal variability of the Congo Basin surface hydrologic components from space." EGU General Assembly Conference Abstracts. 2022.

Knoche, Malte, et al. "Combined uncertainty of hydrological model complexity and satellite-based forcing data evaluated in two data-scarce semi-arid catchments in Ethiopia." Journal of hydrology 519 (2014): 2049-2066.

Komi, Kossi, et al. "Modelling of flood hazard extent in data sparse areas: a case study of the Oti River basin, West Africa." Journal of Hydrology: Regional Studies 10 (2017): 122-132.

Laprise, René, et al. "Climate projections over CORDEX Africa domain using the fifth-generation Canadian Regional Climate Model (CRCM5)." Climate Dynamics 41 (2013): 3219-3246.

Lebel, Thierry, and Abdou Ali. "Recent trends in the Central and Western Sahel rainfall regime (1990–2007)." Journal of hydrology 375.1-2 (2009): 52-64.

Li, Yu, et al. "An automatic change detection approach for rapid flood mapping in Sentinel-1 SAR data." International journal of applied earth observation and geoinformation 73 (2018): 123-135.

Liu, Dongju, and Jian Yu. "Otsu method and K-means." 2009 Ninth International conference on hybrid intelligent systems. Vol. 1. IEEE, 2009.

Lorenz, Manuel, Jan Bliefernicht, and Harald Kunstmann. "Bias correction of daily precipitation for ungauged locations using geostatistical approaches: A case study for the CORDEX-Africa ensemble." International Journal of Climatology 42.12 (2022): 6596-6615.

Mancini, Francesco, Francesca Grassi, and Nicola Cenni. "A workflow based on SNAP–StaMPS open-source tools and GNSS data for PSI-Based ground deformation using dual-orbit sentinel-1 data: Accuracy assessment with error propagation analysis." Remote Sensing 13.4 (2021): 753.

Mao, Yuna, et al. "Flood inundation generation mechanisms and their changes in 1953–2004 in global major river basins." Journal of Geophysical Research: Atmospheres 124.22 (2019): 11672-11692.

Mashala, Makgabo Johanna, et al. "A Systematic Review on Advancements in Remote Sensing for Assessing and Monitoring Land Use and Land Cover Changes Impacts on Surface Water Resources in Semi-Arid Tropical Environments." Remote Sensing 15.16 (2023): 3926.

McKee, Thomas B., Nolan J. Doesken, and John Kleist. "The relationship of drought frequency and duration to time scales." Proceedings of the 8th Conference on Applied Climatology. Vol. 17. No. 22. 1993.

Mengistu, Achamyeleh G., Leon D. van Rensburg, and Yali E. Woyessa. "Techniques for calibration and validation of SWAT model in data scarce arid and semi-arid catchments in South Africa." Journal of Hydrology: Regional Studies 25 (2019): 100621.

Mengistu, Tarekegn Dejen, et al. "Impacts and implications of land use land cover dynamics on groundwater recharge and surface runoff in East African Watershed." Water 14.13 (2022): 2068.

Moges, Mamaru A., and Semu Ayalew Moges. "Characteristics of future extreme precipitation and temperature in Lake Tana basin, Ethiopia." Extreme hydrology and climate variability. Elsevier, 2019. 59-69.

Mokhov, I. I., and A. V. Eliseev. "Modeling of global climate variations in the 20th-23rd centuries with new RCP scenarios of anthropogenic forcing." Doklady Earth Sciences. Vol. 443. No. 2. Springer, 2012.

Mustafa, Wan Azani, Haniza Yazid, and Mastura Jaafar. "An improved sauvola approach on document images binarization." Journal of Telecommunication, Electronic and Computer Engineering (JTEC) 10.2 (2018): 43-50.

Nash, J. Eamonn, and Jonh V. Sutcliffe. "River flow forecasting through conceptual models part I—A discussion of principles." Journal of hydrology 10.3 (1970): 282-290.

Ndehedehe, Christopher E., et al. "Modelling the impacts of global multi-scale climatic drivers on hydro-climatic extremes (1901–2014) over the Congo basin." Science of The Total Environment 651 (2019): 1569-1587.

Neitsch, Susan L., et al. Soil and water assessment tool theoretical documentation version 2009. Texas Water Resources Institute, 2011.

Ocio, D., T. Beskeen, and K. Smart. "Fully distributed hydrological modelling for catchment-wide hydrological data verification." Hydrology Research 50.6 (2019): 1520-1534.

Onyutha, Charles. "Analyses of rainfall extremes in East Africa based on observations from rain gauges and climate change simulations by CORDEX RCMs." Climate Dynamics 54.11-12 (2020): 4841-4864.

Pan, YongHao, et al. "River direction prediction of Shuangliu District Fu River based on ArcSWAT model." Journal of Physics: Conference Series. Vol. 2277. No. 1. IOP Publishing, 2022.

Park, Jong-Yoom, et al. "Assessing climate change impact on hydrological components of Yongdam dam watershed using RCP emission scenarios and SWAT model." Journal of the Korean Society of Agricultural Engineers 56.3 (2014): 19-29.

Paz, Santiago Mendoza, and Patrick Willems. "The skill of statistical downscaling in future climate with high-resolution climate models as pseudo-reality." Journal of Hydrology: Regional Studies 48 (2023): 101477.

Pierce, David W., Daniel R. Cayan, and Bridget L. Thrasher. "Statistical downscaling using localized constructed analogs (LOCA)." Journal of hydrometeorology 15.6 (2014): 2558-2585.

Risser, Mark D., et al. "Identifying and correcting biases in localized downscaling estimates of daily precipitation return values." Climatic Change 169.3-4 (2021): 33.

Sarr, M. A., et al. "Comparison of downscaling methods for mean and extreme precipitation in Senegal." Journal of Hydrology: Regional Studies 4 (2015): 369-385.

Schmidli, Jürg, Christoph Frei, and Pier Luigi Vidale. "Downscaling from GCM precipitation: a benchmark for dynamical and statistical downscaling methods." International Journal of Climatology: A Journal of the Royal Meteorological Society 26.5 (2006): 679-689.

Shahabi, Himan, et al. "Flood detection and susceptibility mapping using sentinel-1 remote sensing data and a machine learning approach: Hybrid intelligence of bagging ensemble based on k-nearest neighbor classifier." Remote Sensing 12.2 (2020): 266.

Shrestha, Sangam, et al. "Evaluation of adaptation options for reducing soil erosion due to climate change in the Swat River Basin of Pakistan." Ecological Engineering 158 (2020): 106017.

Sirisena, T. A., Shreedhar Maskey, and Roshanka Ranasinghe. "Hydrological model calibration with streamflow and remote sensing based evapotranspiration data in a data poor basin." Remote sensing 12.22 (2020): 3768.

Sittichok, K., et al. "Statistical seasonal rainfall and streamflow forecasting for the Sirba watershed, West Africa, using sea-surface temperatures." Hydrological Sciences Journal 61.5 (2016): 805-815.

Smith, Matthew J., et al. "Changing how earth system modeling is done to provide more useful information for decision making, science, and society." Bulletin of the American Meteorological Society 95.9 (2014): 1453-1464.

Sridhar, Venkataramana, et al. "Water Budgets and Droughts under Current and Future Conditions in the Congo River Basin." Congo Basin Hydrology, Climate, and Biogeochemistry: A Foundation for the Future (2021).

Tripathy, Pratyush, and Teja Malladi. "Global Flood Mapper: a novel Google Earth Engine application for rapid flood mapping using Sentinel-1 SAR." Natural Hazards 114.2 (2022): 1341-1363.

Tshimanga, R. M., and D. A. Hughes. "Climate change and impacts on the hydrology of the Congo Basin: The case of the northern sub-basins of the Oubangui and Sangha Rivers." Physics and Chemistry of the Earth, Parts A/B/C 50 (2012): 72-83.

Uddin, Kabir, Mir A. Matin, and Franz J. Meyer. "Operational flood mapping using multi temporal Sentinel-1 SAR images: A case study from Bangladesh." Remote Sensing 11.13 (2019): 1581.

Van Vuuren, Detlef P., et al. "The representative concentration pathways: an overview." Climatic change 109 (2011): 5-31.

Vekaria, Darshil, et al. "A change detection approach to flood inundation mapping using multi-temporal Sentinel-1 SAR images, the Brahmaputra River, Assam (India): 2015–2020." Journal of Earth System Science 132.1 (2022): 3.

Verhagen, Arianne P., Raymond WJG Ostelo, and Arno Rademaker. "Is the p value really so significant?." Australian Journal of Physiotherapy 50.4 (2004): 261-262.

Wheeler, Sarah Ann, et al. "Developing a water market readiness assessment framework." Journal of Hydrology 552 (2017): 807-820.

Yan, Kun, et al. "Regional versus physically based methods for flood inundation modelling in data scarce areas: an application to the Blue Nile." (2014).

Yang, Xiao, et al. "Multi-threshold image segmentation for melanoma based on Kapur’s entropy using enhanced ant colony optimization." Frontiers in Neuroinformatics 16 (2022): 1041799.

Yasir, Muhammad, Tiesong Hu, and Samreen Abdul Hakeem. "Simulating reservoir induced Lhasa streamflow variability using ArcSWAT." Water 12.5 (2020): 1370.

Yin, Peng-Yeng. "Multilevel minimum cross entropy threshold selection based on particle swarm optimization." Applied mathematics and computation 184.2 (2007): 503-513.

Zango, Baba-Serges, et al. "Impacts of urbanization and climate change on water quantity and quality in the Carp River watershed." Journal of Water and Climate Change 13.2 (2022): 786-816.

Chapter 3

Study area and study material

3.1 Study Area

The Congo River Basin (CRB), located in central Africa, has been selected as the study area of this research work (see figure 1.1). The CRB is one of the largest drainage basins in the world, situated in Central Africa. It covers an extensive area of approximately 3.7 million square kilometers (1.4 million square miles), making it the second-largest river basin in terms of size, after the Amazon Basin (Tshimanga et al., 2014). The CRB is characterized by a dense network of rivers and tributaries. The Congo River itself is a crucial component, with a length of about 4,700 kilometers (2,920 miles), making it the second-longest river in Africa after the Nile. Major tributaries include the Kasai, Sangha, Oubangui, Aruwimi, and Lomami rivers. The basin spans multiple countries, including the Democratic Republic of the Congo (DRC), the Republic of the Congo, Central African Republic, Zambia, Angola, Cameroon, and Tanzania. The central part of the basin is often referred to as the Congo Rainforest, one of the world's largest rainforests, which plays a significant role in the hydrological and climatic dynamics of the region. The CRB is renowned for its rich biodiversity, hosting a diverse array of plant and animal species. The rainforest within the basin acts as a major carbon sink and contributes significantly to global climate regulation. This basin is a vital source of freshwater, supporting the livelihoods of millions of people in the surrounding countries. It facilitates agriculture, fishing, and transportation, playing a crucial role in the economic activities of the region.

3.2 Ecological and economical importance of the CRB

The CRBs complex hydrological system, anchored by the Congo River and its tributaries, contributes to the regulation of regional and global climates (Beyene et al., 2012). The rich mosaic of ecosystems within the CRB supports intricate ecological interactions and provides essential ecosystem services, influencing weather patterns, fostering genetic diversity, and ensuring the livelihoods of local communities. Preserving the ecological integrity of the CRB is crucial for the well-being of Central Africa and holds major global significance for biodiversity conservation and climate stability. It also sustains a range of economic activities that contribute significantly to the livelihoods of the communities residing in the region (Jean Hugues, 2011). Some of the prominent economic activities surrounding the CRB include:

- Agriculture: The fertile soils within the basin support diverse agricultural practices, which is fundamental for local economic activity, providing food security and income (Comptour et al., 2020).
- Fishing: The rivers and water bodies in the CRB are rich in fish species (Zamba et al., 2019). Fishing serves as a means of livelihood for many communities along the riverbanks.
- Transportation: The Congo River serves as a natural transportation route. It facilitates the movement of goods and people, particularly in areas where road infrastructure is limited (Munyangeyo, 2021). River transportation is a cost-effective and efficient means of connecting remote communities and transporting goods to markets.
- Tourism: The unique biodiversity and natural beauty of the CRB, especially the Congo Rainforest, attract tourists interested in ecotourism and wildlife observation. Tourism

generates income for local communities and promotes conservation efforts (Jean Hugues, 2011).

3.3 Hydrology of the CRB

The CRB serves as a vital hydrological system with intricate dynamics that significantly influence the surrounding regions. The primary source of water for the CRB is the Congo River itself, along with its extensive network of tributaries (figure 3.1). The basin's hydrological patterns are intricately linked to precipitation in the Upper Congo Basin (UCB). The amount of rainfall, particularly during the wet season, plays a crucial role in determining the water flow within the basin (Tshimanga et al., 2022). The basin experiences distinct wet and dry seasons, with variations in precipitation influencing flood dynamics. Given the vast size of the basin, ranging from the humid rainforest regions to drier areas, the average annual rainfall exhibits considerable variability. Understanding the spatial distribution of rainfall within the CRB is essential for comprehending the seasonal fluctuations in water levels, which, in turn, impact the basin's ecological and economic dynamics (Karam et al., 2023). The relationship between precipitation, river flow, and the diverse landscapes within the CRB underscores the complex nature of its hydrological system and highlights the importance of comprehensive monitoring and analysis for sustainable management of this critical resource.

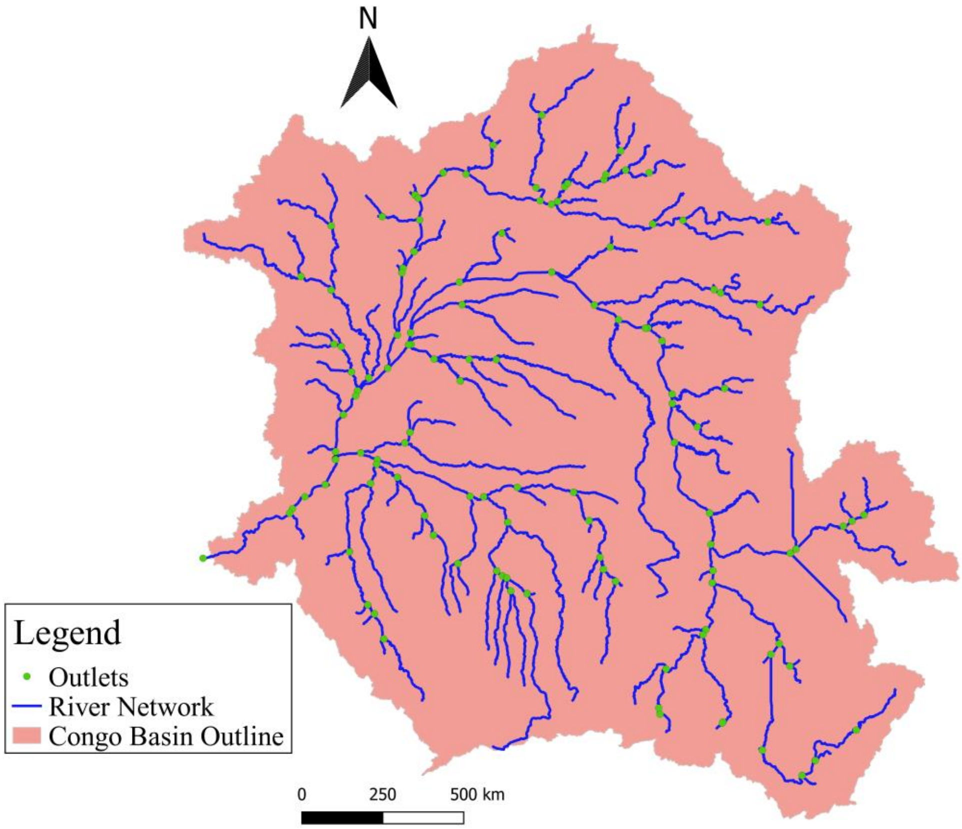

Figure 3.1 Congo River Basin outline along with its extensive river network and outlet locations

Evaporation in the CRB results in the loss of water from rivers and moist surfaces, impacting the water balance and ecosystem dynamics (Crowhurst et al., 2020). This process influences river flow, temperature regulation, and precipitation patterns. High evaporation rates in the warm and humid climate of the CRB contribute to reduced water availability of water resources for both ecosystems and human activities (Karam et al., 2022).

3.4 Available Data

3.4.1 Meteorological Variables

In this study, a dataset was compiled from the Congo Basin Water Resources Research Center (CRREBaC), encompassing 121 monthly measured precipitation time series and 17 measured minimum and maximum temperature time series spanning from 1956 to 2019. Daily rainfall observations from 1961 to 2019 were specifically obtained at the Kinshasa-Mbinza station, supplemented by additional data from the WFDEI reanalysis dataset, which provides daily time series for various meteorological variables. To ensure data reliability, a screening process was implemented for the observed precipitation data, excluding values with variations exceeding 10% of the total calculated using WFDEI, resulting in a refined set of 50 precipitation stations. For areas lacking observational data, the more dependable WFDEI dataset was utilized at 12 stations. Additionally, projected climate data from 11 experiments obtained from CORDEX were incorporated, employing the inverse distance weighting (IDW) method to interpolate over 63 locations in the basin.

3.4.2 Hydrological Response Units (HRUs)

Land-use characteristics of the CRB were obtained by downloading relevant data from https://earthexplorer.usgs.gov/. The specific details and categorizations of land use within the basin are provided in table 3.1 (Arnold et al., 2012). In the process of delineating the HRUs, which are distinct areas characterized by unique combinations of topographical features, land-use patterns, and soil attributes, a total of twelve HRUs were identified.

Table 3.1 Land-use characteristics of the Congo River Basin (Arnold et al., 2012)

Land Use/Cover Type	SWAT Code	Area (%)
1. Water	WATR	2.70
2. Residential area (urban)	URMD	0.02
3. Dryland cropland and pasture	CRDY	3.87
4. Mosaic cropland/grassland	CRGR	0.12
5. Mosaic cropland/woodland	CRWO	7.15
6. Grassland	GRAS	0.19
7. Shrubland	SHRB	0.31
8. Savanna	SAVA	28.27
9. Deciduous broad-leaf forest	FODB	13.70
10. Evergreen broad-leaf forest	FOEB	42.89
11. Mixed forest	FOMI	0.18
12. Barren or sparsely vegetated	BSVG	0.58

3.4.3 Sentinal-1 Imagery

Sentinel-1 images capturing the region around the Oubangui River were acquired from the Alaska Satellite Facility (ASF) Data Search Vertex (https://www.earthdata.nasa.gov/, accessed on March 31st, 2023). Figure 3.2 illustrates an unprocessed example of a Sentinel image retrieved specifically for this study. The download procedure involves specifying search parameters to refine the dataset of interest. For this study, filters were applied to extract surface water information, refining criteria such as the satellite, imaging mode, processing level, polarization, acquisition times, orbit number, footprint, and processing details.

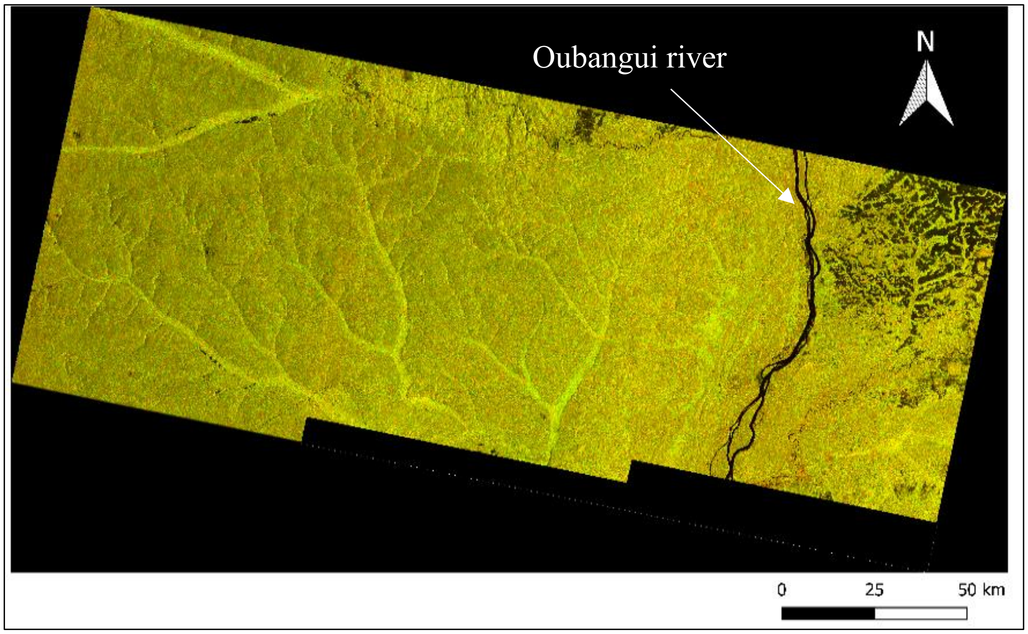

Figure 3.2 Raw unprocessed sentinel-1 image of a section of the Oubangui river downloaded from the Alaska Satellite Facility (ASF) Data Search Vertex (https://www.earthdata.nasa.gov/, accessed on March 31st, 2023)

The Sentinel-1 image is identified by its code: S1A_IW_GRDH_1SDV_20160124T043248_20160124T043303_009631_00E080_4C8A, and decoding this code reveals pertinent information about the image:

- Satellite Identifier (S1A): This indicates that the image was acquired by the Sentinel-1A satellite, which is part of the Sentinel-1 mission operated by the European Space Agency.
- Imaging Mode (IW): This refers to the imaging mode used to acquire the data. In this case, "IW" stands for "Interferometric Wide."
- Processing Level (GRDH): This signifies the level of processing applied to the raw radar data. "GRDH" indicates that the data has undergone Ground Range-Detection and High-Resolution processing. This level typically includes calibration, radiometric correction, and geolocation.

- Polarization (1SDV): This provides information about the polarization modes used during image acquisition. "1SDV" suggests that the image was acquired with a single polarization mode, and "SDV" might refer to the specific polarization configuration (e.g., Horizontal-Horizontal, Vertical-Vertical, etc.).
- Acquisition Start and End Times (20160124T043248_20160124T043303): The timestamps indicate when the image acquisition started and ended. In this example, the acquisition began on January 24, 2016, at 04:32:48 UTC and ended at 04:33:03 UTC on the same day.
- Orbit Number (009631): This is a unique identifier for the satellite's orbital pass. It helps track the satellite's position and movement over time.
- Footprint Identifier (00E080): This part of the code refers to the footprint or coverage area of the image, in terms of latitude and longitude coordinates.
- Processing Identifier (4C8A): This provides information about the specific processing version or settings applied to this image. It indicates that certain corrections or enhancements were applied during processing.

3.5 References

Arnold, Jeffrey G., et al. "SWAT: Model use, calibration, and validation." Transactions of the ASABE 55.4 (2012): 1491-1508.

Beyene, T., F. Ludwig, and W. H. P. Franssen. "The potential consequences of climate change in hydrology regime of the Congo River Basin." Climate change scenarios for the Congo Basin. No. 11. Climate Service Centre, 2012. 59-104.

Comptour, Marion, et al. "Agricultural innovation and environmental change on the floodplains of the Congo River." The Geographical Journal 186.1 (2020): 16-30.

Crowhurst, David M., Simon J. Dadson, and Richard Washington. "Evaluation of evaporation climatology for the Congo Basin wet seasons in 11 global climate models." Journal of Geophysical Research: Atmospheres 125.6 (2020): e2019JD030619.

Jean Hugues, N. L. O. M. "The economic value of Congo basin protected areas goods and services." Journal of sustainable development 4.1 (2011): 130.

Karam, Sara, et al. "Impacts of Climate Change on Hydrological Regimes in the Congo River Basin." Sustainability 15.7 (2023): 6066.

Karam, Sara, et al. "Assessing the impacts of climate change on climatic extremes in the Congo River Basin." Climatic Change 170.3-4 (2022): 40.

Munyangeyo, Aaron. Assessment and Proposals for Improved Transportation Safety on Congo River. MS thesis. Høgskolen på Vestlandet, 2021.

Paris, Adrien, et al. "Monitoring Hydrological Variables from Remote Sensing and Modeling in the Congo River Basin." Congo Basin Hydrology, Climate, and Biogeochemistry: A Foundation for the Future (2022): 339-366.

Tshimanga, Raphael M., et al. "Towards a framework of catchment classification for hydrologic predictions and water resources management in the ungauged basin of the Congo River:

An a priori approach." Congo Basin Hydrology, Climate, and Biogeochemistry: A Foundation for the Future (2022): 469-498.

Tshimanga, Raphael M., and Denis A. Hughes. "Basin-scale performance of a semi-distributed rainfall-runoff model for hydrological predictions and water resources assessment of large rivers: The Congo River." Water Resources Research 50.2 (2014): 1174-1188.

Zamba, A. I., et al. "Fish community assemblages in relation to environmental variables in the Lefini River, middle Congo River basin (Republic of Congo)." Cymbium 43 (2019): 83-95.

Chapter 4

Assessing the impacts of climate change on climatic extremes in the Congo River Basin

Abstract

The Congo River Basin, located in central Africa, is the second-largest river basin in the world, after the Amazon. It has a drainage area of approximately 3.7 M km2 and is home to 75 million people. A significant part of the population is exposed to recurrent floods and droughts, and climate change is likely to worsen these events. Climate change studies of the Congo River basin have so far focused on annual and seasonal precipitation, but little attention was paid to extreme climatic events. This study aims to assess future changes in rainfall-induced flash floods and drought regimes in the Congo basin from the present day to 2100, using four selected extreme climatic indices as proxies to these two natural disasters. The indices are the total annual precipitation (PCPTOT), the number of days where rainfall is above 20 mm (PCP20), the standardized precipitation index (SPI), and the standardized precipitation-evapotranspiration index (SPEI). The indices were calculated with the statistically downscaled output of eleven Regional Climate Models (RCMs) from the Coordinated Downscaling Experiment (CORDEX-AFRICA) under two Representative Concentration Pathways: RCP 8.5 (high emissions scenario) and RCP 4.5 (moderate emissions scenario). Precipitation and temperature simulated by the RCMs were statistically downscaled using quantile mapping, while wind speed, solar radiation, and relative humidity were projected using K-nearest neighbor downscaling. The evolution of the indices was then assessed between the reference period (1976–2005) and three future periods (2011–2040, 2041– 2070, and 2071–2100). Multimodel average results suggest that (i) independently of the scenario and period, PCPTOT and SPI will increase in the north, east, and western extremities of the basin and decrease in the basin's center. (ii) The maximum increase (+ 24%) and decrease (− 6%) in PCPTOT were both projected under RCP 8.5 in the 2071–2100 period. (iii) PCP20 will increase independently of the period and scenario. Under RCP 8.5, in the 2071–2100 period, PCP20 will increase by 94% on average over the whole watershed. (iv) The SPEI results suggest that in all periods and scenarios, the rise in evapotranspiration due to higher temperatures will offset annual precipitation increases in the north, east, and western extremities of the basin. Increased evaporation will exacerbate the decrease in annual precipitation in the center, leading to increased drought frequency in the entire basin.

Keywords Congo River Basin · Climate indices · Droughts · Floods · Precipitation · Evapotranspiration · Downscaling · RCM · SPEI · SPI

4.1 Introduction

The Congo River Basin (Figure 4.1) is in central Africa and has a drainage area of approximately 3.7 M km2. It is the second-largest river basin in the world, after the Amazon. It encompasses nine political boundaries, including Angola, Burundi, Central African Republic, Democratic Republic of Congo, Cameroon, Republic of Congo, Rwanda, Tanzania, and Zambia (Tshimanga et al. 2020). The Congo basin hosts the world's second-largest rainforest, which is crucial for the global carbon cycle. Like other rainforests in the world, its distribution and composition are likely to be influenced by changes in regional rainfall characteristics resulting from global warming (Malhi and Wright 2004). The Congo basin, along with the western Pacific Ocean and the Amazon basin, is a significant source of major storms. It also experiences droughts: there is evidence of rainforest contraction and forest composition changes during dry periods in the past 3000 years (Lewis et al. 2009; Malhi et al. 2013). It is, therefore, vital that climatic changes in the basin be studied to provide credible information for mitigation and adaptation planning (Creese et al. 2019). Despite its importance, the basin remains primarily understudied and has not received adequate attention in hydrological and climate research (Tshimanga and Hughes 2014). Between 1960 and 2019, over 11,566,029 people were affected by flooding in the countries that comprise the Congo basin. There were 3062 casualties, and the total economic damages are estimated to be 96 billion USD (EM-DAT 2020). These extreme events in the Congo basin are related to rainfall variability, which may be exacerbated by climate change at a level that may challenge the livelihood of people living in the basin. Hence, it is crucial to analyze the current and future evolution of extreme events, such as precipitation and drought frequency/intensity, for the preservation of local infrastructure and livelihood sustainability, between the reference period (1976–2005) and three future periods (2011–2040, 2041–2070, and 2071–2100).

Several authors have examined the impacts of climate change on hydroclimatic variables in various regions, including the Congo basin. Tshimanga and Hughes (2014) used Climate Model Intercomparison Project phase 3 (CMIP3) GCMs to study the effects of climate change on the Congo basin's hydrology in terms of runoff in near-future projections of the northern sub-basins of the Oubangui and Sangha Rivers. Their results point to a significant increase in evapotranspiration and a 10% decrease in total runoff. Onyutha (2020) derived twelve Extreme Rainfall Indices (ERIs) from observed 1961–1990 daily rainfall across East Africa. The ERIs were calculated with the outputs of six Regional Climate Models (RCMs) driven by twenty-six CMIP5 (Climate Model Intercomparison Project phase 5) models. They found that the ensemble means of the RCMs reproduced observed ERIs better than the individual RCMs. Jenkins et al. (2002) examined the ability of GCMs to produce realistic climatology in West Africa using the Tropical Rain Measuring Mission (TRMM) satellite and simulated rainfall rates from the Community Climate Model version 3.6 (CCM3). Although GCMs do carry uncertainties, the authors stated that they offer a good solution to predicting climate change in West Africa due to their capability of capturing mesoscale systems and their accurate consideration of orographic features. Creese et al. (2019) conducted a study on climate change in the Congo basin, focusing on wetting in the December-February season (DJF), using nineteen CMIP5 GCM models. They were able to quantify and define the spectrum of rainfall variation in the basin between 1979–2005 and 2074–2100. They found that in DJF, the seasonal rainfall would vary from 2 to 160 mm throughout the various models between the past and future periods.

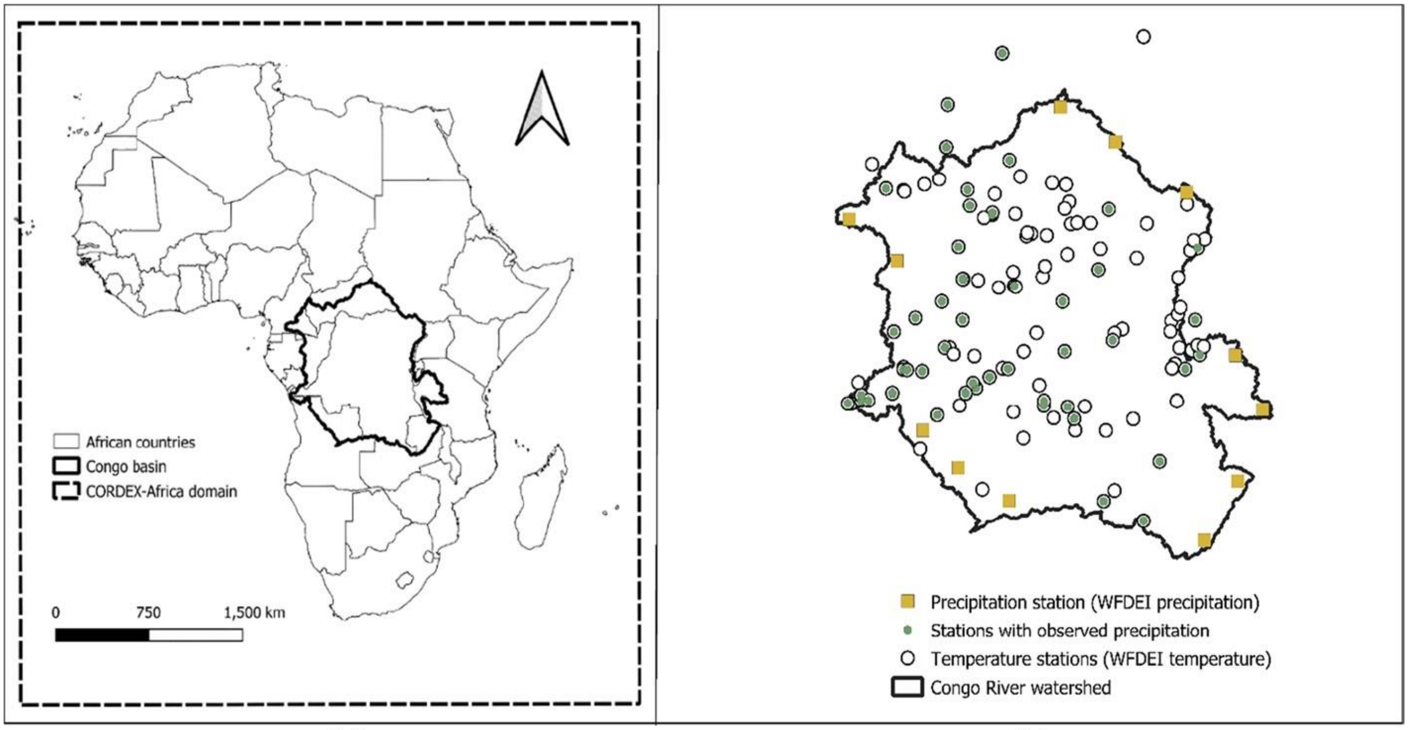

(a) (b)

Figure 4.1 (a) Extent and location of the Congo basin. (b) Observation stations in (or near) the Congo basin for which precipitation and temperature data were available (either from direct observations or WFDEI reanalysis).

Mao et al. (2019) analyzed river flooding in the basin in relation to what season the flooding occurred, to differentiate the different causes of flooding, such as intense rainfall events or an excess of soil moisture. They found a link between progressive climate change and an observed increase in inundation events throughout multiple watersheds globally, including the Congo basin. They also used the annual maximum daily flood extent to define a flood seasonality index. The mean flood date (MD) between 1953 and 2004 and the seasonality index were used to qualitatively classify floods in the Congo basin (among other watersheds) into several event-driven categories. They showed that the combination of soil moisture excess and extreme precipitation events was the main contributor to flood events in the Congo basin. Ndehedehe et al. (2019) modeled the impacts of global multi-scale climatic drivers on mean annual hydroclimatic extremes such as the Standardized Precipitation Index (SPI) and Standardized Runoff Index (SRI) between 1901 and 2014 in the Congo basin. Statistical relationships and coupled variability between SPI and global climate models were examined. They developed a predictive framework with a non-linear autoregressive neural network to analyze the connectivity between SPI patterns and global ocean–atmosphere regimes. The study showed that the Congo basin could be characterized by severe multi-year droughts between 1901 and 2014, which affected 40–50% of the land area. The study showed that as of 1994, the hydrological regimes of the basin have changed due to drought intensification.

The focus of the above studies that considered the Congo basin were either extreme events in the recent past (Ndehedehe et al. (2019); Mao et al. (2019)) or average annual and seasonal precipitation and evapotranspiration in the future (Creese et al. (2019)). The only study dealing with extreme events in the future (Onyutha 2020) focused on east Africa and only considered rainfall-related indices. Furthermore, the RCM data they used was not further corrected, while it is known that RCM precipitation can significantly differ from ground observations, in terms of both magnitude and seasonal patterns. Given the importance of the entire Congo basin and the vulnerability of its inhabitants, up-to-date knowledge about flood and drought regimes in the current and future periods has become increasingly relevant. Annual average precipitation and evaporation examined in previous studies are pertinent for practical use, but extreme values have a greater impact on the vulnerability of the basin's population. Understanding climatic extremes can help improve water resources management and water-related disaster risk reduction and guide adaptation policies. Therefore, the current study aims at assessing future changes in rainfall and drought regimes in the Congo basin from the present time to 2100, using four selected climate indices: the average annual total precipitation, PCPTOT; the number of days where precipitation is above 20 mm, PCP20; The Standard Precipitation Index, SPI; and the Standard Precipitation Evaporation Index, SPEI. The indices were selected because of their direct link to floods and/or drought regimes. The evolution of the four climate indices between the reference period (1976–2005) and three future periods (2011–2040, 2041–2070, and 2071–2100) was assessed. The indices were calculated at 63 locations in the basin using the statistically downscaled output of eleven Regional Climate Models (RCMs) from the Coordinated Downscaling Experiment (CORDEX-AFRICA), under two Representative Concentration Pathways: RCP 8.5 (high emission scenario) and RCP 4.5 (moderate emission scenario). The indices were then interpolated over the basin using the Inverse Distance Weighting (IDW) method. Finally, the results are analyzed to provide an insight into the future of the basin in terms of flood and drought regimes, as well as related socioeconomic vulnerabilities in the basin.

4.2 Materials and methods

4.2.1 Available data

A total of 121 monthly measured precipitation times series and 17 measured minimum and maximum temperature time series were obtained from the Congo basin Water Resources Research Center (CRREBaC). The time series ranged from 1956 to 2019. The authors were able to secure the 1961–2019 daily rainfall observations at the Kinshasa-Mbinza station, but not at other locations in the basin. An alternative source of data was obtained from the WFDEI (Watch Forced Era Interim: Weedon et al. 2018) reanalysis data set; it contains daily time series of precipitation, minimum temperature, maximum temperature, relative humidity, wind speed, and solar radiation. While station data is generally considered more precise than the reanalysis data, there seemed to be many erroneous values in the observational data received by the authors. Therefore, the authors decided to discard any observed precipitation data where the annual totals were varied by more than 10% of the total calculated using WFDEI. The number of precipitation stations dropped to 50 after applying this screening method. The WFDEI data set was used at 12 stations located in areas without observational data to provide good spatial coverage within the watershed. Given that temperature estimates in the WFDEI database are more reliable than precipitation estimates, we decided to use the WFDEI time series at 130 locations.

Projected precipitation as well as minimum and maximum temperature from 11 climate change experiments obtained from the CORDEX (Coordinated Downscaling Experiment: Giorgi and Gutowski 2015) team (https:// cordex. org/ domai ns/ region- 5- africa/) were interpolated over 63 locations in the basin using the inverse distance weighting (IDW) method. Each time series spans from 1950 to 2100. Each climate change experiment consists of driving a regional climate model (RCM) by a global circulation model (GCM) under either Representative Concentration Pathway (RCP) 4.5 or RCP 8.5. RCPs are scenarios that include time series of emissions and concentrations of the full suite of greenhouse gases through to 2100. RCP 4.5 is a pathway (scenario) where radiative forcing peaks at approximately 4.5 W m^{-2} before 2100. RCP 8.5 is a higher intensity pathway for which radiative forcing reaches or exceeds 8.5 W m^{-2} by 2100. The characteristics of the climate change experiment (institution, driving GCM, RCM) are given in Table A2.1 (appendix 2). The spatial resolution of each RCM is approximately 50 km.

4.2.2 Methodology

The methodology is outlined in Figure 4.2. In the first phase, available monthly observed precipitation and temperature time series are screened before the retained time series are temporally disaggregated using the fragment method to obtain daily time series. In the second phase, daily precipitation and temperature time series are statistically downscaled using quantile mapping and the outputs of eleven RCM/GCM combinations under both RCP 4.5 and RCP 8.5 scenarios. The result gives downscaled and bias-corrected precipitation and temperature time series representing past, present, and future conditions starting in 1976 and ending in 2100. Daily WFDEI humidity (HMD), wind speed (WND), and solar radiation (RSDS) time series are downscaled using the nearest-neighbor approach. The third and final phase involves developing four indices to evaluate the present and future daily precipitation (PCP) results from the downscaling. These indices are analyzed using a reference period and three future study periods to project the changes that will occur in the watershed in the near future. The reference period is between 1976 and 2005, future period 1 is between 2011 and 2040, future period 2 is between 2041 and 2070, and future period 3 is between 2071 and 2100. Present and future daily max temperature (TMP), daily min TMP, HMD, WND, and RSDS will be used to evaluate present and future evapotranspiration. Finally, HMD, WND, and RSDS combined with daily PCP will allow us to develop the SPEI index.

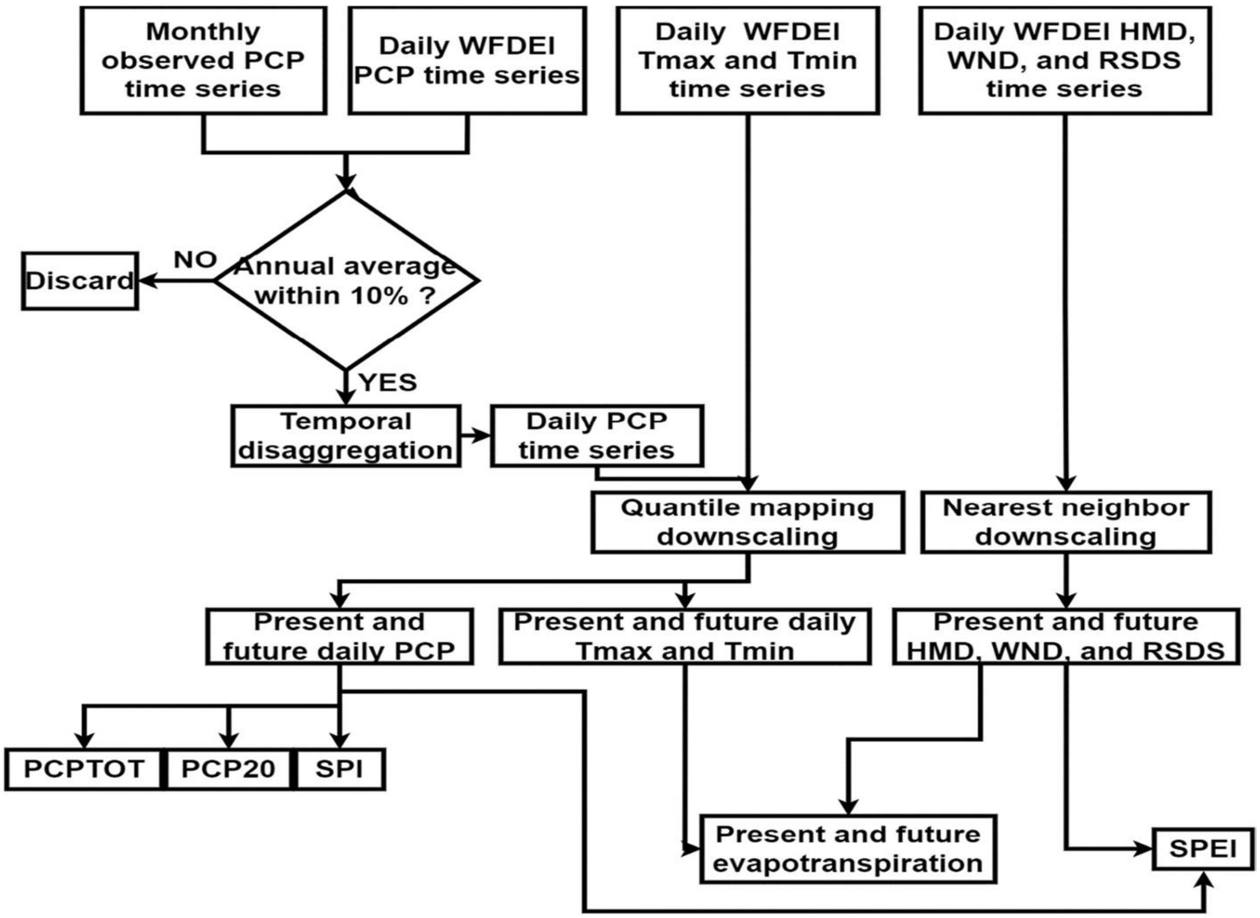

Figure 4.2 Methodology flowchart, where PCP stands for precipitation, HMD is humidity, WND is wind speed, RSDS is solar radiation, PCPTOT is total annual precipitation index, PCP20 is number of days where precipitation is above 20 mm index, SPI is the Standardized Precipitation Index, SPEI is Standardized Precipitation Evapotranspiration Index, and Tmax and Tmin are the maximum and minimum temperatures, respectively

4.2.3 Temporal disaggregation

Monthly observed rainfall time series were temporally disaggregated to the daily time step using the fragment method. The fragment method was first introduced by Harms and Campbell (1967) to increase the time scale of standardized historical rainfall. This conversion, which has no impact on monthly averages, was necessary as the calculation of PCP20 requires daily data. For each year of observed rainfall ($Y_{seasonal,obs}$) from Eq. 4.1, a year in WFDEI precipitation was chosen as follows: if the year was between 1979 and 2019, the same year was selected in the WFDEI data; if the year was anterior to 1979, the year in the WFDEI rainfall ($Y_{seasonal,WFDEI}$) with the average rainfall value closest to that of the average observed rainfall was chosen. Daily precipitation of Y_{sim} at a given station STA $_i$ was calculated using Eq 4.1 (Sittichok et al. 2016):

$$Y_{daily,sim,STAi} = Y_{daily,WFDEI,STAi}(Y_{annual,obs}/Y_{annual,WFDEI}) \qquad (4.1)$$

This disaggregation method was used for all retained stations to generate daily PCP time series while maintaining the regional variations in rainfall across the watershed.

4.2.4 Downscaling

The quantile mapping technique, also known as the quantile–quantile (Q-Q) transformation, was adopted to generate a climate variable's statistical distribution to be as similar as possible to the statistical distribution of the corresponding observed variable during the historical period. According to Hakala et al. (2018), the quantile mapping technique outperforms other methods such as the delta-change approach, local intensity scaling, and power transformation. It has been proven to have higher success in reducing biases in GCM-RCM precipitation compared to other methods. First, the historical data set was separated into the calibration and validation data sets. The calibration period was composed of odd-number years in the reference period, while the validation period is composed of even-number years in the same period. Each month's daily time series was extracted for the conforming periods from both the observational and RCM simulations (Angelina et al. 2015). Secondly, the empirical cumulative distribution functions of the observed calibrated period (F_{OBS}) and the RCM outputs (F_{RCM}) was developed. Finally, RCM simulations were corrected and generated for the validation period and for future periods using Eq. 4.2 for the transformation.

$$X_{CORR} = F_{-OBS1}\left(F_{RCM}(X_{RCM})\right) \qquad (4.2)$$

X_{CORR} is the corrected variable and X_{RCM} is the extracted value from the raw RCM simulations. The probability mass function (pmf) of PCP occurrence and the probability distribution function (pdf) of PCP intensity were generated. If the pdf/pmf of the corrected value was more similar to that of the observations than that of the non-corrected value, then the Q-Q transformation was used on the future RCM simulations for the variable in question. Future values of HMD, WND, and SLR were downscaled using the nearest neighbor approach. For each day in the future period (df), one day was chosen from the historical period from the same month (dh), and the absolute difference between the closest average temperature of df and dh was minimal. The HMD, SLR, and HMD of dh were then assigned to df.

4.2.5 Climate indices

Four indices were employed to analyze the evolution of extreme events in the future: total annual precipitation (PCPTOT), number of days where precipitation is above 20 mm (PCP20), the Standard Precipitation Index (SPI) and the Standard Precipitation-Evapotranspiration Index (SPEI).

4.2.5.1 PCPTOT

The total annual precipitation index groups the annual total precipitation on wet days, where rainfall is above or equal to 1 mm of rain:

$$\mathrm{PCPTOT_j} = \sum_{i=1}^{I} \mathrm{RR_{ij}} \qquad (4.3)$$

where RR_{ij} represents the daily precipitation on wet days, for which i represents the number of days in a certain time period j.

4.2.5.2 PCP20

This index is the average number of days per year when the rainfall is above 20 mm. The index of PCP20 is a standardized climate extreme index (https://www.climdex.org/ learn/ indices/#index-R20mm). And it is also included in the definitions of the 27 core indices (http://etccdi. pacificclimate.org/list_ 27_ indices.shtml)

$$\mathrm{PCP20_{ij}} = \sum_{i=1}^{I} \mathrm{RR_{ij}} > 20\mathrm{mm} \qquad (4.4)$$

PCP20 serves as a significant extreme climatic index compared to PCP10 or PCP30 due to its threshold level, which signifies a substantial volume of precipitation. PCP20 indicates the occurrence of extreme precipitation events where 20mm or more of rainfall is recorded within a certain timeframe. This threshold is significant because it represents a considerable amount of precipitation that can lead to various impacts such as flooding, soil erosion, and infrastructure damage. Compared to PCP10, which denotes a lower threshold and may capture less severe events, and PCP30, which sets a higher bar for extreme precipitation, PCP20 strikes a balance by identifying events that are sufficiently intense to cause significant impacts but still occur with some frequency.

4.2.5.3 SPI

SPI is a widely used index used to characterize meteorological drought at various timescales. It was first proposed by Mckee et al. (1993) and has been used by many authors in various regions around the World (e.g., Bodian 2014). It is, in essence, a standardizing transform of the probability of observed precipitation (Guttman 1998):

$$\text{SPI} = \frac{PCPTOT_i - PCPTOT_m}{Si} \qquad (4.5)$$

where PCPTOT,i represents the sum of precipitation for a given year i; PCPTOT,m represents the mean value of precipitation over the reference period; and Si is the standard deviation of precipitation aggregated at the user-defined time scale. In this paper, SPI is calculated on an annual time scale. It can be deduced from Eq. 4.5 that the average SPI over the reference period is equal to zero. Degrees of humidity and drought can be assessed using the SPI classes outlined in Table 4.1.

4.2.5.4 SPEI

SPEI is an extended version of SPI. SPEI is calculated using the same method as for the SPI, which defines the degree of drought in different classes (Lebel and Ali 2009). The fundamental difference between these two indicators is that SPI is calculated based on precipitation, while SPEI is based on the difference between precipitation and potential evapotranspiration (PCP-ET_0). Then, this cumulative value of PCP- ET_0 over m months, the loglogistic law is adjusted to three parameters (Vicente-Serrano et al. 2010). SPEI for a given period can be calculated from:

$$SPEI = CDF^{-1}_{norm(0.1)}(CDF_{log-logistic}(PCP - ET_0)) \qquad (4.6)$$

where $CDF^{-1}_{norm(0,1)}$ is the inverse cumulative distribution function of the normal distribution with mean zero and standard deviation 1 and $CDF_{log-logistic}$ is the cumulative distribution function of the log-logistic distribution fitted to PCP- ET_0. The reference evapotranspiration (ET_0) value used in this paper is the reference evapotranspiration proposed by Neitsch et al. (2011) for alfalfa. The method requires various inputs such as solar radiation, air temperature, relative humidity, and wind speed. The equations needed to calculate the reference evapotranspiration are given in the supplementary materials (Appendix 1). The degree of humidity and drought can be assessed using SPEI with the same classes as for SPI presented in Table 4.1.

Table 4.1 - Classes of SPI

SPI Class	Degree of humidity or drought
SPI > 2,0	Extreme humidity
1,5 < SPI < 2,0	High humidity
1,0 < SPI < 1,5	Moderate humidity
-1,5 < SPI < 1,0	Moderate drought
-2,0 < SPI < -1,5	Severe drought
SPI < -2.0	Extreme drought

4.2.6 Statistical testing

The two-sample t test (Snedecor and Cochran 1989) was used to assess the significance of changes in PCPTOT and PCP20 between the reference period and future periods. The purpose of the t-test is to compare the means of two independent data sets. It takes a sample from each of the two sets and creates the problem statement by assuming a null hypothesis that the two means are equal. Based on the applicable formulas, certain values are calculated and compared to the standard values and the assumed null hypothesis is accepted or rejected accordingly. Given that multiple time series are available for each climate index and that each series' mean and standard deviation are different, each time series was standardized using its mean and standard deviation of the reference period. The standardized series were then combined prior to performing the t test.

4.3 Results and discussion

A total of 63 stations were retained for precipitation (51 daily time series were obtained by disaggregation and 12 were added from the WFDEI precipitation), and 121 time series of maximum and minimum temperature from the WFDEI reanalysis were downscaled using the quantile mapping downscaling method. Humidity, solar radiation, and wind speed were downscaled using the nearest-neighbor technique. The four indices were calculated for the reference period 1, period 2, and period 3. The results were interpolated over the watershed using the inverse distance method. The results of the analysis are discussed below.

4.3.1 Impact of the temporal disaggregation on the magnitudes and trends of PCP20, PCPTOT, SPI, and SPEI

The impacts of the temporal disaggregation were assessed on the climatic indices at the only station at which the authors were able to secure daily observed data: the Kinshasa-Mbinza station (latitude= −4.36; longitude=15.25). The results of the assessment are shown in Appendix 3. The difference in average annual precipitation between WFDEI and the observations is only 28 mm (2%), and the disaggregated time series have the same mean as the observation. It was found that the number of wet days is underestimated in both WFDEI and the disaggregated time series. This led to a significant underestimation of PCP20 when the disaggregated time series were used. In the 1979–2013 period where there are valid values in all three data sets, PCP20 was 25.72 days per year in the observations, 5.85 days per year in the WFDEI data set, and 6.5 in the disaggregated data set. For the Kinshasa-Mbinza station, the magnitude of PCP20 will be severely underestimated when the disaggregated time series is used. However, the temporal disaggregation did not seem to affect the trend of that index. The magnitudes and trends of other indices (PCPTOT, SPI, SPEI) were only marginally affected.

4.3.2 Spatial distribution of indices in the reference period

Figure 4.3(a) shows the spatial distribution of the average annual total precipitation in the entire watershed for the reference period (1976–2005). The average annual precipitation ranges from 645 to 1000 mm/year in the south-eastern part of the basin up to 1948 mm/ year. The highest average annual precipitation values are observed in the center and western parts of the basin. Figure 4.3(b) shows the spatial distribution of the average PCP20 (a proxy for the frequency of high-intensity precipitation) for the reference period, where the average annual number of days with rainfall above 20 mm ranges between 1.6 days and 8.2 days. The highest rainfall intensity occurs close to the western border of the Congo basin. Figure 4.3(c) depicts the spatial distribution of SPEI in the Congo basin for the reference period, where values range from − 0.12 to 0.61. SPEI in the reference period suggests a dryer climate in the central west compared to the rest of the watershed. SPI in the reference period is by definition zero throughout the entire basin.

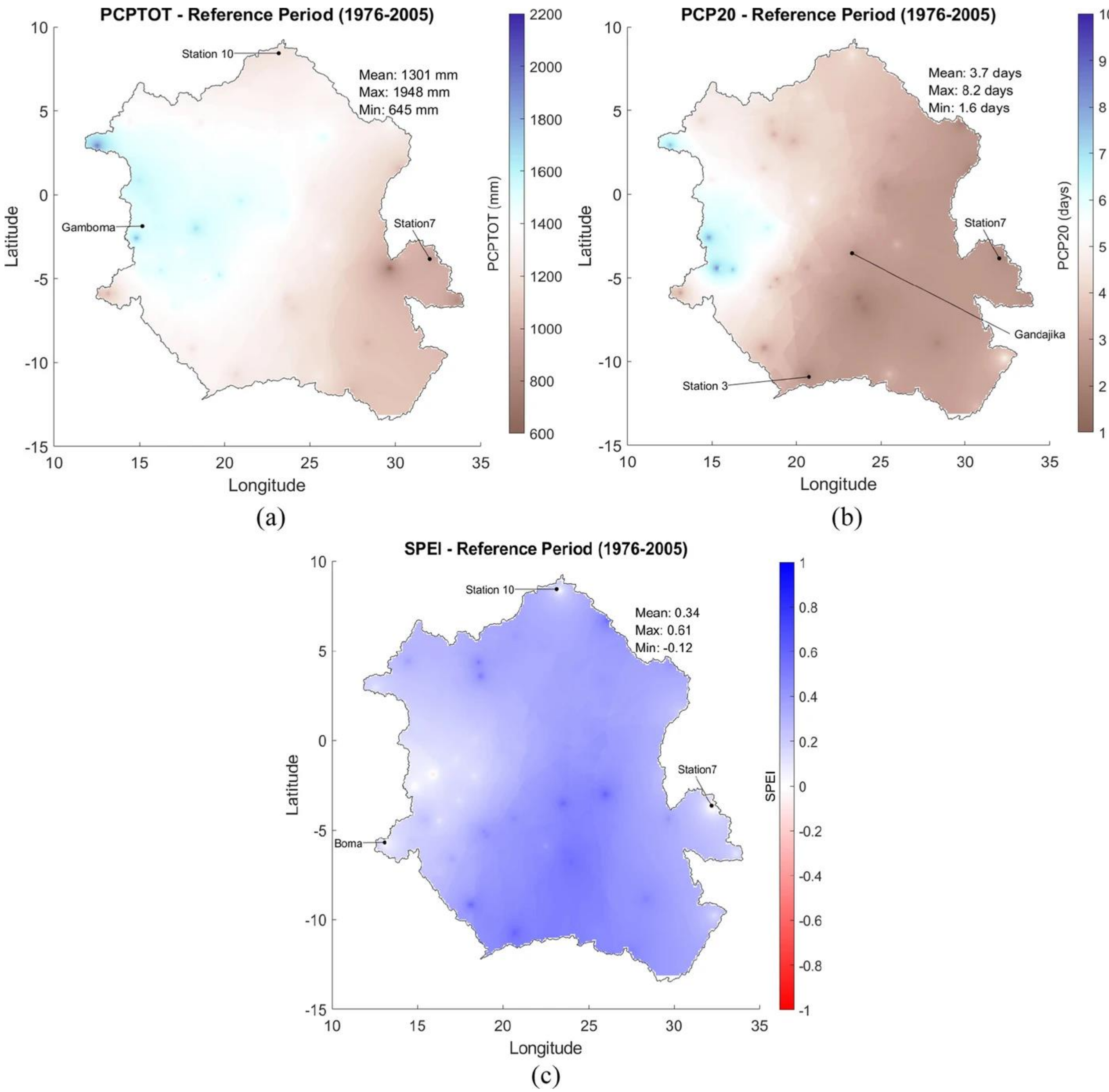

Figure 4.3 Spatial distribution of multimodel average (a) PCPTOT (mm), (b) PCP20 (days), and (c) SPEI in the Congo basin for the reference period of 1976–2005

4.3.3 Projections for PCPTOT

Figure 4.4(a) shows the spatial distribution of the multimodel average total precipitation and (b) the percentage change in the total precipitation that can be expected in the basin for the three study periods under RCP 4.5 and RCP 8.5 scenarios. Under RCP 4.5, the spatial average of the percent change in PCPTOT is very small: it is equal to 1.9% in period 1, 1.6% in period 2, and 1.1% in period 3. Under RCP 8.5, it increases from 1.6% in period 1 to 3.2% in period 2. It reaches 5.4% in period 3. The highest increases are expected in the northern part of the basin in period 3 under RCP 8.5

While the spatial average of the percent change in PCPTOT is not high (as shown in Figure 4.4(b)), local changes can differ significantly from the average. Figure 4.4(b) shows that changes in PCPTOT are generally non-significant under RCP 4.5, except from the extreme western and eastern regions of the basin where slight localized increases are expected in periods 1, 2, and 3. An increase in PCPTOT is expected under RCP 8.5 in the north-western and northern regions of the basin in periods 2 and 3, respectively.

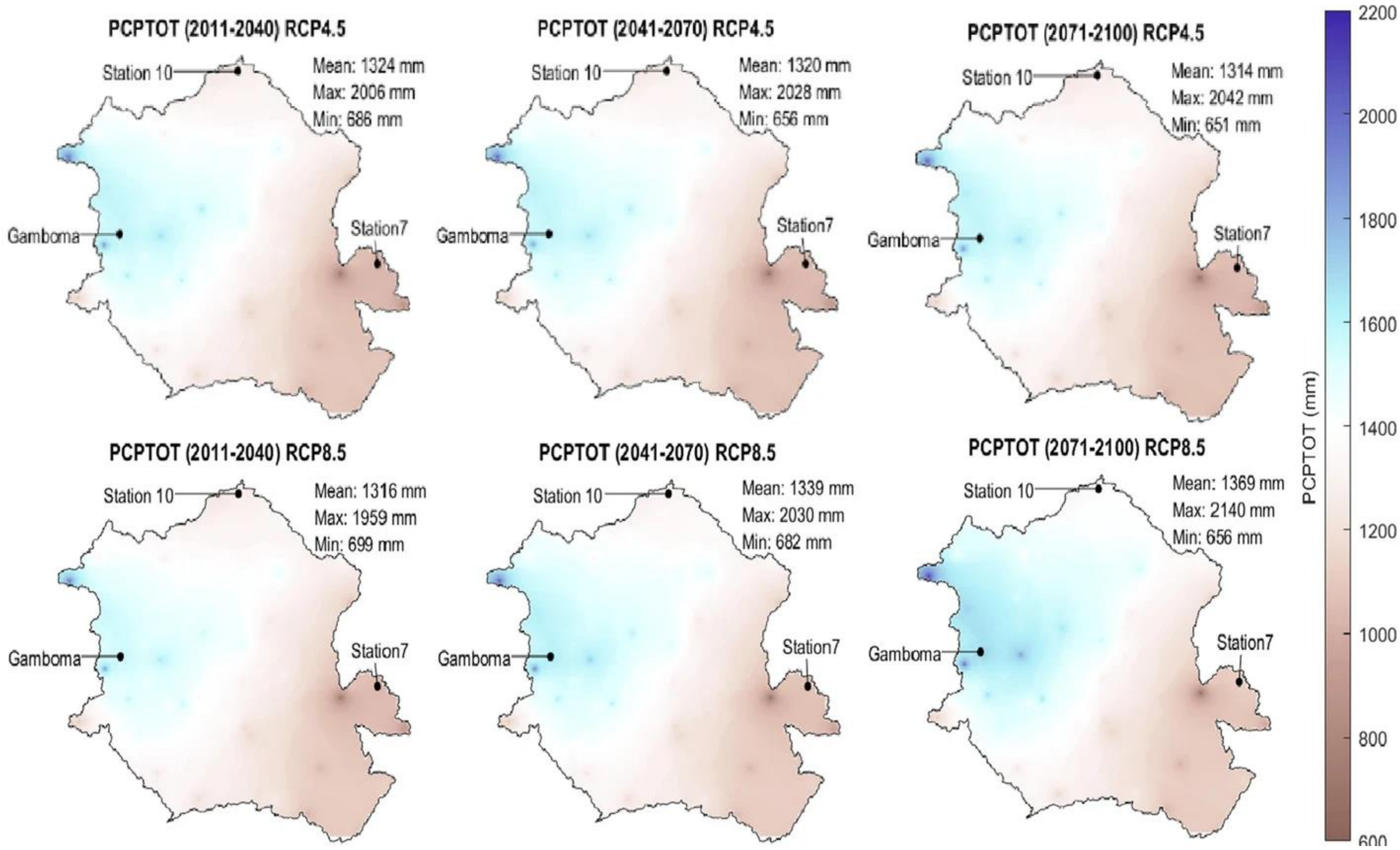
PCPTOT (2011-2040) RCP4.5
Station 10
Mean: 1324 mm
Max: 2006 mm
Min: 686 mm
Gamboma
Station7
PCPTOT (2041-2070) RCP4.5
Station 10
Mean: 1320 mm
Max: 2028 mm
Min: 656 mm
Gamboma
Station7
PCPTOT (2071-2100) RCP4.5
Station 10
Mean: 1314 mm
Max: 2042 mm
Min: 651 mm
Gamboma
Station7
PCPTOT (2011-2040) RCP8.5
Station 10
Mean: 1316 mm
Max: 1959 mm
Min: 699 mm
Gamboma
Station7
PCPTOT (2041-2070) RCP8.5
Station 10
Mean: 1339 mm
Max: 2030 mm
Min: 682 mm
Gamboma
Station7
PCPTOT (2071-2100) RCP8.5
Station 10
Mean: 1369 mm
Max: 2140 mm
Min: 656 mm
Gamboma
Station7
PCPTOT (mm)
2200
2000
1800
1600
1400
1200
1000
800
600

(a)

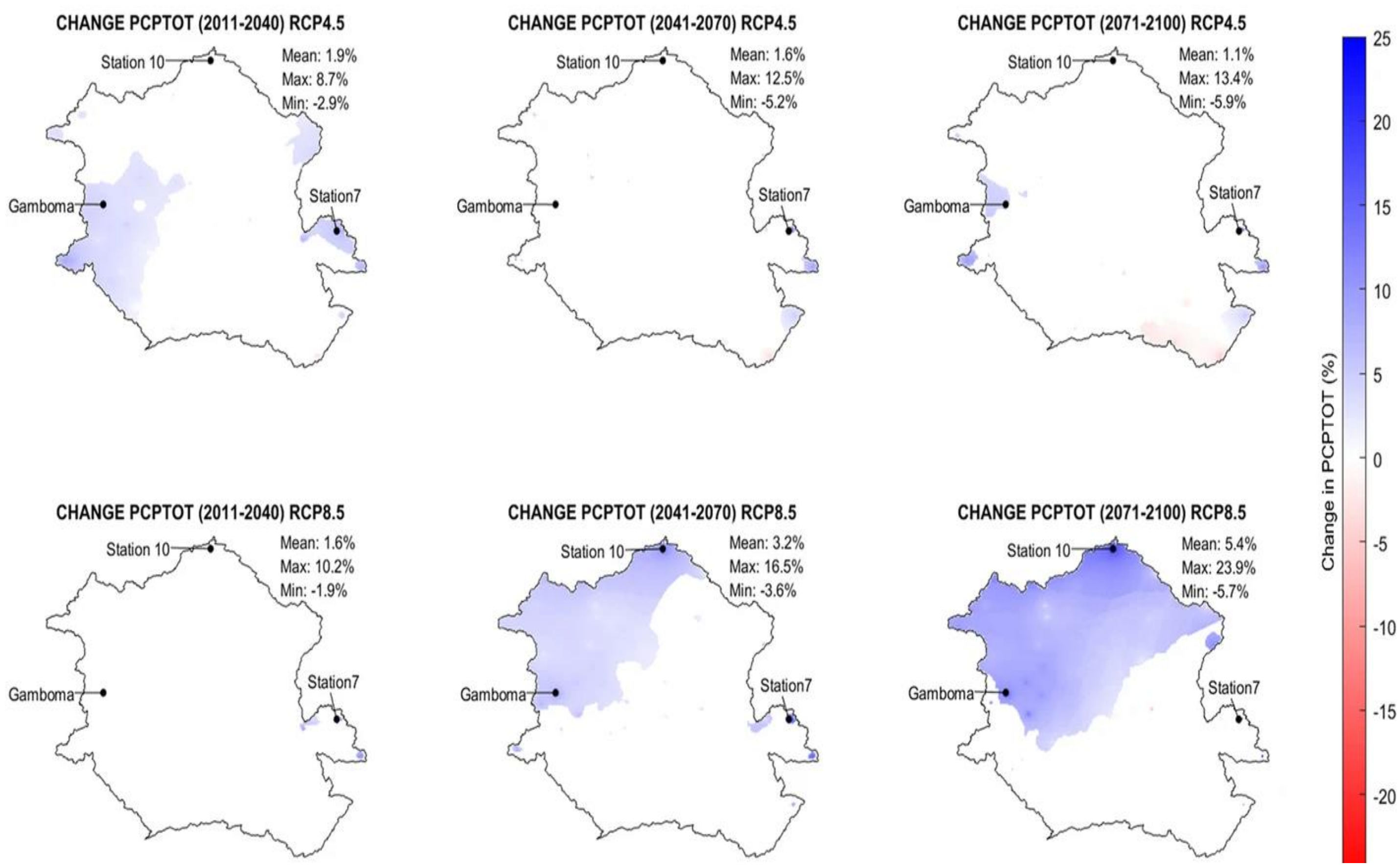

(b)

Figure 4.4 Spatial variation of multimodel averages of (a) PCPTOT and (b) the change of PCPTOT for three future periods ((2011–2040), (2041–2070), (2071–2100)) under RCP 4.5 and RCP 8.5; white spaces correspond to non-significant changes

Under RCP 4.5, the increase in the spatial average of PCPTOT is modest (under 2%) and slightly decreasing from period 1 to period 3, but the maximum and minimum changes in the basin become more extreme with time (the minimum value gradually decreases from − 2.9% in period 1 to − 5.2% in period 2 and − 5.9% in period 3; the maximum value gradually increases from 8.6% in period 1 to 12.5% in period 2 and to 13.4% in period 3).

Under RCP8.5, the average PCPTOT displays an increasing trend with time. Similarly as under scenario RCP4.5, the maximum value of PCPTOT displays an increasing trend (10.2% in period 1, 16.5% in period 2 and 23.9% in period 3) while the minimum value of PCPTOT displays a decreasing trend (− 1.9% in period 1, − 3.6% in period 2, and − 5.7% in period 3). Changes in PCPTOT are generally not significant in period 1, while significant increases are observed in the North-west part of the basin (period 2) and in the northern half of the basin (period 3).

Among the 63 stations used in this study, station 7 (east), station 10 (north), and the town of Gamboma (west) experienced the greatest increase in PCPTOT and were selected for further analysis. Figure 4.5 shows boxplots of the average annual total precipitation, PCPTOT at these three stations. PCPTOT increases at all three stations independently of the RCP scenario.

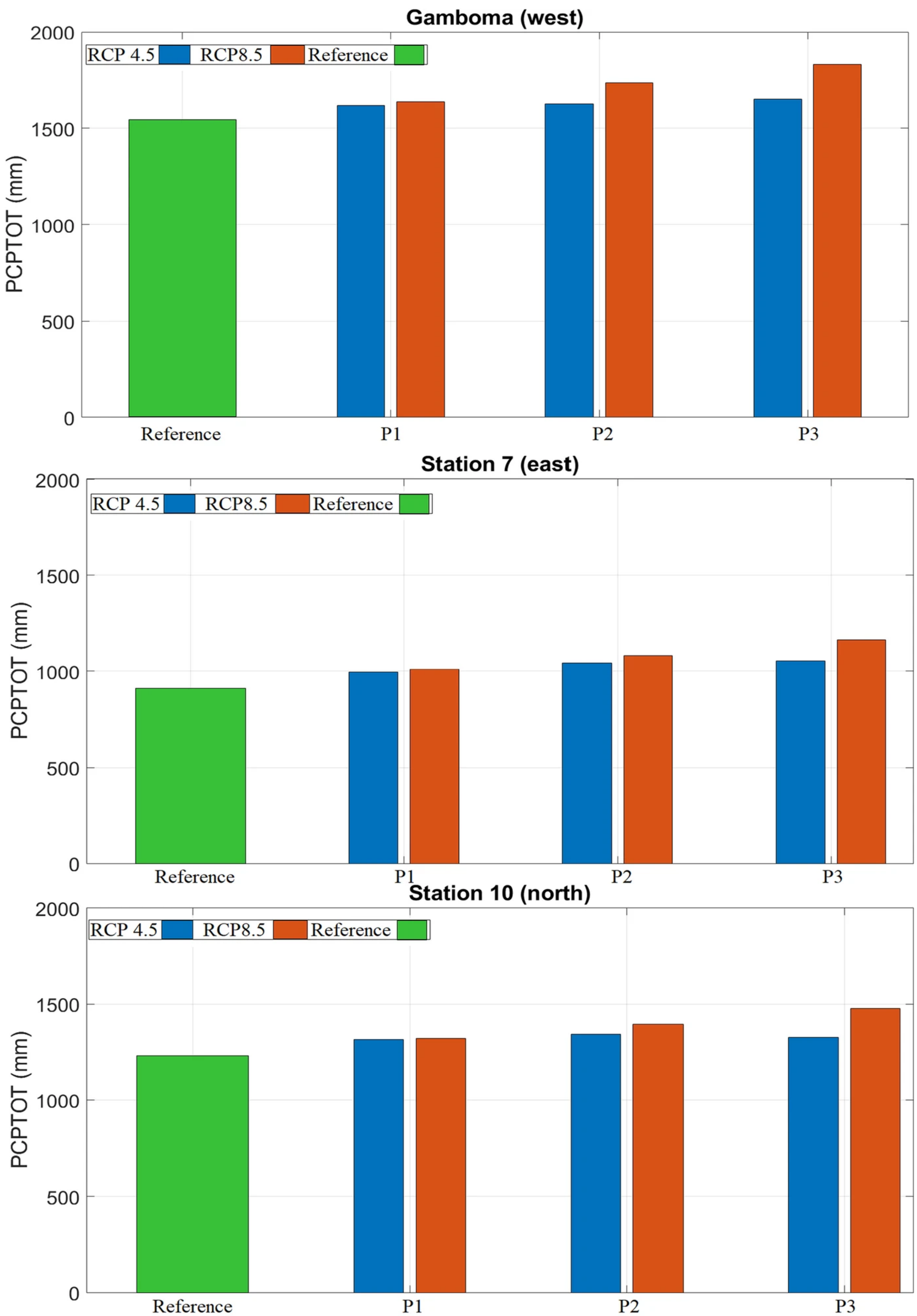
Gamboma (west)
RCP 4.5
RCP8.5
Reference
PCPTOT (mm)
2000
1500
1000
500
0
Reference
P1
P2
P3
Station 7 (east)
RCP 4.5
RCP8.5
Reference
PCPTOT (mm)
2000
1500
1000
500
0
Reference
P1
P2
P3
Station 10 (north)
RCP 4.5
RCP8.5
Reference
PCPTOT (mm)
2000
1500
1000
500
0
Reference
P1
P2
P3

(a)

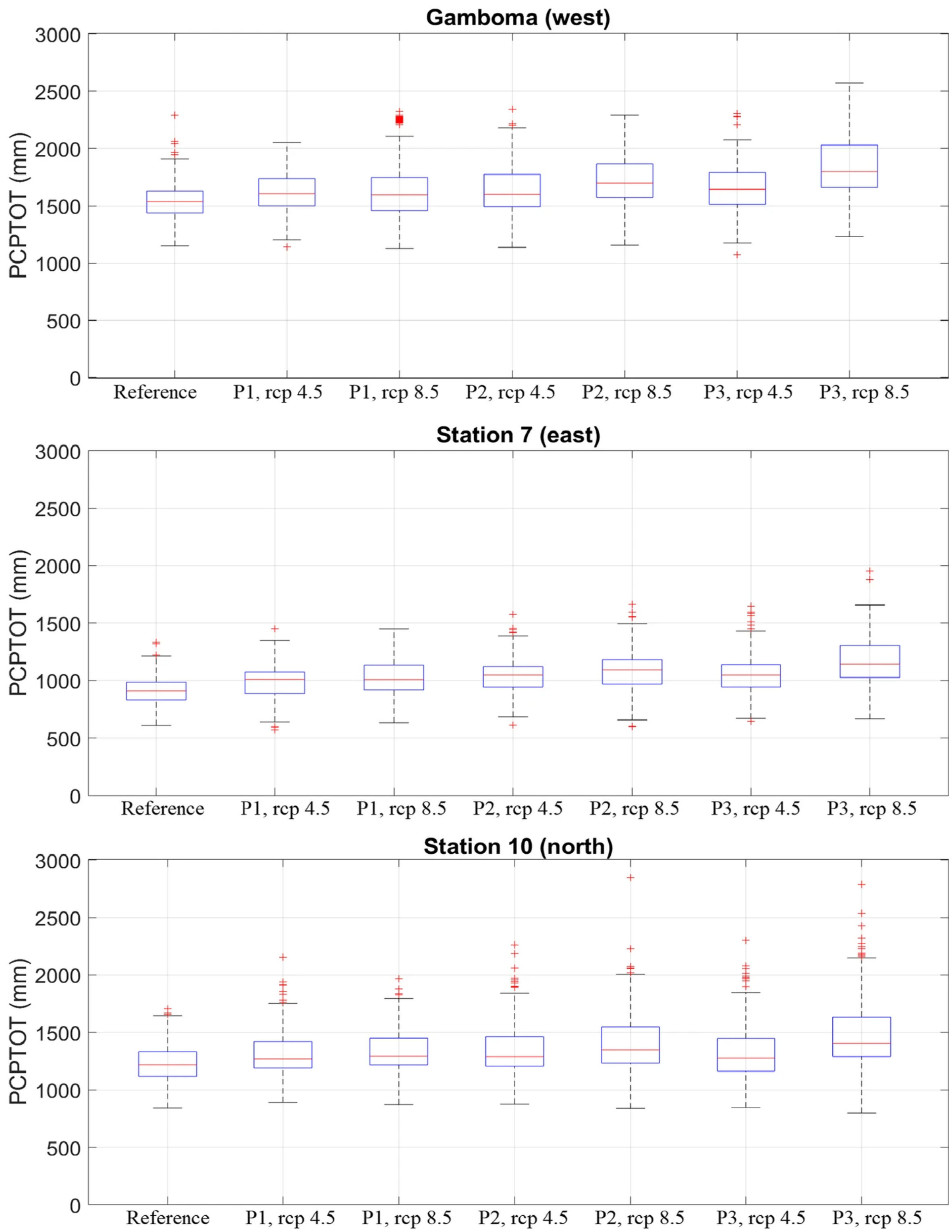
Gamboma (west)
PCPTOT (mm)
3000
2500
2000
1500
1000
500
0
Reference
P1, rcp 4.5
P1, rcp 8.5
P2, rcp 4.5
P2, rcp 8.5
P3, rcp 4.5
P3, rcp 8.5
Station 7 (east)
PCPTOT (mm)
3000
2500
2000
1500
1000
500
0
Reference
P1, rcp 4.5
P1, rcp 8.5
P2, rcp 4.5
P2, rcp 8.5
P3, rcp 4.5
P3, rcp 8.5
Station 10 (north)
PCPTOT (mm)
3000
2500
2000
1500
1000
500
0
Reference
P1, rcp 4.5
P1, rcp 8.5
P2, rcp 4.5
P2, rcp 8.5
P3, rcp 4.5
P3, rcp 8.5

(b)

Figure 4.5 (a) Average values and (b) boxplots of PCPTOT under RCP 4.5 and RCP 8.5 scenarios for the reference period (Reference: 1976–2005) and three future periods (P1: 2011–2040), (P2: 2041–2070), (P3: 2071– 2100) for selected locations in the Congo basin: station 7 (east), station 10 (north), and Gamboma (west).

4.3.4 Projections for PCP20

Figure 4.6(a) shows the spatial distribution of the multimodel average PCP20, while Figure 4.6(b) shows the percent change of PCP20 under RCP 4.5 and RCP 8.5 scenarios for the three future study periods. The magnitude of PCP20 in these figures should be considered cautiously since the authors have found that at one particular station (Kinshasa-Mbinza), and PCP20 is underestimated when temporally disaggregated time series are used (see appendix 3).

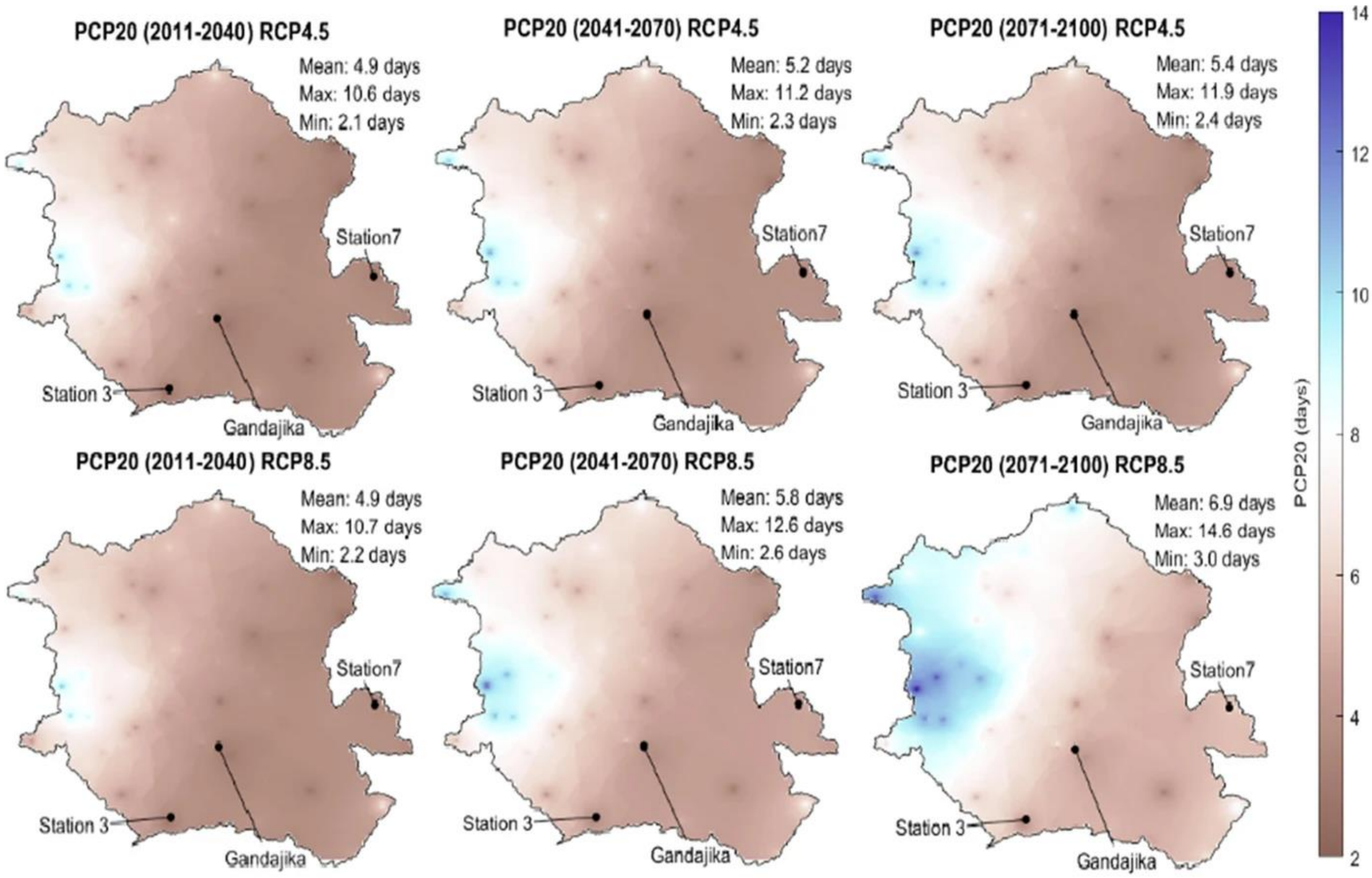
PCP20 (2011-2040) RCP4.5
Mean: 4.9 days
Max: 10.6 days
Min: 2.1 days
PCP20 (2041-2070) RCP4.5
Mean: 5.2 days
Max: 11.2 days
Min: 2.3 days
PCP20 (2071-2100) RCP4.5
Mean: 5.4 days
Max: 11.9 days
Min: 2.4 days
PCP20 (2011-2040) RCP8.5
Mean: 4.9 days
Max: 10.7 days
Min: 2.2 days
PCP20 (2041-2070) RCP8.5
Mean: 5.8 days
Max: 12.6 days
Min: 2.6 days
PCP20 (2071-2100) RCP8.5
Mean: 6.9 days
Max: 14.6 days
Min: 3.0 days
Station7
Station 3
Gandajika
PCP20 (days)
14
12
10
8
6
4
2

(a)

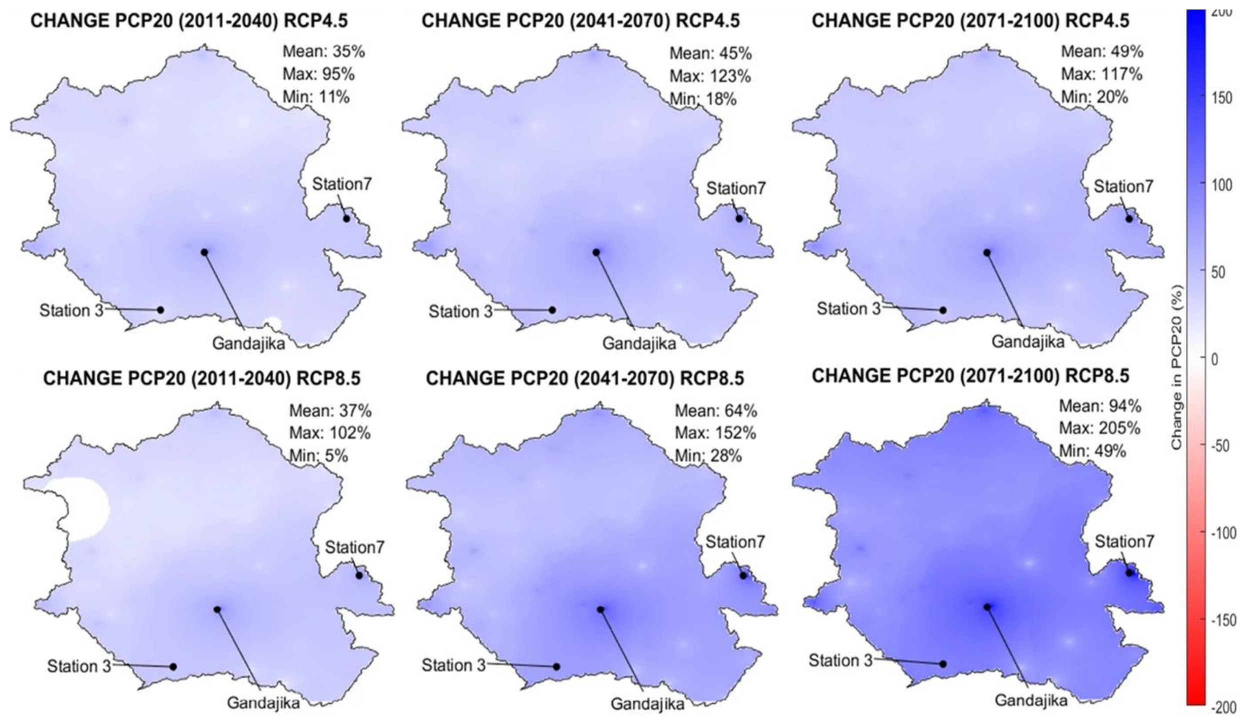

(b)

Figure 4.6 Spatial variation of (a) average PCP20 and (b) average change of PCP20 for three future periods ((2011–2040), (2041–2070), and (2071–2100)) under RCP 4.5 and RCP 8.5

Under RCP 4.5, there is a substantial increase in the average PCP20: 35% in period 1, 45% in period 2, and 49% in period 3. Compared to all other stations used in the study, the increase of PCP20 is particularly important at three locations: the city of Gandajika, station 3, and station 7 (Figure 4.6). In period 3, this increase intensifies and spreads out slightly in the noted areas. Under RCP 8.5, there is a drastic increase in the areal average PCP20 (37% in period 1, 64% in period 2 and 94% in period 3). For period 3, most of the basin experiences intense rainfall events, as PCP20 increases by 49–205%. This rise in the frequency of high-intensity rainfall events could likely lead to increased flooding, which could have various impacts on the watershed's hydrological regime.

This includes negative impacts on socioeconomics, agriculture, biodiversity, hydropower, and the environment.

Stations in the watershed that have the highest increase in PCP20 and show potential for future floods or environmental perturbations include station 7 (east), station 3 (south), and the town of Gandajika (central region). The boxplots and charts in Figure 4.7 show changes in PCP20 for both RCP scenarios at the locations of interest. Out of the three stations, station 7 will likely undergo the most severe increase in heavy rainfall events in the entire basin, with an increase of approximately 2.5–4.5 days of intense rain per year, according to RCP scenarios 4.5 and 8.5, respectively. These changes should however be interpreted with care as PCP20 in the disaggregated time series is underestimated according to the assessment in Appendix 3.

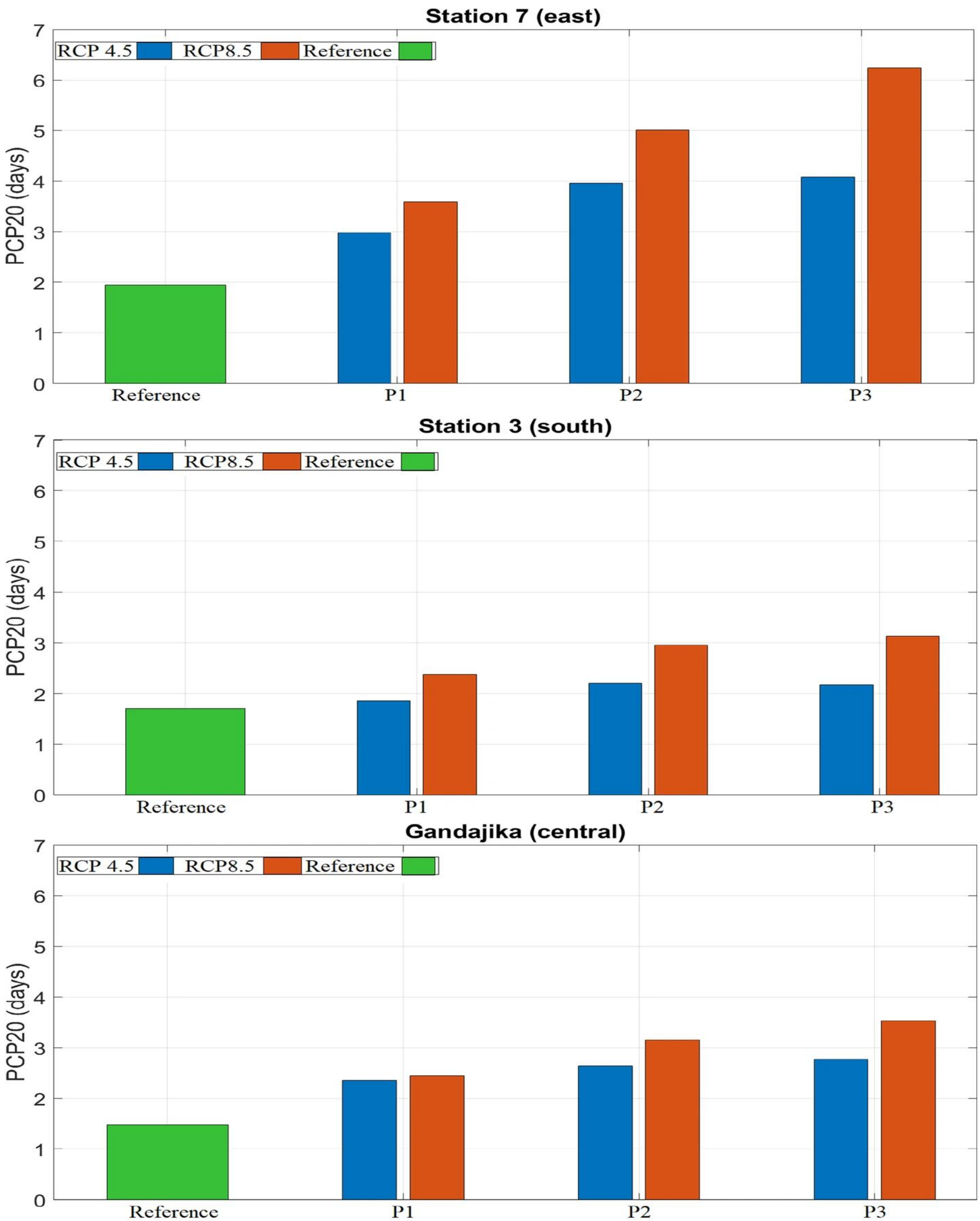

Station 7 (east)
RCP 4.5
RCP8.5
Reference
PCP20 (days)
Reference
P1
P2
P3
Station 3 (south)
Gandajika (central)
0
1
2
3
4
5
6
7

(a)

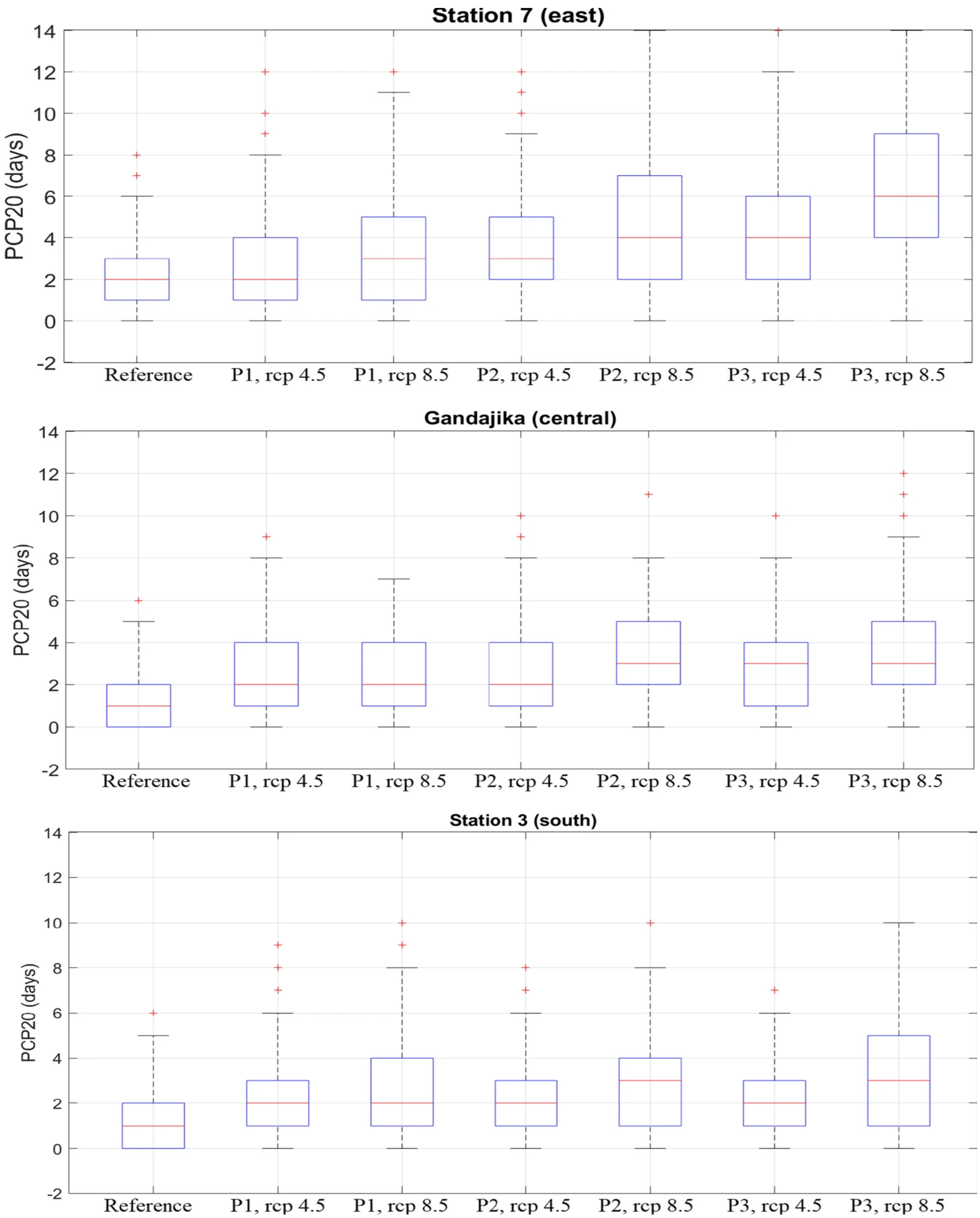
Station 7 (east)
PCP20 (days)
14
12
10
8
6
4
2
0
-2
Reference
P1, rcp 4.5
P1, rcp 8.5
P2, rcp 4.5
P2, rcp 8.5
P3, rcp 4.5
P3, rcp 8.5
Gandajika (central)
PCP20 (days)
14
12
10
8
6
4
2
0
-2
Reference
P1, rcp 4.5
P1, rcp 8.5
P2, rcp 4.5
P2, rcp 8.5
P3, rcp 4.5
P3, rcp 8.5
Station 3 (south)
PCP20 (days)
14
12
10
8
6
4
2
0
-2
Reference
P1, rcp 4.5
P1, rcp 8.5
P2, rcp 4.5
P2, rcp 8.5
P3, rcp 4.5
P3, rcp 8.5

(b)

Fig. 4.7 (a) Average values and (b) boxplots of PCP20 under RCP 4.5 and RCP 8.5 scenarios for the reference period (1976–2005) and three future periods ((2011–2040), (2041–2070), (2071–2100)) for selected locations in the Congo basin: station 7 (east), Gandajika (central region), and station 3 (south).

4.3.5 Projections for SPI

The spatial distribution of the multimodel average SPI for the three future periods and the two emission scenarios is presented in Figure 4.8. As expected, it closely follows that of annual precipitation. There is a progressive increase of SPI in the north, east, and western extremities of the Basin and a decrease of SPI in the center of the Basin for both scenarios. The most extreme changes occur under RCP 8.5 in period 3. These results suggest that the center of the Basin will become dryer, while the north, east, and western extremities of the Basin will become wetter in the future.

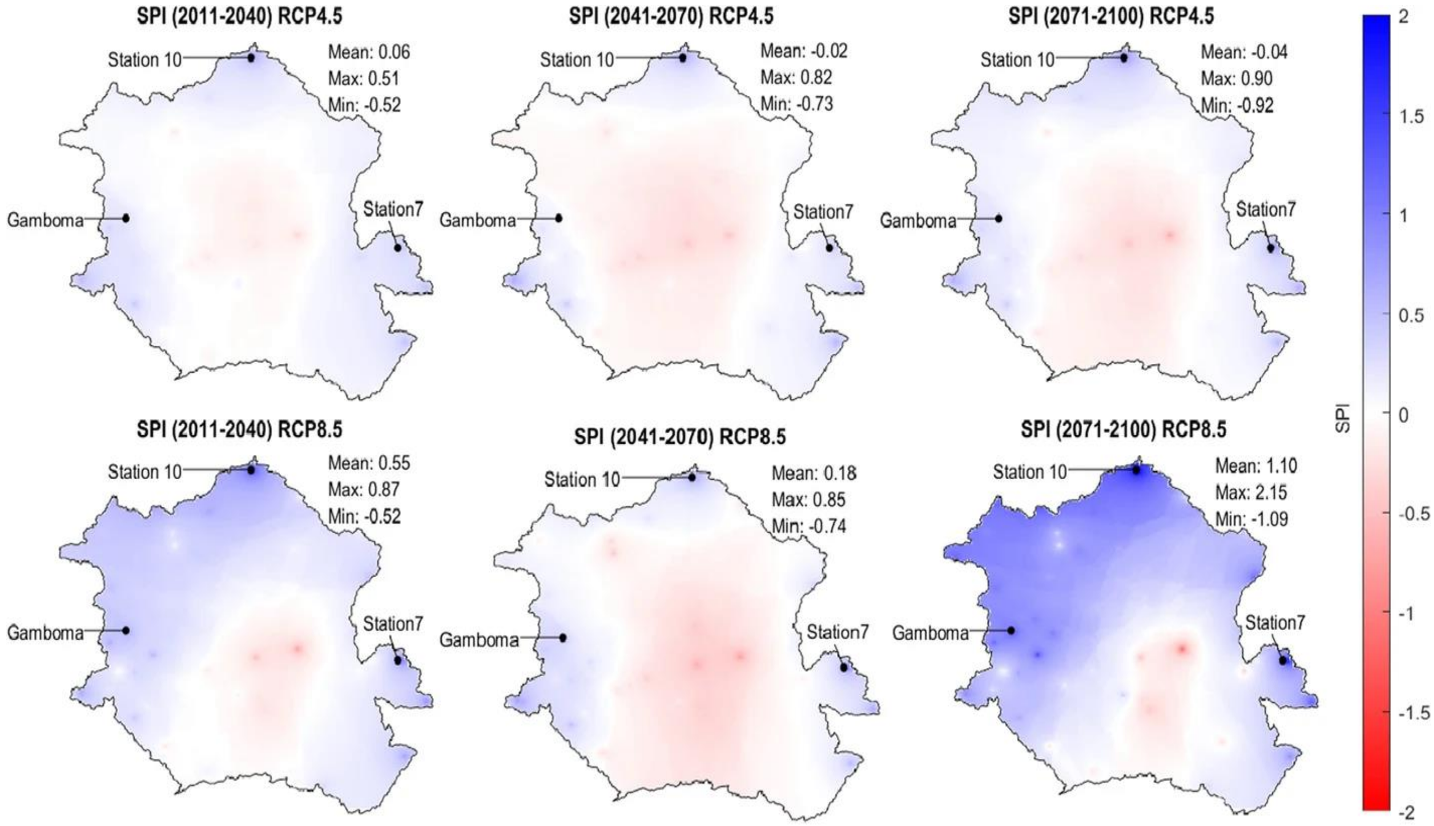

Figure 4.8 Spatial variation of multimodel average SPI for three future periods ((2011–2040), (2041 2070), (2071–2100)) under RCP 4.5 and RCP 8.5

Under RCP 4.5, the spatial average of SPI goes from 0.06 in the period 1 to − 0.02 in period 2 and − 0.04 in period 3. Under RCP 8.5, it decreases from 0.55 in period 1 to 0.18 in period 2 and increases again to 1.1 in period 3. This is consistent with the findings that total precipitation changes are expected to be marginal.

4.3.6 Projections for SPEI

The SPEI index accounts for precipitation and potential evapotranspiration (PET) and is used mostly to determine drought and dry conditions. Figure 4.9 shows changes in the average multimodel SPEI which are depicted on spatial distribution maps of the Congo basin for the three future periods under the two RCP scenarios.

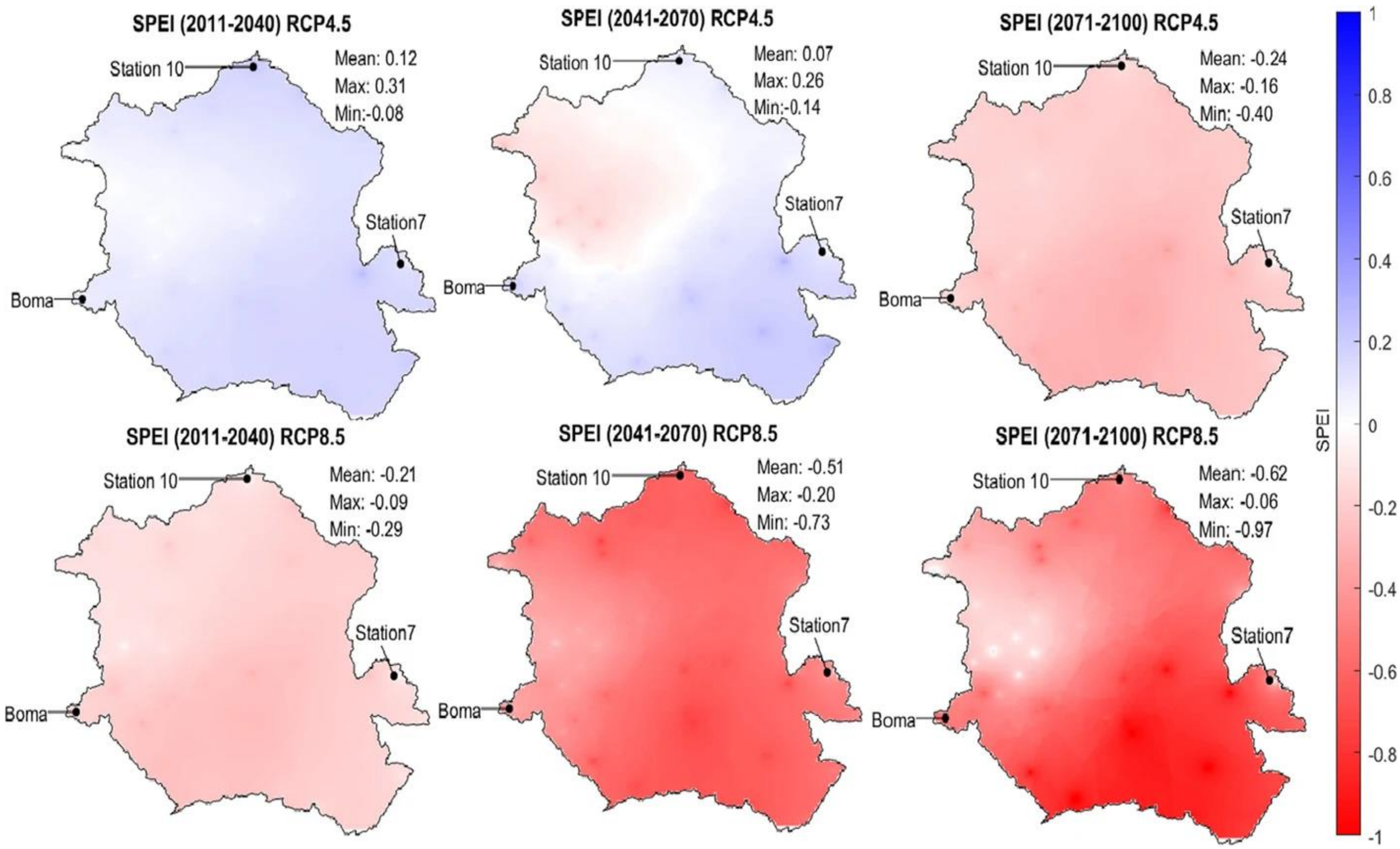

Figure 4.9 Spatial variation of multimodel average SPEI for three future periods ((2011–2040), (2041–2070), and (2071–2100)) under RCP 4.5 and RCP 8.5

Under RCP 4.5, the spatial average of SPEI decreases from 0.12 in period 1 to 0.07 in period 2 and − 0.24 in period 3, on average. Under RCP 8.5, the spatial average decreases from − 0.21 in period 1 to − 0.51 in period 2 and − 0.62 in period 3. Values of SPI range from − 1.09 to 2.15, while SPEI values range from − 0.06 to − 0.97, respectively, for period 3, under RCP 8.5. This difference is due to the consideration of evapotranspiration. The fundamental difference between these two indicators is that SPI is calculated based on precipitation, while SPEI is based on the difference between precipitation and potential evapotranspiration. Although precipitation was shown to increase over most of the basin, SPEI systematically decreases independent of the emission scenario. That means that the increase in evapotranspiration (due to a rise in temperature caused by climate change) will offset the increase in precipitation in areas where rainfall amounts are expected to increase. It will exacerbate the severity of droughts in areas where precipitation is expected to decrease. As expected, the decrease in SPEI is less severe under RCP 4.5 than under RCP 8.5. Finally, locations that are most impacted by extreme changes/evaporation increases include station 10 (north) and various stations in the southeast regions of the basin.

The next part of the results focuses on areas that experience the most significant changes in SPEI. These areas include station 10 (north), represented in Figure 4.10. This figure shows the relative frequency of SPEI classes for the reference period and the three future periods under (a) RCP 4.5 and (b) RCP 8.5.

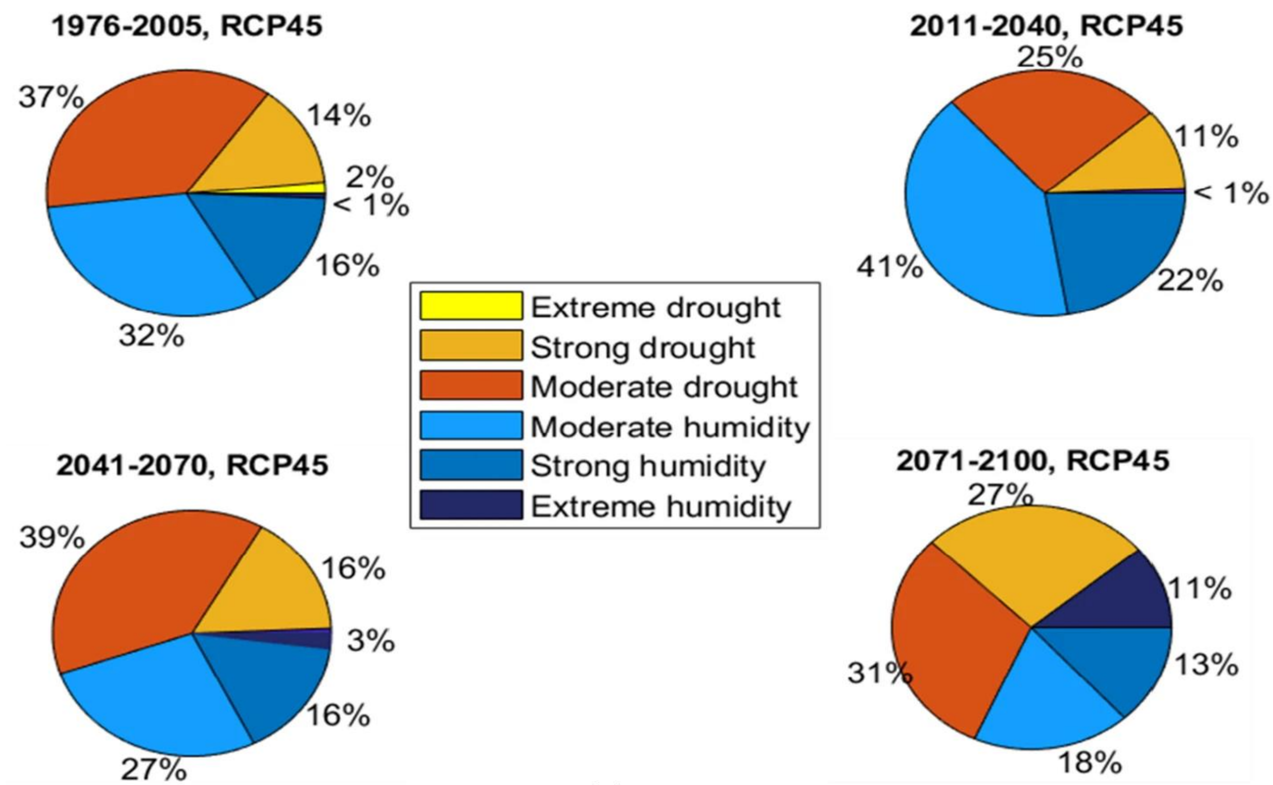

1976-2005, RCP45
37%
14%
2%
< 1%
16%
32%
2011-2040, RCP45
25%
11%
< 1%
41%
22%
Extreme drought
Strong drought
Moderate drought
Moderate humidity
Strong humidity
Extreme humidity
2041-2070, RCP45
39%
16%
3%
16%
27%
2071-2100, RCP45
27%
11%
31%
13%
18%

(a)

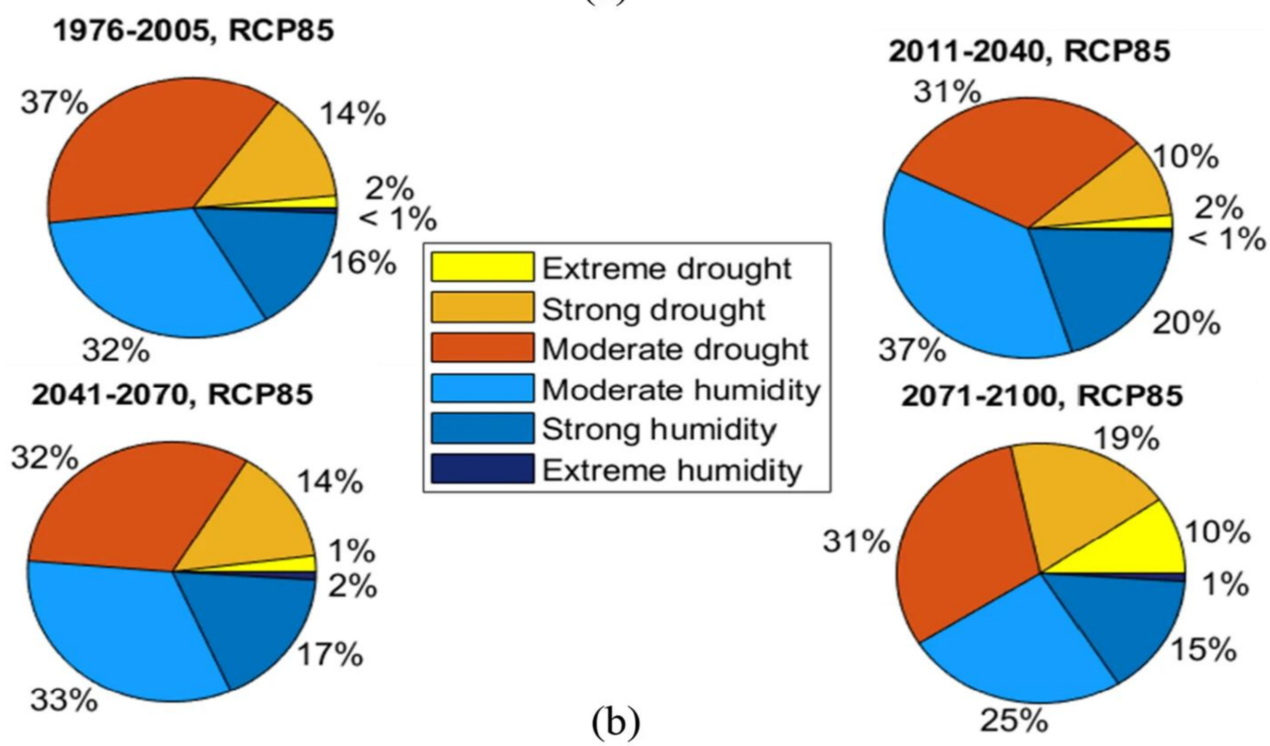

1976-2005, RCP85
37%
14%
2%
< 1%
16%
32%
2011-2040, RCP85
31%
10%
2%
< 1%
20%
37%
Extreme drought
Strong drought
Moderate drought
Moderate humidity
Strong humidity
Extreme humidity
2041-2070, RCP85
32%
14%
1%
2%
17%
33%
2071-2100, RCP85
19%
31%
10%
1%
15%
25%

(b)

Figure 4.10 Multimodel average SPEI pie chart at Station 10 under RCP 4.5 (a) and RCP 8.5 (b) for the reference period and three future periods ((2011–2040), (2041–2070), and (2071–2100))

For station 10, humidity decreases throughout all the periods, whereas drought frequency increases significantly. The frequency of extreme drought at station 10 increases from 2 to 10% under RCP 8.5. Simultaneously, the frequency of extreme humidity increases from less than 1% to 11% under RCP 4.5.

4.3.7 Discussion

The climate regime in the Congo River basin directly affects the livelihood of 75 million people living in the watershed and the health of one of the planet's largest rainforests and carbon sink with direct links to the global climate. However, the basin is understudied, partly because of the lack of observational data (Creese et al. 2019). While annual and seasonal precipitation and evaporation have received some attention in the literature, the authors are not aware of any projection of extreme daily precipitation, probably because reliable daily precipitation records are rare. While most studies suggest a stagnation or an increase in total rainfall in the future, little information is available about whether that increase would offset the increase in evaporation resulting from higher air temperatures. The lack of reliable daily precipitation records was tackled in our study by disaggregating monthly observed precipitation time series using the fragment method.

Multiple studies (Wong et al. 2017; Beck et al. 2017; Berg et al. 2018) have successfully used WFDEI, which performs well when used to drive hydrological models. However, in a study over West Africa, Satgé et al. (2020) found that reanalysis data sets such as WFDEI present the lower statistical scores at the daily time step compared to satellite-based precipitation datasets but their performance increases at the monthly time step. The impact of the temporal disaggregation on the magnitude and trends of PCP20, PCPTOT, SPI, and SPEI was examined at the Kinshasa-Mbinza station, where daily precipitation was available. For that particular climate station, the temporal disaggregation led to an underestimation of PCP20, but did not affect the trend of PCP20 in the future. Unfortunately, the conclusion cannot be generalized to other locations in the Congo basin. Therefore, the values of PCP20 presented this paper and in Figs. 6 and 7 are most likely underestimated and hence should be interpreted with caution.

Despite the limitations in the datasets used, the results in this paper strongly suggest that there will be a moderate increase in total precipitation in most of the basin (especially in the northern half of the basin from the mid-century under RCP 8.5). The change in total precipitation in the central and southern parts of the basin was not found to be significant, except for a small area in the South-east where a small decrease (up to -6%) is expected under RCP4.5 in period 3. These findings are consistent with those of Tshimanga and Hughes (2014), Haensler et al. (2013), and Mba et al. (2018), who found that annual total precipitation amounts over the Congo basin are not likely to change severely in the future. Creese et al. (2019) found a moderate trend towards wetting over the Congo basin in the CMIP5 models. The results of this study also suggest that an increase in the number of days with high-intensity rainfall (PCP20) is expected over the entire watershed, suggesting a possible increase in flash flood events. According to our PCP20 projections, all locations of the Congo basin will undergo a higher frequency of heavy rainfall. This means that local people will likely observe more intense and frequent periods of flooding in the foreseeable future where preparedness for such events through systematic policy implementation for -disaster risk reduction is essential. At the same time, as our projections for SPEI show, the frequency of droughts will increase even at locations where total precipitation is expected to increase in the future. This means that increased evaporation resulting from higher temperatures will offset the rise in total precipitation at these locations. The result will be an exacerbation of extreme lows and extreme highs, leading to impacts on both ends of the spectrum. The fact that flash floods and drought are expected to occur in the same areas is not a contradiction as the two events have different time scales (a few hours to a few days for floods, a season to several years for a drought). Therefore, economic losses may increase unless concrete preventative measures are put into place to minimize flooding risks. Finally, the evolution of SPEI over time shows that increased evaporation resulting from rising temperatures will outweigh the overall increase in PCP. As a result, local people in the basin will face an increase in the annual drought frequency, and consequently, this could lead to a possible collapse in food security in the region.

The projected increase in drought frequency may have impacts beyond the limits of the basin by modifying the spatial distribution of forested areas, the biomass production in these areas, and hence their carbon sequestration capabilities. Hubau et al. (2020) listed droughts as a potential reason for an observed carbon sink saturation that started after 2010 in African tropical forests. The loss of tropical forest carbon sequestration policy would have far-reaching consequences on the global climate and climate change adaptation/mitigation policies. It is therefore of crucial importance to further look into the biophysical impact of the projected change of climate regime on a range of sectors: forest distribution and ecosystem services, including carbon sequestration; hydrological regimes; agriculture and cattle grazing, etc.

4.4 Conclusions

Four climate indices (total annual precipitation, PCPTOT; number of days where PCP is above 20 mm, PCP20; the Standardized Precipitation Index, SPI; and the Standardized Precipitation-Evaporation Index, SPEI) were selected and estimated using the downscaled outputs from eleven regional climate models under representative concentration pathways RCP 4.5 (moderate greenhouse gas emissions scenario) and RCP 8.5 (high greenhouse gas emissions scenario). Relative changes in these indices were analyzed in three future periods (2011–2040, 2041–2070, and 2071–2100) and compared to the historical reference period (1976–2005). It was found that (a) under RCP 8.5, there is an expected increase in total PCP and SPI, in the north-western and northern region of the basin in periods 2 and 3, respectively; (b) the maximum increase in PCPTOT (+ 24%) and the minimum value of SPEI (− 0.97) were both projected under RCP 8.5 in the period from 2071 to 2100; and (c) PCP20 will increase independently of the period and scenario, in the entire watershed. Under RCP 8.5 in the 2071–2100 period, PCP20 will increase by 94% on average over the whole watershed. An increase in the number of days with high-intensity rainfall is expected over the entire watershed, suggesting a possible increase in flood events. Finally, the SPEI index points to an increase in drought throughout most of the basin, as the increase in evaporation resulting from rising temperatures will outweigh the overall rise in PCP. This study portrays a basin that will undergo an intensification in drought and flood frequency in the future. It can also be used to guide the development of adaptation approaches towards enhancing flood and disaster management, vulnerability mapping, flood monitoring systems, early warning systems, development of infrastructure, and other socioeconomical aspects.

4.5 References

Angelina A, Gado Djibo A, Seidou O, Seidou Sanda I, Sittichok K (2015) Changes to flow regime on the Niger River at Koulikoro under a changing climate. Hydrol Sci J 60(10):1709–1723. https:// doi. org/ 10. 1080/ 02626 667. 2014. 916407

Beck HE, Vergopolan N, Pan M, Levizzani V, van Dijk AIJM, Weedon GP, Brocca L, Pappenberger F, Huffman GJ, Wood EF (2017) Global-scale evaluation of 22 precipitation datasets using gauge observations and hydrological modeling. Hydrol Earth Syst Sci 21:6201–6217. https:// doi. org/ 10. 5194/ hess- 21- 6201- 2017

Berg P, Donnelly C, Gustafsson D (2018) Near-real-time adjusted reanalysis forcing data for hydrology. Hydrol Earth Syst Sci 22:989–1000. https:// doi. org/ 10. 5194/ hess- 22- 989- 2018

Bodian A (2014) Caractérisation de la variabilité temporelle récente des précipitations annuelles au Sénégal (Afrique de l'Ouest). Physio-Géo 8:297–312. https:// doi. org/ 10. 4000/ physi ogeo. 4243

Creese A, Washington R, Jones R (2019) Climate change in the Congo Basin: processes related to wetting in the December–February dry season. Clim Dyn 53(5–6):3583–3602. https:// doi. org/ 10. 1007/ s00382- 019- 04728-x

EM-DAT, CRED, EM-DAT, The Emergency Events Database, Univ. Cathol. Louvain - CRED, Brussels, Belgium, 2020. www. emdat. be. Accessed 04 08, 2021

Giorgi F, Gutowski WJ (2015) Regional Dynamical Downscaling and the CORDEX Initiative. Annu Rev Environ Resour 40:467–490. https:// doi. org/ 10. 1146/ annur ev- envir on- 102014-021217

Guttman NB (1998) Comparing the palmer drought index and the standardized precipitation index. J Am Water Resour Assoc 34(1):113–121. https:// doi. org/ 10. 1111/j. 1752- 1688. 1998. tb059 64.x

Haensler A, Saeed F, Jacob D (2013) Assessing the robustness of projected precipitation changes over central Africa on the basis of a multitude of global and regional climate projections. Clim Change 121:349–363. https:// doi. org/ 10. 1007/ s10584- 013- 0863-8

Hakala K, Addor N, Seibert J (2018) Hydrological Modeling to Evaluate Climate Model Simulations and Their Bias Correction. J Hydrometeorol 19(8):1321–1337. https:// doi. org/ 10. 1175/ jhm-d- 17- 0189.1

Harms AA, Campbell TH (1967) An extension to the Thomas-Fiering Model for the sequential generation of streamflow. Water Resour Res 3(3):653–661. https:// doi. org/ 10. 1029/ wr003 i003p 00653

Hubau W, Lewis SL, Phillips OL, Affum-Baffoe K, Beeckman H, Cuní-Sanchez A, Daniels AK et al (2020) “Asynchronous Carbon Sink Saturation in African and Amazonian Tropical Forests.” Nature 579, no. 7797 (March 5, 2020): 80–87. https:// doi. org/ 10. 1038/ s41586- 020- 2035-0.

Jenkins GS, Adamou G, Fongang S (2002) The Challenges of Modeling Climate Variability and Change in West Africa. Clim Change 52(3):263–286. https:// doi. org/ 10. 1023/a: 10137 41803 144

Lebel T, Ali A (2009) Recent trends in the Central and Western Sahel rainfall regime (1990–2007). J Hydrol 375(1–2):52–64. https:// doi. org/ 10. 1016/j. jhydr ol. 2008. 11. 030

Lewis SL, Lopez-Gonzalez G, Sonké B et al (2009) Increasing carbon storage in intact African tropical forests. Nature 457:1003–1006

Li X, Meshgi A, Wang X, Zhang J, Tay SHX, Pijcke G, Manocha N, Ong M, Nguyen MT, Babovic V (2018) Three resampling approaches based on method of fragments for daily-to-subdaily precipitation disaggregation. Int J Climatol 38:e1119–e1138. https:// doi. org/ 10. 1002/ joc. 5438

Malhi Y, Adu-bredu S et al (2013) African rainforests: past, present and future. Philos Trans R Soc Lond B Biol Sci. https:// doi. org/ 10. 1098/ rstb. 2012. 0312

Malhi Y, Wright J (2004) Spatial patterns and recent trends in the climate of tropical rainforest regions. Philos Trans R Soc B Biol Sci 359:311–329. https:// doi. org/ 10. 1098/ rstb. 2003. 1433

Mao Y, Zhou T, Leung LR, Tesfa TK, Li H, Wang K, Tan Z, Getirana A (2019) Flood Inundation Generation Mechanisms and Their Changes in 1953–2004 in Global Major River Basins. J Geophys

Res Atmos 124(22):11672–11692. https:// doi. org/ 10. 1029/ 2019j d0313 81

Mba WP, Longandjo G-NT, Moufouma-Okia W, Bell J-P, James R, Vondou DA, Haensler A, FotsoNguemo TC, Guenang GM, Tchotchou ALD, Kamsu-Tamo PH, Takong RR, Nikulin G, Lennard CJ, Dosio A (2018) Consequences of 1.5 °C and 2 °C global warming levels for temperature and precipitation changes over Central Africa. Environ Res Lett 13, 055011. https:// doi. org/ 10. 1088/ 1748- 9326/ aab048

McKee TB, Doesken NJ, Kleist J (1993) The relationship of drought frequency and duration to time scales. Eighth Conference on Applied Climatology, Department of Atmospheric Science Colorado State University, 17–22.

Ndehedehe CE, Anyah RO, Alsdorf D, Agutu NO, Ferreira VG (2019) Modelling the impacts of global multi-scale climatic drivers on hydro-climatic extremes (1901–2014) over the Congo basin. Sci Total Environ 651:1569–1587. https:// doi. org/ 10. 1016/j. scito tenv. 2018. 09. 203

Neitsch SL, Arnold JG, Kiniry JR, Williams JR (2011) Soil and Water Assessment Tool Theoretical Documentation Version 2009. Texas Water Resources Institute. Available electronically from http:// hdl. handle. net/ 1969.1/ 128050. Accessed 04 08, 2021

Nkiaka E, Nawaz N, Lovett J (2017) Evaluating Global Reanalysis Datasets as Input for Hydrological Modelling in the Sudano-Sahel Region. Hydrology 4:13. https:// doi. org/ 10. 3390/ hydro logy4 010013

Onyutha C (2020) Analyses of rainfall extremes in East Africa based on observations from rain gauges and climate change simulations by CORDEX RCMs. Clim Dyn 54(11–12):4841–4864. https:// doi. org/ 10. 1007/ s00382- 020- 05264-9

Satgé F, Defrance D, Sultan B, Bonnet M-P, Seyler F, Rouché N, Pierron F, Paturel J-E (2020) Evaluation of 23 gridded precipitation datasets across West Africa. J Hydrol 581:124412. https:// doi. org/ 10. 1016/j. jhydr ol. 2019. 124412

Sittichok K, Djibo AG, Seidou O, Saley HM, Karambiri H, Paturel J (2016) Statistical seasonal rainfall and streamflow forecasting for the Sirba watershed, West Africa, using sea-surface temperatures. Hydrol Sci J, 1–11. https:// doi. org/ 10. 1080/ 02626 667. 2014. 944526

Snedecor, George W. and Cochran, William G. (1989), Statistical Methods, Eighth Edition, Iowa State University Press. Tshimanga, R. M., & Hughes, D. A. (2012). Climate change and impacts on the hydrology of the Congo Basin: The case of the northern sub-basins of the Oubangui and Sangha Rivers. Physics and Chemistry of the Earth, Parts A/B/C, 50–52, 72–83. https:// doi. org/ 10. 1016/j. pce. 2012. 08. 002

Tshimanga RM, Hughes DA (2014) Basin-scale performance of a semidistributed rainfall-runoff model for hydrological predictions and water resources assessment of large rivers: The Congo River, Water Resour. Res., 50 https:// doi. org/ 10. 1002/ 2013W R0143 10

Tshimanga RM, Bola G, Kabuya P, Nkaba L, Neal J, Hawker L, Trigg AM, Bates P, Hughes AD, Hughes Laraque A, Woods R, Wagener T (2020) Towards a framework of catchment classification for hydrologic predictions and water resources management in the ungauged Basin of the Congo River: An a priori approach. Accepted: American Geophysical Union – AGU Willey.

Vicente-Serrano SM, Beguería S, López-Moreno JI (2010) A Multiscalar Drought Index Sensitive to Global Warming: The Standardized Precipitation Evapotranspiration Index. J Clim 23(7):1696–1718. https:// doi. org/ 10. 1175/ 2009j cli29 09.1

Weedon, G. P., G. Balsamo, N. Bellouin, S. Gomes, M. J. Best, and P. Viterbo. 2018. The WFDEI Meteorological Forcing Data. Research Data Archive at the National Center for Atmospheric Research, Computational and Information Systems Laboratory. https:// doi. org/ 10. 5065/ 486N-8109.

Wong JS, Razavi S, Bonsal BR, Wheater HS, Asong ZE (2017) Inter-comparison of daily precipitation products for large-scale hydro-climatic applications over Canada. Hydrol Earth Syst Sci 21:2163– 2185. https:// doi. org/ 10. 5194/ hess- 21- 2163- 2017

Appendix 1: Evaporation estimation

For the evaporation estimation, the following Penman-Monteith equation derived for alfalfa was used:

$$\lambda E = \frac{\Delta \cdot (H_{net} - G) + \rho_{air} \cdot c_p \cdot [e_z^0 - e_z]/r_a}{\Delta + \gamma \cdot (1 + {}^{r_c}/_{r_a})}$$

$$r_a = \frac{114}{u_z}$$

$$r_c = \frac{49}{1.4 - 0.4\frac{CO_2}{330}}$$

where λE = latent heat flux density (MJ m^{-2}d^{-1});
E = depth rate evaporation;
Δ = slope of saturation vapor pressure-temperature curve (kPa ˚C^{-1});
H_{net} = the net radiation (MJ m^{-2}d^{-1});
G = heat flux density to the ground (M.J. m^{-2}d^{-1});
ρ_{air} = air density (kg/m^{-3})

c_p = specific heat at constant pressure (MJ kg^{-1} °C^{-1});
e_z^0 = saturation vapor pressure of air at height z (kPa);
e_z = water vapor pressure of air at height z (kPa);
Υ = psychrometric constant (kPa °C^{-1});
r_c = plant canopy resistance (s/m);
r_a = aerodynamic resistance/diffusion resistance of the air layer (s/m).
CO_2: concentration of carbon dioxide in part per millions (400)

Appendix 2: GCM/RCM model combinations

Table 4.2 – Characteristics of the GCM/RCM model combinations used in the study

No.	Driving GCM	GCM Institute	RCM	RCM Institute	Driving GCM
1	Canadian Earth System Model Version 2	Canadian Centre for Climate Modeling and Analysis	Canadian Regional Climate Model 4	Canadian Centre for Climate Modeling and Analysis	Canadian Earth System Model Version 2
2	Canadian Earth System Model Version 2	Canadian Centre for Climate Modeling and Analysis	Rossby Centre regional atmospheric model, version 4	Swedish Meteorological and Hydrological Institute	Canadian Earth System Model Version 2
3	Centre National de Recherches Météorologiques, Climate Model 5	National Centre for Meteorological Research	Rossby Centre regional atmospheric model, version 4	Swedish Meteorological and Hydrological Institute	Centre National de Recherches Météorologiques, Climate Model 5
4	Queensland Climate Change Centre of Excellence (QCCCE) and Commonwealth Scientific and Industrial Research Organization (CSIRO)	The Commonwealth Scientific and Industrial Research Organization	Rossby Centre regional atmospheric model, version 4	Swedish Meteorological and Hydrological Institute	Queensland Climate Change Centre of Excellence (QCCCE) and Commonwealth Scientific and Industrial Research Organization (CSIRO)

5	European community Earth-System Model	Irish Centre for High-End Computing	Rossby Centre regional atmospheric model, version 4	Swedish Meteorological and Hydrological Institute	European community Earth-System Model
6	Institut Pierre Laplace Climate Model version 5A	Institute Pierre Simon Laplace	Rossby Centre regional atmospheric model, version 4	Swedish Meteorological and Hydrological Institute	Institut Pierre Laplace Climate Model version 5A
7	Model for Interdisciplinary Research on Climate, version 5	Center for Climate System Research/ National Institute for Environmental Studies/ Frontier Research Center for Global Chance, Japan Agency for Marine-Earth Science and Technology	Rossby Centre regional atmospheric model, version 4	Swedish Meteorological and Hydrological Institute	Model for Interdisciplinary Research on Climate, version 5
8	Hadley Centre Global Environment Model version 2	Met Office Hadley Centre	Rossby Centre regional atmospheric model, version 4	Swedish Meteorological and Hydrological Institute	Hadley Centre Global Environment Model version 2
9	Max Plank Institute Earth System Model	Max Planck Institute for Meteorology	Rossby Centre regional atmospheric model, version 4	Swedish Meteorological and Hydrological Institute	Max Plank Institute Earth System Model
10	Norwegian Earth System Model	Norwegian Climate Centre	Rossby Centre	Swedish Meteorological	Norwegian Earth System Model

			regional atmospheric model, version 4	and Hydrological Institute	
11	Geophysical Fluid Research Laboratory Earth System Model	National Oceanic and Atmospheric Administration-Geophysical Fluid Dynamics Laboratory	Rossby Centre regional atmospheric model, version 4	Swedish Meteorological and Hydrological Institute	Geophysical Fluid Research Laboratory Earth System Model

Appendix 3. Impact of the temporal disaggregation on the magnitudes and trends of PCP20, PCPTOT, SPI and SPEI

The impacts of the temporal disaggregation were assessed on the climatic indices at the only station at which the authors were able to secure daily observed data: the Kinshasa-Mbinza station (latitude = -4.36; longitude=15.25). The precipitation time series and the average annual precipitation of the three data sets (observations, WFDEI and disaggregated), are presented on Figure 4.11 and 4.12, which shows the average monthly total precipitation for each data set, while the average number of days where precipitation is above a given threshold in the 1979-2013 period (period where data is available in all three data sets) is presented on Figure 4.13.

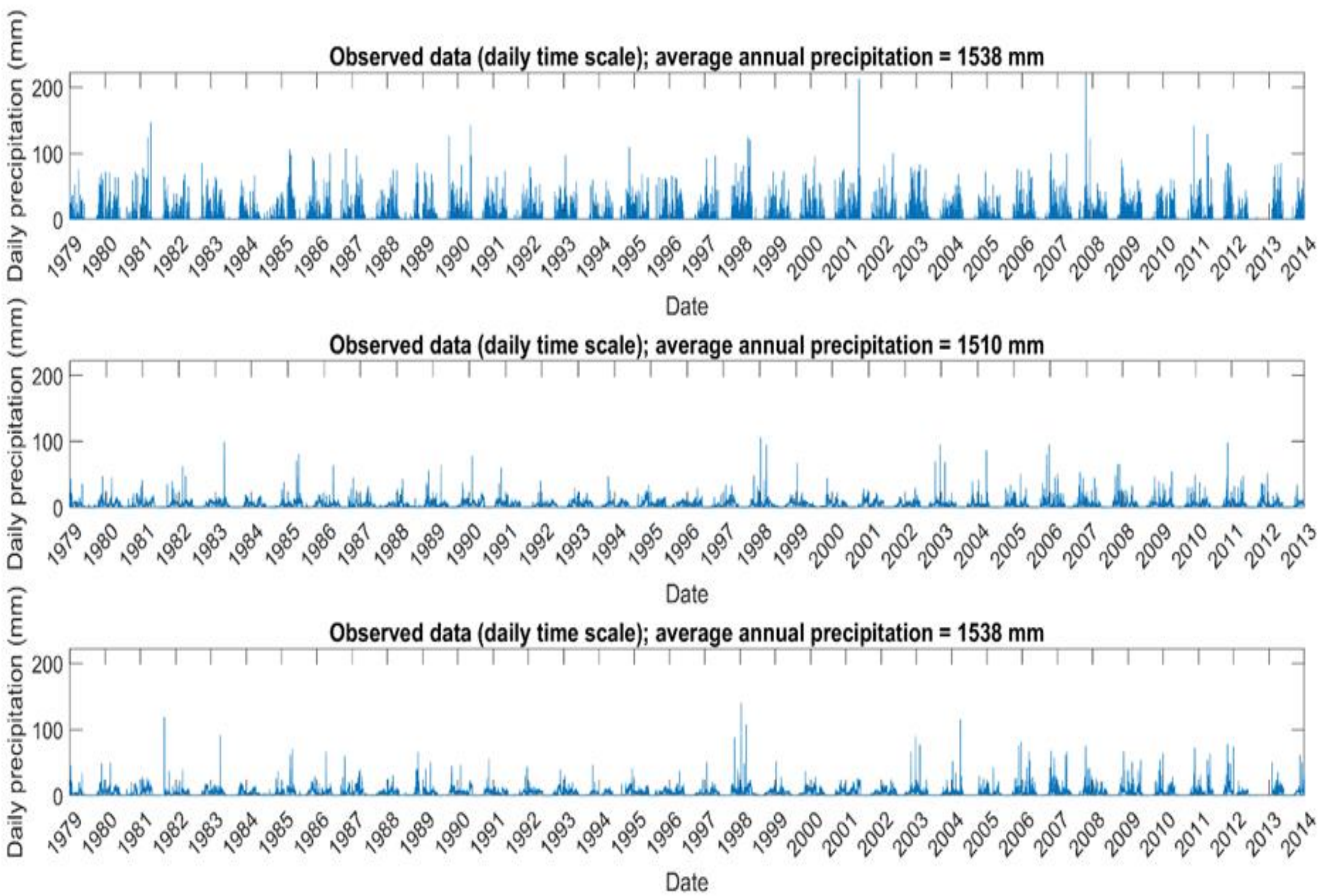

Figure 4.11 Time series of observed, WFDEI and disaggregated precipitation time series at the Kinshasa-Mbinza station.

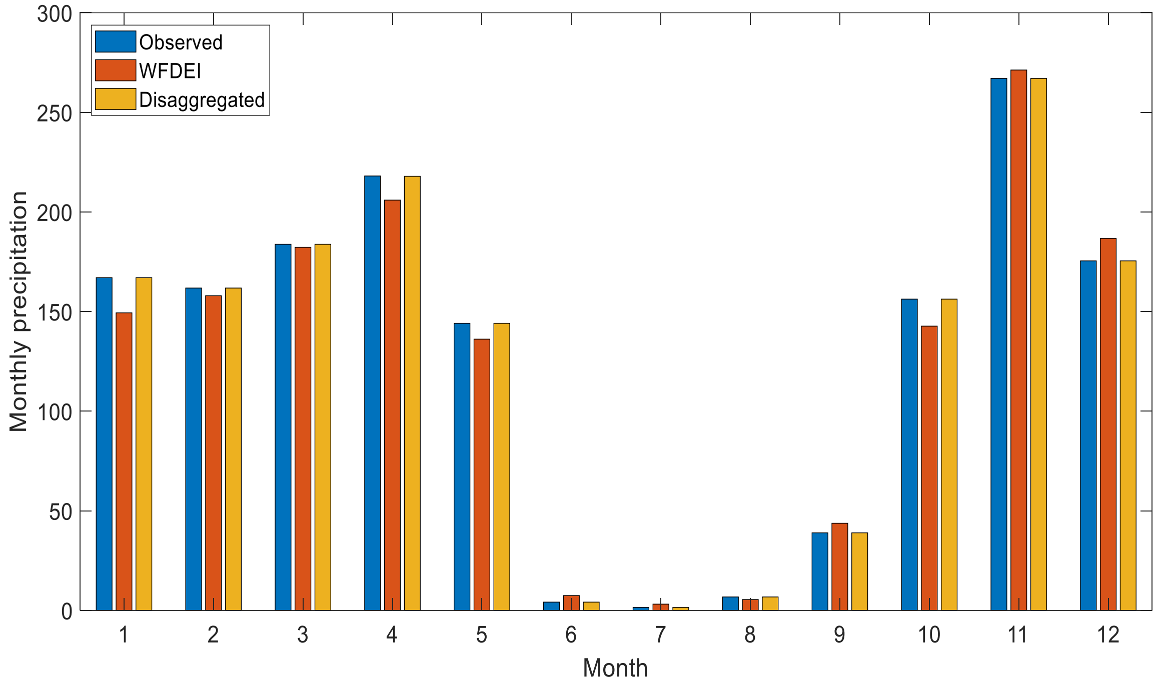

Figure 4.12 Average monthly total for the observed, WFDEI and disaggregated precipitation time series at the Kinshasa-Mbinza station

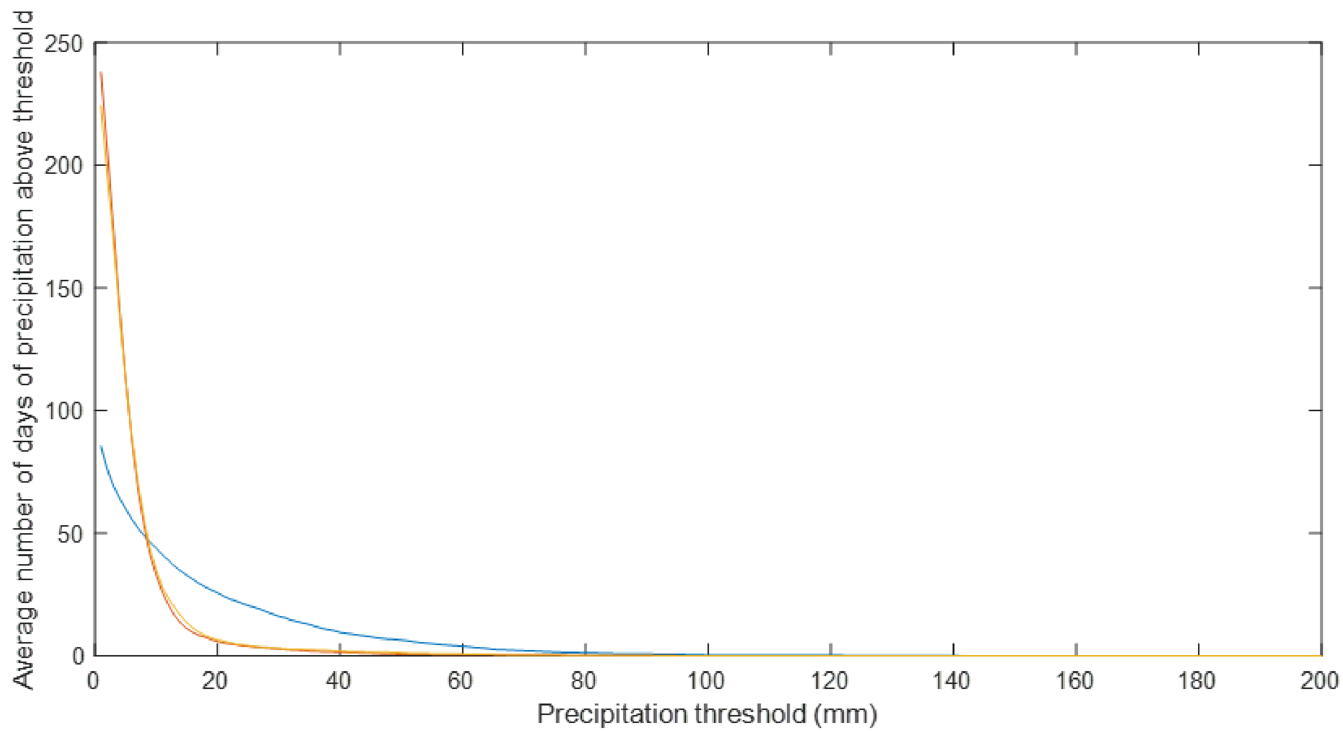

Figure 4.13 Average number of days with precipitation above a predefined threshold for the observed, WFDEI and disaggregated precipitation time series at the Kinshasa-Mbinza station

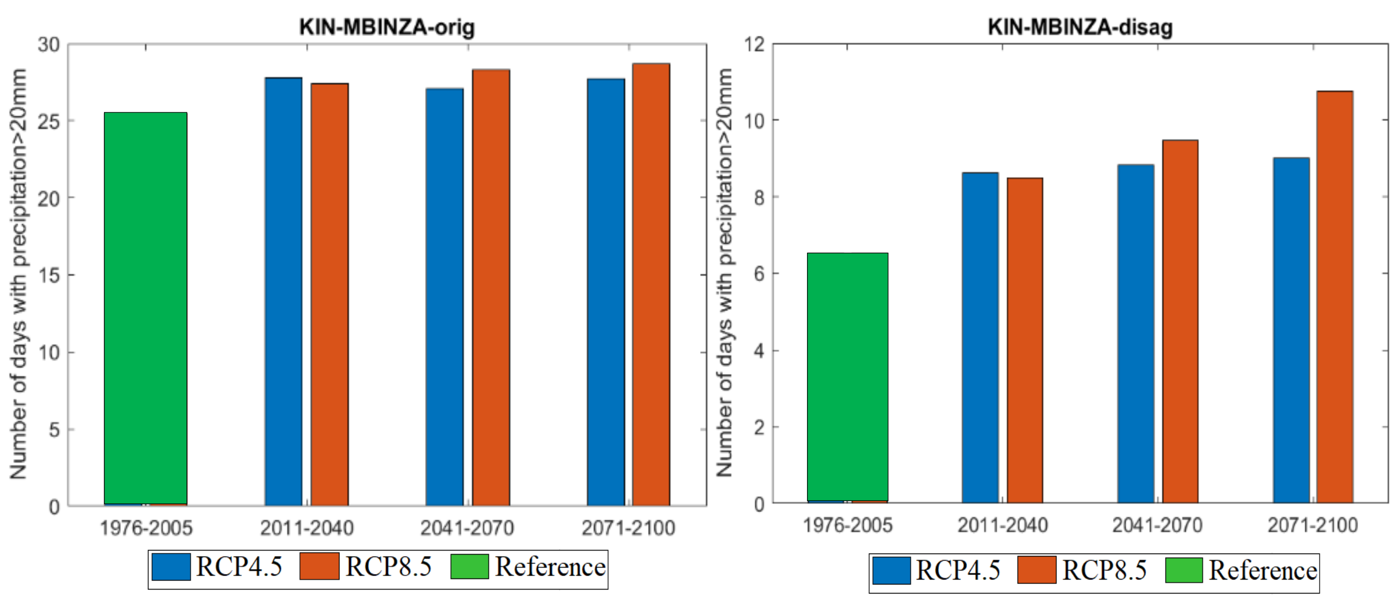

(a) (b)

Figure 4.14 Evolution of PCP20 depending on whether observed time series or disaggregated time series are used: a) using observed daily time series; b) using disaggregated daily time series

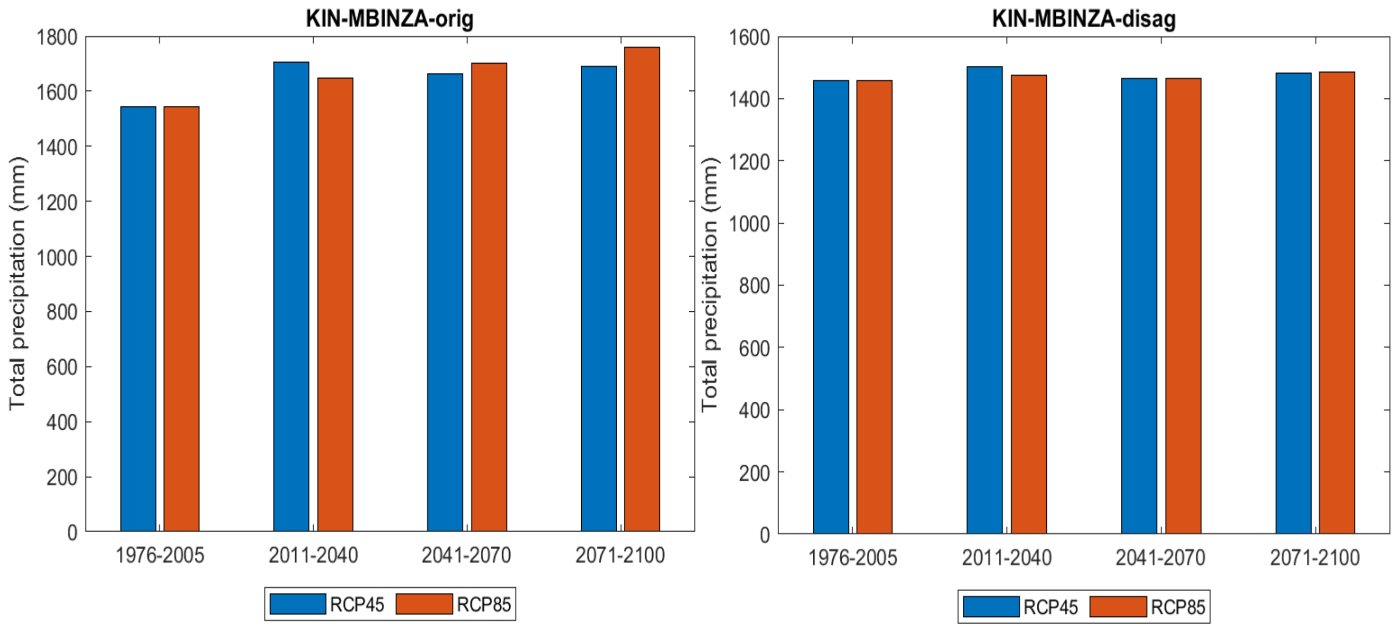

(a) (b)

Figure 4.15 Evolution of PCPTOT depending on whether observed time series or disaggregated time series are used: a) using observed daily time series; b) using disaggregated daily time series

Figures 4.16 to 4.19 show the evolution of SPI and SPEI, estimated using observed daily precipitation and disaggregated time series, under RCP 4.5 and RCP 8.5 scenarios at the Kinshasa-Mbinza station. In all cases, disaggregation does not impact the trend in increased extreme humidity and extreme drought magnitude in SPI, nor does it offset the trend of increased extreme humidity and seemingly constant extreme drought magnitude in SPEI, between the reference and last future period.

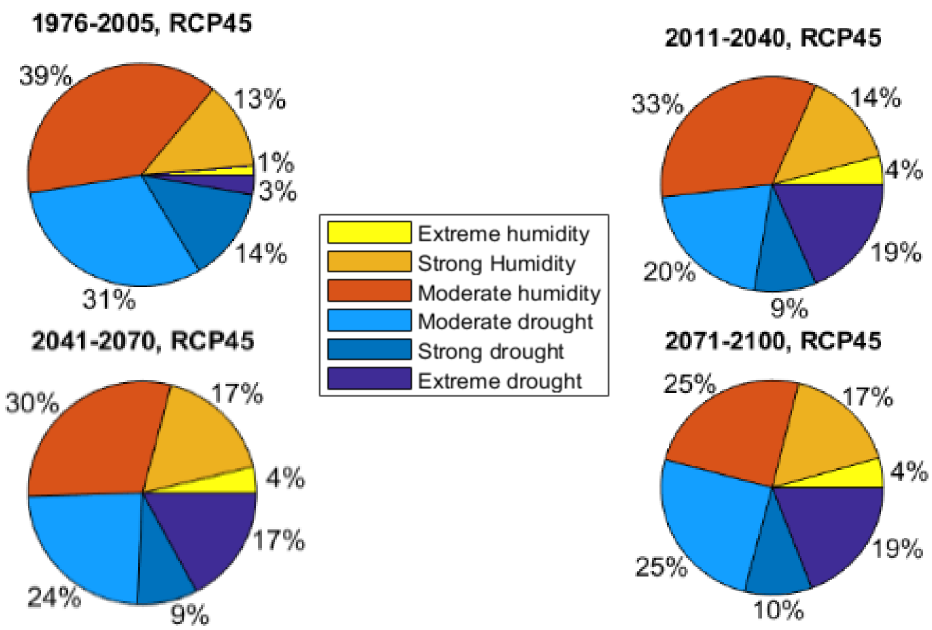

(a)

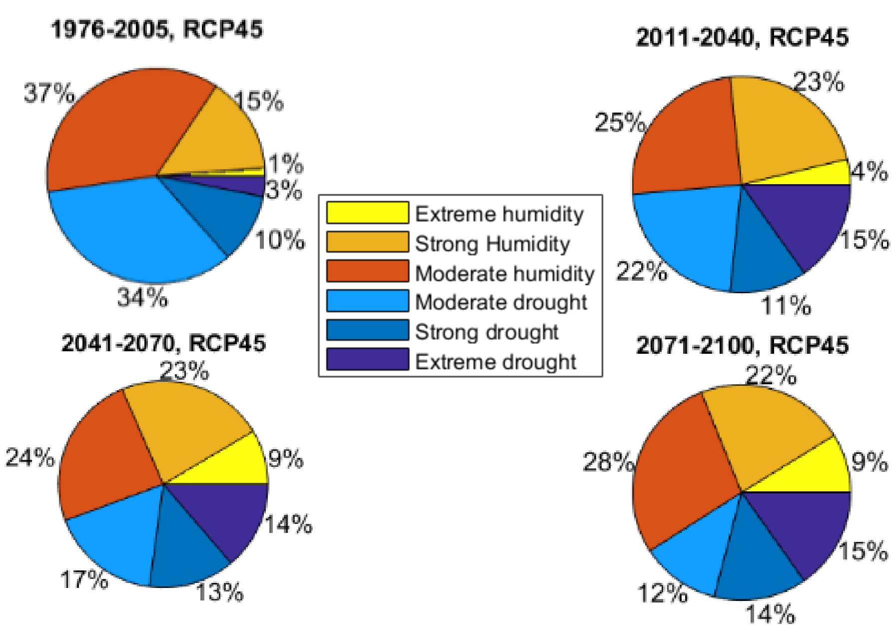

(b)

Figure 4.16 Evolution of SPI under RCP4.5 depending on whether observed time series or disaggregated time series are used: : a) using observed daily time series; b) using disaggregated daily time series

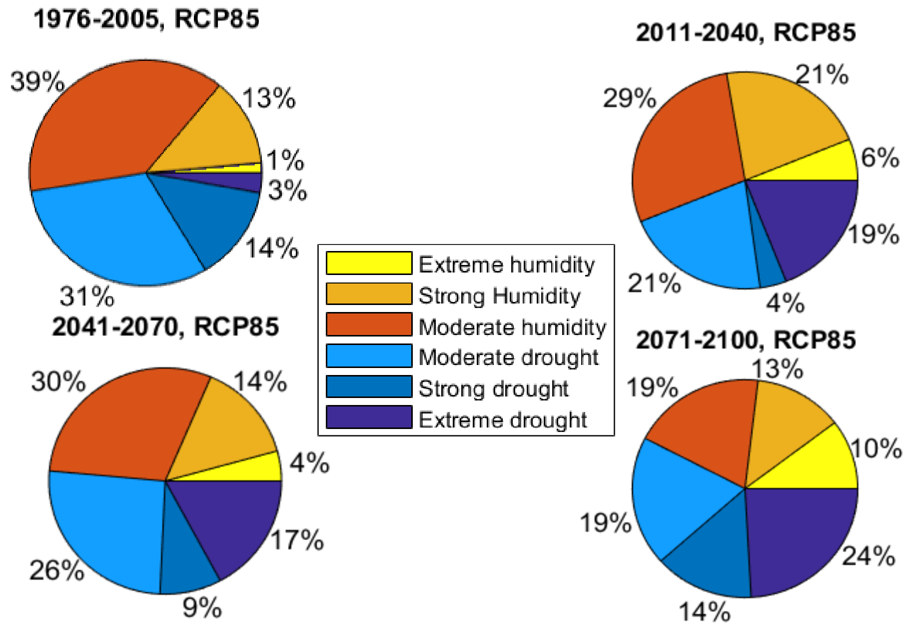

(a)

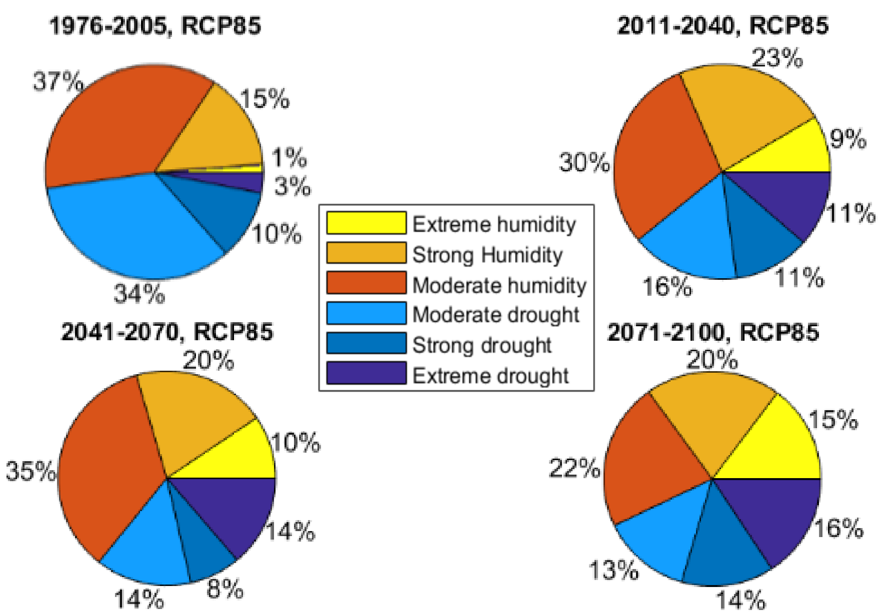

(b)

Figure 4.17 Evolution of SPI under RCP8.5 depending on whether observed time series or disaggregated time series are used: : a) using observed daily time series; b) using disaggregated daily time series

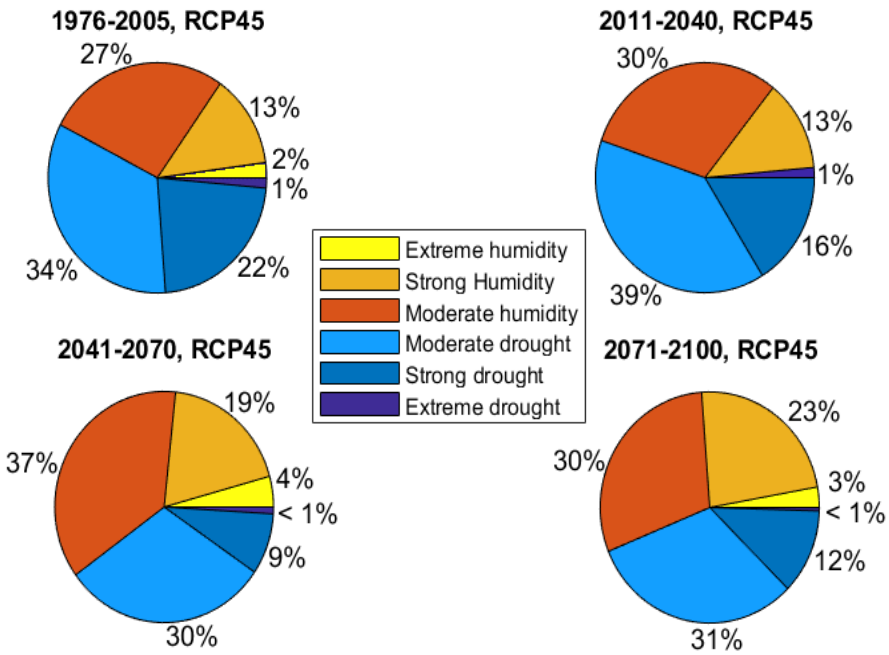
1976-2005, RCP45
27%
13%
2%
1%
22%
34%
2011-2040, RCP45
30%
13%
1%
16%
39%
Extreme humidity
Strong Humidity
Moderate humidity
Moderate drought
Strong drought
Extreme drought
2041-2070, RCP45
19%
37%
4%
< 1%
9%
30%
2071-2100, RCP45
23%
30%
3%
< 1%
12%
31%

(a)

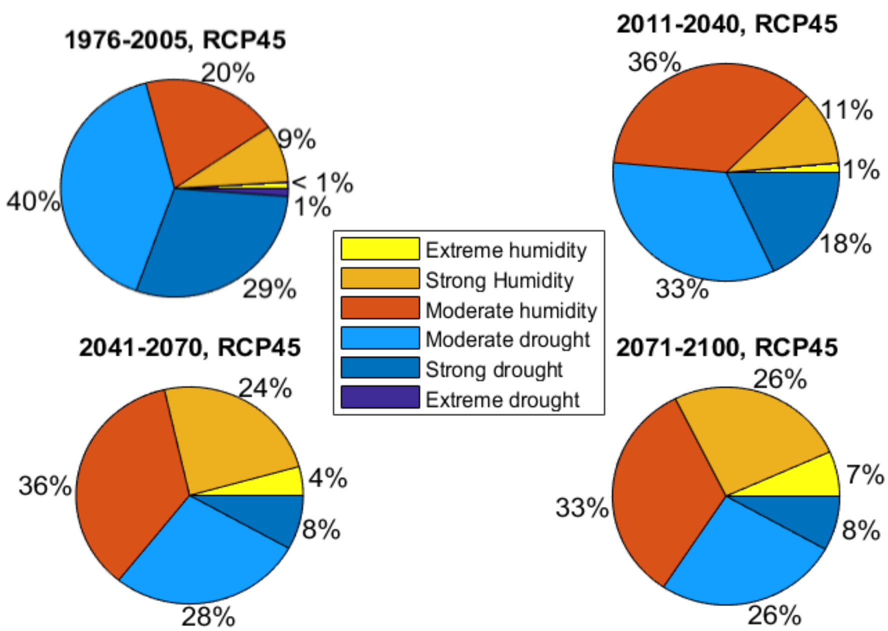
1976-2005, RCP45
20%
9%
40%
< 1%
1%
29%
2011-2040, RCP45
36%
11%
1%
18%
33%
Extreme humidity
Strong Humidity
Moderate humidity
Moderate drought
Strong drought
Extreme drought
2041-2070, RCP45
24%
36%
4%
8%
28%
2071-2100, RCP45
26%
7%
33%
8%
26%

(b)

Figure 4.18 Evolution of SPEI under RCP4.5 depending on whether observed time series or disaggregated time series are used: : a) using observed daily time series; b) using disaggregated daily time series

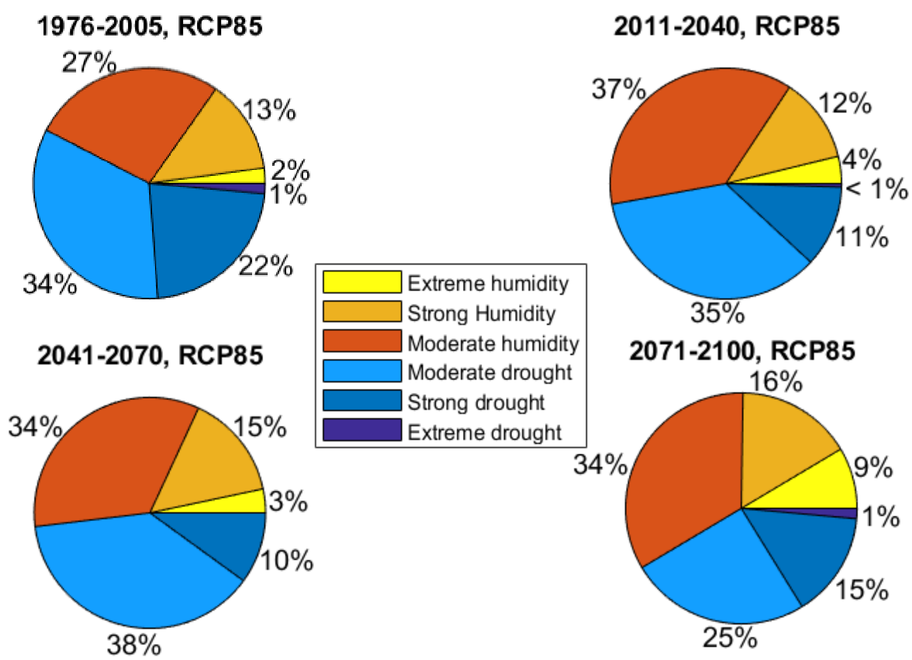

(a)

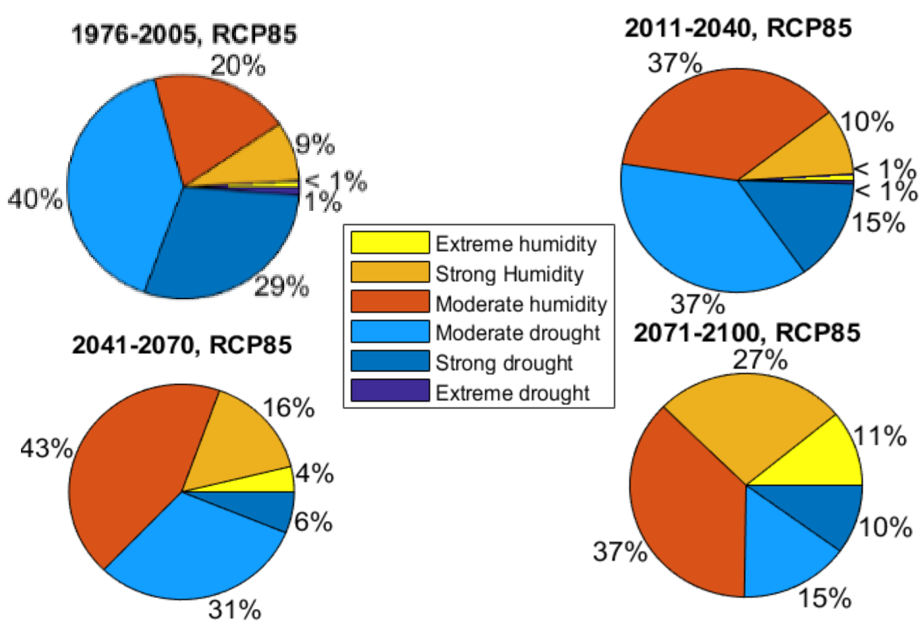

(b)

Figure 4.19 Evolution of SPEI under RCP8.5 depending on whether observed time series or disaggregated time series are used: : a) using observed daily time series; b) using disaggregated daily time series

Chapter 5
Impacts of Climate Change on Hydrological Regimes in the Congo River Basin

Abstract

Surface water resources are essential for a wide range of human activities, such as municipal water supply, fishing, navigation, irrigation, and hydropower. Their regime is also linked to environmental sustainability, water-related risks, human health, and various ecosystem services. Global warming is expected to modify surface water availability, quality, and distribution and therefore affect water use productivity as well as the incidence of water-related risks. Thus, it is important for communities to plan and adapt to the potential impacts of climate change. The Congo River Basin, home to 75 million people, is subject to recurrent flood and drought events, which are expected to worsen as a result of climate change. This study aims to assess future modifications of the hydrological regime of the Congo River and the socio–economic impacts of these projected changes for three future periods: 2011–2041, 2041–2070, and 2071–2100. A Soil and Water Assessment Tool (SWAT) model of the Congo River Basin was developed, calibrated, and validated using daily rainfall observations combined with daily time series of precipitation, temperatures, relative humidity, solar radiation, and wind speed derived from the WFDEI (Watch Forced Era Interim) reanalysis data set. The outputs of ten Regional Climate Models (RCMs) from the Coordinated Downscaling Experiment (CORDEX-AFRICA) were statistically downscaled to obtain future climate time series, considering two Representative Concentration Pathways: RCP8.5 and RCP4.5. The calibrated model was used to assess changes in streamflow in all reaches of the Congo River. Results suggest relative changes ranging from −31.8% to +9.2% under RCP4.5

and from −42.5% to +55.5% under RCP 8.5. Larger relative changes occur in the most upstream reaches of the network. Results also point to an overall decrease in discharge in the center and southern parts of the basin and increases in the northwestern and southeastern parts of the basin under both emission scenarios, with RCP8.5 leading to the most severe changes. River discharge is likely to decrease significantly, with potential consequences for agriculture, hydropower production, and water availability for human and ecological systems.

5.1 Introduction

The Congo River Basin (Figure 5.1a) is located in the central region of Africa and spans over nine political boundaries. It is home to one of the largest watersheds in the world, with an estimated drainage area of 3.7 million square kilometers (Tshimanga, 2022). It is home to a growing population that currently stands at 75 million people. It is an important source of water, food, and transportation for the region, and it plays a vital role in the economies of the countries it passes through. The Congo basin is home to the second-largest rainforest in the world, which plays a crucial role in the global carbon cycle. Like other rainforests, the distribution and makeup of the Congo basin's rainforest may be impacted by variations in local rainfall patterns due to global warming (Malhi & Wright, 2004). The Congo basin is a considerable source of major drought and storm events. Drought events in these regions are common and can affect thousands of people (World Bank, 2022). Evidence suggests that throughout the dry periods for the past 3000 years, the rainforest in the Congo basin has contracted and undergone significant changes in its composition (Lewis et al., 2009; Malhi et al., 2013). It is becoming ever more important to study the climate changes occurring in the Congo basin in order to provide reliable information for planning related to mitigation and adaptation (Creese et al., 2019). However, despite the importance of the Congo basin, it has not been adequately studied and has not received sufficient attention in research on hydrology and climate (Tshimanga et al., 2014). From 1960 to 2019, more than 11.5 million people in the countries of the Congo basin were affected by flooding. There were 3062 fatalities and severe economic losses that are estimated to be around $96 billion (EM-DAT, 2021).

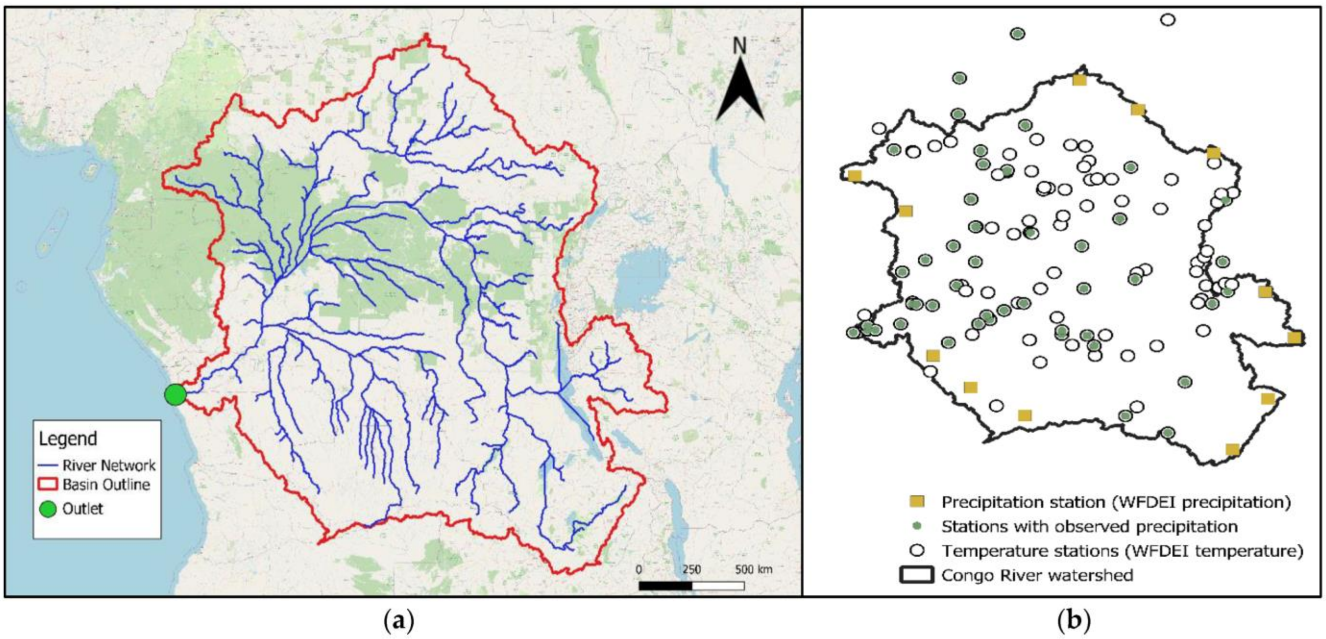

Figure 5.1 (a) Geographical location of the Congo River Basin with the river network and the outlet location and (b) location of observed rainfall stations and location of WFDEI precipitation and temperature stations in the Congo River Basin.

The general objective of this paper is to assess the impacts of climate change on the hydrological regime of the Congo River. Specific objectives include the development of a hydrological model of the Congo River Basin and the quantification of expected changes in average flow in three future periods (2011–2040, 2041–2070, and 2071–2100). The results will be spatially mapped in order to support climate change adaptation policies that will protect local infrastructure and ensure the sustainability of people's livelihoods.

Several studies have investigated the effects of climate change on hydroclimate variables in the study area. Tshimanga and Hughes (2014) analyzed the effects of climate change on the hydrology of the Oubangui and Sangha watersheds, focusing on near-future runoff. The analysis was based on climate models (CMIP3 GCMs). Their research found that evapotranspiration is likely to significantly increase, and total runoff is expected to decline by 10%.

Sridhar et al. (2021) evaluated the Congo River Basin's land use and land cover from 1992 to 2012, revealing a decrease in forests and native vegetation and a slight increase in urban and cropland areas. The study found that a framework combining the hydroclimate assessment of total water storage with hydrological SWAT models and remote sensing is feasible within the basin. Significant declines in forests and shrublands and increases in urban areas in the Oubangui and Middle Congo regions led to notable changes in the water budget and an increase in streamflow. Variations in temperature and precipitation at the basin scale have had an impact on streamflow and exacerbated total water storage conditions. Projections for the future indicate that increased temperatures and variable precipitation will lead to sub-basin-scale differences, with overall increases in evapotranspiration and runoff and more frequent drought events in the basin.

Santos et al. (2022) conducted a comprehensive comparison of various satellite-based precipitation products as inputs for a hydrological SWAT model in the Congo River Basin. The research found that products based on satellite-only sources tend to overestimate the peaks of the rainy season.

However, satellite products that consider gauge calibration were found to have better agreements with one another. The overall precipitation patterns were found to have a significant impact on the model's performance, resulting in different values for streamflow and water balance components.

Kitambo et al. (2022) used a large collection of in situ and satellite-derived data, including a long-term record of surface water height and surface water extent, to examine the surface hydrology and seasonal variability in the Congo River Basin. They found that the surface water height data from multiple satellite missions were consistent with in situ measurements and that the surface water extent data from various satellites accurately represented the hydrological patterns in the basin over a period of approximately 25 years. The data also revealed significant variability in the surface water height and extent in the

Congo River, with annual amplitudes of over 5 m in certain northern subbasins and smaller variations in the main stream and Cuvette Centrale tributaries. Their results provide an understanding of the seasonal hydrological variability in the Congo River Basin.

Cerkasova et al. (2018) created an application of the SWAT model that was used to develop a hydrology and water quality model for a vast watershed of the transboundary Vilija River in Europe. The primary aim was to investigate the impacts of climate change. It was found that although the RCP8.5 scenario represented the extreme range of projected changes, the hydrologic regime of the Vilija River is still expected to undergo significant changes in the RCP4.5 scenario. This is mainly due to the anticipated increase in precipitation, which is projected to be higher in the RCP4.5 scenario than in the RCP8.5 scenario.

Park et al. (2014) conducted research to assess how climate change may affect different hydrological components of the Yongdam watershed (930 km2), including evapotranspiration, surface runoff, lateral flow, return flow, and streamflow. The SWAT model was calibrated and validated using daily soil moisture and streamflow data. The results indicate that future climate change is expected to increase evapotranspiration, surface runoff, baseflow, and streamflow by 11.8%, 36.8%, 20.5%, and 29.2%, respectively. These findings suggest that future temperature and precipitation increases, as predicted by the RCP emission scenarios, will likely lead to an overall increase in hydrological patterns.

Anjum et al. (2019) examined the potential effects of anticipated climate changes on the outflows of a humid subtropical basin located in the westerly dominated region of the Hindukush Mountains. Using six GCMs and two RCPs, 4.5 and 8.5, they downscaled precipitation and temperature projections and calibrated a SWAT model to find that climate changes could significantly impact the seasonality of river discharge.

The focus of these previous studies that consider the Congo basin are either seasonal studies on the variation of the hydrological regime or studies on the climatological properties surrounding the basin. In light of the significance of the study area and its vulnerabilities to hydrological variations, it is crucial to have a current understanding of food and drought patterns in the present and in the future. While extreme climatology of the Congo basin has been studied in the past, future hydrological regimes give us a more in-depth perception of the physical variations occurring within the basin, which gives a sharper idea of the potential vulnerability of the basin. By understanding hydrological conditions, it is possible to improve water resource management, reduce the risk of water-related disasters, and develop adaptation policies. This study aims to evaluate the potential changes in hydrological patterns in the Congo basin from the present until 2100.

5.2 Materials and Methods

5.2.1 Available Data

The Congo basin Water Resources Research Center (CRREBaC) facilitated monthly precipitation time series as well as maximum and minimum temperature time series. Daily rainfall observations ranged from the years 1961 to 2019 at the Kinshasa–Mbinza station; however, the authors were not able to obtain observations at other locations in the basin. Alternatively, precipitation, maximum and minimum temperatures, relative humidity, solar radiation, and daily wind speed time series were obtained from the Watch Forced Era Interim (WFDEI) reanalysis data set (Weedon et al., 2018). As measured station records are usually deemed to be more accurate than reanalysis data (Le Page et al., 2015), there appeared to be a considerable amount of incorrect data in the observation records. Thus, any observed rainfall data in which the yearly totals are different by ten percent or more of that of the WFDEI data set were discarded. After this distinction, the observed rainfall stations lowered from 121 stations to 50 stations. The WFDEI was also used at additional stations to provide appropriate spatial coverage of the study area for a total of 87 precipitation stations. Given that the WFDEI database derives a temperature estimate that provides higher accuracy than precipitation estimates, the authors chose to utilize the WFDEI time series for 128 stations. Similarly, WFDEI was used for relative humidity, solar radiation, and wind speed at 82 locations. The geographical location of the Congo basin and the outlet location (gauge used for calibration and validation) can be observed in Figure 51a, and the observation stations for precipitation and temperature are shown in Figure 5.1b.

Ten climate change experiments were conducted by the Coordinated Downscaling Experiment (CORDEX) group (https://cordex.org/domains/region-5-africa/, accessed on 31 January 2022) (Giorgi & Gutowski, 2015) to gather information on projected precipitation and maximum and minimum temperatures from 1950 to 2100. The trials entailed utilizing GCMs to drive the RCMs under two circumstances, namely RCP4.5 and RCP8.5.

To generate a statistical distribution of a climate parameter that closely matches the observed parameter in the historical period, the quantile–quantile (Q–Q) transformation is used. As per Hakala et al. (2018), this method outperforms other approaches, such as the delta-change method, local intensity scaling, and power transformation in reducing biases in GCM–RCM precipitation. The detailed procedure conducted in this paper for bias correction is described by Karam et al. (2022). The details of the institutions and the driving GCM and RCM are presented in Table 5.1.

Table 5.1 Characteristics of the GCM/RCM model combinations used in the study.

No.	Driving GCM	GCM Institute	RCM	RCM Institute
1	Canadian Earth System Model Version 2	Canadian Centre for Climate Modeling and Analysis	Canadian Regional Climate Model 4	Canadian Centre for Climate Modeling and Analysis
2	Canadian Earth System Model Version 2	Canadian Centre for Climate Modeling and Analysis	Rossby Centre regional atmospheric model, version 4	Swedish Meteorological and Hydrological Institute

3	Centre National de Recherches Météorologiques, Climate Model 5	National Centre for Meteorological Research	Rossby Centre regional atmospheric model, version 4	Swedish Meteorological and Hydrological Institute
4	Queensland Climate Change Centre of Excellence (QCCCE) and Commonwealth Scientific and Industrial Research Organization (CSIRO)	The Commonwealth Scientific and Industrial Research Organization	Rossby Centre regional atmospheric model, version 4	Swedish Meteorological and Hydrological Institute
5	European community Earth-System Model	Irish Centre for High-End Computing	Rossby Centre regional atmospheric model, version 4	Swedish Meteorological and Hydrological Institute
6	Institut Pierre Laplace Climate Model version 5A	Institute Pierre Simon Laplace	Rossby Centre regional atmospheric model, version 4	Swedish Meteorological and Hydrological Institute
7	Model for Interdisciplinary Research on Climate, version 5	Center for Climate System Research/National Institute for Environmental Studies/Frontier Research Center for Global Chance, Japan Agency for Marine-Earth Science and Technology	Rossby Centre regional atmospheric model, version 4	Swedish Meteorological and Hydrological Institute
8	Max Plank Institute Earth System Model	Max Planck Institute for Meteorology	Rossby Centre regional atmospheric model, version 4	Swedish Meteorological and Hydrological Institute

9	Norwegian Earth System Model	Norwegian Climate Centre	Rossby Centre regional atmospheric model, version 4	Swedish Meteorological and Hydrological Institute
10	Geophysical Fluid Research Laboratory Earth System Model	National Oceanic and Atmospheric Administration-Geophysical Fluid Dynamics Laboratory	Rossby Centre regional atmospheric model, version 4	Swedish Meteorological and Hydrological Institute

5.2.2 Model Setup

The SWAT (Soil and Water Assessment Tool) is a hydrological and water-quality model developed by the Agricultural Research Service (ARS) of the United States Department of Agriculture (USDA). It was developed by Arnold et al. in 1998 and is a physically based, semi-distributed continuous model used to simulate the impact of land management practices on water, sediment, and agricultural chemical yields in large, complex watersheds.

ArcSWAT was developed as an extension to the ArcGIS software version 10.7, and was used in conjunction with SWAT as a graphical user interface. This tool combines spatial and climatic inputs to set up and run the SWAT model and to visualize and analyze the results of the models within the ArcGIS platform (Pan et al., 2022). ArcSWAT comes with a global database of default parameters which allows users to quickly develop a functional model of any area. ArcSWAT discretizes the watershed into sub-watersheds and Hydrological Response Units (HRUs) based on user-specified location of outlets and the HRU definition method. An HRU is a unique combination of topographical, land-use management, and soil characteristics (Arnold et al., 1998).

The hydrological simulations conducted in the SWAT use the water balance equation which is utilized at the HRU scale for each time step:

$$SW_t = SW_0 + \sum_{i=1}^{t}(R_{day} - Q_{surf} - E_a - w_{seep} - Q_{gw} \quad (5.1)$$

where SW is the soil water content at time 0 and at a time step, t. R_{day} is the precipitation amount, Q_{surf} is the surface runoff, E_a is the evapotranspiration, w_{seep} is the water entering the vadose zone from the soil profile, and Q_{gw} is the return flow on a specific day, i, in units of mm. Rainfall is then subdivided into infiltration and surface runoff using the curve number (CN) method (Neitsch et al., 2011):

$$Q_{surf} = \frac{(P-0.2)^2}{(P-0.8S)} \quad (5.2)$$

where the surface runoff (Q_{surf}) is derived as a function of the total precipitation (P) in mm and the soil moisture content (S), a no-dimension parameter expressed in terms of a CN ranging from 0 to 100. The constants 0.2 and 0.8 are coefficients that are used to adjust the relationship between the surface runoff and the other variables. The surface runoff increases as the total precipitation increases. This is because more precipitation leads to more runoff. The surface runoff decreases as the soil moisture content increases. This is because a higher soil moisture content means that more of the precipitation will be absorbed by the soil and less will run off.

A total of 223 sub-watersheds and twelve HRUs were delineated (Figure 5.2), and land use characteristics of the Congo River Basin are depicted in Table 5.2. The remainder of the model development consists of setting up and calibrating the model, validating the model's predictions, and analyzing and interpreting the results to inform land use and management decisions.

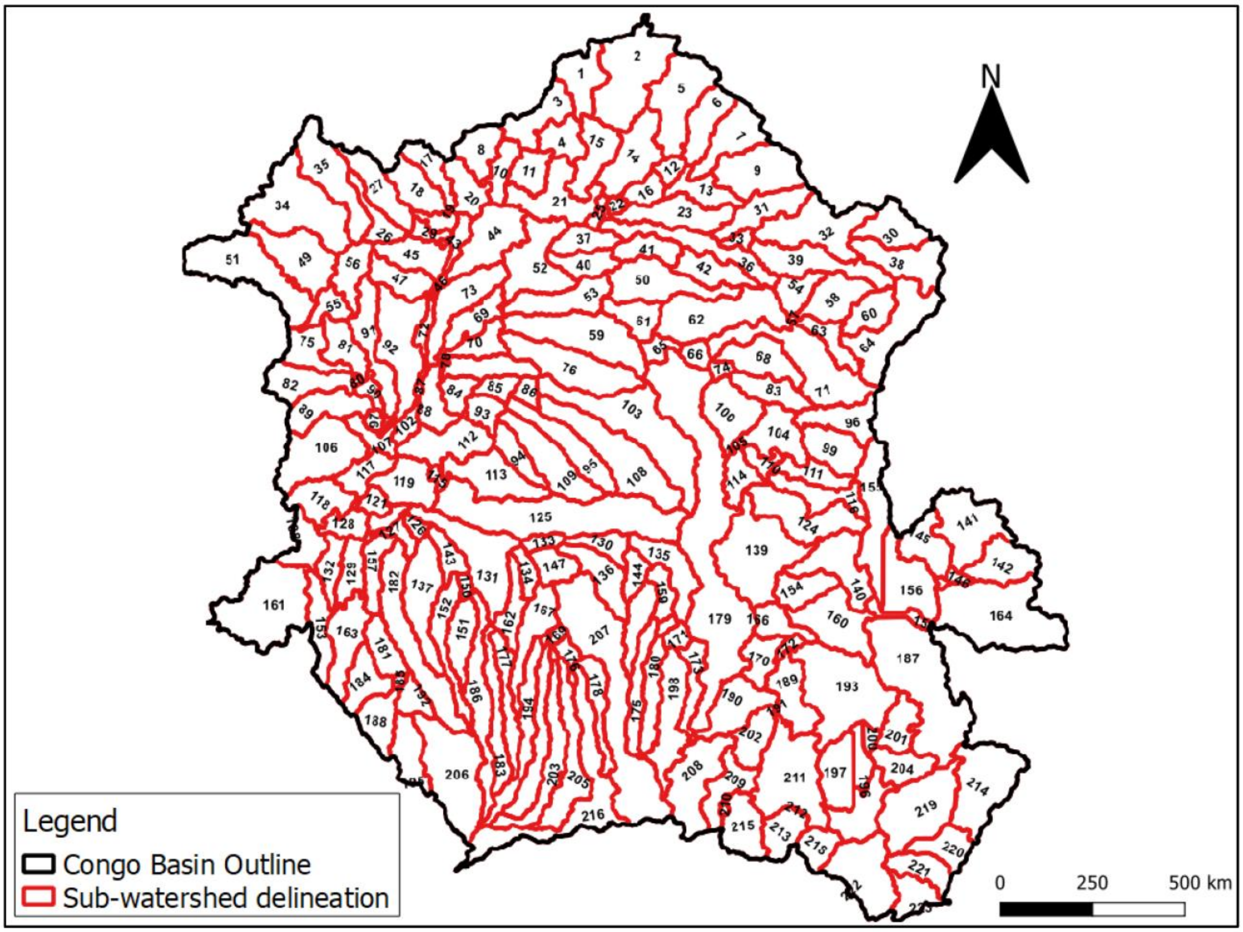

Figure 5.2 Sub-watersheds in the Congo basin model

Table 5.2 Land-use characteristics of the Congo River Basin (Arnold et al., 2012)

Land Use/Cover Type	SWAT Code	Area (%)
1. Water	WATR	2.70
2. Residential area (urban)	URMD	0.02
3. Dryland cropland and pasture	CRDY	3.87
4. Mosaic cropland/grassland	CRGR	0.12

5. Mosaic cropland/woodland	CRWO	7.15
6. Grassland	GRAS	0.19
7. Shrubland	SHRB	0.31
8. Savanna	SAVA	28.27
9. Deciduous broad-leaf forest	FODB	13.70
10. Evergreen broad-leaf forest	FOEB	42.89
11. Mixed forest	FOMI	0.18
12. Barren or sparsely vegetated	BSVG	0.58

5.2.3 Calibration and Validation

Calibration and validation are important steps in the model development process, as they help to ensure that the model is accurately representing the processes that are being simulated. The calibration process involves adjusting the model parameters and input data to improve the accuracy of the model predictions. The validation process involves evaluating the performance of the calibrated model using additional data that was not used in the calibration process. This helps to determine the accuracy and reliability of the model under different conditions and to identify any potential biases or errors in the model.

Potential uncertainties in the SWAT discharge model stem from various sources, including parameterization, input data quality, model assumptions, and spatial/temporal scale disparities. Errors in assigning hydrological parameters, inaccuracies in input data such as precipitation and land use/land cover, and simplifications in representing hydrological processes can lead to discrepancies between simulated and observed discharge. Calibration and validation against observed data help to mitigate these uncertainties.

5.2.3.1 Performance Measures

The performance of the calibration and validation is evaluated using statistical and graphical methods. This study uses the Nash–Sutcliffe efficiency coefficient (NS) (Nash & Sutcliffe, 1970) and the percentage bias (PBIAS) (Gupta et al., 1999) as statistical measures of the accuracy and performance of the model. The NS coefficient is a dimensionless measure that ranges from −∞ to 1, with values closer to 1 indicating a better fit between the observed and simulated values. It is given by the following equation:

$$\mathrm{NS} = 1 - \frac{\sum_{i=1}^{n}(Q_m - Q_s)_i^2}{\sum_{i=1}^{n}(Q_{m,i} - Q_m)^2} \qquad (5.3)$$

where Q is the discharge, m is the measured data, s is the simulated data, i is the time step, and n is the total number of periods.

The PBIAS is another measure of model accuracy that is calculated by comparing the mean of the observed values to the mean of the simulated values and expressing the difference as a percentage of the observed mean. A PBIAS value of 0 indicates that the model is unbiased, while positive and negative values indicate a tendency for the model to underestimate or overestimate the observed values, respectively.

$$\mathrm{PBIAS} = 100 \times \frac{\sum_{i=1}^{n}(Q_m - Q_s)_i}{\sum_{i=1}^{n} Q_{m,i}} \qquad (5.4)$$

The statistical measures obtained in this paper will be compared to the model performance criteria illustrated in Table 5.3 (Moriasi et al., 2007).

Table 5.3 Model performance criteria (Moriasi et al., 2007)

	Satisfactory	**Good**	**Very Good**
NS	0.5–0.7	0.7–0.8	0.8–1.0
PBIAS (%)	15–25	10–15	Less than 10%

5.2.3.2. Sensitivity Analysis

The calibration and the sensitivity analysis were conducted using the SUFI2 (Sequential Uncertainty Fitting) algorithm produced in the SWATCUP program (Abbaspour, 2007). The sensitivity analysis is used to evaluate the sensitivity of the model's output to changes in different input parameters. It is computed by altering one parameter while all other parameters remain unchanged. The effectiveness of the changed parameter is then evaluated with t-stat and p-value, which are determined with a multiple regression analysis using the following equation (Abbaspour, 2007):

$$g = \alpha + \sum_{i=1}^{m} \beta_i b_i \qquad (5.5)$$

where g is the objective function used to determine the model calibration effectiveness, b is the parameter in question, α is equal to the regression constant, β is the technical coefficient attached to the variable b, and m corresponds to the number of parameters.

The p-value is a statistical measure that represents the probability of obtaining a test statistic at least as extreme as the one observed, assuming that the null hypothesis is true. The t-statistic is used to determine whether the mean of a population is significantly different from a hypothesized value. If the absolute value of t-stat is relatively high and the p-value is relatively small, the parameter is considered to have a high sensitivity (Abbaspour, 2007). Typically, a p-value lower than 0.05 indicates that the parameter is significantly sensitive (Verhagen, 2004).

Given the large number of parameters of the SWAT model, only a small subset is calibrated. That subset was selected after a sensitivity analysis, which consists of slightly modifying the parameter values and seeing their impact. Choosing sensitivity parameters for calibration requires a combination of expert knowledge, sensitivity analysis, and trial and error. Initially, the most important input parameters must be identified; then, a reasonable range of values must be chosen. This range should be based on the published literature or previous modeling studies. If the model performance is not satisfactory, the sensitivity parameters should be adjusted, and the calibration process should be repeated.

Twelve parameters were chosen for the calibration with the help of several recommendations by authors who conducted similar studies (Arnold et al., 2012; Zango et al., 2022; Abbaspour et al., 2015;El-Khoury et al., 2015; Khoi & Thom, 2015). The parameters included in the sensitivity analysis are shown in Table 5.4.

Table 5.4. Parameters used for calibration/validation

Parameter Name	**Parameter Description**	**Variation Range**
r_HRU_SLP.hru	Average slope steepness (m/m)	0.1–0.5
r_ESCO.bsn	Soil evaporation compensation factor	0.1–0.5
r_EPCO.bsn	Plant uptake compensation factor	0.1–0.4

r_REVAPMN.gw	Threshold depth of water in the shallow aquifer for ‘revap’ to occur (mm)	0.1–1.0
r_GWQMN.gw	Threshold water depth in the shallow aquifer for flow	0–0.5
r_GW_REVAP.gw	Groundwater ‘revap’ coefficient	−0.1–0.1
r_SOL_AWC.sol	Available water capacity	−0.5–0.1
r_ESCO.hru	Soil evaporation compensation factor	0–0.3
r_ALPHA_BF.gw	Baseflow alpha factor	0.01–1
r_CN2.mgt	Initial SCS CNII value	−0.2–0.5
r_RCHRG_DP.gw	Deep aquifer percolation fraction	0–10
r_SOL_BD.sol	Moist bulk density (Mg/m^3 or g/cm^3)	0.01–2.0

5.3. Results and Discussion

5.3.1. Sensitivity Analysis

The results of the global sensitivity analysis are shown in Table 5.5. The parameter with the most influence on the performance of the model is the deep aquifer percolation fraction (RCHRG_DP) with a t-stat and p-value of −0.09 and 0.92, respectively, whereas the least sensitive parameter is the average slope steepness (HRU_SLP) with a t-stat and a p-value of 0 and 0.99, respectively.

Table 5.5 Sensitivity analysis result

Parameter Name	t-Stat	p-Value	Rank

r_RCHRG_DP.gw	−0.09	0.92	1 (most sensitive)
r_SOL_AWC.sol	−0.06	0.95	2
r_SOL_BD.sol	−0.05	0.96	3
r_CN2.mgt	−0.04	0.97	4
r_REVAPMN.gw	−0.02	0.97	5
r_GW_REVAP.gw	0.03	0.97	6
r_GWQMN.gw	−0.02	0.98	7
r_EPCO.bsn	0.01	0.99	8
r_ESCO.hru	0.01	0.99	9
r_ALPHA_BF.gw	0.01	0.99	10
r_ESCO.bsn	0.01	0.99	11
r_HRU_SLP.hru	0.00	0.99	12 (least sensitive)

5.3.2. Calibration and Validation Performance

The calibration was performed for twelve parameters identified in the previous section. The outputs of the calibrated and validated model are shown in Figure 5.3, while the optimal fitted values for each parameter are shown in Table 5.6. The model demonstrates good performance for the discharge at the watershed outlet in calibration. According to Moriasi et al. (2007), the NS coefficient is in the satisfactory range ($0.5 < NS = 0.64 < 0.7$), and the PBIAS = 1.2% is also very good (near 0). In the validation stage, an excellent performance was achieved with an NS equivalent to 0.88 and a PBIAS of −3.6%. However, the graphical comparison between the observed and simulated values shows that the model often tends to underestimate the peaks, which has proven to be a common problem in rainfall-runoff modeling (Zango et al., 2022; Sharma & Regonda, 2021). This discrepancy can be due to the quality of climate data input and the spatial variation of the study area. In fact, spatial repartition of rain gauges and data scarcity of such a large catchment may lead to extreme precipitation events being overlooked, notably in large areas with a single rain gauge, where intense precipitation events would not be detected.

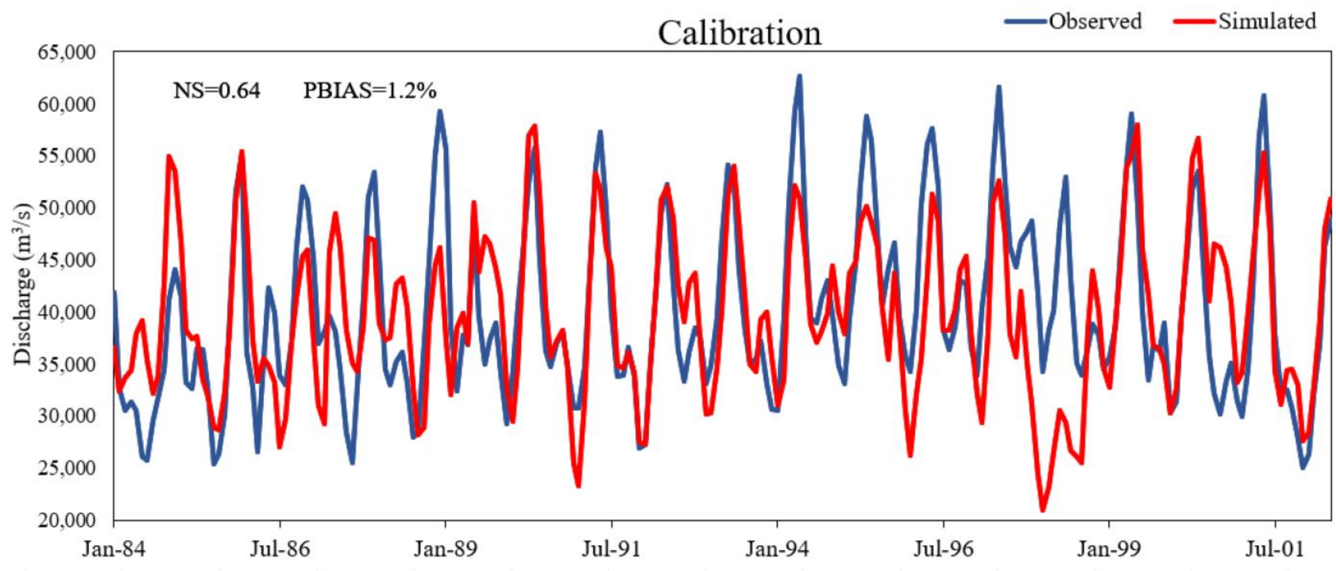

(a)

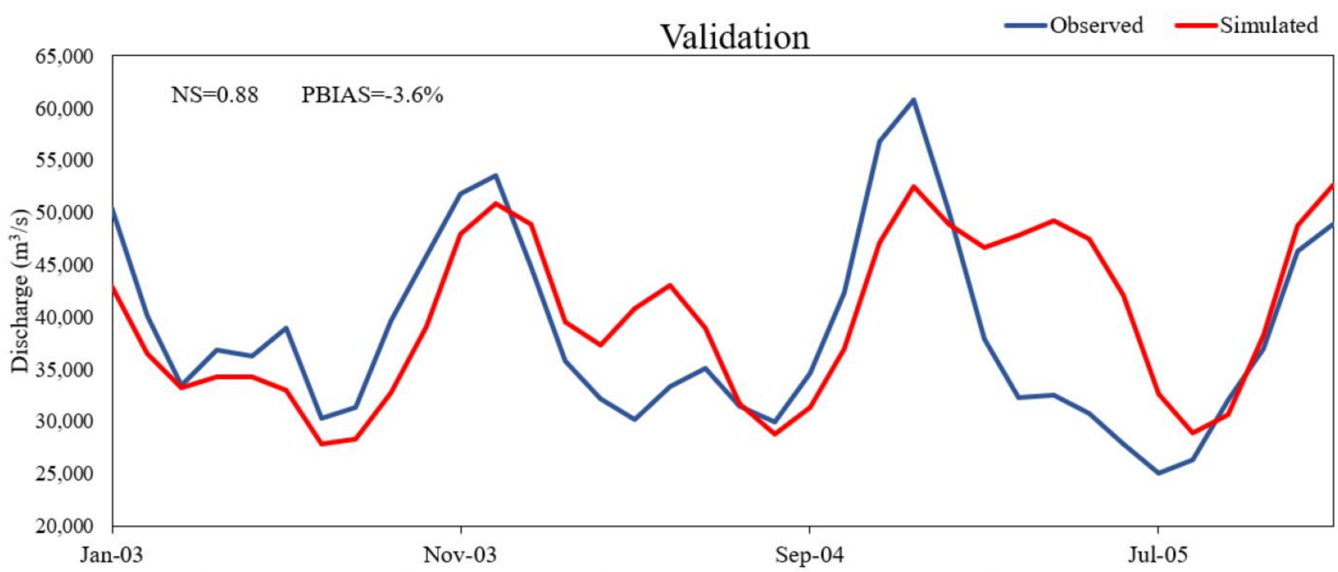

(b)

Figure 5.3 (a) Calibration and (b) validation performance at the defined Congo River Basin outlet

Table 5.6 Parameters used for calibration/validation

Parameters	**Optimal Fitted Values**

r_HRU_SLP.hru	0.447
r_ESCO.bsn	0.345
r_EPCO.bsn	0.249
r_REVAPMN.gw	0.917
r_GWQMN.gw	0.194
r_GW_REVAP.gw	−0.068
r_SOL_AWC.sol	−0.362
r_ESCO.hru	0.140
r_ALPHA_BF.gw	0.268
r_CN2.mgt	−0.298
r_RCHRG_DP.gw	7.979
r_SOL_BD.sol	1.360

5.3.3. Projections for River Discharge

Figure 5.4 shows the average annual river discharge in cubic meters per second (cms) in the study area for a reference period of 1976 to 2005. The river discharge in this period ranges from 97 to 67,981 cms, with an average discharge value of 4713 cms. The highest discharge value can be observed at the outlet, while the southern part of the basin is the largest section in the basin with the least amount of discharge. In fact, minimal discharge can be observed in the extremities of the entire basin, except for near the outlet.

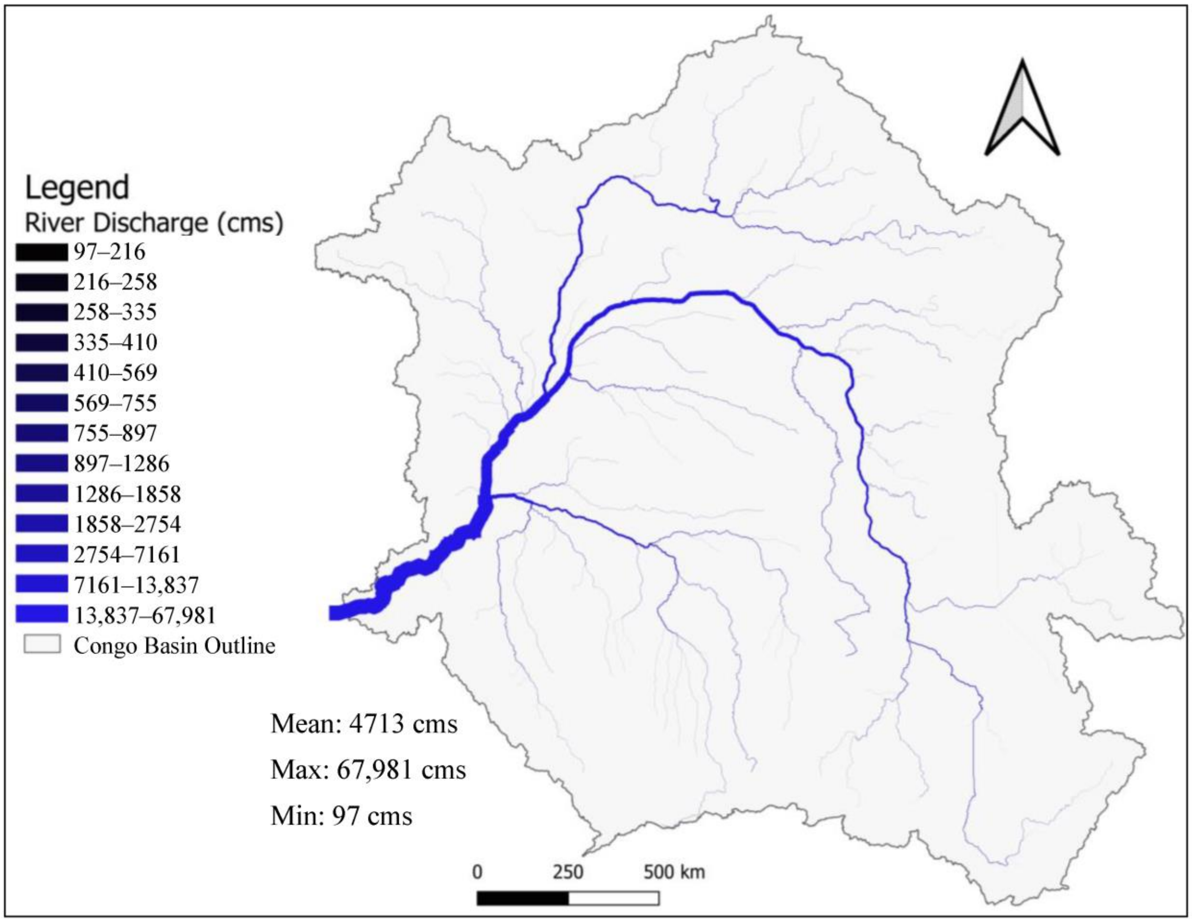

Figure 5.4. Average annual Congo River Basin discharge (cms) during reference period (1976–2005).

Figure 5.5 shows the average annual Congo River Basin discharge (cms) for RCP 4.5 for three future periods (2011–2040); (2041–2070); (2071–2100). These projections do not show any extreme variations between periods; however, a slight decrease in average annual discharge can be observed. The average discharge for period 1, period 2, and period 3 are 4597, 4417, and 4423 cms, respectively. This also predicts a decrease in average annual flow since the reference period (4713 cms). The maximum discharge located at the outlet of the basin for period 1, period 2, and period 3 are 66,382, 63,827, and 63,745 cms, respectively. Throughout all periods, the highest discharge value can be observed in the western stream leading towards the outlet. Similar to the reference period, the southern part of the basin is the largest section in the basin with the least amount of discharge, and minimal discharge can be observed in the extremities of the entire basin, except for near the outlet.

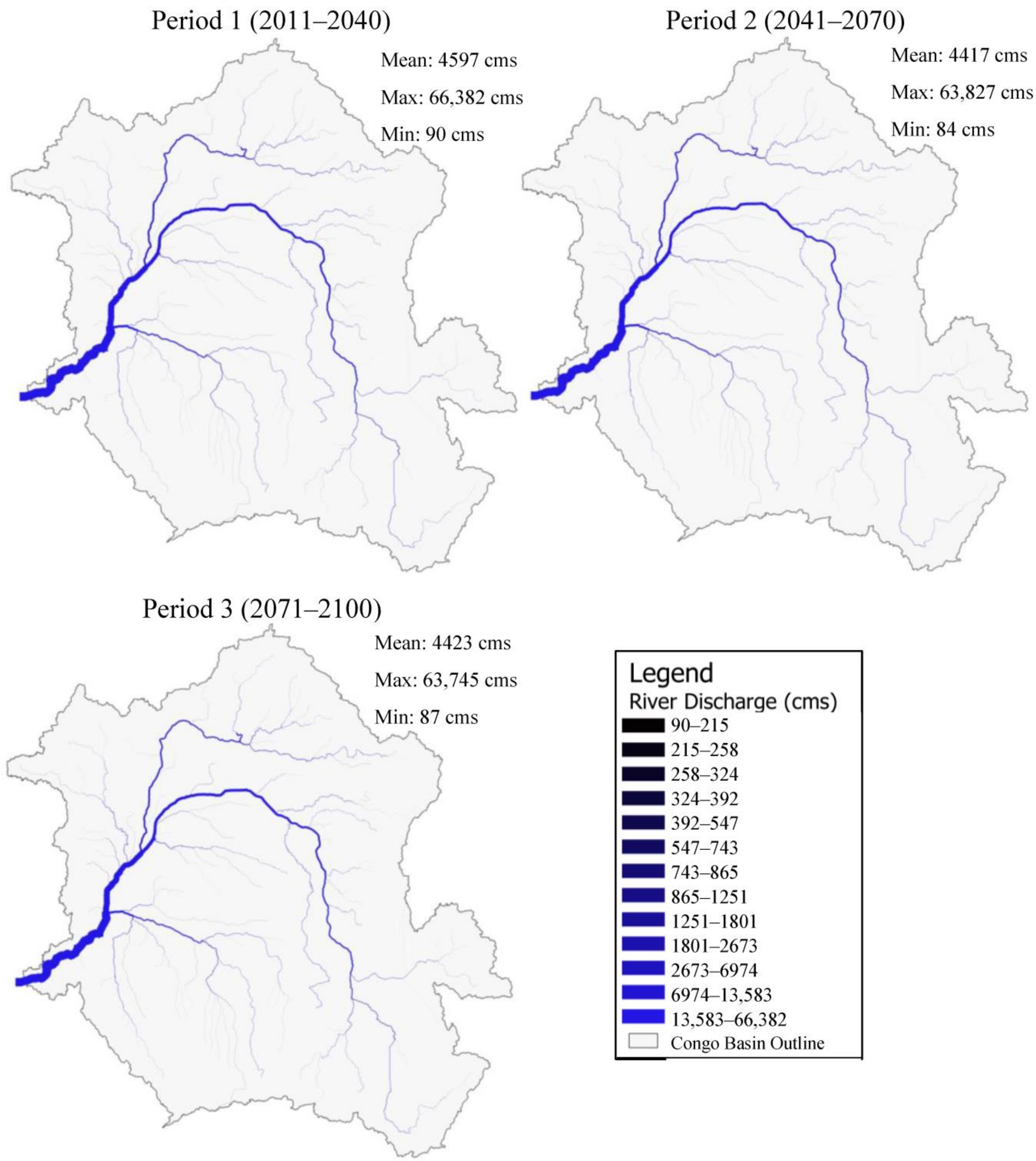

Figure 5.5 Average annual Congo River Basin discharge (cms) for RCP 4.5 for three future periods (2011–2040); (2041–2070); (2071–2100).

Figure 5.6 shows the percent change in average annual discharge for RCP 4.5 for three future periods (2011–2040); (2041–2070); (2071–2100). The average percent change of discharge for period 1, period 2, and period 3 are −1.8%, −6.1%, and −6.0%, respectively. The decrease in river discharge can be observed, especially in the center and southwestern sections of the basin, while the extremities of the basin show the most increase. The maximum and minimum changes occur in period 3 and period 2, with 9.2% change and −31.8% change, respectfully. Similar to what was represented in Figure 5.5, an overall decrease of the average discharge can be observed.

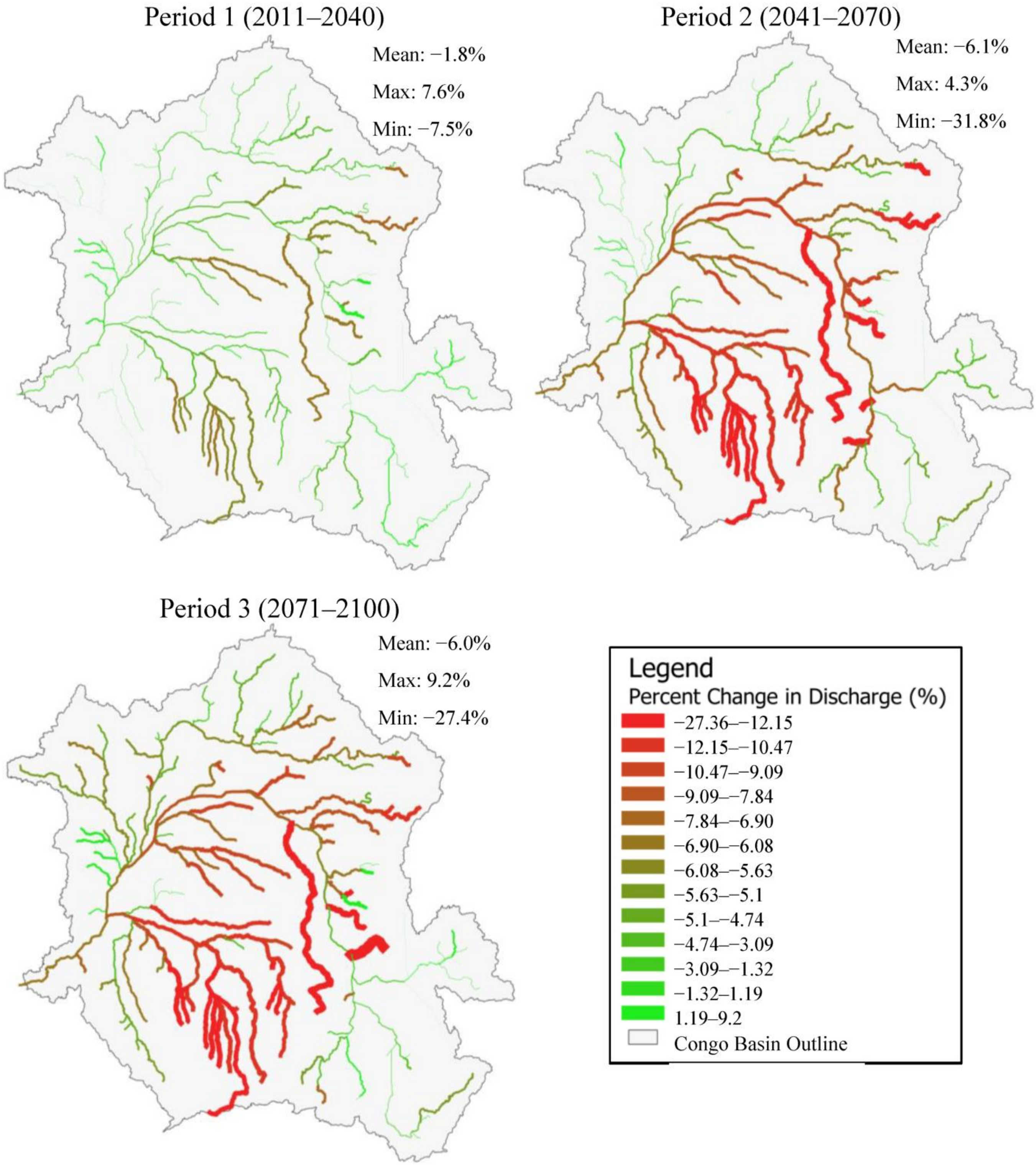
Period 1 (2011–2040)
Mean: −1.8%
Max: 7.6%
Min: −7.5%
Period 2 (2041–2070)
Mean: −6.1%
Max: 4.3%
Min: −31.8%
Period 3 (2071–2100)
Mean: −6.0%
Max: 9.2%
Min: −27.4%
Legend
Percent Change in Discharge (%)
−27.36–−12.15
−12.15–−10.47
−10.47–−9.09
−9.09–−7.84
−7.84–−6.90
−6.90–−6.08
−6.08–−5.63
−5.63–−5.1
−5.1–−4.74
−4.74–−3.09
−3.09–−1.32
−1.32–1.19
1.19–9.2
Congo Basin Outline

Figure 5.6 Percent change of average annual Congo River Basin discharge (%) for RCP 4.5 for three future periods (2011–2040); (2041–2070); (2071–2100)

Figure 5.7 shows the average annual discharge (cms) in the Basin for RCP 8.5 for three future periods (2011–2040); (2041–2070); (2071–2100). Similar to Figure 5.5, these projections do not show any extreme variations between periods; however, there is a fluctuation in average annual discharge where average flow in period 2 decreases from period 1, and then there is a significant increase in period 3 above that of the first period. The maximum discharge located at the outlet of the basin, for period 1, period 2, and period 3 are 65,337, 65,259, and 67,870 cms, respectively. When looking at the mean value of discharge in all three periods, a decrease in average annual flow since the reference period (4713 cms) can be observed. Similar to the projections using RCP4.5, RCP8.5 predicts throughout all periods that the highest discharge value is located near the outlet. The southern part of the basin is the largest section in the basin with the least amount of discharge, and minimal discharge can be observed in the extremities of the entire basin, except for near the outlet.

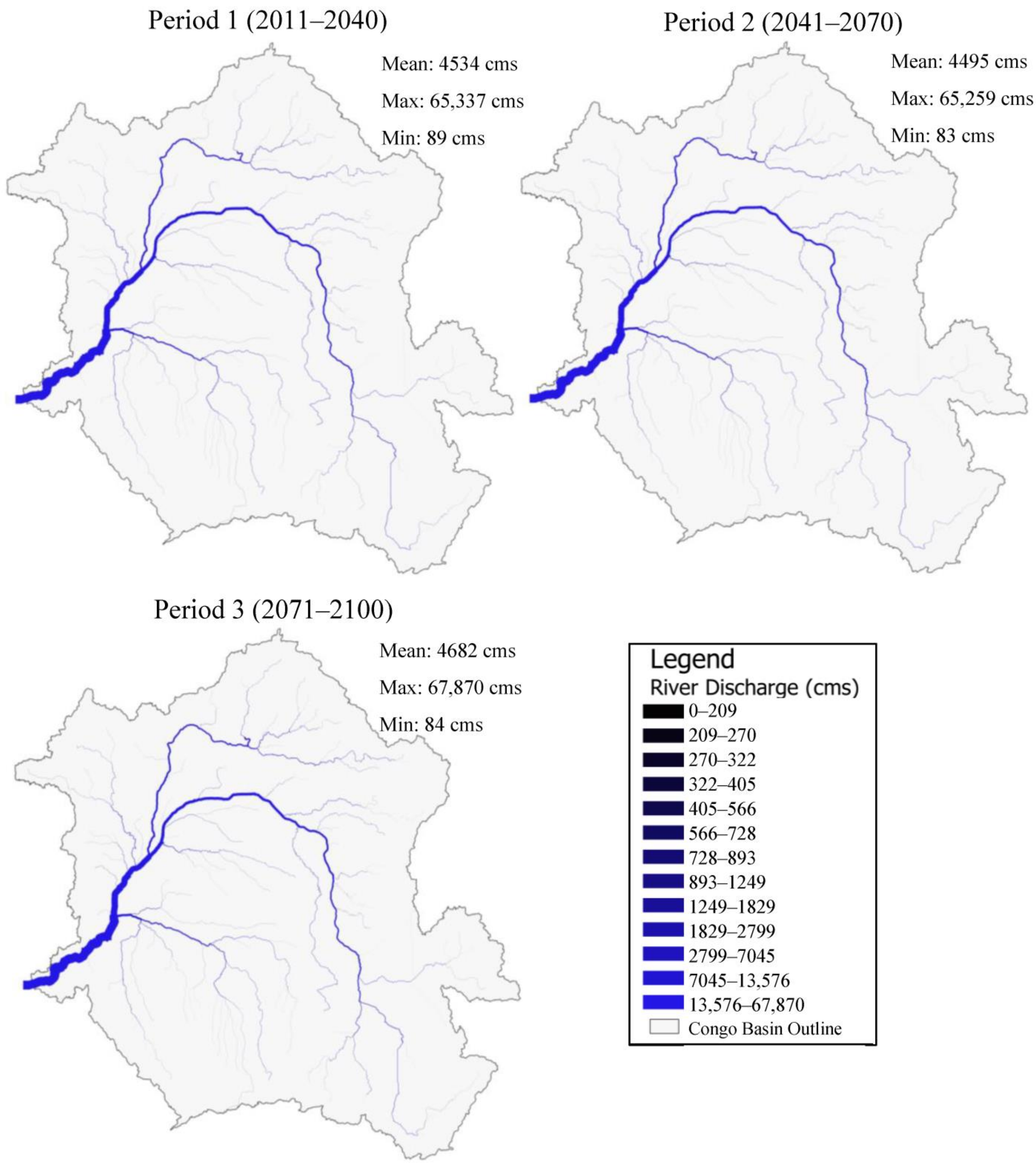
Period 1 (2011–2040)
Mean: 4534 cms
Max: 65,337 cms
Min: 89 cms
Period 2 (2041–2070)
Mean: 4495 cms
Max: 65,259 cms
Min: 83 cms
Period 3 (2071–2100)
Mean: 4682 cms
Max: 67,870 cms
Min: 84 cms
Legend
River Discharge (cms)
0–209
209–270
270–322
322–405
405–566
566–728
728–893
893–1249
1249–1829
1829–2799
2799–7045
7045–13,576
13,576–67,870
Congo Basin Outline

Figure 5.7. Average annual Congo River Basin discharge (cms) for RCP 8.5 for three future periods (2011–2040); (2041–2070); (2071–2100).

Figure 5.8 shows the percent change in average annual discharge for RCP 8.5 for three future periods (2011–2040); (2041–2070); (2071–2100). The average percent change of discharge fluctuates between periods. The change increases in the second period then descends nearly to zero in the final period. The average percent change of discharge for period 1, period 2, and period 3 are −3.1%, −3.9%, and 0.25%, respectively. The decrease in discharge can be observed, especially in the middle and the southwest areas of the watershed, while the northwestern section shows a significant increase. There is also a stream in the southeast that shows a maximum increase of flow. The maximum and minimum changes occur in period 3 with values of 55.5% and −42.5%, respectfully. The observed pattern of changes in discharge reflects the basin's geographical diversity and the complexities of climate variability and change. In figure 5.8 we notice that the southeast region of the basin will be experiencing increased discharge, while the rest of the southern portion of the basin will experience increase drought, this difference may be attributed to factors such as enhanced precipitation, changes in land use and runoff dynamics from higher elevations, or shifts in hydrological processes. Climate change impacts, including changes in temperature and precipitation patterns, further contribute to the spatial variability in river discharge across the basin.

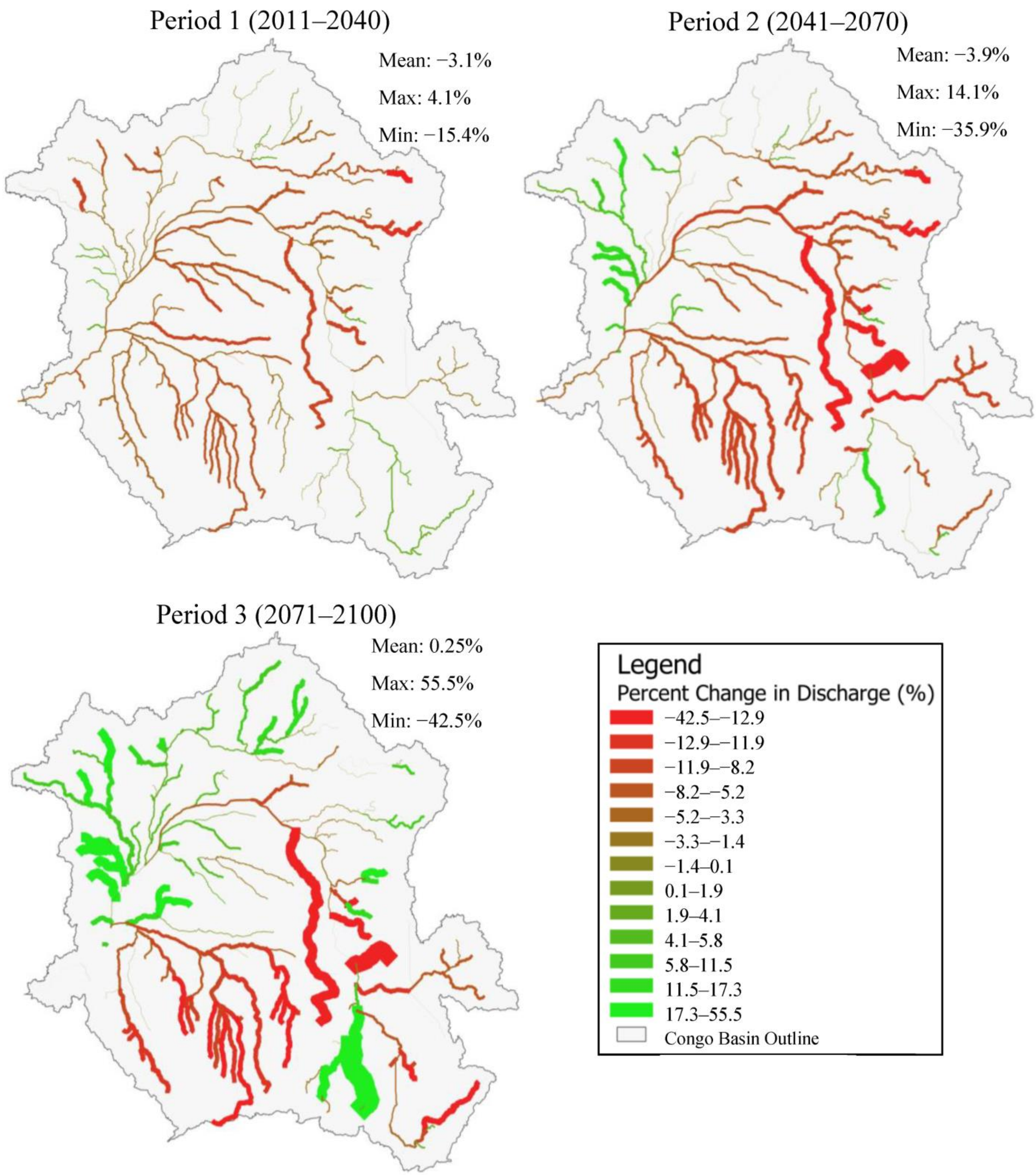
Period 1 (2011–2040)
Mean: −3.1%
Max: 4.1%
Min: −15.4%
Period 2 (2041–2070)
Mean: −3.9%
Max: 14.1%
Min: −35.9%
Period 3 (2071–2100)
Mean: 0.25%
Max: 55.5%
Min: −42.5%
Legend
Percent Change in Discharge (%)
−42.5–−12.9
−12.9–−11.9
−11.9–−8.2
−8.2–−5.2
−5.2–−3.3
−3.3–−1.4
−1.4–0.1
0.1–1.9
1.9–4.1
4.1–5.8
5.8–11.5
11.5–17.3
17.3–55.5
Congo Basin Outline

Figure 5.8 Percent Change of average annual Congo River Basin discharge (%) for RCP 8.5 for three future periods (2011–2040); (2041–2070); (2071–2100).

5.4. Discussion

5.4.1. Correlation with Climatological and Hydrological Studies

The results from this paper are consistent with a previous study by the authors where the future projections of climate extremes for the Congo River Basin were analyzed. Karam et al. (2022) projected several climate indices, including yearly precipitation (PCPTOT), the number of days in a year where precipitation was above 20 mm (PCP20), the Standardized Precipitation Index (SPI), as well as the Standardized Precipitation-Evaporation Index (SPEI), over the entire Congo basin (Karam et al., 2022). In their paper, the authors evaluated the results of 11 regional climate models that utilized RCP4.5 and RCP8.5. The authors also examined the abovementioned climate indices for similar future periods and observed an increase in PCPTOT and PCP20 in the western and northern areas of the basin. The SPEI index demonstrated that there will be an increase in drought in most of the watershed area, and the authors suggested that this is due to the increase in evapotranspiration, which will outweigh the rise in precipitation due to a consistent annual increase of temperatures. Figure 5.9 below is an adaptation of the spatial variation of multi-model average SPEI results published by Karam et al. (2022) showing that evaporation will offset the increase of PCPTOT in future periods under RCP4.5 and RCP8.5. The spatial average of SPEI in both RCP scenarios are exponentially decreasing over the basin area; in RCP4.5, for periods 1, 2, and 3, the SPEI average is 0.12, 0.07, and −0.24, respectively, and in RCP8.5, for periods 1, 2, and 3, the SPEI average is −0.21, −0.51, and −0.62, respectively.

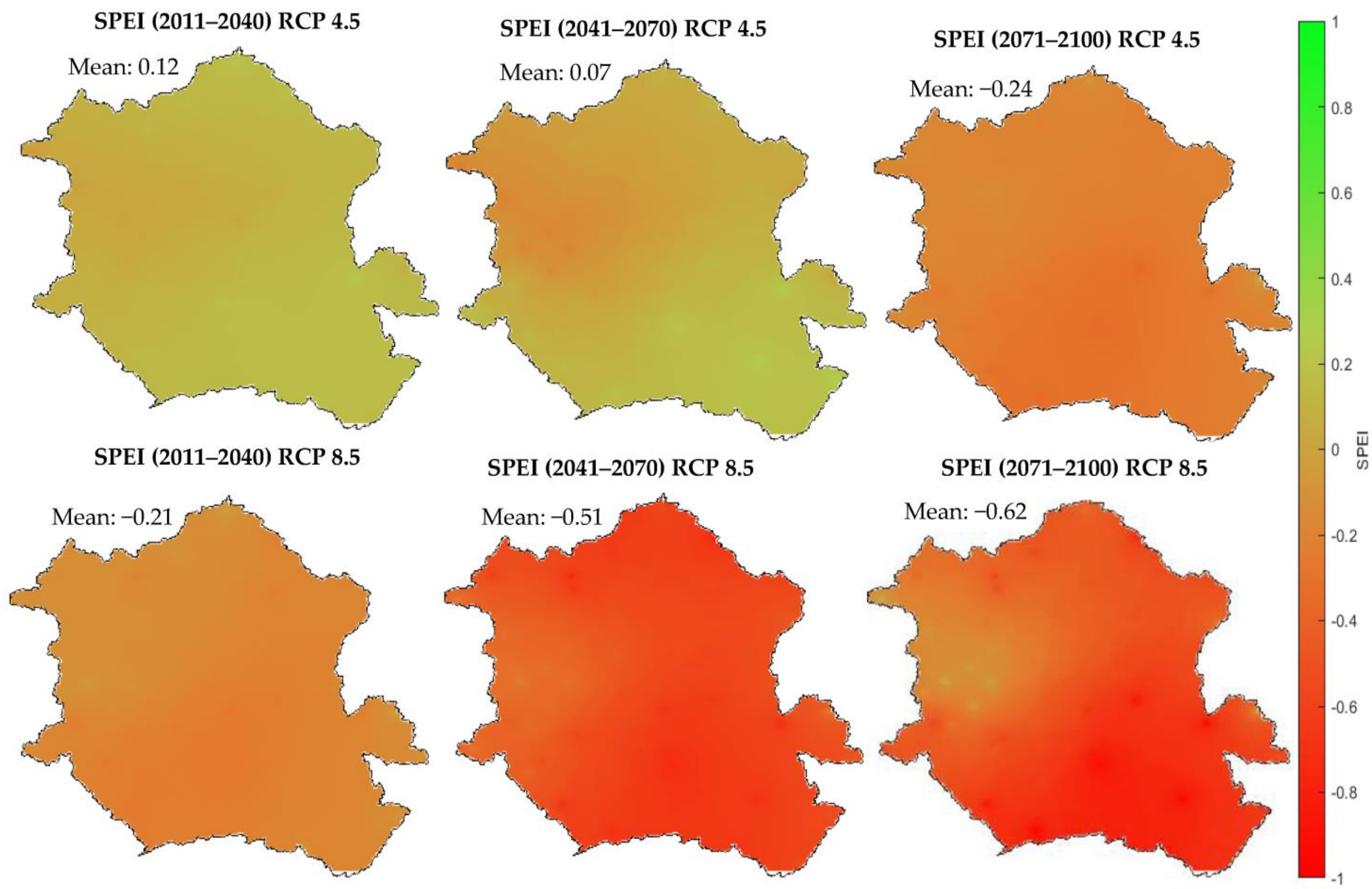

Figure 5.9. Spatial variation of multi-model average SPEI for three future periods (2011–2040); (2041–2070); (2071–2100)

The results from the climatic study conducted by Karam et al. (2022) correlate well with the results obtained from the hydrological study conducted in this paper. The rise in temperatures and higher drought regimes may lead to an overall decrease in discharge in the middle and southern regions of the study area. Yet, high-intensity rainfalls and increased annual precipitation may lead to increased discharge, especially in the northern and western extremities of the basin. This investigation illustrates a basin that is expected to experience an escalation in both drought and flood occurrences in the near and late future.

Moreover, a hydrological study of the Congo basin conducted by Tshimanga et al. (2012) downscaled GCM data to assess the impacts of climate change on the hydrology of the basin. The authors found that changes in river discharge would vary spatially and estimated a decrease in runoff for near-future projections. Major changes in the basin relate to increase in evapotranspiration due to higher air temperature. The results correlate well with the findings of this study, which emphasize the urgent need for effective adaptation strategies to mitigate the impacts of climate change on the hydrology of the Congo basin.

Aloysius and Saiers (2017) found that precipitation is likely to become more variable, and discharge is likely to increase in the short term (between 2016 and 2035) and vary considerably in the long term (between 2046 and 2065). Compatible with the findings of this study, Aloysius and Saiers (2017) produced valuable insight demonstrating that changes in river discharge could have significant impacts on the water resources, ecosystems, and livelihoods of the region.

In the case where decision-makers have to use this information, it is important that the spatiotemporal variability of the impacts is considered appropriately for adaption planning and resilience building. For example, in sub-regions of the basin where projections point to an increase in drying conditions or droughts, priority and emphasis should be given to water storage approaches, incentives for water conservation practices for famers, and the promotion of water efficiency focused irrigation or water use methods. It is also important that water security and food security institutions and policies take note of these projects at the sub-national level and design interventions and ‘fit to purpose’ solutions for the local context.

5.4.2. Potential Impacts of Projected Changes

The hydrological regime of the Congo basin influences the lives of 75 million habitants. Yet, insufficient observational data has contributed to the basin being inadequately studied (Creese et al., 2019). An overall decrease in average annual discharge and increased fluctuating peak discharge are expected to have significant socio–economic impacts on the Congo River Basin. Here are some potential socio-economic changes that could occur:

Impact on Agriculture: The Congo River Basin supports a significant portion of agriculture in the region. Changes in hydrological patterns such as the predicted alterations in precipitation, flooding, and droughts, could disrupt agricultural activities. Floods could damage crops and infrastructure, while droughts could lead to water shortages for irrigation. This could result in reduced agricultural productivity, affecting food security and livelihoods of farmers.

Water Resource Management: The Congo River and its tributaries are vital water sources for drinking, irrigation, transportation, and industrial use. Changes in hydrological patterns could lead to shifts in water availability and quality. Competing demands for water resources among various sectors could intensify, leading to conflicts over access and allocation. Effective water resource management strategies would become increasingly important to mitigate these conflicts and ensure sustainable use of water resources.

Impact on Fisheries: The CRB is home to diverse aquatic ecosystems supporting valuable fisheries. Changes in hydrological patterns could alter water temperatures, flow regimes, and habitats, affecting fish populations and migration patterns. This could have significant implications for local communities dependent on fishing for food and income. Adaptation measures such as diversification of livelihoods or introduction of alternative fishing techniques may be necessary to cope with these changes.

Infrastructure Vulnerability: Infrastructure such as dams, roads, bridges, and buildings may be vulnerable to the impacts of changes in hydrological patterns, including increased flooding and erosion. This could disrupt transportation networks, hinder access to essential services, and increase maintenance costs for infrastructure. Investments in resilient infrastructure and disaster preparedness measures would be crucial to minimize these impacts and ensure continued socio-economic development.

Health Risks: Changes in hydrological patterns could influence the prevalence and distribution of water-related diseases such as malaria and waterborne illnesses. Increased flooding could lead to stagnant water pools, providing breeding grounds for disease. Also, droughts could lead to water scarcity, compromising hygiene and sanitation practices. Efforts to strengthen public health infrastructure, improve access to clean water and sanitation, and enhance disease surveillance systems would be essential to mitigate health risks.

Impact on Biodiversity: The CRB holds a rich biodiversity, including numerous plant and animal species found nowhere else on Earth. Changes in hydrological patterns could disrupt ecosystems and threaten biodiversity through habitat loss, fragmentation, and altered ecological dynamics. Conservation efforts, including protected area management, habitat restoration, and sustainable land use practices, would be crucial to safeguard the region's biodiversity and the ecosystem services it provides.

The socio–economic impacts of climate change are likely to be significant and far-reaching, and it will be important for communities and governments to work together to adapt to and mitigate these impacts.

5.5. Conclusions

The future hydrological conditions of the Congo basin were evaluated for three time periods (2011–2041, 2041–2070, and 2071–2100). A SWAT model was calibrated and validated and used to assess the impacts of climate change on water quantity. The model was run using daily rainfall observations combined with daily data on precipitation, temperatures, relative humidity, solar radiation, and wind speed from the WFDEI dataset. Future climate data was obtained by statistically downscaling the output of ten Regional Climate Models under RCP4.5 and RCP8.5.

To summarize, the projections suggest four key highlights: first, the rise in temperatures can lead to high incidents of drought regimes in the basin and an overall decrease in discharge in the center and southwestern parts of the basin; second, the high-intensity rainfalls and increase in annual precipitation may lead to increased discharge, especially in the northern and northwestern extremities of the basin; third, the maximum and minimum changes occur in period 3 under RCP 8.5, with values of 55.5% and −42.5%, respectfully, indicating that the high emissions scenario displays the most significant discharge variations throughout the basin in the next few decades; and lastly, the projections do not show any extreme variations between periods—however a slight decrease in average annual discharge is observed. The average discharge under RCP4.5 for period 1, period 2, and period 3 are 4597, 4417, and 4423 cms, respectively. The average discharge under RCP8.5 for period 1, period 2, and period 3 are 4534, 4495, and 4682 cms, respectively. Overall, this study portrays a basin that will experience increased drought and food scarcity in the future. This information can be used to inform the development of adaptation strategies to improve food and disaster management, create vulnerability maps, establish food monitoring systems in the wake of drying conditions, establish early warning systems, build resilient infrastructure, and address other socio–economic impacts to transition from a vulnerable to a resilient future.

5.6 References

Tshimanga, Raphael M., et al. "Towards a framework of catchment classification for hydrologic predictions and water resources management in the ungauged basin of the Congo River: An a priori approach." Congo Basin Hydrology, Climate, and Biogeochemistry: A Foundation for the Future (2022): 469-498.

Malhi, Yadvinder, and James Wright. "Spatial patterns and recent trends in the climate of tropical rainforest regions." Philosophical Transactions of the Royal Society of London. Series B: Biological Sciences 359.1443 (2004): 311-329.

World Bank. World Bank Group Macroeconomic Models for Climate Policy Analysis. World Bank, 2022: Washington, DC, USA.

Lewis, Simon L., et al. "Increasing carbon storage in intact African tropical forests." Nature 457.7232 (2009): 1003-1006.5.

Malhi, Y.; Adu-Bredu, S.; Asare, R.A.; Lewis, S.L.; Mayaux, P. African rainforests: Past, present and future. Philos. Trans. R. Soc. B Biol. Sci. 2013, 368, 20120312. [CrossRef]

Creese, Amy, R. Washington, and R. Jones. "Climate change in the Congo Basin: processes related to wetting in the December–February dry season." Climate Dynamics 53 (2019): 3583-3602.

Tshimanga, Raphael M., and Denis A. Hughes. "Basin-scale performance of a semidistributed rainfall-runoff model for hydrological predictions and water resources assessment of large rivers: The Congo River." Water Resources Research 50.2 (2014): 1174-1188.

EM-DAT; CRED. The Emergency Events Database. Available online: www.emdat.be (accessed on 4 August 2021).

Sridhar, Venkataramana, et al. "Water Budgets and Droughts under Current and Future Conditions in the Congo River Basin." Congo Basin Hydrology, Climate, and Biogeochemistry: A Foundation for the Future (2021).

Dos Santos, V., et al. "Evaluating the performance of multiple satellite-based precipitation products in the Congo River Basin using the SWAT model." Journal of Hydrology: Regional Studies 42 (2022): 101168.

Kitambo, Benjamin, et al. "Large-scale spatio-temporal variability of the Congo Basin surface hydrologic components from space." EGU General Assembly Conference Abstracts. 2022.

Čerkasova, Natalja, Georg Umgiesser, and Ali Ertürk. "Development of a hydrology and water quality model for a large transboundary river watershed to investigate the impacts of climate change–A SWAT application." Ecological Engineering 124 (2018): 99-115.

Park, Jong-Yoom, et al. "Assessing climate change impact on hydrological components of Yongdam dam watershed using RCP emission scenarios and SWAT model." Journal of the Korean Society of Agricultural Engineers 56.3 (2014): 19-29.

Anjum, Muhammad Naveed, Yongjian Ding, and Donghui Shangguan. "Simulation of the projected climate change impacts on the river flow regimes under CMIP5 RCP scenarios in the westerlies dominated belt, northern Pakistan." Atmospheric Research 227 (2019): 233-248.

Weedon, G.P. et al. "The WFDEI Meteorological Forcing Data. Research Data Archive at the National Center for Atmospheric Research, Computational and Information Systems Laboratory". 2018. Available online: https://rda.ucar.edu/datasets/ds314.2/ (accessed on 31 February 2022).

Le Page, Michel, et al. "Comparison of meteorological forcing (WFDEI, AGRI4CAST) to in-situ observations in a semi arid catchment. The case of Merguellil in Tunisia." EGU General Assembly Conference Abstracts. 2015.

Giorgi, Filippo, and William J. Gutowski Jr. "Regional dynamical downscaling and the CORDEX initiative." Annual review of environment and resources 40 (2015): 467-490.

Hakala, Kirsti, Nans Addor, and Jan Seibert. "Hydrological modeling to evaluate climate model simulations and their bias correction." Journal of Hydrometeorology 19.8 (2018): 1321-1337.

Karam, Sara, et al. "Assessing the impacts of climate change on climatic extremes in the Congo River Basin." Climatic Change 170.3-4 (2022): 40.

Arnold, Jeffrey G., et al. "Large area hydrologic modeling and assessment part I: model development 1." JAWRA Journal of the American Water Resources Association 34.1 (1998): 73-89.

Pan, YongHao, et al. "River direction prediction of Shuangliu District Fu River based on ArcSWAT model." Journal of Physics: Conference Series. Vol. 2277. No. 1. IOP Publishing, 2022.

Arnold, Jeffrey G., et al. "SWAT: Model use, calibration, and validation." Transactions of the ASABE 55.4 (2012): 1491-1508.

Neitsch, Susan L., et al. Soil and water assessment tool theoretical documentation version 2009. Texas Water Resources Institute, 2011.

Nash, J. Eamonn, and Jonh V. Sutcliffe. "River flow forecasting through conceptual models part I—A discussion of principles." Journal of hydrology 10.3 (1970): 282-290.

Gupta, Hoshin Vijai, Soroosh Sorooshian, and Patrice Ogou Yapo. "Status of automatic calibration for hydrologic models: Comparison with multilevel expert calibration." Journal of hydrologic engineering 4.2 (1999): 135-143.

Moriasi, Daniel N., et al. "Model evaluation guidelines for systematic quantification of accuracy in watershed simulations." Transactions of the ASABE 50.3 (2007): 885-900.

Abbaspour, Karim C. "User manual for SWAT-CUP, SWAT calibration and uncertainty analysis programs." Swiss Federal Institute of Aquatic Science and Technology, Eawag, Duebendorf, Switzerland 93 (2007).

Verhagen, Arianne P., Raymond WJG Ostelo, and Arno Rademaker. "Is the p value really so significant?" Australian Journal of Physiotherapy 50.4 (2004): 261-262.

Zango, Baba-Serges, et al. "Impacts of urbanization and climate change on water quantity and quality in the Carp River watershed." Journal of Water and Climate Change 13.2 (2022): 786-816.

Abbaspour, Karim C., et al. "A continental-scale hydrology and water quality model for Europe: Calibration and uncertainty of a high-resolution large-scale SWAT model." Journal of hydrology 524 (2015): 733-752.

El-Khoury, Antoun, et al. "Combined impacts of future climate and land use changes on discharge, nitrogen and phosphorus loads for a Canadian river basin." Journal of environmental management 151 (2015): 76-86.

Khoi, Dao Nguyen, and Vu Thi Thom. "Parameter uncertainty analysis for simulating streamflow in a river catchment of Vietnam." Global ecology and conservation 4 (2015): 538-548.

Sharma, Vimal Chandra, and Satish Kumar Regonda. "Multi-spatial resolution rainfall-runoff modelling—A case study of Sabari river basin, India." Water 13.9 (2021): 1224.

Tshimanga, R. M., and D. A. Hughes. "Climate change and impacts on the hydrology of the Congo Basin: The case of the northern sub-basins of the Oubangui and Sangha Rivers." Physics and Chemistry of the Earth, Parts A/B/C 50 (2012): 72-83.

Aloysius, Noel, and James Saiers. "Simulated hydrologic response to projected changes in precipitation and temperature in the Congo River basin." Hydrology and Earth System Sciences 21.8 (2017): 4115-4130.

Chapter 6

An efficient method to generate flood maps using Sentinal-1 SAR imagery and SWAT modelling: a case study of the upper Congo River sub-basin

Abstract

Surface water resources play a pivotal role in a multitude of human activities, ranging from providing water for cities, supporting fishing and navigation, facilitating irrigation, to generating hydropower. Additionally, the hydrological patterns of river systems have profound consequences on environmental sustainability, water-related hazards, human well-being, and a wide array of ecosystem services. With the anticipation of global warming affecting surface water availability, quality, and distribution, it has become imperative to analyze water utilization efficiency and the prevalence of water-related risks. Hence, it is crucial for communities to devise strategies and adapt to the potential consequences of climate change. This is particularly pressing in the Congo River Basin, home to 75 million people, where recurring floods and droughts are projected to worsen due to climate change impacts. This study presents an innovative approach to mapping floods in the Oubangui River section of the Congo Basin. It combines Sentinel-1 Synthetic Aperture Radar (SAR) imagery with a meticulously calibrated and validated Soil and Water Assessment Tool (SWAT) model. The methodology involves extracting surface water data from SAR images and establishing a relationship between pixels and water discharge values. This information enables the creation of a spatial pixel probability distribution, facilitating accurate mapping of flooded and dry areas. The results underscore the efficiency and accuracy of this approach, with an 85.9% accuracy in predicting water pixels and a 97.9% accuracy in predicting land pixels. The approach significantly enhances the region's ability to respond effectively to flood events, offering valuable insights for flood mapping and disaster management in this ecologically important and vulnerable area.

Keywords Congo River Basin · Oubangui River section · Sentinel-1 · Synthetic Aperture Radar (SAR) · flood mapping · SWAT · pixel-discharge relationship.

6.1 Introduction

The Congo Basin, located in central Africa, is one of the world's most significant and ecologically diverse regions. Encompassing approximately 3.7 million square kilometers, it is the second-largest tropical rainforest in the world after the Amazon (Tshimanga et al., 2020). This immense, lush, dense forest is home to an extraordinary array of biodiversity, including countless plant and animal species, many of which are found nowhere else on Earth (Paris et al., 2022). It plays a pivotal role in regulating regional and global climate patterns and contributes to maintaining the planet's ecological balance.

In the northern part of the Congo Basin, particularly in the Central African Republic and the Democratic Republic of Congo (DRC), the region is subject to significant climate and hydrological variability (Tshimanga et al., 2022; Karam et al., 2022). This variability is characterized by fluctuating rainfall patterns, prolonged droughts, and irregular flooding events, all of which have profound implications for the local ecosystems and the millions of people who rely on the basin for their livelihoods. The hydrological cycle in this region is closely linked to the Congo River and its tributaries, which play a crucial role in maintaining the balance of water resources. Notably, the

Oubangui River, a major tributary of the Congo River, is of immense importance to the northern part of the basin. Its flow not only sustains the diverse ecosystems and supports the livelihoods of local communities but also serves as a critical transportation route, facilitating trade and connectivity within the region. The challenges posed by climate and hydrological variability in the northern Congo Basin highlight the urgent need for sustainable efforts and adaptive strategies to protect this vital natural resource.

The principal objectives of this study is the development of an a computationally efficient flood mapping methodology. This method entails the integration of discharge data derived from a meticulously calibrated and validated SWAT (Soil and Water Assessment Tool) model with the utilization of Sentinel-1 Synthetic Aperture Radar (SAR) imagery. The primary goal of this innovative approach is to optimize and expedite the flood mapping process when compared to conventional software like HEC-RAS and similar tools, which often demand significant time and resources. By harnessing the combined capabilities of SWAT modeling and Sentinel-1's radar data, this study aims to provide a cost-efficient and prompt solution for flood mapping. Ultimately, the objective is to enhance preparedness and response mechanisms for flood events, evaluate areas prone to flooding, and elevate the overall effectiveness of flood risk management strategies. This approach promises to achieve these goals in a more efficient and accessible manner, thereby advancing flood-related decision-making processes.

Several studies have conducted flood mapping using Sentinel-1 SAR images or hydrodynamic modeling. While hydrodynamic modeling is a powerful tool, it is often computationally intensive due to the complex and dynamic nature of fluid flow (Lennon et al., 2023). Traditional methods, such as Finite Difference or Finite Element methods, require significant computational resources and time to simulate the intricate details of water behavior accurately. As a result, there is a growing need for more efficient and innovative approaches to address these computational challenges.

Dasallas et al., (2019) developed a HEC-RAS flood model by combining 1D modeling for channel flows and 2D modeling for overbank flows to simulate river overflow inundation. The verification was done by applying the simulation to the 2011 Baeksan river levee breach event in South Korea.

De Paiva et al., (2013) employ the MGB-IPH model to hydrologically and hydrodynamically model the Amazon River basin. Validation was conducted using remotely sensed observations. The MGB-IPH is a physically based model resolving all land hydrological processes and includes a 1-D river hydrodynamic module with a simple floodplain storage model.

Kitambo et al., (2022) studied the hydroclimatic characteristics of the Congo basin, by analyzing surface water height and extent data from satellite and in situ observations. The findings reveal significant annual amplitude variations in water levels in different subbasins, and contribute to understanding the timing of annual flood dynamics.

Fatras et al., (2021) studied the hydrological dynamics of the Congo River Basin using satellite data from 2010 to 2017. The study found that the mean flooded area for the entire CRB is approximately 89,408 km^2, equivalent to 2.39% of the basin. The analysis also provided insights into the timing of floods.

Tripathy & Malladi (2022) introduced the Global Flood Mapper (GFM), a user-friendly web application that quickly generates flood maps from Sentinel-1 satellite data, simplifying the process for non-technical users. The GFM improves existing flood mapping methods by mapping flood peaks and reducing false positives in hilly terrain. The accuracy of GFM-generated flood maps is demonstrated by comparing them with Sentinel-2 MSI-derived maps and field photographs.

Vekaria et al., (2023) employed an automated approach using Sentinel-1 SAR data and Google Earth Engine to assess monsoonal flood events along the Brahmaputra River from 2015 to 2020. Analyzing 144 SAR images identified varying flood extents, with the most extensive inundation occurring in 2015 and 2016 (around 6 lakh hectares) and another peak in 2019 and 2020. The accuracy of flood mapping, assessed through binarization thresholding and removal of water bodies and shadows, yielded impressive results of 93.6% and 95.15% for the pre-flood events of 2019 and 2020, respectively. The study also linked flood trends with precipitation data and conducted damage assessment, emphasizing the advantages of this technology-driven approach for rapid flood assessment.

Uddin et al., (2019) conducted a study in Bangladesh to identify flood-damaged areas to enhance flood response efforts. The study utilized Sentinel-1 satellite imagery from various months in 2017 to map flood extents and combined this with pre-flood land cover data from Landsat-8 images. The flood mapping achieved a high accuracy of 96.44%, while the land cover map accuracy was 87.51%. The results showed that flood-affected areas ranged from 2.01% to 7.01% of the total area, with cropland damage varying from 1.51% to 5.30%.

Shahabi et al., (2020) introduced a novel flood susceptibility mapping technique for the Haraz watershed in northern Iran. The approach employs ensemble models, utilizing bagging as a meta-classifier and various base classifiers like K-Nearest Neighbor (KNN) coarse, cosine, cubic, and weighted models, alongside Sentinel-1 sensory data. The results highlight the superiority of the Bagging–Cubic–KNN ensemble model, which reduced overfitting, minimized variance issues, and improved prediction accuracy.

Amitrano et al., (2018) introduced a method for rapid flood mapping using Sentinel-1 SAR data, focusing on ground range detected (GRD) images provided by the European Space Agency. The methodology comprises two processing levels that produce event maps with progressively higher resolution. The first level employs texture measures and amplitude information, eliminating the need for thresholding. The second level involves change detection on the full-resolution GRD product. The approach is user-friendly and emphasizes suitability for end-users in flood mapping applications.

Li et al., (2018) introduced a two-step automated change detection process for rapid flood mapping using Sentinel-1 (SAR) data. It involves selecting a reference image based on a Jensen-Shannon divergence index and applying saliency detection to initialize an expectation-maximization-based generalized Gaussian mixture model (GGMM), which is enhanced by a fully connected conditional random field (FCRF) model to produce accurate flood change maps.

The previous studies outlined above attempted to improve the accuracy and efficiency of flood maps while minimizing technical and computationally complex methods (Li et al., 2018; Amitrano et al., 2018; Shahabi et al., 2020). While some studies mention the accuracy of their flood mapping methods, there is limited validation against ground truth data, which is essential for confirming the reliability of the results. Some studies also introduce complex methodologies for flood mapping, and while these methods can provide high accuracy, they may not be user-friendly or accessible to non-technical users, limiting their practical application. The studies that analyzed flood trends over multiple years assume stationarity in flood patterns, however, with changing climate conditions, this assumption may not hold true, and future flood patterns could differ significantly. This study suggests a new method to create a streamlined and precise flood mapping technique by combining discharge data from a well-calibrated and validated SWAT model with Sentinel-1 SAR data. This approach seeks to accelerate and enhance flood mapping, offering a more efficient alternative to conventional software methods.

6.2 Methodology

The previous studies outlined above attempted to improve the accuracy and efficiency of flood maps while minimizing technical and computationally complex methods (Li et al., 2018; Amitrano et al., 2018; Shahabi et al., 2020). While some studies mention the accuracy of their flood mapping methods, there is limited validation against ground truth data, which is essential for confirming the reliability of the results. Some studies also introduce complex methodologies for flood mapping, and while these methods can provide high accuracy, they may not be user-friendly or accessible to non-technical users, limiting their practical application. The studies that analyzed flood trends over multiple years assume stationarity in flood patterns, however, with changing climate conditions, this assumption may not hold true, and future flood patterns could differ significantly. This study

suggests a new method to create a streamlined and precise flood mapping technique by combining discharge data from a well-calibrated and validated SWAT model with Sentinel-1 SAR data. This approach seeks to accelerate and enhance flood mapping, offering a more efficient alternative to conventional software methods.

6.2.1 Study Area

This case study is focused on the Congo River basin, specifically in the sub-basin that contains the main section of the Oubangui River. This sub-basin was chosen due to its characteristics of high flood variability (Tshimanga et al., 2022). Figure 6.1 shows the entirety of the Congo basin along with its river network and a zoom-in on the sub-basin in question.

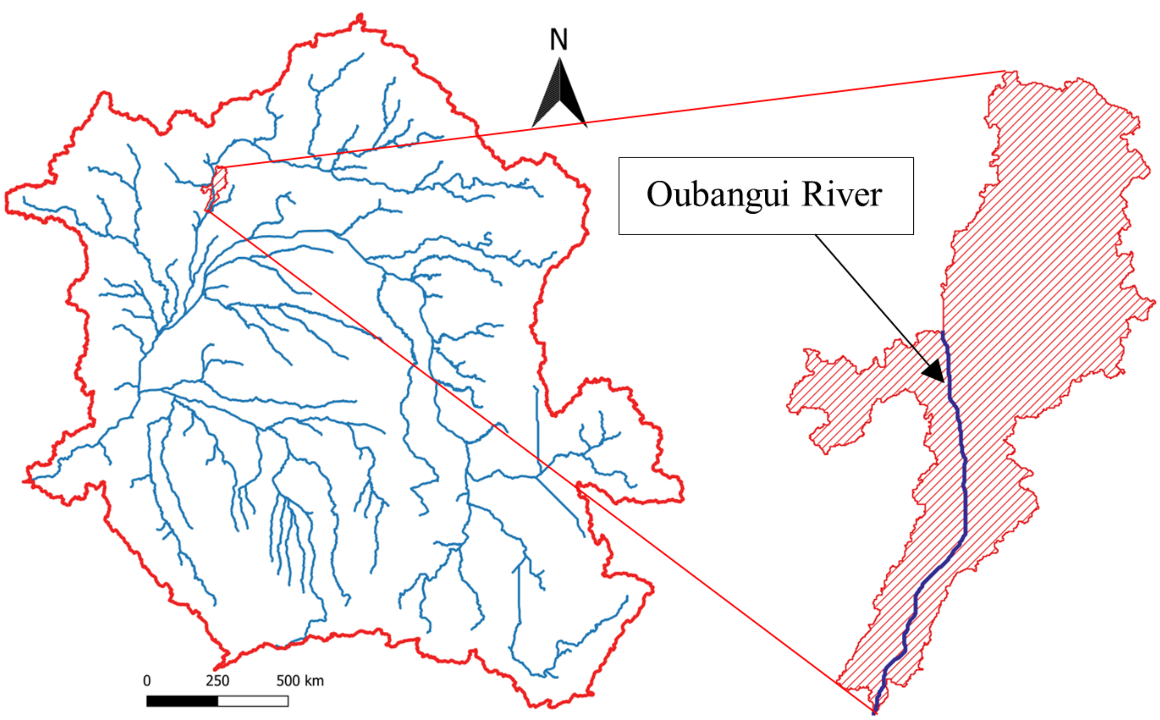

Figure 6.1. Congo River basin outline and river network along with the Oubangui River sub-basin location.

6.2.2 Available data

6.2.2.1 Climate and Hydrological Data

A precipitation time series with daily rainfall observations ranging from 1961 to 2019 was facilitated by the Congo Basin Water Resources Research Center (CRREBaC). Other meteorological data sets, such as daily precipitation and minimum and maximum temperature time series, were acquired for 87 and 128 different locations within the basin, respectively, from the Watch Forced Era Interim (WFDEI) reanalysis data set. Additionally, other essential meteorological parameters such as relative humidity, solar radiation, and wind speed time series were obtained from WFDEI for 82 stations. With this, ten climate change experiments were conducted by the CORDEX-AFRICA group (https://cordex.org/domains/region-5-africa/, accessed on 31 January 2022) (Giorgi & Gutowski, 2015) to project precipitation and temperatures ranging from 1950 to 2100. The experiments conducted utilized ten Global Climate Models (GCMs) to drive the Regional Climate Models (RCMs) under two greenhouse gas emission scenarios, namely Representative Concentration Pathways (RCP)4.5 and RCP8.5. For downscaling, the quantile-quantile (Q-Q) transformation was used, and a statistical distribution was generated for a climate parameter that closely matches the observed climate parameter in the historical period, enabling the projection of fine-scale climate information from the coarse-scale model outputs (Sarr et al., 2015; Cannon et al., 2015). The Q-Q downscaling was chosen due to its capabilities of outperforming other methods, according to Hakala et al. (2018). The detailed procedure conducted in this paper for bias correction, as well as the institutions and driving GCM/RCM combinations that were utilized are described by Karam et al. (2022).

A Soil and Water Assessment Tool (SWAT) model was developed, calibrated, and validated for the entirety of the Congo River Basin study area (Figure 6.1), by Karam et al. (2023). The model demonstrates good performance for the discharge at the watershed outlet and projections for average annual river discharge in the Congo basin for the reference period of 1976 to 2005 and three future periods of 2011-2040, 2041-2070, and 2071-2100, under RCP4.5 and RCP8.5 scenarios, were successfully attained. The river discharge simulation data achieved by Karam et al. (2023) were utilized in this study to create a pixel-discharge relationship to assess the accuracy of surface water extraction of fully processed sentinel-1 images of the Oubangui River located in sub-watershed #43 of the Congo River Basin (Figure 6.1), and to re-create surface water images based on pixel quantity and reverse mapping.

6.2.2.2 Sentinal-1 Imagery

Sentinel-1 images of the region surrounding the Oubangui River were downloaded from the Alaska Satellite Facility (ASF) Data Search Vertex (https://www.earthdata.nasa.gov/, accessed on March 31st, 2023). Figure 6.2 shows an example of a raw, unprocessed sentinel image that was downloaded for this case study. The ASF provides access to a collection of Sentinel-1 data, which can be valuable for various remote sensing applications. The downloading process involves defining the search parameters to narrow down the dataset of interest. In this case, filters were applied for surface water extraction to specify the satellite, imaging mode, processing level, polarization, acquisition times, orbit number, footprint, and processing details. The Sentinel-1 image information can be decoded from its code S1A_IW_GRDH_1SDV_20160124T043248_20160124T043303_009631_00E080_ 4C8A.

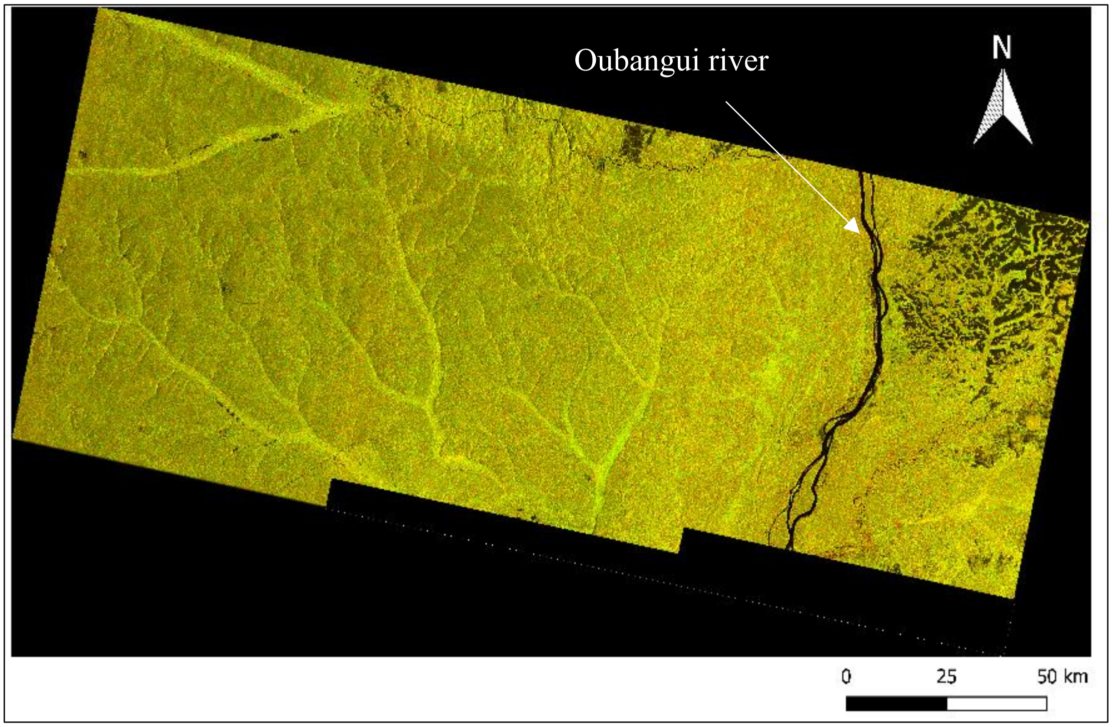

Figure 6.2 Raw unprocessed sentinel-1 image of a section of the Oubangui River downloaded from the Alaska Satellite Facility (ASF) Data Search Vertex (https://www.earthdata.nasa.gov/, accessed on March 31st, 2023) with the identification code S1A_IW_GRDH_1SDV_20160124T043248_20160124T043303_009631_00E080_4C8A

6.2.3 Methodology Flowchart

The following figure 6.3 illustrates the methodology flowchart. It displays the steps taken to fulfill the objectives and determines whether this new method of developing flood maps by combining SWAT outputs and sentinel-1 imagery is accurate and reliable. The steps involve downloading the sentinel-1 images for the study area and processing them in a way relevant to surface water extraction. Then, a histogram analysis and threshold determination are done to create a binary pixel image of the study area, where each pixel represents either water or land. The SWAT simulation discharge output is then used to develop a pixel-discharge relationship for which a particular discharge value can yield the corresponding water pixel number value. This is combined into a spatial pixel probability distribution which is used to remap the flooded or dry area. The accuracy of this method is then determined for analysis and discussion.

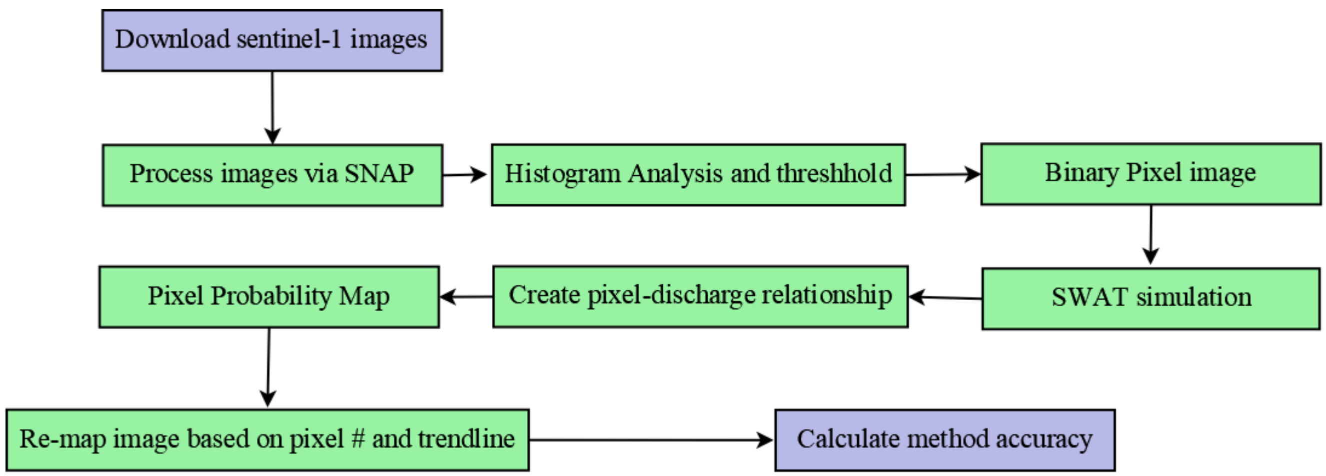

Figure 6.3 Methodology flowchart

6.2.4 Sentinal-1 Image Processing and Histogram Analysis

Floods show three distribution patterns within the Congo basin based on location (northwest, southeast, and west/east), with single peaks in the north and south but dual peaks along the Equator (Tshimanga et al., 2022). The output from the calibrated SWAT model was used to determine the approximate dates of the yearly extreme flood and drought occurrences between 2015 and 2022. In the Oubangui region, flooding incidents were prevalent in August, September, and October, while drought events were prominent in January and February. Therefore, two sentinel images were downloaded for each year between 2015-2022 on high and low peak discharge dates. Only the images with matching pixel numbers, coordinates, and sizes were utilized for this study to avoid inconsistency.

In order to process the downloaded sentinel-1 images for the purpose of surface water extraction and flood mapping, the Sentinel Application Platform (SNAP) software was utilized. It is a comprehensive tool developed by the European Space Agency (ESA). It provides a range of tools and functionalities used to analyze, visualize, and manipulate satellite remote-sensing data. Figure 6.4 shows a graphical depiction of how the images were processed. This graph was based on processing suggestions and comparisons made by several authors (Mancini et al., 2021; Amitrano et al., 2018; Li et al., 2018; Vekaria et al., 2022; Hu et al., 2020). Calibration was used to refine the satellite sensor data by accounting for inherent sensor biases, radiometric distortions, and atmospheric interferences. This resulted in improved accuracy and reliability for subsequent analysis and interpretation of the image in question. Terrain Correction is a module used to correct terrain effects, especially in areas with significant topography; this step is essential for accurate flood mapping. Image Subset was used to subset the image to the specific area of interest, and speckle filtering was used to reduce the noise inherent in radar images, which can be done using filters like Lee, Gamma-MAP, or Enhanced Lee. The "Change Detection" module was used to identify areas that have undergone significant changes between two or more radar acquisitions. Flooded areas often exhibit changes in backscatter intensity. The ellipsoid correction was used to compensate for the curvature of the Earth's surface by adjusting the satellite image to match a theoretical ellipsoid model, thus ensuring accurate geometric representation and measurements in the remote sensing data.

The image was finally converted to a Tagged Image File Format (TIFF), which transforms the satellite data from its original format into the widely used image file format that preserves the data's georeferencing and metadata, facilitating compatibility with various software and enables further analysis and visualization of the remote sensing data.

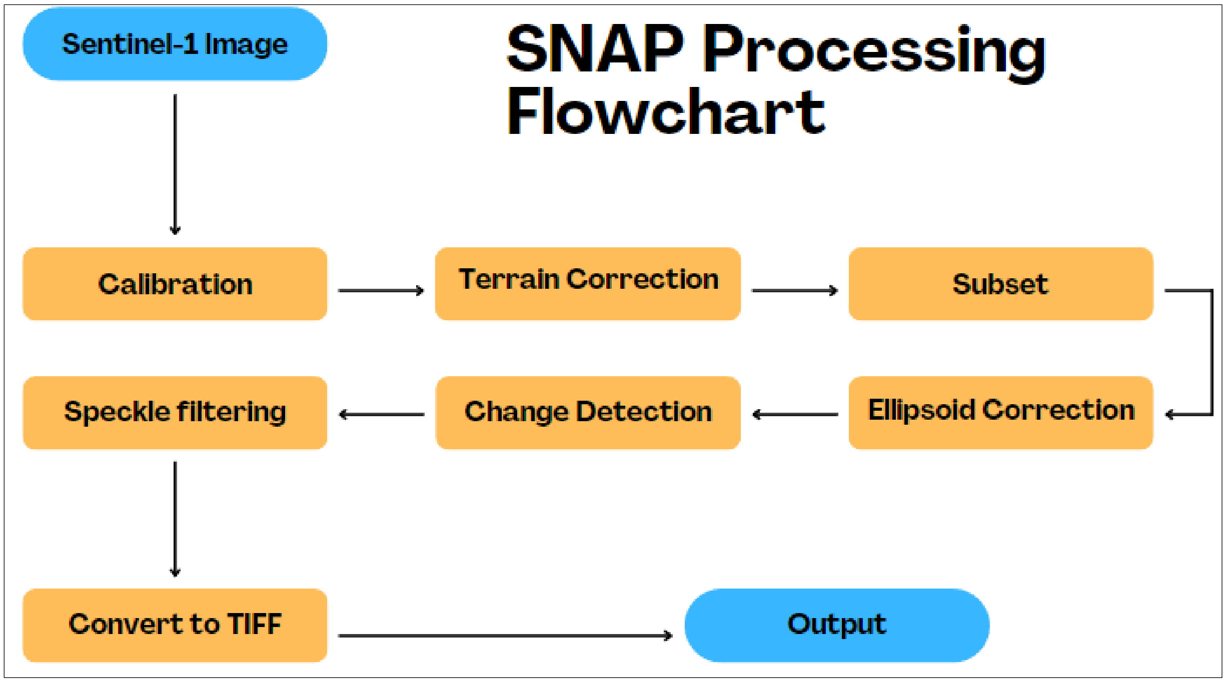

Figure 6.4. Graphical depiction of the Sentinel Application Platform (SNAP) software process used on downloaded sentinel-1 images of the Oubangui River

Histogram analysis is a technique used for exploring and understanding the distribution of pixel intensities in a Sentinel-1 SAR image (Yang et al., 2022). The histogram of each satellite image was generated and displayed in SNAP, and was analyzed by examining the shape of the distribution, the location of the peaks and valleys, and the range of intensities covered by the image. The main clusters or modes in the histogram were identified, corresponding to different land cover types or land use in the image. For example, water, urban areas, and vegetation may have distinct intensity distributions that appear as separate peaks in the histogram (Mustafa et al., 2018). The histogram of each image was compared with optical imagery to validate the interpretation of the histogram and identify potential errors or discrepancies. Once validated, the images were acceptable for analysis with regards to developing a threshold, for land and water classification.

6.2.5 Otus's Method

The histogram of the input image is utilized for its frequency distribution of the pixel intensities. The histogram is normalized by dividing each bin by the total number of pixels in the image, so that the histogram values sum up to 1. The cumulative sums of the normalized histogram are computed from both directions, which represent the cumulative distribution functions (CDF) of the pixel intensities.

Otsu's method is used to find the threshold value that maximizes the between-class variance while minimizing the within-class variance (Liu & Jian, 2009). This is achieved by calculating the intra-class- and inter-class variance for each possible threshold value and then selecting the threshold value that yields the maximum between-class variance. The intra-class variance measures the spread of pixel intensities within each class, while the inter-class variance measures the separation between the two classes (land and water) in terms of their mean intensities. The between-class variance is the sum of the products of the class probabilities and the squared differences between the class means and the overall mean.

Once the optimal threshold is obtained, all the pixels with intensity values below the threshold are classified as land, and those with intensity values above the threshold are classified as water. Figure

6.5a is a representation of the histogram of the sentinel-1 image depicted in figure 6.5b along with its threshold value, which was determined using Ostus's method.

It is also important to note the reason for the appearance of dark surfaces in the sentinel image, that may not represent the river network in question. The dB scale in SAR images measures the intensity of radar signals returned from the Earth's surface. Lower dB values represent smoother surfaces with less backscatter, like water bodies. This is because water surfaces tend to reflect less radar energy back to the sensor due to their smoothness and lack of surface features compared to rougher surfaces like land or vegetation. That's why, water bodies usually appear as darker areas with lower dB values in SAR imagery. Land surfaces, on the other hand, may show higher dB values due to the presence of structures, vegetation, or surface roughness that result in stronger radar reflections. In the upper right corner of Figure 6.5 (b), noticeable dark spots are apparent within the image. These dark spots are a consequence of deforestation occurring in the area, resulting in a reduction in surface roughness.

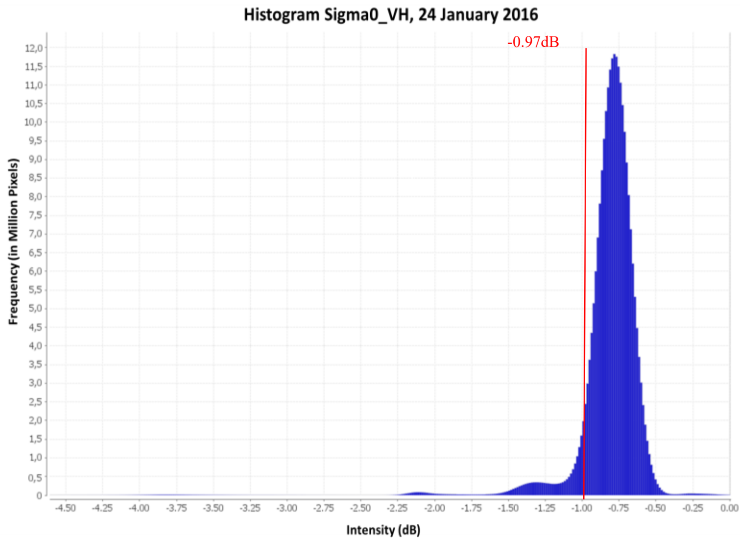

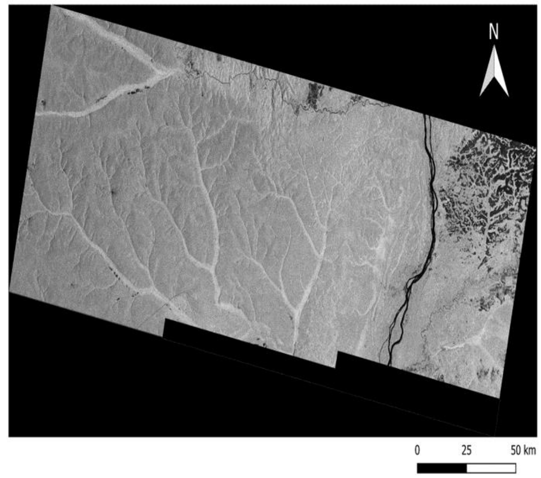

(a) (b)

Figure 6.5. Representation of the a) characteristic histogram for VH polarization with threshold value for the b) radar image of 24 January 2016, the Oubangui river.

6.2.6 Spatial distribution of water pixel probability

Once a threshold is determined for each Sentinel-1 image using Otsu's method, the pixel intensities are transformed into a binary format. In this binary representation, a pixel is assigned a value of 1 if its intensity is above the threshold, signifying water, and a value of 0 is assigned if the intensity is below the threshold value, indicating land. By applying this conversion, a clear differentiation between water and land pixels is established. The following figure 6.6b shows an example of this conversion for the binary representation of the Sentinel-1 image depicted in figure 6.6a, where the white pixels represent the binary value 0 (land pixels) and the blue pixels represent the binary value 1 (water pixels).

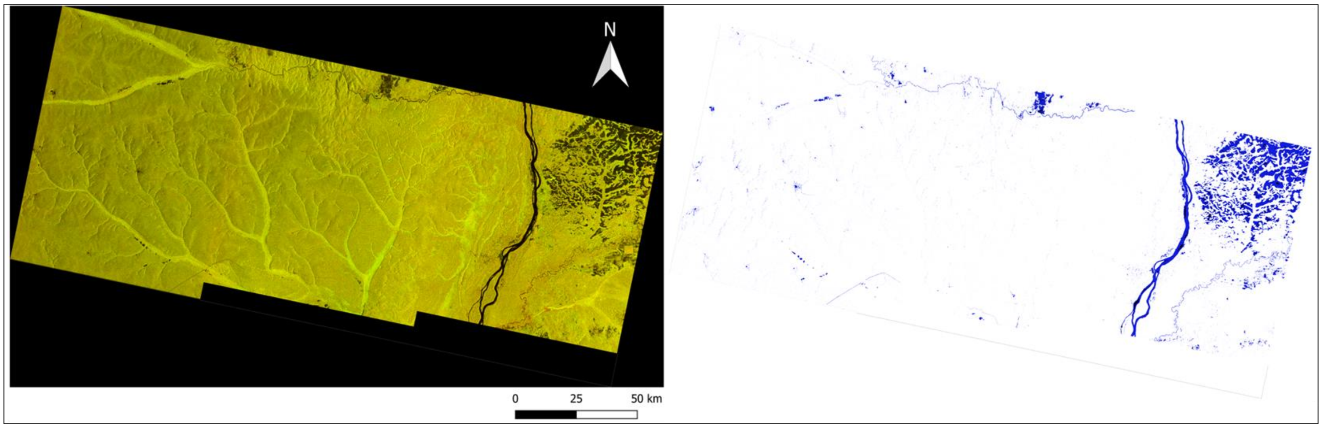

(a) (b)

Figure 6.6. Comparison between a) raw unprocessed sentinel-1 image of a section of the Oubangui River downloaded from the Alaska Satellite Facility (ASF) Data Search Vertex (https://www.earthdata.nasa.gov/, accessed on March 31st, 2023), and b) the same image post-processing and converted for binary representation of land and water pixels.

The objective is to create a map depicting the spatial distribution of water pixel probabilities by calculating the frequency of pixels labeled as water (having a binary value of 1) for each geographic coordinate across the image collection, using equation 6.3. By accumulating this information, a spatial probability distribution can be generated, illustrating the likelihood of water presence in various regions within the study area. This map aids in understanding the dynamic behavior of water bodies and their fluctuations over time.

$$P(x,y) = \left[\sum_{i=0}^{n} B(x,y)\right] \cdot 100/T \qquad (6.3)$$

Where P is the percent chance that a pixel at coordinate (x,y) will be labeled as water (having a binary value of 1). B(x,y) is the number of pixel values labeled as water within the image set at a specified coordinate, and T is the total number of images in the Sentinel-1 radar image set.

6.2.7 Surface water map generation based on water pixel availability

Creating a high-resolution water surface map from a probability table involves a step-by-step process that utilizes spatial coordinates and pixel probabilities to comprehensively depict water and land distribution. Given a table specifying the probability P(x, y) of a pixel at coordinate (x, y), the map generation begins at a chosen initial water pixel coordinate (x_0, y_0) for which its probability of being a water pixel is confirmed to be 1.0. Once the initial pixel is classified as water, the map generation process extends to its neighboring pixels (x_{0+1}, y_0), (x_0, y_{0+1}), (x_{0-1}, y_0), (x_0, y_{0-1}), (x_{0+1}, y_{0+1}), (x_{0-1}, y_{0-1}), (x_{0-1}, y_{0+1}), and (x_{0+1}, y_{0-1}). The classification of these neighbors is determined by their respective probabilities P(x_{0+1}, y_0), P(x_0, y_{0+1}), and so forth. The following figure 6.7 shows a simplified visualization of the grid scheme. The iterative approach continues, with each newly classified pixel serving as a starting point for classifying its unprocessed neighbors. Following this pattern, the entire map is systematically generated, pixel by pixel, incorporating the probabilistic information into the visual representation of water and land areas until the predetermined number of water pixels is exacerbated.

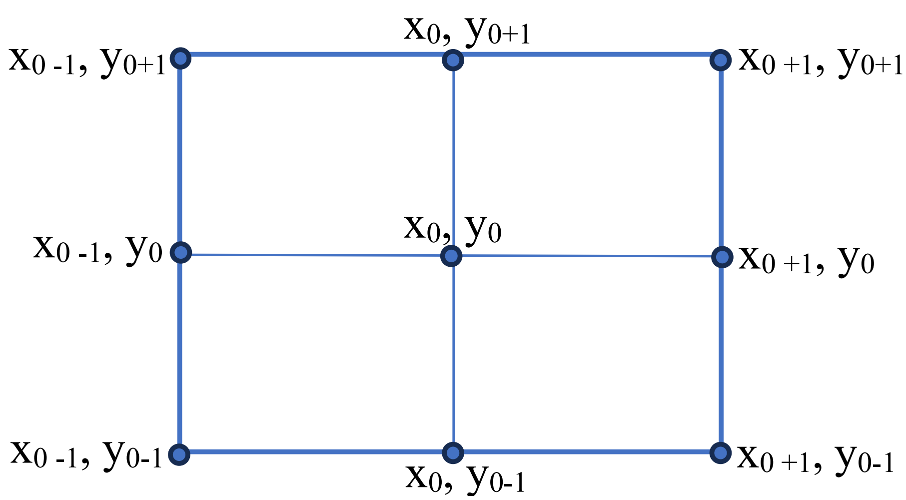

Figure 6.7. Simplified visualization of the grid scheme for a pixel located at (x0, y0) coordinate and neighboring pixels.

The following flowchart represents a sequential process for classifying pixels based on their probabilities, beginning with the highest probability pixels. It ensures that the available pixels to be classified are used efficiently according to their probabilities. The first initialization begins by setting the count of remaining pixels to be classified equal to the total number of pixels that need to be classified (minus the first initial predetermined water pixel). Then the pixels are sorted by probability, i.e., arranged in descending order, and the highest probability gets priority. This way, the pixel with the highest probability is at the beginning of the list. Then, the process involves iterating through each pixel in the sorted list until all available pixels have been sorted. Isolated pixels at a distance of approximately 2 km away from the main river network were removed for the purpose of accuracy, as isolated pixels do not represent water, it is rather a discrepancy that can be found in satellite image processing.

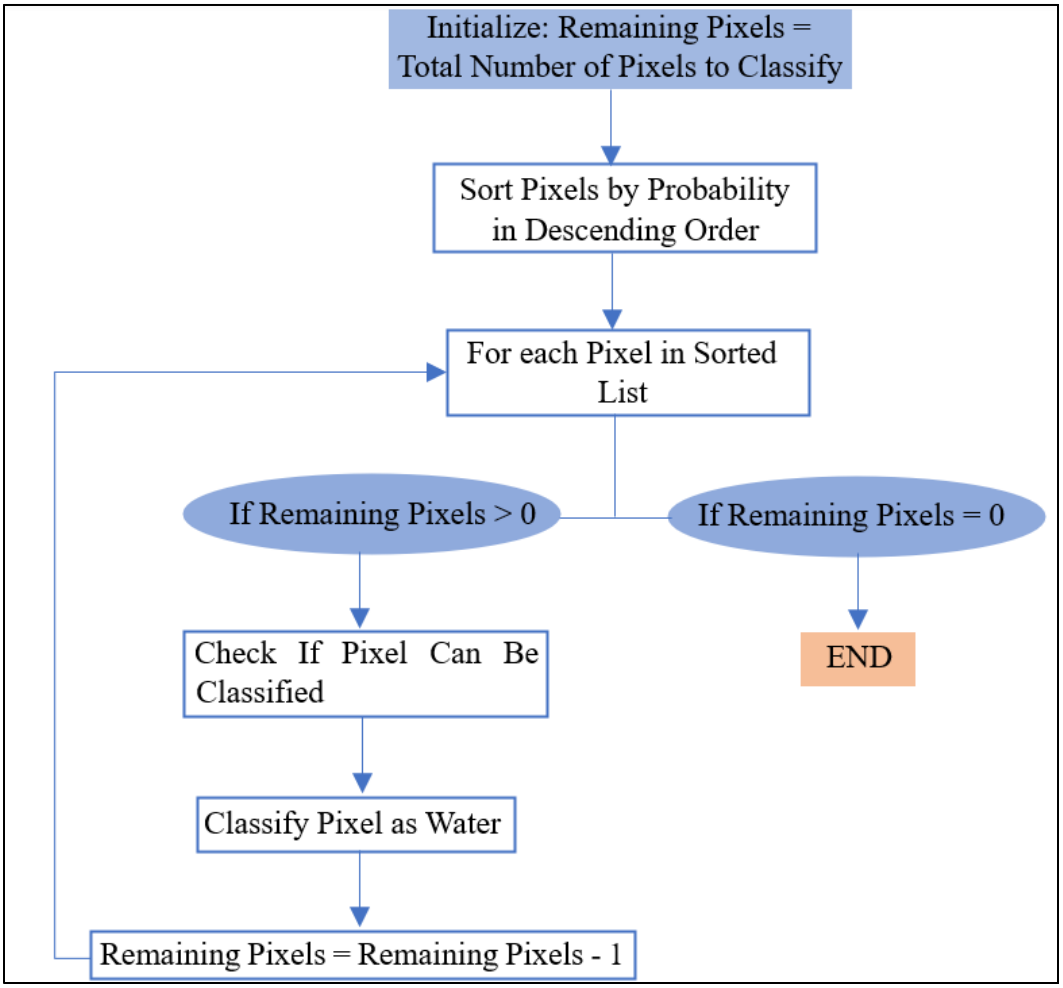

Figure 6.8. Flowchart representing a sequential process for classifying pixels based on their probabilities

In the process of extending the flood area to cover all relevant pixels, an important step involves addressing situations where all pixels with probabilities above zero have been chosen, but there are still pixels left in the distribution to be sorted. In such cases, neighboring pixels with a probability of zero are employed. This entails iterating through the map latitudinally, considering the neighboring pixels of the border pixels of the main river network. By doing so, the flood extension process ensures thorough coverage of all pixels within the designated area, guaranteeing a good water distribution in the final map. This systematic iteration through neighboring pixels, ensures that no area is overlooked or left unclassified in the mapping process.

6.3 Results and discussion

Figure 6.9 below shows the pixel-discharge relationship at various periods between 2015-2022. These dates were chosen based on observed data for which discharge was at it's highest and lowest peak for each year. This graph demonstrates a good correlation between water pixel number and discharge value; generally, when the discharge rises, water pixel number values rise as well, and when discharge is low, water pixel number value is also found to be lower. The trend line is given by the following equation:

$$y = 4E\text{-}05x + 1.5866 \qquad (6.4)$$

Where y and x represent y-axis and x-axis values, respectively. This equation can be used to estimate the number of water pixels the map will have at a certain time period based on the SWAT discharge output.

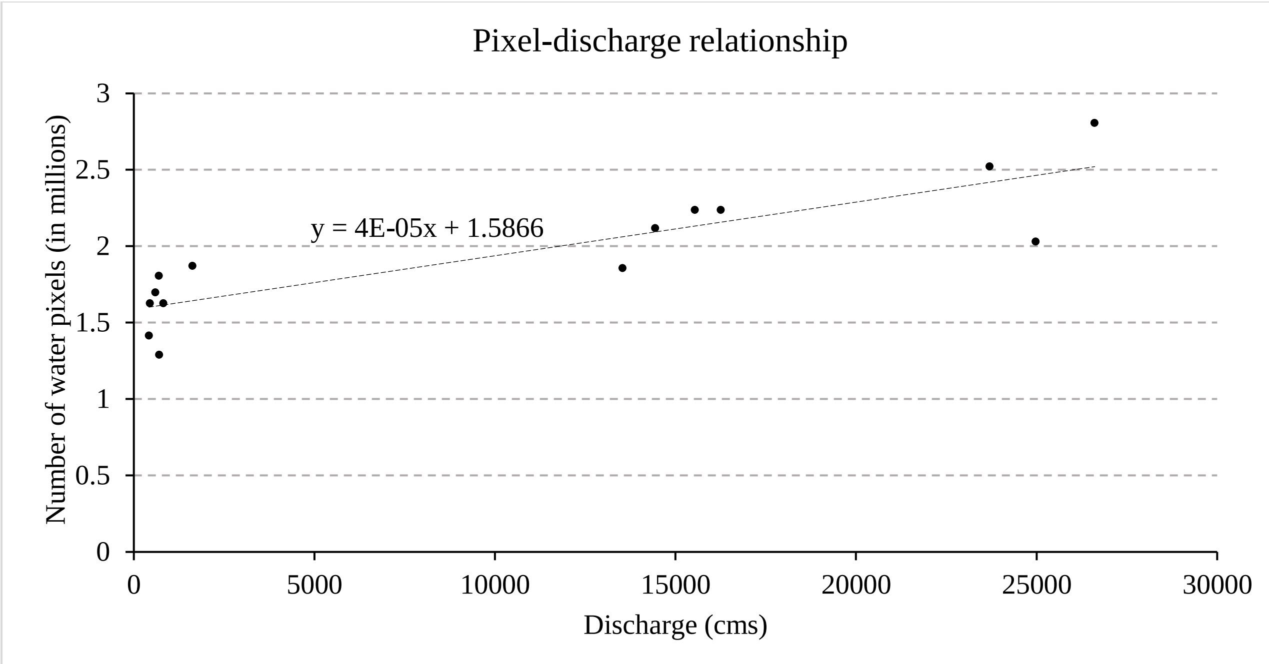

Figure 6.9. Water pixel number and SWAT output discharge relationship with trendline and linear equation.

6.3.1 Water surface map generation and accuracy

Table 6.1a below, provides crucial numerical insights into the pixel characteristics and discharge relationship observed in the original Sentinel image captured on January 24th, 2016. Whereas table 6.1b presents a breakdown of water and land classifications within the flood map generated using our innovative method on the same date. Additionally, this table offers a snapshot of the method's accuracy when applied to this particular Sentinel-1 SAR image. Table 6.1c, we delve into the overarching results, offering a percentage-based assessment of water and land classification accuracy for the flood maps produced using our novel approach. Across ten distinct Sentinel-1 SAR images acquired between 2017 and 2021, the method consistently achieves an average accuracy rate of 79.1% for correctly identifying water areas as water and an impressive average accuracy rate of 93.0% for correctly classifying land areas as land. These results underscore the method's reliability and consistency in delivering accurate flood mapping outcomes across a range of temporal scenarios. To clarify, the dates utilized for determining accuracy were distinct from those employed for establishing the pixel-discharge relationship. These two aspects were kept separate to ensure the accuracy assessment remained independent of the pixel-discharge relationship determination.

Table 6.1a. Pixel characteristics and discharge relationship for sentinel-1 image taken January 24th, 2016

Date	Discharge (cms)	Number of water pixels	Number of land pixels	Total pixels
January 24th, 2016	13540	101257	1769372	1870629

Table 6.1b. Pixel characteristics and discharge relationship for produced flood map on January 24th, 2016, using new method

Pixel classification	Discharge (cms)	Number of water pixels	Number of land pixels	Percentage Accuracy
Water Classified as water	13540	87182		86.1%
Water classified as land		14075		
Land classified as water			34951	98.0%
Land classified as land			1734421	

Table 6.1c. Percentage accuracy of water and land classification for produced flood maps using new method

Date of taken Sentinel-1	Sentinel-1 SAR image ID	Percentage accuracy of land classification	Percentage accuracy of water classification

SAR image			
February 11th, 2017	S1A_IW_GRDH_1SDV_20170211T043251_20170211T043316_015231_018F27_3D9D	91.0%	79.2%
October 9th, 2017	S1A_IW_GRDH_1SDV_20171009T043306_20171009T043331_018731_01F9B1_6850	94.2%	86.0%
February 18th, 2018	S1A_IW_GRDH_1SDV_20180218T043303_20180218T043328_020656_0235FC_D08B	94.9%	78.9%
September 22nd, 2018	S1A_IW_GRDH_1SDV_20180922T043313_20180922T043338_023806_0298E8_76C4	83.5%	79.6%
February 13th, 2019	S1A_IW_GRDH_1SDV_20190213T043241_20190213T043310_025906_02E264_244A	96.7%	72.4%
August 24th, 2019	S1A_IW_GRDH_1SDV_20190824T043318_20190824T043343_028706_033FE6_5DBE	95.9%	77.8%
February 8th, 2020	S1A_IW_GRDH_1SDV_20200208T043247_20200208T043316_031156_0394EB_A256	96.7%	68.4%
August 20th, 2020	S1A_IW_GRDH_1SDV_20200830T043325_20200830T043350_034131_03F6C9_2392	89.8%	88.9%
January 21st, 2021	S1A_IW_GRDH_1SDV_20210121T043323_20210121T043348_036231_043FDE_A5B6	95.6%	78.4%
October 24th, 2021	S1A_IW_GRDH_1SDV_20211024T043332_20211024T043357_040256_04C503_1FCF	91.9%	81.1%
	AVERAGE	**93.0%**	**79.1%**

6.3.2 Water surface map generation for future projections

This new method was used to predict the flood plain under future conditions, using discharge outputs from the calibrated and validated swat model. The following table 6.2a, b, and c, shows the results of the frequency analysis conducted for the historical period (1952-2010), and three future periods (2011-2040), (2041-2070), (2071-2100), while demonstrating the 25-, 50-, and 100-year floods for RCP4.5 and RCP8.5, respectively.

Table 6.2a. Frequency analysis results demonstrating 25-, 50-, and 100-year floods for the historical period

Period of Interest	25-Year Flood (cms)	50-Year Flood (cms)	100-Year Flood (cms)
Historical Period (1952-2010)	30127.1 cms	36061.6 cms	41834.4 cms

Table 6.2b. Frequency analysis results demonstrating 25-, 50-, and 100-year floods for three future periods under RCP4.5

Period of Interest	25-Year Flood (cms)	50-Year Flood (cms)	100-Year Flood (cms)
Future Period 1 (2011-2040)	32124.6	37927.4	43578.7
Future Period 2 (2041-2070)	32215.9	38376.3	44425.0
Future Period 3 (2071-2100)	33361.0	39931.3	46410.8

Table 6.2c. Frequency analysis results demonstrating 25-, 50-, and 100-year floods for three future periods under RCP8.5

Period of Interest	25-Year Flood (cms)	50-Year Flood (cms)	100-Year Flood (cms)
Future Period 1 (2011-2040)	34126.4	39976.2	45548.5
Future Period 2 (2041-2070)	38236.9	40673.3	48691.0
Future Period 3 (2071-2100)	39367.2	41765.4	51993.0

The most significant changes in flood frequency over time are evident in the above tables displaying frequency analysis results for historical and future periods. In the historical period (1952-2010), the 25-, 50-, and 100-year floods were measured at 30,127.1 cms, 36,061.6 cms, and 41,834.4 cms, respectively. The future projections under two different RCPs reveal substantial increases in flood magnitudes. The flood regime of future period 3 under RCP8.5 shows a substantial projected increase of approximately 30.6%, 38.6%, and 72.3% for the 25-year, 50-year, and 100-year flood, respectfully. These periods were chosen to be displayed in the following figure 6.10 a, b, and c, since they represent the most significant changes in flood frequencies, reflecting the potential long-term impacts of climate change, and thus necessitating proactive mitigation and adaptation measures.

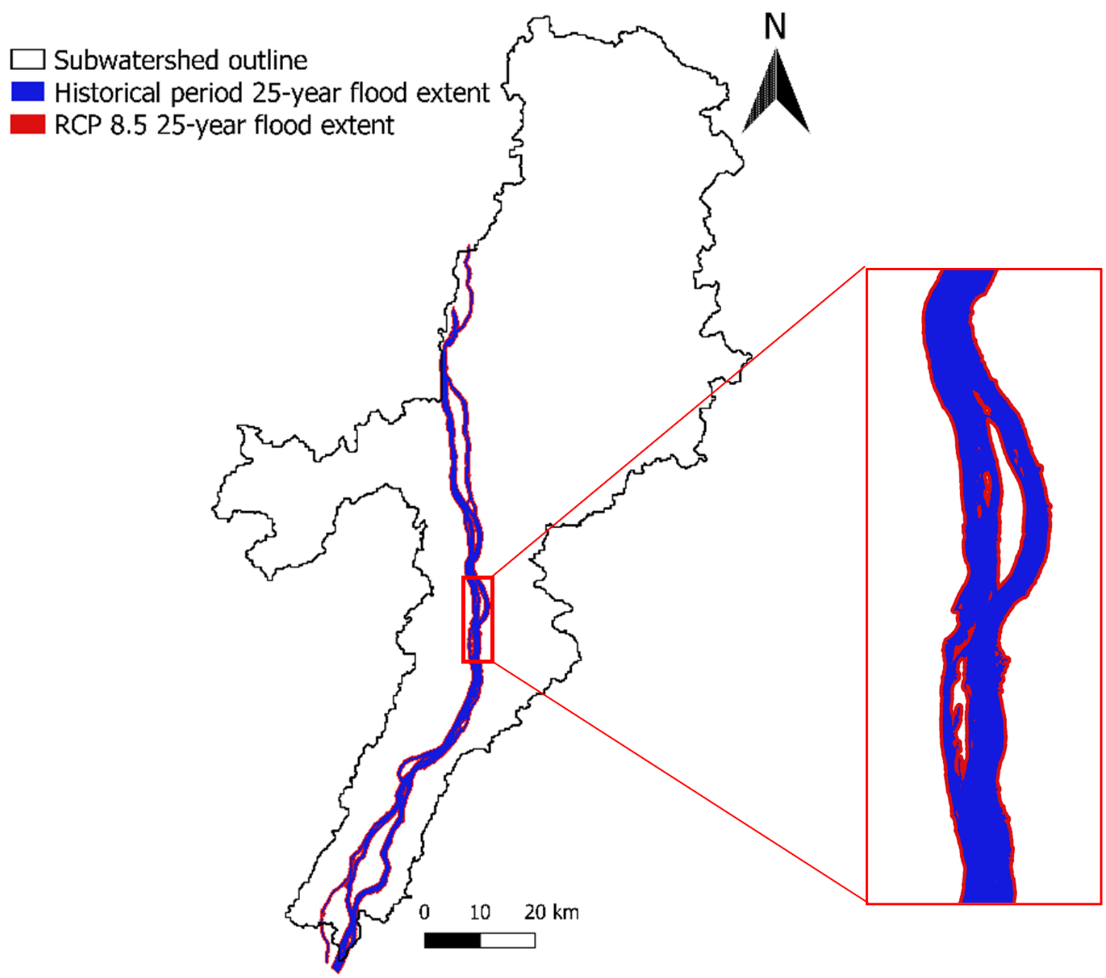

(a)

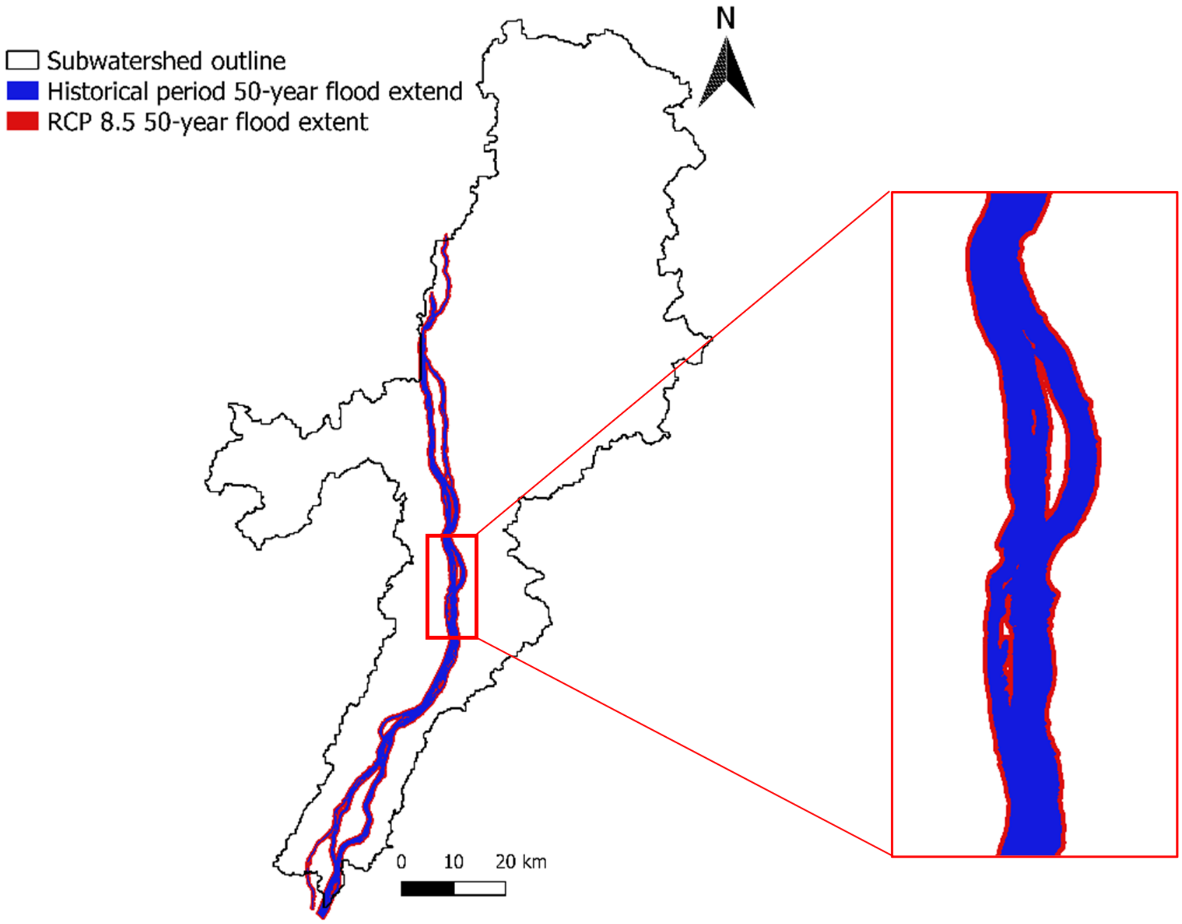
Subwatershed outline
Historical period 50-year flood extend
RCP 8.5 50-year flood extent
N
0
10
20 km

(b)

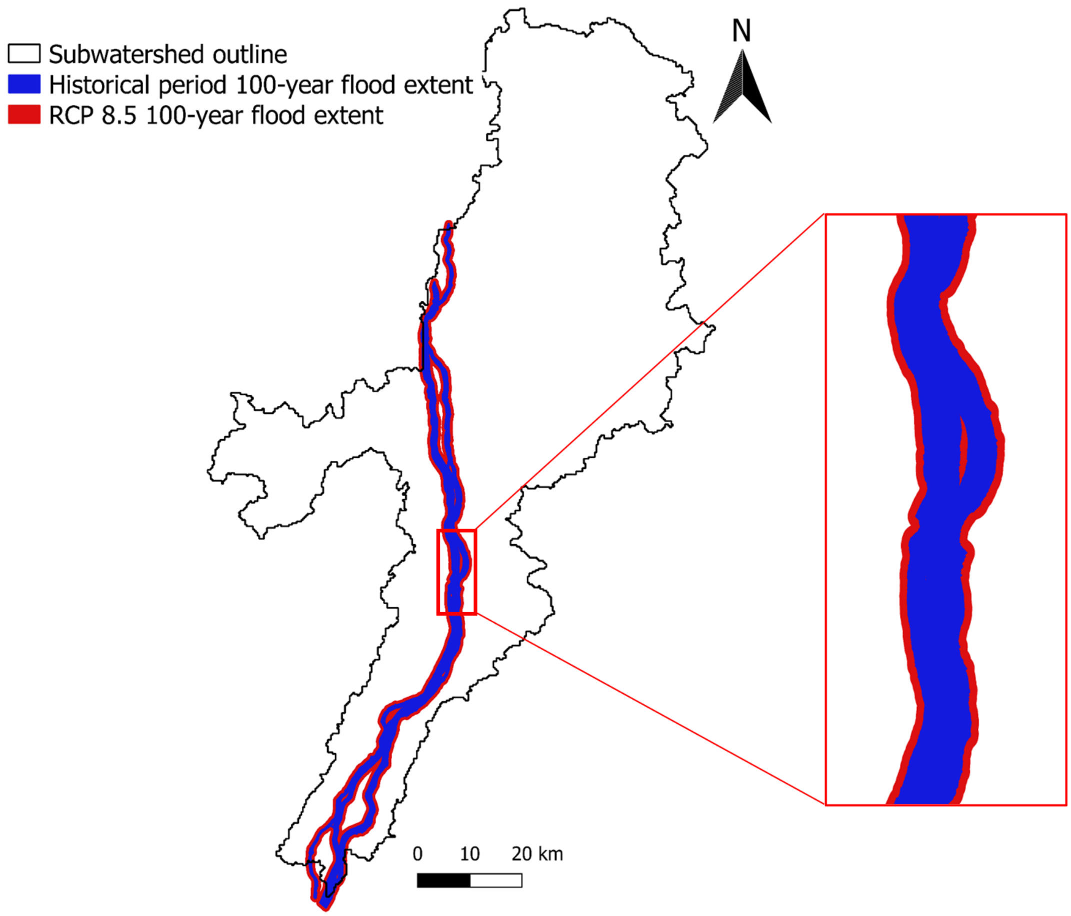

(c)

Figure 6.10. Demonstration of the flood plain extent of the a)25-year, b) 50-year, and c) 100-year floods for future period 3 (2071-2100) under RCP8.5 and the 25-year floods of the historical period (1952-2010).

The analysis of projected floodplain expansion from 2071 to 2100 under the RCP8.5 scenario reveals concerning trends. The 25-year floodplain area increased by 68.29 km² (a 12% increase), the 50-year floodplain expanded by 123.34 km² (a 20% increase), and the 100-year floodplain grew by 314.70 km² (a 30% increase). The progressive expansion of the floodplain in all these scenarios serves as a clear indicator of the potential trend of heightened flood risk in the region over time due to climate change. It underlines the urgency of implementing comprehensive strategies to adapt to these changing conditions, including enhanced infrastructure resilience, improved land-use planning, and measures to reduce greenhouse gas emissions to mitigate the impacts of climate change. Failure to address this issue could lead to devastating consequences for the environment, communities, and the economy in the years to come. The following table 6.3a and b provide information about floodplain expansion under RCP4.5 and RCP8.5, for the three future periods.

Table 6.3a. Flood plain expansion for the 25-year, 50-year, and 100-year flood under RCP4.5 for three future periods

Period of Interest	25-Year Flood (km^2)	50-Year Flood (km^2)	100-Year Flood (km^2)
Future Period 1 (2011-2040)	36.36	37.93	43.58
Future Period 2 (2041-2070)	43.12	67.64	87.60
Future Period 3 (2071-2100)	59.78	99.79	215.42

Table 6.3b. Flood plain expansion for the 25-year, 50-year, and 100-year flood under RCP8.5 for three future periods

Period of Interest	25-Year Flood (km^2)	50-Year Flood (km^2)	100-Year Flood (km^2)
Future Period 1 (2011-2040)	38.40	42.25	62.71
Future Period 2 (2041-2070)	59.98	71.32	116.24
Future Period 3 (2071-2100)	68.29	123.34	314.70

These tables allow for a comparison of floodplain expansion between two different emissions scenarios, RCP4.5 and RCP8.5, and across multiple future time periods which were produced using the new method. The percentage increase in floodplain areas tends to be higher for larger return periods (e.g., 100-Year Flood) and later future periods, reflecting a potentially greater impact of climate change on flood risks over time. The data provides insights into how climate change, as reflected in these emission scenarios, impacts flood risks and the potential for increased floodplain areas over time.

6.3.3 Discussion

Considering its relative accuracy and mostly it’s low computational requirements, the utilization of a combination of a calibrated and validated SWAT model with Sentinel-1 SAR images to create flood maps for the Oubangui River section within the Congo Basin presents a promising and efficient approach, particularly when contrasted with the time-consuming nature of traditional flood mapping software like HEC-RAS. However, the Congo Basin's sheer size poses a significant challenge. Covering approximately 3.7 million square kilometers, it is an enormous area to monitor, and obtaining Sentinel-1 images for the entire basin can be a logistical challenge. These images provide valuable data but need to be downloaded and processed, consuming substantial processing power and storage capacity. Consequently, in our study, we opted to focus on a specific sub-watershed of the Oubangui River instead of the entire basin to manage these constraints. This strategic decision allowed us to work with a manageable data subset while still capturing meaningful flood information.

One of the key advantages of this approach is its accuracy. The combination of discharge data from the SWAT model and Sentinel-1 imagery offers a robust foundation for flood mapping. By calibrating and validating the SWAT model, users ensure that the hydrological component of the methodology is reliable. On the other hand, the SAR images provide timely and high-resolution data for flood detection, allowing users to accurately delineate flood extents. This method is user-friendly, which is a significant benefit for both researchers and disaster management practitioners. Unlike traditional flood modeling software, which often demands a steep learning curve and specialized expertise, this approach simplifies the process. With the right tools and guidance, users can quickly generate flood maps without diving into complex software operations. This user-friendly aspect makes the methodology accessible to a broader audience, including local authorities and emergency responders who may need rapid flood information during critical situations.

The study's relevance is paramount in the context of current environmental and disaster management challenges that states and communities have to deal with. It addresses critical issues related to flood mapping using an innovative and efficient methodology. Some key points highlighting the study's significance:

- Timely and Accurate Flood Mapping: With the increasing frequency and intensity of floods due to climate change, having a method that can rapidly and precisely map flood extents is crucial. This study offers a solution that can significantly improve response times during flood events.
- Resource Efficiency: Traditional flood mapping software often requires substantial resources, both in terms of time and technology. This study's approach offers a cost-effective alternative, making flood mapping accessible to a wider range of organizations, stakeholders and regions.

- Risk Assessment: Accurate flood maps are essential for identifying and assessing flood-prone areas. This information is invaluable for urban planning, disaster preparedness, and risk reduction strategies for national and subnational actors, agencies and institutions.
- Better/Integrated Disaster Management and Climate Change Adaptation :Rapid and accurate flood mapping can significantly improve disaster management efforts. It enables authorities to allocate resources efficiently, evacuate vulnerable areas in a timely manner, and minimize the impact of floods on communities. As climate change continues to alter precipitation patterns and increase the frequency of extreme weather events, having an efficient flood mapping method becomes even more critical. This study contributes to the capacity to adapt to these changing conditions.

6.4 Conclusions

In conclusion, this study has demonstrated the efficacy and precision of our innovative flood mapping approach in the Oubangui River section of the Congo Basin. By integrating Sentinel-1 SAR imagery with discharge data from a calibrated and validated SWAT model, we established a pixel-discharge relationship that enables the accurate prediction of water (85.9%) and land (97.9%) pixels. With the innovative approach presented in this study for mapping floods in the Oubangui River section of the CRB, traditional hydrodynamic models such as HEC-RAS may no longer be necessary. The methodology offers a time-saving and computationally simpler alternative. Traditional hydrodynamic models like HEC-RAS require detailed topographic data and extensive computational resources to simulate flow dynamics and predict flood extents accurately. In contrast, the proposed method utilizes SAR imagery to directly extract surface water data and establish relationships between pixels and water discharge values, without the need for intricate hydraulic modeling. This streamlined approach eliminates the need for complex model setup, calibration, and validation processes associated with hydrodynamic models, potentially saving significant time and computational resources. Additionally, the methodology's high accuracy in predicting flooded and dry areas, as demonstrated by the study's results, highlights its effectiveness in supporting flood mapping and disaster management efforts in the Congo Basin. By enhancing the region's ability to respond effectively to flood events, this approach offers valuable insights for improving flood resilience and disaster preparedness in ecologically important and vulnerable areas like the Congo River Basin.

The methodology has not been without its challenges, particularly in managing the vast geographical area and the computational demands inherent in processing such extensive datasets. However, our focus on specific sub-watersheds has proven instrumental in mitigating these challenges. Looking ahead, the acceptable accuracy and user-friendly nature of our method position is a valuable asset for flood mapping endeavours. This approach significantly enhances the capacity to respond effectively to flood events in an ecologically significant and vulnerable region like the Congo Basin. Showing potential to enhance disaster management strategies and contribute to environmental conservation efforts, the method holds great promise and marks a significant step forward in the field of flood mapping, as a powerful tool to safeguard communities and ecosystems in the face of an evolving climate and environmental challenges/crises. Overall, we reiterate that by simplifying the flood mapping process, this study offers information and knowledge to support regions with limited resources and technology to improve flood risk assessment and management. The study's relevance lies in its potential to scale to a given context and how we approach flood mapping, making it more efficient, cost-effective, and accessible and thereby enhanced capacity to respond to floods, safeguard communities, and adapt to the changing climate.

6.5 References

Amitrano, Donato, et al. "Unsupervised rapid flood mapping using Sentinel-1 GRD SAR images." IEEE Transactions on Geoscience and Remote Sensing 56.6 (2018): 3290-3299.

Arnold, Jeffrey G., et al. "Large area hydrologic modeling and assessment part I: model development 1." JAWRA Journal of the American Water Resources Association 34.1 (1998): 73-89.

Cannon, Alex J., Stephen R. Sobie, and Trevor Q. Murdock. "Bias correction of GCM precipitation by quantile mapping: how well do methods preserve changes in quantiles and extremes?" Journal of Climate 28.17 (2015): 6938-6959.

Dasallas, Lea, Yeonsu Kim, and Hyunuk An. "Case study of HEC-RAS 1D–2D coupling simulation: 2002 Baeksan flood event in Korea." Water 11.10 (2019): 2048.

Fatras, Christophe, et al. "Hydrological dynamics of the Congo Basin from water surfaces based on L-band microwave." Water Resources Research 57.2 (2021): e2020WR027259.

Giorgi, Filippo, and William J. Gutowski Jr. "Regional dynamical downscaling and the CORDEX initiative." Annual review of environment and resources 40 (2015): 467-490.

Hakala, Kirsti, Nans Addor, and Jan Seibert. "Hydrological modeling to evaluate climate model simulations and their bias correction." Journal of Hydrometeorology 19.8 (2018): 1321-1337.

Hu, Shunshi, et al. "Automatic extraction of water inundation areas using Sentinel-1 data for large plain areas." Remote Sensing 12.2 (2020): 243.

Karam, Sara, et al. "Assessing the impacts of climate change on climatic extremes in the Congo River Basin." Climatic Change 170.3-4 (2022): 40.

Karam, Sara, et al. "Impacts of Climate Change on Hydrological Regimes in the Congo River Basin." Sustainability 15.7 (2023): 6066.

Kitambo, Benjamin, et al. "Large-scale spatio-temporal variability of the Congo Basin surface hydrologic components from space." EGU General Assembly Conference Abstracts. 2022.

Lennon, Kyle R., Gareth H. McKinley, and James W. Swan. "Scientific machine learning for modeling and simulating complex fluids." Proceedings of the National Academy of Sciences 120.27 (2023): e2304669120.

Li, Yu, et al. "An automatic change detection approach for rapid flood mapping in Sentinel-1 SAR data." International journal of applied earth observation and geoinformation 73 (2018): 123-135.

Liu, Dongju, and Jian Yu. "Otsu method and K-means." 2009 Ninth International conference on hybrid intelligent systems. Vol. 1. IEEE, 2009.

Mancini, Francesco, Francesca Grassi, and Nicola Cenni. "A workflow based on SNAP–StaMPS open-source tools and GNSS data for PSI-Based ground deformation using dual-orbit sentinel-1 data: Accuracy assessment with error propagation analysis." Remote Sensing 13.4 (2021): 753.

Mao, Yuna, et al. "Flood inundation generation mechanisms and their changes in 1953–2004 in global major river basins." Journal of Geophysical Research: Atmospheres 124.22 (2019): 11672-11692.

Mustafa, Wan Azani, Haniza Yazid, and Mastura Jaafar. "An improved sauvola approach on document images binarization." Journal of Telecommunication, Electronic and Computer Engineering (JTEC) 10.2 (2018): 43-50.

Ndehedehe, Christopher E., et al. "Modelling the impacts of global multi-scale climatic drivers on hydro-climatic extremes (1901–2014) over the Congo basin." Science of The Total Environment 651 (2019): 1569-1587.

Paris, Adrien, et al. "Monitoring Hydrological Variables from Remote Sensing and Modeling in the Congo River Basin." Congo Basin Hydrology, Climate, and Biogeochemistry: A Foundation for the Future (2022): 339-366.

De Paiva, Rodrigo Cauduro Dias, et al. "Large-scale hydrologic and hydrodynamic modeling of the Amazon River basin." Water Resources Research 49.3 (2013): 1226-1243.

Sarr, M. A., et al. "Comparison of downscaling methods for mean and extreme precipitation in Senegal." Journal of Hydrology: Regional Studies 4 (2015): 369-385.

Shahabi, Himan, et al. "Flood detection and susceptibility mapping using sentinel-1 remote sensing data and a machine learning approach: Hybrid intelligence of bagging ensemble based on k-nearest neighbor classifier." Remote Sensing 12.2 (2020): 266.

Sridhar, Venkataramana, et al. "Water Budgets and Droughts under Current and Future Conditions in the Congo River Basin." Congo Basin Hydrology, Climate, and Biogeochemistry: A Foundation for the Future (2021).

Tripathy, Pratyush, and Teja Malladi. "Global Flood Mapper: a novel Google Earth Engine application for rapid flood mapping using Sentinel-1 SAR." Natural Hazards 114.2 (2022): 1341-1363.

Tshimanga, Raphael M., et al. "Towards a framework of catchment classification for hydrologic predictions and water resources management in the ungauged basin of the Congo River: An a priori approach." Congo Basin Hydrology, Climate, and Biogeochemistry: A Foundation for the Future (2022): 469-498.

Tshimanga RM, Bola G, Kabuya P, Nkaba L, Neal J, Hawker L, Trigg AM, Bates P, Hughes AD, Hughes Laraque A, Woods R, Wagener T (2020) Towards a framework of catchment classification for hydrologic predictions and water resources management in the ungauged Basin of the Congo River: An a priori approach. Accepted: American Geophysical Union – AGU Willey.

Tshimanga, R. M., and D. A. Hughes. "Climate change and impacts on the hydrology of the Congo Basin: The case of the northern sub-basins of the Oubangui and Sangha Rivers." Physics and Chemistry of the Earth, Parts A/B/C 50 (2012): 72-83.

Uddin, Kabir, Mir A. Matin, and Franz J. Meyer. "Operational flood mapping using multi-temporal Sentinel-1 SAR images: A case study from Bangladesh." Remote Sensing 11.13 (2019): 1581.

Vekaria, Darshil, et al. "A change detection approach to flood inundation mapping using multi-temporal Sentinel-1 SAR images, the Brahmaputra River, Assam (India): 2015–2020." Journal of Earth System Science 132.1 (2022): 3.

Yang, Xiao, et al. "Multi-threshold image segmentation for melanoma based on Kapur's entropy using enhanced ant colony optimization." Frontiers in Neuroinformatics 16 (2022): 1041799.

Chapter 7

Conclusion and recommendations for future work

7.1 Conclusions

In this thesis, we have proposed new approaches to understand climate change impacts on the Congo River Basin (CRB), emphasizing regions with high potential for extreme climatic and hydrological events, such as the Oubangui River section. The first study focuses on assessing future changes in rainfall-induced flash floods and drought regimes, employing four selected extreme climatic indices as proxies. By utilizing statistically downscaled output from eleven Regional Climate Models (RCMs) under different emission scenarios, our findings reveal significant changes in precipitation patterns, with potential increases in drought frequency and flash floods in specific regions. The second study explores the hydrological implications of climate change in the CRB, utilizing a Soil and Water Assessment Tool (SWAT) model calibrated with daily observations and downscaled climate data. Our results indicate substantial alterations in streamflow, with potential consequences for agriculture, hydropower, and water availability for human and ecological systems, emphasizing the need for adaptive strategies. The third study introduces an innovative flood mapping approach for the Oubangui River section, combining Sentinel-1 Synthetic Aperture Radar (SAR) imagery with a calibrated and validated SWAT model. This novel methodology demonstrates high accuracy in predicting water and land pixels, providing a valuable tool for flood mapping and disaster management in the vulnerable CRB. Collectively, these studies contribute to a comprehensive understanding of climate change impacts on the CRB's hydrological patterns and underscore the importance of adaptive strategies and effective disaster management in this ecologically significant region.

7.2 Limitations and constraints of the research

While this research contributes valuable insights to understanding climate change impacts on the CRB, it is important to acknowledge certain limitations and constraints inherent in the studies:

Data Uncertainty and Scarcity:

The reliability of the findings heavily depends on the accuracy of the input data. Data scarcity in the CRB have led to limitations in the representativeness of the observed and downscaled data, potentially introducing uncertainties in the model outcomes.

Model Assumptions and Simplifications:

The methodologies employed, such as the use of extreme climatic indices and the SWAT model, involve assumptions and simplifications that may not fully capture the complexity of the natural system. Model uncertainties and limitations in representing intricate processes could impact the accuracy of projections.

Climate Models Limitations:

The utilization of multiple RCMs is recommended to capture the uncertainty in the projections, and the choice of RCMs may influence the outcomes. We used 20 RCMs and four GCMs, which are less than the total number of available model simulations. Furthermore, our work is based on CMIP five despite the fact that CMIP 6 simulations are available.

Socioeconomic Dynamics and Adaptive Strategies:

While the studies emphasize the need for adaptive strategies, the incorporation of socioeconomic factors, human behaviors, and policy responses in the face of climate change is complex. The research may not fully capture the dynamic interplay between environmental changes and societal responses.

Generalization to Other Basins:

The flood mapping technique that was developed in the third paper has a specific focus on the Oubangui River section, which may limit the generalizability of findings to other river basins or regions with different geological, climatic, and socioeconomic characteristics.

Technology and Resource Constraints:

The novel flood mapping approach introduced in the third study relies on advanced technology such as Sentinel-1 SAR imagery. Accessibility and manipulation of such technology may pose constraints for broader application, particularly in regions with limited resources.

Assessment of Ecosystem Response:

The ecological implications of the observed and projected hydrological changes in the CRB, including potential impacts on biodiversity and ecosystem services, may not be fully addressed, and further research may be needed to comprehensively understand these aspects.

Despite these limitations, the research provides a foundational understanding of climate change impacts in the CRB, serving as a starting point for future studies and highlighting the importance of considering uncertainties in climate modeling and the need for integrated, multidisciplinary approaches to address the challenges posed by climate change in this ecologically significant region.

7.3 Recommendations for future work

Building on the insights gained from the current research and considering its limitations, several recommendations for future work are proposed.

Enhanced Data Collection and Validation:

Invest in more extensive and accurate data collection efforts for the CRB, addressing data scarcity and ensuring the availability of high-quality observational data. Additionally, thorough validation of downscaled and modeled data against ground truth observations will improve the reliability of future projections.

Continuous Monitoring and Evaluation:

Establish long-term monitoring programs to continuously assess and validate model predictions against real-world observations. This iterative process will enhance the accuracy and reliability of climate models over time.

Long-Term Climate Analysis:

Extend the analysis of future climate impacts to longer timeframes or consider dynamic assessment periods that adapt to evolving climate conditions. This approach would enable a more nuanced understanding of long-term trends and variability in the CRB.

Integration of Socioeconomic Factors:

Integrate socioeconomic factors, human behavior, and adaptive strategies into climate models to better understand the reciprocal influences between environmental changes and human responses. This holistic approach will provide a more realistic assessment of the potential impacts and inform more effective adaptation strategies.

Cross-Basin Comparative Studies:

Conduct comparative studies with other river basins facing similar climate challenges to identify commonalities and differences. This broader perspective can contribute to a more comprehensive understanding of climate change impacts on the CRB and on river basins globally.

Ecological Impact Assessment:

Undertake in-depth assessments of the ecological impacts resulting from the observed and projected hydrological changes in the CRB. This includes investigating potential effects on biodiversity, ecosystem services, and overall ecosystem health.

Stakeholder Engagement and Policy Integration:

Foster collaboration with local communities, governments, and relevant stakeholders to better understand local perspectives and incorporate community-driven adaptive strategies into climate change mitigation and adaptation policies.

By addressing these recommendations, future research endeavors can contribute to a more nuanced and comprehensive understanding of climate change impacts on the CRB, fostering effective strategies for sustainable water resource management and resilience-building in the face of evolving climate dynamics.